



**Calhoun: The NPS Institutional Archive**  
**DSpace Repository**

---

Theses and Dissertations

1. Thesis and Dissertation Collection, all items

---

1994

# Impact of physical processes on maritime frontogenesis

Thompson, William Travis

Monterey, California. Naval Postgraduate School

---

<http://hdl.handle.net/10945/42923>

---

This publication is a work of the U.S. Government as defined in Title 17, United States Code, Section 101. Copyright protection is not available for this work in the United States.

*Downloaded from NPS Archive: Calhoun*



Calhoun is the Naval Postgraduate School's public access digital repository for research materials and institutional publications created by the NPS community. Calhoun is named for Professor of Mathematics Guy K. Calhoun, NPS's first appointed -- and published -- scholarly author.

**Dudley Knox Library / Naval Postgraduate School**  
**411 Dyer Road / 1 University Circle**  
**Monterey, California USA 93943**

<http://www.nps.edu/library>

AD-A283 105



①

# NAVAL POSTGRADUATE SCHOOL Monterey, California



94-25252



243Pr

## DISSERTATION

DTIC  
ELECTE  
AUG 11 1994  
S B D

### Impact of Physical Processes on Maritime Frontogenesis

by

William Travis Thompson

June 1994

Dissertation Advisor:

R. T. Williams

Approved for public release, distribution is unlimited.

THIS QUALITY INSPECTED 1

94 8 10 013

REPORT DOCUMENTATION PAGE			Form Approved OMB No 0704-0188	
<small>Public reporting burden for this collection of information is estimated to average 1 hour per response, including the time for reviewing instructions, searching existing data sources, gathering and maintaining the data needed, and completing and reviewing the collection of information. Send comments regarding this burden estimate or any other aspect of this collection of information, including suggestions for reducing this burden, to Washington Headquarters Services, Directorate for Information Operations and Reports, 1215 Jefferson Davis Highway, Suite 1204, Arlington, VA 22202-4302 and to the Office of Management and Budget, Paperwork Reduction Project (0704-0188), Washington, DC 20503</small>				
1. AGENCY USE ONLY (Leave blank)	2. REPORT DATE June 1994	3. REPORT TYPE AND DATES COVERED Doctoral Dissertation		
4. TITLE AND SUBTITLE IMPACT OF PHYSICAL PROCESSES ON MARITIME FRONTOGENESIS			5. FUNDING NUMBERS	
6. AUTHOR(S) Thompson, William Travis				
7. PERFORMING ORGANIZATION NAME(S) AND ADDRESS(ES) Naval Research Laboratory Marine Meteorology Division 7 Grace Hopper Avenue Monterey, CA 93943-5502			8. PERFORMING ORGANIZATION REPORT NUMBER	
9. SPONSORING/MONITORING AGENCY NAME(S) AND ADDRESS(ES)			10. SPONSORING/MONITORING AGENCY REPORT NUMBER	
11. SUPPLEMENTARY NOTES The views expressed in this thesis are those of the author and do not reflect the official policy or position of the Department of Defense or the United States Government.				
12a. DISTRIBUTION/AVAILABILITY STATEMENT Approved for public release; distribution unlimited.			12b. DISTRIBUTION CODE	
13. ABSTRACT (Maximum 200 words) A hydrostatic primitive equation model initialized in a highly baroclinically unstable state was used to simulate maritime cyclogenesis and frontogenesis. In order to identify boundary layer physical processes important in maritime frontogenesis, several different simulations were performed. An adiabatic and inviscid simulation provided the control for these experiments. The two different boundary layer parameterizations used were a K-theory parameterization and a second-order closure scheme. Results indicated that strong warm and cold fronts formed in the adiabatic and inviscid case but that the near-surface wind speed and vertical motion fields were unrealistic. In the K-theory simulation, the results were somewhat more realistic but convergence and vorticity were weaker. Results from the second-order closure simulation demonstrated that turbulent mixing of momentum was most important in producing the frontogenetic (and frontolytic) effects of the transverse secondary circulation.				
14. SUBJECT TERMS frontogenesis, second-order closure, semi-geostrophic, frontolysis, geostrophic, secondary circulation, boundary layer, quasi-geostrophic, turbulence			15. NUMBER OF PAGES 243	
			16. PRICE CODE	
17. SECURITY CLASSIFICATION OF REPORT UNCLASSIFIED	18. SECURITY CLASSIFICATION OF THIS PAGE UNCLASSIFIED	19. SECURITY CLASSIFICATION OF ABSTRACT UNCLASSIFIED	20. LIMITATION OF ABSTRACT UL	

Approved for public release; distribution is unlimited

# Impact of Physical Processes on Maritime Frontogenesis

by

William Travis Thompson  
B. S., San Jose State University, 1979  
M. S., San Jose State University, 1981

Submitted in partial fulfillment of the  
requirements for the degree of

DOCTOR OF PHILOSOPHY IN METEOROLOGY

from the


NAVAL POSTGRADUATE SCHOOL

June 1994


Author:


  
William Travis Thompson


Approved by:


  
Kenneth L. Davidson  
Professor of Meteorology

  
Robert L. Haney  
Professor of Meteorology

  
Richard H. Franke  
Professor of Mathematics

  
Carlyle H. Wash  
Professor of Meteorology

  
Roland W. Garwood  
Professor of Oceanography

  
R. Terry Williams  
Professor of Meteorology  
Dissertation Supervisor

Approved by:

  
Robert L. Haney, Chairman, Department of Meteorology

Approved by:

  
Richard S. Elster, Dean of Instruction



When you can measure what you are speaking about, and express it in numbers, you know something about it; but when you cannot measure it, when you cannot express it in numbers, your knowledge is of a meager and unsatisfactory kind: it may be the beginning of knowledge, but you have scarcely, in your thoughts, advanced to the stage of science.

- *Sir William Thomson, Lord Kelvin of Largs (1824-1907)*

<b>Accession For</b>	
NTIS GRA&I	<input checked="" type="checkbox"/>
DTIC TAB	<input type="checkbox"/>
Unannounced	<input type="checkbox"/>
Justification	
By	
Distribution/	
<b>Availability Codes</b>	
Dist	Avail and/or Special
A-1	

## ABSTRACT

A hydrostatic primitive equation model initialized in a highly baroclinically unstable state was used to simulate maritime cyclogenesis and frontogenesis. In order to identify boundary layer physical processes important in maritime frontogenesis, several different simulations were performed. An adiabatic and inviscid simulation provided the control for these experiments. The two different boundary layer parameterizations used were a K-theory parameterization and a second-order closure scheme. Results indicated that strong warm and cold fronts formed in the adiabatic and inviscid case but that the near-surface wind speed and vertical motion fields were unrealistic. In the K-theory simulation, the results were somewhat more realistic but convergence and vorticity were weaker. Results from the second-order closure simulation demonstrated that turbulent mixing of momentum was most important in producing the frontogenetic (and frontolytic) effects of the transverse secondary circulation.

## TABLE OF CONTENTS

I.	INTRODUCTION . . . . .	1
II.	LITERATURE REVIEW . . . . .	3
	A. INTRODUCTION . . . . .	3
	B. FRONTS AND BAROCLINIC WAVES . . . . .	3
	C. STRUCTURE OF FRONTAL ZONES . . . . .	4
	D. FRONTOGENESIS . . . . .	7
	1. Quasi-Geostrophic Frontogenesis . . . . .	7
	2. Semi-Geostrophic Frontogenesis . . . . .	8
	3. Quasi-geostrophic Versus Semi-geostrophic Frontogenesis . . . . .	13
	4. Frontogenesis With the Primitive Equations . . . . .	15
	E. IMPORTANCE OF BOUNDARY LAYER PROCESSES . . . . .	16
III.	DESCRIPTION OF PROPOSED WORK . . . . .	23
IV.	NUMERICAL EXPERIMENTS . . . . .	27
	A. REGIONAL FORECAST MODEL . . . . .	27
	B. INITIAL AND BOUNDARY CONDITIONS . . . . .	29
	C. BOUNDARY LAYER PARAMETERIZATIONS . . . . .	30
	1. Introduction . . . . .	30
	2. Adiabatic and Nearly Inviscid Case . . . . .	31
	3. K-Theory Boundary Layer Parameterization . . . . .	31
	4. Second-Order Closure Boundary Layer Parameterization . . . . .	34
	D. EVALUATION OF FRONTOGENETIC FORCING . . . . .	41
V.	RESULTS . . . . .	43
	A. ADIABATIC AND NEARLY INVISCID AT HIGH VERTICAL RESOLUTION . . . . .	43
	1. Development . . . . .	43
	2. Frontal Structure and Circulation . . . . .	46
	3. Frontal Development . . . . .	48
	4. Summary . . . . .	49
	B. K-THEORY BOUNDARY LAYER . . . . .	50
	1. Development . . . . .	50

2.	Frontal Structure and Circulation . . . . .	52
3.	Frontal Development . . . . .	55
4.	Insulated Surface Simulation . . . . .	58
5.	Neutral Eddy Coefficient Simulation . . . . .	60
6.	Summary . . . . .	62
C.	SECOND-ORDER CLOSURE BOUNDARY LAYER . . . . .	63
1.	Development . . . . .	63
2.	Frontal Structure and Circulation . . . . .	64
3.	Frontal Development . . . . .	67
4.	Insulated Surface Simulation . . . . .	69
5.	Free Slip Surface Simulation . . . . .	71
6.	Level 2 Simulation . . . . .	72
7.	Summary . . . . .	74
VI.	DISCUSSION . . . . .	77
A.	INTRODUCTION . . . . .	77
B.	PROCESSES DIRECTLY INFLUENCING FRONTAL GRADIENTS . . . . .	78
C.	PROCESSES INFLUENCING THE TRANSVERSE VERTICAL CIRCULATION . . . . .	82
VII.	CONCLUSIONS . . . . .	89
	APPENDIX . . . . .	201
	REFERENCES . . . . .	218
	DISTRIBUTION LIST . . . . .	226

## **LIST OF TABLES**

<b>4.1</b>	<b>MODEL CHARACTERISTICS . . . . .</b>	<b>97</b>
<b>4.2</b>	<b>VERTICAL STRUCTURE . . . . .</b>	<b>98</b>
<b>5.1</b>	<b>SUMMARY . . . . .</b>	<b>99</b>
<b>6.1</b>	<b>FULL PHYSICS VS. NO DRAG . . . . .</b>	<b>100</b>

## LIST OF FIGURES

5.1	Initial sea surface temperature field (C) over the entire model domain. . . . .	101
5.2	Meridional cross sections of the initial a) potential temperature (K) and b) zonal wind component ( $\text{m s}^{-1}$ ) from the surface to 10 mb and from the northern boundary to the southern boundary. . . . .	102
5.3	Time series of minimum surface pressure (mb) for adiabatic and inviscid simulation (AI), K-theory simulation (KTH), and second-order closure simulation (20C). . . . .	104
5.4	a) surface pressure (mb) and b) near-surface potential temperature (K) fields at hour 72. . . . .	105
5.5	a) 850 mb relative vorticity ( $\times 10^{-6} \text{ s}^{-1}$ ), b) divergence ( $\times 10^{-6} \text{ s}^{-1}$ ), and c) vertical motion ( $\times 10^{-5} \text{ mb s}^{-1}$ ) at hour 72. . . . .	107
5.6	Near-surface potential temperature (K) fields at hour 84 (AI). . . . .	110
5.7	Near-surface potential temperature (K) fields at hour 96 (AI). . . . .	111
5.8	Near-surface potential temperature (K) fields at hour 108 (AI). . . . .	112
5.9	850 mb relative vorticity ( $\times 10^{-6} \text{ s}^{-1}$ ) at hour 108 (AI). . . . .	113
5.10	a) surface pressure (mb) and b) near-surface potential temperature (K) fields at hour 120 (AI). . . . .	114
5.11	Vertical cross section of potential temperature (K) at hour 72 From the surface to $\sim 500$ mb and from 0 to 1320 km. The plane of the cross section, denoted by AB, is shown in Fig. 4b (AI). . . . .	116
5.12	Cross section of potential temperature (K) at hour 84. The plane of the cross section, denoted by CD, is shown in Fig. 6 (AI). . . . .	117
5.13	Cross section of potential temperature (K) at hour 96. The plane of the cross section, denoted by EF, is shown in Fig. 7 (AI). . . . .	118
5.14	Cross section of potential temperature (K) at hour 108. The plane of the cross section, denoted by GH, is shown in Fig. 8 (AI). . . . .	119
5.15	Cross sections of a) along-front wind component and b) front-normal wind component ( $\text{m s}^{-1}$ ) at hour 108 (AI). . . . .	120
5.16	Cross section of divergence ( $\times 10^{-4} \text{ s}^{-1}$ ) at hour 108 (AI). . . . .	122
5.17	Cross section of vertical motion ( $\mu \text{ b s}^{-1}$ ) at hour 108 (AI). . . . .	123
5.18	Cross section of relative vorticity ( $\times 10^{-4} \text{ s}^{-1}$ ) at hour 108. The plane of the cross section, denoted by GH, is shown in Fig. 9 (AI). . . . .	124

5.19	a) total adiabatic frontogenetic forcing ( $\times 10^{-11} \text{ K s}^{-1} \text{ m}^{-1}$ ) at hour 72 at 850 mb, b) tilting term, c) stretching deformation, and d) shearing deformation. . . . .	125
5.20	Total adiabatic frontogenetic forcing at hour 108 at 850 mb (AI). . .	129
5.21	a) cross section of total adiabatic frontogenetic forcing ( $\text{K s}^{-1} \text{ m}^{-1}$ ) at hour 108 and b) stretching deformation (AI). . . . .	130
5.22	Time series of minimum surface pressure (mb) (KTH). . . . .	132
5.23	Near-surface potential temperature (K) fields at hour 84 (KTH). . . .	133
5.24	Near-surface potential temperature (K) fields at hour 96 (KTH). . . .	134
5.25	Near-surface potential temperature (K) fields at hour 108 (KTH). . .	135
5.26	850 mb relative vorticity ( $\times 10^{-6} \text{ s}^{-1}$ ) at hour 108 (KTH). . . . .	136
5.27	a) surface pressure (mb) and b) near-surface potential temperature (K) fields at hour 120 (KTH). . . . .	137
5.28	Cross section of potential temperature (K) at hour 84. The plane of the cross section is shown in Fig. 23 (KTH). . . . .	139
5.29	Cross section of potential temperature (K) at hour 96. The plane of the cross section is shown in Fig. 24 (KTH). . . . .	140
5.30	Cross section of potential temperature (K) at hour 108. The plane of the cross section is shown in Fig. 25 (KTH). . . . .	141
5.31	a) cross section of along-front wind component and b) front-normal wind component ( $\text{m s}^{-1}$ ) at hour 108 (KTH). . . . .	142
5.32	Cross section of divergence ( $\text{s}^{-1}$ ) at hour 108 (KTH). . . . .	144
5.33	Cross section of vertical motion ( $\mu \text{ b s}^{-1}$ ) at hour 108 (KTH). . . . .	145
5.34	Cross section of vorticity at ( $\times 10^{-4} \text{ s}^{-1}$ ) hour 108. The plane of the cross section is shown in Fig. 26 (KTH). . . . .	146
5.35	Total adiabatic frontogenetic forcing at hour 108 ( $\times 10^{-10} \text{ K s}^{-1} \text{ m}^{-1}$ ) at 850 mb (KTH). . . . .	147
5.36	Cross section of total adiabatic frontogenetic forcing ( $\text{K s}^{-1} \text{ m}^{-1}$ ) at hour 84 (KTH). . . . .	148
5.37	Cross section of total adiabatic frontogenetic forcing at hour 96 (KTH). . . . .	149
5.38	a) cross section of total adiabatic frontogenetic forcing at hour 108, b) tilting term, and c) diabatic term (KTH). . . . .	150

5.39	Surface sensible heat flux ( $\text{W m}^{-2}$ ) at hour 108 (KTH).	153
5.40	Near-surface potential temperature (K) fields at hour 84 (KTH no flux).	154
5.41	Near-surface potential temperature (K) fields at hour 96 (KTH no flux).	155
5.42	Near-surface potential temperature (K) fields at hour 108 (KTH no flux).	156
5.43	a) cross section of potential temperature (K) at hour 84, b) at hour 96, and c) at hour 108. The planes of the cross sections are shown in Figs. 40, 41, and 42 (KTH no flux).	157
5.44	a) normalized eddy coefficient for momentum ( $K_m$ ) and b) normalized eddy coefficient for heat ( $K_h$ ) (KTH).	160
5.45	Near-surface potential temperature (K) fields at hour 108 (KTH no stab).	162
5.46	Cross section of potential temperature (K) at hour at hour 108. The plane of the cross section is shown in Fig. 45 (KTH no stab).	163
5.47	Time series of minimum surface pressure (mb) (2OC).	164
5.48	Near-surface potential temperature (K) fields at hour 84 (2OC).	165
5.49	Near-surface potential temperature (K) fields at hour 96 (2OC).	166
5.50	Near-surface potential temperature (K) fields at hour 108 (2OC).	167
5.51	850 mb relative vorticity ( $\times 10^{-6} \text{ s}^{-1}$ ) at hour 108 (2OC).	168
5.52	a) surface pressure (mb) and b) near-surface potential temperature (K) fields at 120 hour (2OC).	169
5.53	Cross section of potential temperature (K) at hour 84. The plane of the cross section is shown in Fig. 48 (2OC).	171
5.54	Cross section of potential temperature (K) at hour 96. The plane of the cross section in shown in Fig. 49 (2OC).	172
5.55	Cross section of vorticity ( $\times 10^{-4} \text{ s}^{-1}$ ) at hour 96 (2OC).	173
5.56	Cross section of vertical motion ( $\mu \text{ b s}^{-1}$ ) at hour 96 (2OC).	174
5.57	Cross section of potential temperature (K) at hour 108. The plane of the cross section is shown in Fig. 50 (2OC).	175
5.58	a) cross section of along-front wind component and b) front-normal wind component ( $\text{m s}^{-1}$ ) at hour 108.	176



5.59	Cross section of vorticity ( $\times 10^{-4} \text{ s}^{-1}$ ) at hour 108. The plane of the cross section is shown in Fig. 51 (2OC).	178
5.60	Cross section of divergence ( $\times 10^{-4} \text{ s}^{-1}$ ) at hour 108 (2OC).	179
5.61	Cross section of vertical motion ( $\mu \text{ b s}^{-1}$ ) at hour 108 (2OC).	180
5.62	Total adiabatic frontogenetic forcing ( $\times 10^{-10} \text{ K m}^{-1} \text{ s}^{-1}$ ) at hour 108 at 850 mb (2OC).	181
5.63	Cross section of total adiabatic frontogenetic forcing ( $\times 10^{-10} \text{ K m}^{-1} \text{ s}^{-1}$ ) at hour 84 (2OC).	182
5.64	Cross section of total adiabatic frontogenetic forcing at hour 96 ( $\times 10^{-10} \text{ K m}^{-1} \text{ s}^{-1}$ ) (2OC).	183
5.65	a) cross section of total adiabatic frontogenetic forcing ( $\times 10^{-10} \text{ K m}^{-1} \text{ s}^{-1}$ ) and b) tilting frontogenesis at hour 108. The plane of the cross section is shown in Fig. 62 (2OC).	184
5.66	Surface sensible heat flux ( $\text{W m}^{-2}$ ) at hour 108 (2OC).	186
5.67	Near-surface potential temperature (K) field at hour 84 (2OC no flux).	187
5.68	Near-surface potential temperature (K) field at hour 96 (2OC no flux).	188
5.69	Near-surface potential temperature (K) field at hour 108 (2OC no flux).	189
5.70	a) cross section of potential temperature (K) at hour 84 (the plane of the cross section is shown in Fig. 5.48), b) at hour 96 (see Fig. 5.49), and c) at hour 108 (see Fig. 5.50) (2OC no flux).	190
5.71	Near-surface potential temperature (K) field at hour 84 (2OC no drag).	193
5.72	Near-surface potential temperature (K) field at hour 96 (2OC no drag).	194
5.73	Near-surface potential temperature (K) field at hour 108 (2OC no drag).	195
5.74	a) cross section of potential temperature (K) at hour 84 (cross section plane is shown in Fig. 5.48), b) at hour 96 (see Fig. 5.49), and c) at hour 108 (see Fig. 5.50) (2OC no drag).	196
5.75	Cross section of divergence ( $\times 10^{-4} \text{ s}^{-1}$ ) at hour 108 (2OC no drag).	199
5.76	Cross section of vertical motion ( $\mu \text{ b s}^{-1}$ ) at hour 108 (2OC no drag).	200

5.77	Cross section of potential temperature at hour 108 (2OCL2).	201
5.78	Cross section of vertical motion ( $\mu$ b s <sup>-1</sup> ) at hour 108 (2OCL2).	202
A.1	Norwegian model schematic.	209
A.2	SK model schematic.	210
A.3	Cross section of potential temperature at hour 84 (AI).	211
A.4	Cross section of potential temperature at hour 120 (AI).	212
A.5	Near-surface potential temperature distribution at hour 120 (AI).	213
A.6	Cross section of potential temperature (K) at hour 84 (2OC).	214
A.7	Cross section of potential temperature (K) at hour 108 (2OC).	215
A.8	700 mb temperature distribution at hour 108 (2OC).	216

## ACKNOWLEDGMENTS

I would like to thank the members of my committee; Dr. Kenneth L. Davidson, Dr. Richard H. Franke, Dr. Roland W. Garwood, and Dr. Carlyle H. Wash; for their comments on the manuscript. I would also like to thank the chairman of the committee, Dr. Robert L. Haney, for the time and effort he spent in reviewing and critiquing the manuscript. I am particularly indebted to my advisor, Dr. Terry Williams, for his encouragement at various stages of the research and writing, for the time he devoted to the work, and for his keen insight and guidance. The opportunity to work on the problem of frontogenesis with Dr. Williams was a privilege and an honor. I thank also the many fine professors I encountered during my coursework at the Naval Postgraduate School, including Dr.'s Williams, Haney, Elsberry, Chang, Peng, Schoenstadt, and Garwood.

I am grateful also to members of the faculty of the Department of Meteorology at San Jose State University from whom I learned much about atmospheric science during my undergraduate career and masters degree program. I am especially grateful to the late Dr.'s Albert Miller and Christopher Reigel and to Dr. Kenneth Mackay. I am grateful also to Dr. Peter Lester, my master's thesis advisor, for his tenacity and enthusiasm in the pursuit of scientific research. I also thank Dr. Robert Bornstein, whose guidance, support, encouragement and friendship have meant so much to me.

I thank also my mentor and friend Dr. Stephen D. Burk, head of the Local Scale Simulation Section of the Marine Meteorology Division of the Naval Research Laboratory, who originally developed the one-dimensional version of the second-order closure model and with whom I worked on the three dimensional version which was subsequently used in the present study. I have learned much about me-

teorological modeling, scientific research, and intellectual integrity from Dr. Burk. Dr. Richad Hodur, head of the Mesoscale Modeling Section, developed NORAPS and provided some assistance in the early stages of the present study. I am grateful as well to Mr. Steven Bishop, head of the technical publications section, for his assistance in preparing the figures.

I could not have completed this work without the love and support of my wife, Maureen. I thank her also for her forgiveness of my absence on weekends and evenings for the last several years. I thank my son, Christopher, for his love and understanding. I also thank my parents, Travis and Jean, without whom (trite but true) none of this would have been possible. On a deeper level, however, I am grateful to them for their love and encouragement during the early years of my academic career. I am indebted to them also for providing a loving home environment which was intellectually stimulating; an environment in which academic achievement was valued but self-esteem was paramount.

## I. INTRODUCTION

Much of the rich variety of sensible weather experienced by human-kind is associated with fronts. In many instances, severe weather also is related to ascent in frontal zones. It is little wonder, therefore, that fronts have been a subject of investigation since the inception of the polar front theory during the First World War. The structure of mature frontal zones was fairly well understood at that time due to careful observations and the brilliant insights of Bjerknes and his co-workers. The mechanisms responsible for the genesis of fronts, however, were not addressed in the frontal/cyclone conceptual model of the Bergen School. Indeed, the theory held that the polar front was a semi-permanent, quasi-steady phenomenon which varied in intensity with occurrences of cyclogenesis along it; fronts were thought to be the cause of, rather than a consequence of, cyclogenesis. This concept changed with advances in instability theory during the 1940's. Much of the progress in the understanding of frontogenesis was made using numerical investigations which relied on technology not available until the mid 1960's (e.g., Williams, 1967), although the introduction of the frontogenetic function by Petterssen (1936) as extended by Miller (1948) represented a major contribution. Investigation of fronts and frontogenesis continues to occupy a prominent place in the scientific literature; Keyser and his co-workers recently discussed a generalization of the frontogenetic function (Keyser et al., 1988) and, more recently, Shapiro and Keyser proposed a major revision to the frontal/cyclone conceptual model of the Bergen School (Shapiro and Keyser, 1990).

Although considerable progress has been made, some important questions remain unanswered. There is some controversy over the limiting scale of fronts and the existence of a "brake" on frontogenesis due to a separation of the zone of maximum convergence from the zone of maximum relative vorticity. Issues such as the impact of surface heat fluxes on frontogenesis are unresolved. In fact, some of the most important outstanding issues concern the impact of boundary layer processes, including (but not limited to) surface fluxes of both heat and momentum.

The present study constitutes an attempt to address some of the topics related to the impact of boundary layer processes on maritime frontogenesis. The approach consists of using two different boundary layer parameterization schemes in a numerical simulation of frontogenesis forced by a growing baroclinic wave. An adiabatic and inviscid simulation is also performed as a control. The lower boundary conditions are characteristic of an ocean surface. Various processes are isolated in these schemes in an effort to understand their influence on frontogenesis. In particular, surface fluxes of heat and momentum are removed individually from simulations using each of the parameterization schemes. Comparison of these simulations to the full physics simulations and to the adiabatic and inviscid simulation provides insights into the impact of surface fluxes on frontogenesis. The ability of the two parameterization schemes to realistically represent the effect of turbulent mixing on frontogenesis in general and on the thermally direct ageostrophic circulation about the front in particular is also assessed.

A review of previous work on frontogenesis is presented in Chapter II. Chapter III describes the objectives of this study and details of the model and numerical experiments are discussed in Chapter IV. The results are described in Chapter V and discussed in Chapter VI. In Chapter VII, the conclusions are presented.

## **II. LITERATURE REVIEW**

### **A. INTRODUCTION**

The introduction of the polar front theory by the Bergen School following the First World War, which marked the beginning of meteorology as a quantitative physical science, held that fronts were the dynamic interfaces between differing air masses. The suggestion that fronts form in growing nonlinear baroclinic waves came during the 1940's due to advances in the theory of baroclinic instability attributable to Charney (1947) and Eady (1949). This suggestion was further substantiated by Phillips (1956) and was demonstrated conclusively by Williams (1967). Observational studies have delineated the important structural features of fronts (Sanders, 1955; Ogura and Portis, 1982; Carbone, 1982; Shapiro, 1984; Fleagle et al., 1988; Shapiro and Keyser, 1990), although some controversy has arisen over the limiting scale of frontal zones (Gall et al., 1987). Several analytical and numerical studies of the processes by which frontogenesis occurs have been performed (a brief review appears in Gill (1982)). However, some important questions regarding frontogenesis remain unanswered. One of the most fundamental of these concerns the impact of boundary layer physics on the evolution of fronts.

### **B. FRONTS AND BAROCLINIC WAVES**

Although the polar front theory and subsequent studies during the first half of this century lead to a fairly detailed description of fronts, the theoretical basis for the formation of fronts lagged far behind. The problem which had to be addressed was the creation of small-scale features in a field initially containing only large-scale features. The energy bearing baroclinic modes have scales on the order of 1000

km while frontal scales are 100 km or less. Williams (1967) used the hydrostatic Boussinesq equations in a numerical model to demonstrate that a frontal discontinuity could be produced in a finite time from an initial disturbance with a scale similar to that of the most unstable Eady wave. An analytical treatment of the semi-geostrophic equations by Hoskins and Bretherton (1972) (hereinafter, HB72) showed similar results.

Most studies of frontogenesis have focused on the fronts themselves. Less attention has been focused on the role of fronts as a coupling agent between large-scale baroclinic waves and small-scale dissipative modes. The spectral characteristics of semi-geostrophic fronts and baroclinic waves have been investigated by Andrews and Hoskins (1978) and Gall et al. (1979), respectively. These studies suggest that the spectrum of motions with zonal wavenumber  $\geq 10$  may be representative of processes associated with frontal formation rather than inertial energy transfer (Blumen, 1980).

### C. STRUCTURE OF FRONTAL ZONES

Several years prior to the introduction of the polar front theory, Margules (1906) developed a detailed theory of atmospheric discontinuities. His work anticipated, in many respects, the dynamical views that were to be introduced some 40 years later in that he appreciated the importance of the conversion of available potential energy to kinetic energy. A historical account of subsequent development of the current understanding of atmospheric fronts is given by Palmen and Newton (1969). Detailed descriptions of the structure of intense cold fronts appear in Sanders (1955) and Petterssen (1956). Typically, cold fronts lie in confluent regions associated with a frontal trough. Convective clouds and precipitation accompany the front, often in bands. Warm fronts are accompanied by stratiform clouds. Warm



fronts have recently become the focus of renewed interest. Field observation programs associated with GALE and ERICA showed that strong warm fronts play an important role in cyclogenesis over the western North Atlantic ocean (Nuss, 1989; Chang et al., 1991; Neiman et al., 1991). Cold and warm fronts generally intersect at the center of an extratropical cyclone which is an area characterized by extensive heavy precipitation. At later stages of frontogenesis/cyclogenesis, the site of the intersection is the occluded front formed when the cold front overtakes the warm front and forces it aloft. On the scale of synoptic charts, the front is represented by a zeroth order discontinuity in wind and a first order discontinuity in pressure. Conventional wisdom holds that turbulence and diffusion lead to frontal scales on the order of 10–100 km. Recent studies, however, have indicated that some fronts may have scales on the order of 100 m (Shapiro et al., 1985; Carbone, 1982). A review of observational investigations of fronts is given by Keyser (1986).

A major revision to the classical Norwegian frontal cyclone model was recently proposed by Shapiro and Keyser (1990). In the Shapiro and Keyser model, the warm and cold fronts are separated near the center of the low by a "frontal fracture". Moreover, the warm front extends to the west of the low center; this is referred to as the "bent back" warm front. In the later stages of development, a warm core "seclusion" forms near the center of the low. There is no occlusion in this model. The Shapiro and Keyser model is discussed at length in the Appendix.

Frontal zones are smallest and frontal gradients most intense at the surface. The gradients within the surface frontal zone may be one or two orders of magnitude larger than those observed in the free atmosphere (Sanders, 1955). The surface frontal zone is characterized by strong horizontal convergence and cyclonic vorticity with weak anticyclonic vorticity behind the front associated with the cold air outbreak (Ogura and Portis, 1982). This zone has small vertical extent ( $\sim 100$  mb).

The front becomes more diffuse aloft and extends through the depth of the troposphere. Turbulent fluxes of sensible heat tend to drive the lapse rate on both sides of the front toward neutral, but the differential thermal advection by the ageostrophic wind dominates, stabilizing the warm sector and destabilizing the cold air (Keyser and Anthes, 1982; hereinafter, KA82).

Cold fronts slope toward cold air with slopes on the order of 50–100:1 (i.e., they are nearly horizontal). Warm fronts have slopes toward warm air on the order of 200:1. The sense of the along-front temperature gradient also distinguishes warm fronts from cold fronts. For a cold front parallel to the  $y$  axis,  $\partial T / \partial y < 0$  and, from the thermal wind relationship,  $\partial u / \partial z > 0$  while warm fronts have just the reverse (Keyser and Pecnick, 1987). The sense of the along front temperature gradient has important implications for frontogenesis. The action of cyclonic circulation on the along front temperature gradient is frontolytic for warm fronts and frontogenetic for cold fronts (Gidel, 1978; Keyser and Pecnick, 1987). Cold and warm fronts also often differ in terms of static stability; the air behind the cold (warm) front is typically unstable (stable). Levy (1989) proposes a mechanism whereby differences in stability result in more rapid warm frontogenesis in the early stages of frontal development. In some situations, the warm sector is unstable. In these cases, there may be strong frontogenesis (Nuss, 1989) and an intensification of the ageostrophic transverse vertical circulation (Koch, 1984; Reeder, 1986).

An important aspect of frontal structure is the ageostrophic transverse vertical circulation about the front. The Sawyer-Eliassen equation is a linear partial differential equation which expresses the stream function of the ageostrophic circulation in terms of the geostrophic momentum and thermal fields. This ageostrophic stream function is consistent with a thermally direct circulation centered on the front (Keyser and Shapiro, 1986). A review of Sawyer's analysis is presented by

Eliassen (1960) with derivations of modifications to the Sawyer-Eliassen equation for different forcings to the transverse circulation. The sense and position of the vertical circulation is such that the front is located in a zone of convergence at the surface which helps to intensify it (Williams, 1972). Hoskins (1982) and Shapiro (1987) postulate a feedback between frontogenetic forcing and the vertical circulation. Analyses by Sanders (1955), Ogura and Portis (1982), and Bond and Fleagle (1985) show that the ascent ahead of the front is concentrated into an intense vertical jet while the descent to the rear is more diffuse. This feature is apparent also in simulations of fronts by KA82 and Orlanski et al. (1985).

## D. FRONTOGENESIS

### 1. Quasi-Geostrophic Frontogenesis

The derivation of the quasi-geostrophic equations proceeds from the assumption that the Rossby number ( $V/fL$ ) is small. This is a fairly restrictive assumption and the equations cannot be expected to describe the evolution of small-scale features such as fronts. As discussed by Williams (1967), the conservation of quasi-geostrophic potential vorticity by the quasi-geostrophic system implies that a front at which potential vorticity is large cannot evolve from a state in which the potential vorticity is everywhere small. Nevertheless, Williams and Plotkin (1968), Williams (1968), and Stone (1966) used the quasi-geostrophic equations to investigate frontogenesis forced by a horizontal deformation field. Stone treated only certain limiting cases. Williams and Plotkin used a time dependent, Boussinesq, adiabatic, and inviscid model with rigid surfaces at the top and bottom. They included an initial temperature field which contained a temperature gradient that was invariant with  $z$  and was confined to a zone of finite width. This work was extended by Williams (1968) to include vanishing temperature gradients at infinity

and more general boundary conditions. In these studies, discontinuities formed only as  $t \rightarrow \infty$  and only at the boundaries. Away from the boundaries, the temperature gradient increased toward steady-state values and the scale was the Rossby radius of deformation. The fronts did not slope, had infinite horizontal wind speeds, and zero relative vorticity at the front (with large vorticity to either side). The lack of a slope in the vertical lead to regions of negative static stability. There was a thermally direct vertical circulation.

## 2. Semi-Geostrophic Frontogenesis

There are many situations in which the scaling arguments used in the development of quasi-geostrophic theory are not appropriate. In some of these situations, the Rossby number is  $O(1)$  or larger. In others, the scaling is anisotropic. One situation in which both of these complications are present is atmospheric frontogenesis. By introducing appropriate length scales in the along-front ( $L$ ) and cross-front ( $l$ ) directions, and nondimensionalizing the equations of motion, it can be shown (Pedlosky, 1979; Gill, 1982) that the acceleration in the cross front direction is  $O(l/L) \ll 1$  and therefore it can be neglected. Thus, there is geostrophic balance in the cross-front direction. This approximation, which is referred to by Eliassen (1948) as the geostrophic momentum approximation, greatly simplifies the equations and provides for the advection of the geostrophic momentum by the total wind.

It is convenient also to introduce the "geostrophic coordinates"  $(X, Z, T) = (x + v/f, z, t)$ . For a fluid parcel in purely geostrophic motion,  $x = X$  (HB72). The Jacobian of this transformation is the absolute vorticity and the inverse transformation is

$$x = X - v/f$$

so that the absolute vorticity in  $(x, z, t)$  space is given by

$$f + \partial v / \partial x = \frac{f^2}{f - \frac{\partial v}{\partial X}}$$

Thus, when the relative vorticity is equal to  $f$  in geostrophic coordinate space, the absolute vorticity is infinite and the transformation is discontinuous. In this manner, formation of a discontinuity will occur with a relatively modest increase in vorticity which can be obtained in either the deformation case or the growing Eady wave case. This is in contrast to the quasi-geostrophic system, which will not produce a discontinuity at all in the Eady wave case and requires infinite time for formation of a discontinuity in the deformation case.

The primitive equations incorporating the geostrophic momentum approximation and transformed to geostrophic coordinate space are called the semi-geostrophic equations. The semi-geostrophic system is applicable to a much wider class of phenomena than the quasi-geostrophic equations because of the less restrictive character of the derivation (Hoskins, 1975). Since the ageostrophic velocity is implicit in the transformation of coordinates, the behavior of the system can be more easily analyzed. Further discussion and extensions of the semi-geostrophic system are given by Blumen (1981) and Schubert (1985).

Several authors have discussed semi-geostrophic frontogenesis. Common to most of these studies is the use of the Boussinesq approximation, a domain bounded top and bottom by rigid surfaces at which the vertical velocity vanishes, and a constant Coriolis parameter. The discontinuity in temperature always forms first at the boundary. This does not produce realistic upper tropospheric fronts, but surface fronts are fairly faithfully simulated. It can be shown (Hoskins, 1971) that, when the potential vorticity is constant, analytic solutions always exist provided that the initial temperature field is linear in  $z$  and an arbitrary function of  $x$ .

Hoskins (1971) presented semi-geostrophic solutions for fronts formed by confluence in a deformation wind field. Three different initial temperature fields were used. The first case involved warm temperature at  $x = \infty$  and cold at  $x = -\infty$ . Results showed very realistic fronts forming on the warm side at both the upper and lower boundaries with convergence at the surface and a thermally direct circulation. The second case was identical to the first except that warm air was placed at the origin. In this case, a situation analogous to an occlusion was obtained. The third case was identical to the first except that cold air was placed at the origin. A front formed at the upper boundary only in this case. Numerical solutions were sought for several modified forms of the model:

- 1) if the Boussinesq approximation was not made, frontogenesis proceeded more slowly at the surface than at the "lid";
- 2) for slowly varying potential vorticity, frontogenesis proceeded slightly more slowly at the surface but very slowly at the lid;
- 3) a crude parameterization of latent heat release indicated that precipitation in the rising branch of the thermally direct cell ahead of the front would enhance surface frontogenesis;
- 4) incorporating Ekman layer suction to simulate surface stress resulted in a weaker surface front (enhanced convergence at the surface was frontogenetic, but compensating divergence aloft was frontolytic).

Upper tropospheric frontogenesis was also discussed.

The mathematical development of the techniques used by Hoskins (1971) was given by HB72. They also treated the deformation wind field case and numerically investigated nonBoussinesq effects, the effect of variable potential vorticity,

latent heating, boundary layer suction, and upper tropospheric fronts. In addition, HB72 obtained analytic solutions to the problem of frontogenesis forced by a growing nonlinear baroclinic wave (the most unstable Eady mode). This problem was first investigated numerically by Williams (1967). In this study, the domain was infinite in the y direction with a uniform temperature gradient, providing an infinite reservoir of available potential energy. Initially, the Eady wave growth rate was large as it drew on the infinite source of potential energy. As the wave grew, horizontal shears developed much as suggested by quasi-geostrophic theory. When the perturbation attained finite amplitude, however, the ageostrophic velocity caused a distortion and further contraction of the temperature field, resulting in a realistic front. The analytic solution obtained by HB72 compared quite favorably with Williams' solution, indicating that the assumption of cross-front balance is a good one.

The HB72 baroclinic wave model has been compared to observed fronts by Blumen (1980) and Ogura and Portis (1982). Blumen compared the model to Sanders (1955) analysis and Ogura and Portis compared it to their analysis of a front from the severe environmental storms and mesoscale experiment (SESAME). Although the model was capable of reproducing many features of observed fronts, there were some unrealistic features:

- 1) the model surface wind speed ( $50 \text{ m s}^{-1}$ ) was too large;
- 2) the model vorticity was too small;
- 3) Sanders (1955) showed that the observed front was maintained as a balance between frontogenesis and frontolysis while the model was predominantly frontogenetic;

- 4) the model vertical circulation was too weak; the ascent was less than  $\sim 20\%$  of the value observed by Sanders.

The major failing was that the model did not produce an intense upward vertical jet ahead of the front. In an effort to remedy this situation, Blumen (1980) introduced an Ekman layer into the model. This enhanced the vertical velocity, but the small vertical gradients in the model prevented a significant contribution to frontogenesis. Blumen and Wu (1983) extended this work by including a more sophisticated boundary layer with a specified vertical velocity at the surface. They noted that the vertical velocity at the top of the layer has both an inviscid component associated with ageostrophic divergence at that level and a component due to Ekman layer dynamics. The resultant vertical velocity distribution was more realistic, although the magnitude of the upward motion was only slightly larger ( $6 \times 10^{-2} \text{ m s}^{-1}$  vs  $4 \times 10^{-2} \text{ m s}^{-1}$ ).

Reviews of HB72 have been given by Pedlosky (1979), Holton (1979), and Hoskins (1982). The review by Hoskins is quite extensive and includes both two and three dimensional semigeostrophic frontogenesis and a brief discussion of quasi-geostrophic frontogenesis, which points out the important distinctions between semi-geostrophy and quasi-geostrophy. For the case of a growing Eady wave in the three dimensional semigeostrophic equations, it is necessary to slightly modify the Eady wave and introduce buoyancy gradients in the initial conditions to obtain realistic three dimensional fronts.

Numerical solutions to the three-dimensional semi-geostrophic equations for several different growing nonlinear baroclinic waves (including the Eady case) were obtained by Hoskins and West (1979). With a strong westerly jet, realistic cold and warm frontal zones formed in the growing waves at the leading edge of the cold air.



### 3. Quasi-geostrophic Versus Semi-geostrophic Frontogenesis

It is instructive to compare the approaches taken in the previous two sections. Comparison of quasi-geostrophic and semi-geostrophic frontogenesis following Orlandi et al. (1985) serves to highlight three important dynamical processes which are strongly modulated by boundary layer physics. These processes are 1) a feedback between increasing frontal gradients and increasing ageostrophic convergence, 2) increasing convergence leads to growth in vorticity, and 3) a braking mechanism is postulated based on an imbalance between the mass and wind fields in frontogenesis. Expressions for the substantial time derivatives of the cross front potential temperature gradient and vertical wind shear can be written

$$\frac{d_g}{dt} \left( g \frac{\partial \theta}{\partial x} \right) = -g \frac{\partial \mathbf{V}_g}{\partial x} \cdot \nabla \theta - N^2 \frac{\partial w}{\partial x} - g \left( \mathbf{V}_a \cdot \nabla \frac{\partial \theta}{\partial x} \right)^* - g \left( \frac{\partial \mathbf{V}_a}{\partial x} \cdot \nabla \theta \right)^* \quad (2.1)$$

$$\begin{aligned} \frac{d_g}{dt} \left( f \frac{\partial \mathbf{V}}{\partial z} \right) = & -f \frac{\partial \mathbf{V}_g}{\partial z} \cdot \nabla \mathbf{V}_g - f^2 \frac{\partial \mathbf{U}_a}{\partial z} - f \left( \mathbf{V}_a \cdot \nabla \frac{\partial \mathbf{V}_g}{\partial z} \right)^* \\ & - f \left( \frac{\partial \mathbf{V}_a}{\partial z} \cdot \nabla \mathbf{V}_g \right)^* - \frac{d}{dt} \left( f \frac{\partial \mathbf{V}_a}{\partial z} \right)^{**} \end{aligned} \quad (2.2)$$

where an asterisk (\*) indicates semi-geostrophic terms added to the basic quasi-geostrophic system and two asterisks (\*\*) indicate terms of the full nongeostrophic system.

The fundamental difference between quasi-geostrophic and semi-geostrophic frontogenesis is that the sum of the geostrophic and the ageostrophic wind is used in the horizontal and vertical advection of temperature and geostrophic momentum. This is apparent from the third and fourth terms on the RHS of equations (2.1) and (2.2). This implies that, as the frontal gradients increase, ageostrophic convergence also increases, which brings about still stronger frontal gradients. Evidently, this process will bring about a discontinuity in a relatively short time. If only the first

two terms on the RHS are retained (the quasi-geostrophic case), this process cannot occur. The vorticity equation can be written as

$$\frac{d_g}{dt}(\zeta) = -fD - \zeta D^* - (\mathbf{V}_a \cdot \nabla \zeta)^* \quad (2.3)$$

where  $D$  is the divergence. The second term on the RHS implies that cyclonic vorticity will increase in areas of convergence and decrease in areas of divergence. Thus, this is another mechanism which will enhance frontogenesis in the semi-geostrophic system relative to the quasi-geostrophic system.

A shortcoming of the semi-geostrophic system is that the continual action of the vortex stretching term (the second term on the RHS) leads to unbounded growth in vorticity. Use of the full nongeostrophic equations provides a possible braking mechanism. The divergence equation is

$$\frac{d_g}{dt}(D)^{**} = f\zeta - \nabla^2 p - \left(\frac{\partial u}{\partial x}\right)^{2**} \quad (2.4)$$

The imbalance between  $f$  and  $p$  (which is essentially an imbalance between the mass and the wind fields due to ageostrophic motion <sup>1</sup>) may result in a positive contribution to divergence or a decrease in convergence. This may reduce frontogenesis and (from terms 1 and 2 on the RHS of 2.3) slow the production of cyclonic vorticity. In a high resolution nonhydrostatic simulation of frontogenesis, Gall et al. (1987) found some indication of this braking mechanism (manifested by a separation of the region of maximum convergence from the region of maximum vorticity). However, the cyclonic vorticity continued to increase. Using a simple nonhydrostatic model, Levy and Bretherton (1987) critically examined the braking mechanism and found that, in several different plausible situations, the mechanism was frontogenetic rather than frontolytic. They postulated that the phase shift between the region

---

<sup>1</sup>In quasi-geostrophic and semi-geostrophic frontogenesis, a balance exists between  $f\zeta$  and  $\nabla^2 p$ .

of maximum convergence and the region of maximum vorticity might be due to gravity waves excited by frontogenesis. In a comment on this paper, Garner (1989) criticized the author's analysis as being irrelevant and maintained that the gravity waves are too weak to bring about the observed phase shift. Levy and Bretherton's reply is not compelling. In a two dimensional investigation of warm and cold fronts, Keyser and Pecnick (1987) found no evidence of a dynamical brake on frontogenesis. Thus, further study will be required to verify this braking mechanism.

#### **4. Frontogenesis With the Primitive Equations**

Several authors have examined frontogenesis using the primitive equations. These studies can be viewed in a hierarchy of increasing sophistication. Inviscid, adiabatic, Boussinesq, hydrostatic models were used by Williams (1967) (discussed above) and Williams (1972). Williams (1972) used a horizontal deformation field in a comparison of quasi-geostrophic and nongeostrophic frontogenesis, essentially complementing earlier work (Williams, 1968). Results indicated that the nongeostrophic nonlinear approach provided more realistic fronts with vertical tilt and the tendency to form a discontinuity in finite time. Parameterizations of horizontal and vertical diffusion of heat and momentum were added by Williams (1974), relaxing the adiabatic and inviscid condition. These parameterizations included only the neutral case, involving constant eddy coefficients and a simple Ekman layer. Inclusion of surface stress and turbulent diffusion of heat in this study resulted in the production of quasi-steady state fronts after 1-2 days of integration. Vertical diffusion of heat was found to play a dominant role in determining the steady state structure. NonBoussinesq (fully compressible) effects were introduced by KA82 along with more elaborate boundary layer physics. A two dimensional version of the Pennsylvania State University/National Center for Atmospheric Research (PSU/NCAR) model was used to investigate the effects of differing boundary layer

parameterizations on frontogenesis. A bulk boundary layer and a high resolution K-theory boundary layer were used. The high resolution boundary layer provided the sharpest front. This model was also used by Kuo et al. (1991a) with the high resolution boundary layer. These studies will be discussed in more detail below. Finally, the nonhydrostatic primitive equations were used by Gall et al. (1987) in extremely high horizontal and vertical resolution inviscid integrations designed to determine the minimum scale of fronts. Results indicated that continuously decreasing the vertical mesh size resulted in smaller and smaller frontal scales (results were relatively insensitive to horizontal mesh size given the shallow slope of the front). Thus, no minimum scale could be determined. The introduction of horizontal and vertical diffusion would modify this conclusion. Inviscid nonhydrostatic primitive equation simulations were also performed by Polovarapu and Peltier (1990) with much lower horizontal and vertical resolution. They investigated differences between simulations of baroclinic wave life cycles using the  $f$ -plane and  $\beta$ -plane approximations.

## E. IMPORTANCE OF BOUNDARY LAYER PROCESSES

In general, one can envision that surface stress, static stability, and turbulent diffusion must be important in the formation of zones of large horizontal gradients in the atmosphere. In particular, the formation of discontinuities is not observed in models incorporating turbulent diffusion since turbulent mixing will reduce the magnitude of gradients in temperature and wind speed. Hoskins (1971) and HB72 note that the existence of a Richardson number near the critical value in the vicinity of modeled fronts implies that turbulent mixing will be important. Steady-state fronts were produced by Williams (1974) using simple parameterizations of horizontal and vertical turbulent diffusion of heat and momentum. Using the PSU/NCAR model in a study of explosive marine cyclogenesis, Kuo et al. (1991b) noted that

the structure of modeled fronts was a great deal more realistic when boundary layer physics was included. The physical parameterizations involved the Blackadar (1979) K-theory scheme and surface sensible and latent heat fluxes based on similarity theory. In reality, fronts exist in quasi-steady state for portions of their lifetime due to a balance between the frontogenetic effects of large-scale convergence and the frontolytic effects of the boundary layer.

One of the most important features of frontal structure is the thermally direct ageostrophic vertical circulation in the cross-front plane. Convergence associated with this circulation intensifies cross-front gradients and it increases in magnitude as they do. Several observational and numerical studies have shown this circulation to be forced by the boundary layer. Carbone (1982) demonstrated (using Doppler radar and surface-based observing systems) that the strong vertical updraft in fronts observed in central California resulted from boundary layer forcing. In his comparison of Sanders (1955) analysis to the HB72 model, Blumen (1980) introduced an Ekman layer into the model in an effort to improve the vertical velocity field. Blumen and Wu (1983) further modified the model by specifying the vertical motion at the top of the boundary layer at the initial time in an effort to bring the vertical velocity closer to the observations. They concluded that the low-level vertical motion field was very sensitive to the boundary layer parameterization used. Bond and Fleagle (1985) found boundary layer convergence to be a major component in forcing vertical motion in fronts and storms over the NE Pacific Ocean. Moreover, Fleagle et al. (1988) found that 80% of the upward vertical motion in a cold front over the NE Pacific ocean was attributable to surface forcing.

In their investigation of the effects of impact of boundary layer physical processes on frontogenesis, KA82 utilized a two dimensional version of the PSU/NCAR

model with a growing nonlinear baroclinic wave in the initial conditions and performed four experiments:

- 1) adiabatic and inviscid with moderate vertical resolution;
- 2) bulk-drag boundary layer with moderate vertical resolution;
- 3) adiabatic and inviscid with high vertical resolution (approximately 5 levels in the lowest km);
- 4) high resolution K-theory boundary layer and thermally insulated lower boundary with high vertical resolution.

They did not consider the effects of moisture, surface heat flux, or radiation. Radiation was considered to be of no importance in frontogenesis by HB72. Hoskins (1982) stated that, while moisture may be important in the structure of steady-state fronts, it is not necessary to include it in studying frontogenesis.

The results of KA82 indicated that adding boundary layer physics as in 4) above to the adiabatic and inviscid simulation resulted in almost immediate production of large vertical shears in  $u$  (cross-front) and  $v$  (along-front) which caused vigorous mixing. Frictional depletion of  $v$  momentum resulted in a large ageostrophic  $v$  component and large cross isobaric acceleration in  $u$ , which invalidated the assumption of cross-front balance. A quasi-steady state developed after about 8 h. Vertical fluxes of sensible heat at levels above the surface tended to drive the lapse rates on both sides of the front toward neutral but vertical differential thermal advection dominated. The frictionally driven ageostrophic boundary layer inflow was responsible for contraction of the temperature gradient and thus counteracted the dissipation of potential vorticity due to friction. The frictionally driven ageostrophic boundary layer inflow was also responsible for the creation of a vertical jet ahead

of the surface front after about 8 hours. Thus, the high resolution boundary layer formulation provided a much more realistic vertical velocity field than the bulk boundary layer.

Although the study of KA82 successfully reproduced many features of observed frontogenesis, it suffers from several drawbacks. Most of these stem from the use of the insulated surface condition. For the bulk formulation, the maximum heat flux is required to be at the surface. It is not clear how this can occur with an insulated surface; the bulk formulation applies only in convectively driven, well-mixed conditions. For the high resolution boundary layer, the heat flux at the surface was assumed to be zero and only the nocturnal case was used due to the insulated surface. This is clearly inappropriate in the well mixed area behind the front. For these reasons, the interpretations given by the authors, specifically those regarding the evolution of the thermal field, may not be justified. In particular, the dominance of vertical differential thermal advection over vertical fluxes of sensible heat in controlling static stability requires further investigation. The authors state in their conclusion that three dimensional simulations will eventually be required to answer some of the questions raised in this work. The addition of a third dimension will allow more realistic representation of horizontal divergence which may alter the vertical velocity field. Finally, the authors do not discuss in any detail the differences in model frontogenesis caused by the differing boundary layer parameterizations.

Although there have subsequently been a number of similar studies, none has been as broad in scope as that of KA82. Several other authors have investigated the effect of surface sensible heat fluxes on frontogenesis. Moore (1991) included a surface heat flux parameterization into the two dimensional HB72 framework. Results indicated that the addition of surface heat flux reduced the stability in the frontal zone and, for certain surface temperature distributions, increased frontal

baroclinicity. This study omits processes accounted for in the full primitive equation framework and three dimensional effects. The impact of surface drag on frontogenesis was investigated by Hines and Mechoso (1993). They used a constant surface drag coefficient in an otherwise inviscid simulation of frontogenesis forced by a growing baroclinic wave. Their results showed that a feedback between deformation and warm frontogenesis was sensitive to surface drag. With larger drag coefficients, the feedback was inhibited and the warm front weakened. In an idealized simulation of a warm front near the Gulf Stream, Nuss (1989) found that the effect of stability on surface stress was critical. In fact, he found that a stratification gradient across the front was necessary to enhance frictional convergence and frontogenesis. Stability was also found to play a significant role in the investigation of the pre-ERICA storm by Neiman et al. (1990). In this case, the front moved past the Gulf Stream over the cold ( $\sim 0^\circ\text{C}$ ) waters of the North Atlantic. Stable stratification in the warm sector resulted in decoupling of the momentum from the surface, giving rise to a strong low level jet ( $\sim 40\text{ m s}^{-1}$  at  $\sim 500\text{ m}$ ). Thermal advection associated with the LLJ strengthened the fronts above the surface. In light of the results of Nuss and Neiman et al., the use of a constant drag coefficient by Hines and Mechoso seems to be an unwarranted simplification. In the investigation by Nuss, the sea surface temperature distribution was specified so as to represent the large thermal gradients typical of the Gulf Stream. The generality of these results is thus unclear.

Thus, a number of previous studies have examined various aspects of the impact of boundary layer processes on frontogenesis and the thermally direct ageostrophic vertical circulation. None of these studies, however, have addressed the issue of the specific processes which must be correctly parameterized in order to capture the essential details of maritime atmospheric frontogenesis in three dimensions. Only the two-dimensional study by KA82 addressed the impact of differing parameteri-



zations of the boundary layer on frontogenesis. This study was flawed by the use of an insulated lower boundary. Other investigations of the impact of surface fluxes have been inconclusive in that the models used were highly idealized and therefore unable to assess the nonlinear interactions of surface heat flux with other physical processes. These considerations lead to the basic hypothesis to be examined in the present study.

**[THIS PAGE INTENTIONALLY LEFT BLANK]**

### III. DESCRIPTION OF PROPOSED WORK

The central hypothesis of this study is that increasing the sophistication of the boundary layer parameterization will increase the ability of the model to reproduce the three dimensional features of observed frontogenesis. In particular, it is hypothesized that more realistic representation of the boundary layer will provide an improved simulation of the ageostrophic vertical circulation and frontogenetic processes associated with it.

In an attempt to verify this hypothesis, three different versions of the Navy Operational Regional Atmospheric Prediction System (NORAPS) will be used. These versions will consist of an adiabatic and inviscid run and two turbulence parameterizations of differing levels of sophistication. The model is a hydrostatic primitive equation model with a scheme C grid in the horizontal and a  $\sigma (= p/p_s)$  coordinate system in the vertical. Split explicit time differencing (in which the fast gravity modes are treated separately) is also used. As in KA82, radiation and clouds will not be included. Radiation is of little importance and, while moisture may play an important role, the intent of the present study is investigation of boundary layer turbulent processes occurring near the surface; inclusion of clouds could complicate interpretation of the results. Omission of clouds and radiation will also significantly decrease computational expense. The initial conditions will consist of a highly baroclinically unstable state. The initial wind, temperature, and geopotential fields will be in hydrostatic and thermal wind balance. Prior to the start of the computational cycle, a small amplitude perturbation will be superimposed on the  $v$  wind component and geopotential fields. The lower boundary conditions will be specified so as to simulate an oceanic surface.

The versions of the model are:

1) Adiabatic and inviscid

This version will serve as an experimental control for comparison to versions with physical processes active.

2) K-theory

In this version, the turbulent fluxes of heat and momentum are parameterized by assuming that the fluxes are proportional to the gradients of the mean quantities (with  $K$  being the coefficient of proportionality). The K-theory version involves a mixing length based on Blackadar (1962) which asymptotically approaches a constant value and the eddy coefficients are based on the functional dependence on the Richardson number devised by Louis (1979). This version is similar to that used by KA82 in that the value of  $K$  is a function of the local Richardson number. This experiment will reveal the impact of surface fluxes on a simulation similar to that performed by KA82. The current investigation represents an extension of the work of KA82 also in that three-dimensional aspects of the problem are addressed.

3) Second-order closure boundary layer physics

The second-order closure scheme makes explicit use of the ensemble average variances and covariances of the turbulent heat and momentum fields (turbulent fluxes). This version uses the Mellor and Yamada (1974) level 3 model, in which prognostic equations are used for turbulent kinetic energy and the mean quantities as well as for the variance and covariance of the turbulent temperature and moisture fluctuations. Additional diagnostic equations are included for the turbulent momentum fluxes. This will provide for a fairly realistic treatment of the turbulence, particularly when the turbulence level is changing rapidly. Rapid changes in turbulent kinetic energy are to be expected in frontogenesis; as the strength of the front increases, the wind shear will also increase, as will the buoyant production of TKE. Thus, both the

mechanical and buoyant production terms of the TKE equation will be large, leading to a large local tendency in TKE. The conservative variables are liquid water potential temperature <sup>1</sup> (in this case, liquid water potential temperature reduces to ordinary potential temperature), total water substance, *u* momentum, and *v* momentum. The prognostic equations are solved semi-implicitly using the Thomas algorithm (Richtmeyer and Morton, 1967). This experiment will serve to demonstrate that additional insights can be obtained using a turbulence parameterization more sophisticated than that used by KA82.

The sensitivity to rapid temporal variations in turbulence level will be investigated by using a level 2 version of the model. In a Yamada and Mellor (1982) level 2 scheme, prognostic equations are solved for the mean quantities, but diagnostic equations are used for turbulent kinetic energy and all other turbulence quantities such as the variances of temperature and moisture and the temperature/moisture covariance.

A detailed analysis of frontogenetical forcing will be performed for each of the different parameterizations. It will be possible to determine what processes are most important in frontogenesis (and frontolysis) for each of the parameterizations at various stages in the development of the front.

In order to determine which version gives the most faithful representation of atmospheric frontogenesis, the results can be qualitatively compared to observational studies. The analysis of frontogenetical forcing will facilitate semi-quantitative comparisons with atmospheric fronts; similar analyses have been performed for observed fronts by Sanders (1955), Ogura and Portis (1982), Carbone (1982), and Shapiro (1984).

---

<sup>1</sup> $\theta_L = \theta - (\theta/T)L/c_p Q_L$  where  $Q_L$  is liquid water specific humidity.

Sensitivity studies will also be conducted in order to assess the importance of surface heat and momentum fluxes. While KA82 did not include the effect of surface fluxes, it has been suggested recently (Dorian et al., 1989; Moore, 1991) that horizontally differential surface sensible heating may be important in frontogenesis.

None of these studies, however, provide a complete understanding of the impact of surface fluxes in the maritime case. The importance of surface drag is addressed by Nuss (1989) and Hines and Mechoso (1993). In the present study, a more realistic distribution of surface drag will be used than in Hines and Mechoso and the sea surface temperature field will be more typical of maritime frontogenesis in the open ocean than that used by Nuss.

The results of this study should provide important insights into the three dimensional nature of the boundary layer processes important in frontogenesis. The evolution of the vertical updraft forced by the inflow with model-generated horizontal divergence can also be examined. The frontolytical action of diffusion in combination with frontogenetic aspects of the vertical updraft and vertical gradients above the boundary layer can be studied. The sensitivity study of the surface momentum and sensible heat fluxes should shed some light on these features as well.

## IV. NUMERICAL EXPERIMENTS

### A. REGIONAL FORECAST MODEL

The forecast model is a hydrostatic primitive equation model with  $\sigma (= p/\pi; \pi =$  surface pressure) as the vertical coordinate. The grid is staggered following scheme C. This C staggering involves placing the U component of the wind one half grid interval in the  $x$ -direction away from mass points (the points at which temperature, pressure, moisture, and vertical velocity are defined) and the V component of the wind one-half grid interval in the  $y$  direction away from mass points. In the vertical, the vertical velocity  $d\sigma/dt$  is defined on layer interfaces and all other quantities are defined at the center of each layer (Arakawa and Lamb, 1977). Time integration is performed using the split-explicit method. In this technique, prognostic equations are solved with a centered time difference with forcing due to the meteorological modes and slowest gravity modes. These solutions are then adjusted for the linear terms governing the fast gravity modes (Madala, 1982). Robert time filtering is applied at the end of each time step to prevent solution splitting. Robert time filtering is described by Haltiner and Williams (1980). Fourth-order advection and diffusion are used for all of the prognostic variables (second-order diffusion is used on the first interior row). Diffusion computations on sigma surfaces will lead to spurious sources and sinks of energy when applied to mass and moisture fields. To overcome this problem, the fourth-order diffusion operator is applied to deviations from the standard atmosphere for temperature and moisture. Further details concerning the model can be found in Hodur (1987).

The primitive equations can be expressed in  $\sigma$  coordinates as

$$\begin{aligned} \frac{\partial(\pi u)}{\partial t} = & -\frac{\partial(\pi uu)}{\partial x} - \frac{\partial(\pi uv)}{\partial y} - \frac{\partial(\pi u \dot{\sigma})}{\partial \sigma} \\ & + f\pi v - RT \frac{\partial \pi}{\partial x} - \pi \frac{\partial \Phi}{\partial x} + \pi F + K \nabla_{\sigma}^2 (\nabla_{\sigma}^2 u) \end{aligned} \quad (4.1)$$

$$\begin{aligned} \frac{\partial(\pi v)}{\partial t} = & -\frac{\partial(\pi uv)}{\partial x} - \frac{\partial(\pi vv)}{\partial y} - \frac{\partial(\pi v \dot{\sigma})}{\partial \sigma} \\ & - f\pi u - RT \frac{\partial \pi}{\partial y} - \pi \frac{\partial \Phi}{\partial y} + \pi F + K \nabla_{\sigma}^2 (\nabla_{\sigma}^2 v) \end{aligned} \quad (4.2)$$

$$\begin{aligned} \frac{\partial(\pi T)}{\partial t} = & -\frac{\partial(\pi u T)}{\partial x} - \frac{\partial(\pi v T)}{\partial y} - \frac{\partial(\pi v \dot{\sigma})}{\partial \sigma} + \frac{RT \pi \dot{\sigma}}{\sigma c_p} \\ & + \frac{RT}{c_p} (V \cdot \nabla \pi) + \frac{\pi Q}{c_p} - \frac{RT}{c_p} \int (\nabla \cdot \pi V) d\sigma \\ & + \pi K \nabla_{\sigma}^2 (\nabla_{\sigma}^2 (T - T_s)) + \frac{\pi Q}{c_p} \end{aligned} \quad (4.3)$$

$$\begin{aligned} \frac{\partial(\pi q)}{\partial t} = & -\frac{\partial(\pi u q)}{\partial x} - \frac{\partial(\pi v q)}{\partial y} - \frac{\partial(\pi q \dot{\sigma})}{\partial \sigma} + \pi Q_m \\ & + \pi K \nabla_{\sigma}^2 (\nabla_{\sigma}^2 (q - q_s)) \end{aligned} \quad (4.4)$$

$$\frac{\partial \Phi}{\partial \ln \sigma} = -(RT) \quad (4.5)$$

$$\frac{\partial(\pi \dot{\sigma})}{\partial \sigma} = \int_0^1 (\nabla_{\sigma} \cdot \pi V) d\sigma - (\nabla_{\sigma} \cdot \pi V) \quad (4.6)$$

$$\frac{\partial \pi_s}{\partial t} = - \int_0^1 (\nabla_{\sigma} \cdot \pi V) d\sigma \quad (4.7)$$

Equations (4.1) and (4.2) are the horizontal equations of motion, equation (4.3) is a statement of the first law of thermodynamics, equation (4.4) is the conservation equation for water substance, equation (4.5) is the hydrostatic equation, equation (4.6) is the continuity equation, and (4.7) is the pressure tendency equation.

Characteristics of the model and initialization procedure are summarized in Table 4.1 and the distribution of computational levels in the vertical is given in Table



4.2. With the exception of the  $\sigma$  vertical coordinate, the first six items in Table 4.1 were chosen based on a balance between a desire to resolve the phenomena under study and acceptable running time and memory allocation. The jet speed and perturbation amplitude were chosen so as to give a convenient baroclinic wave growth rate. The horizontal diffusion coefficient is quite conservative and results in very little diffusion. The distribution of vertical levels in Table 4.2 was chosen so as to give high vertical resolution near the surface and near the tropopause; high vertical resolution in the boundary layer is crucial in this study and failure to adequately resolve the tropopause can lead to numerical difficulties.

## B. INITIAL AND BOUNDARY CONDITIONS

The initial conditions for the numerical experiments to be performed consist of a strongly baroclinically unstable regime. This regime involves a  $40 \text{ m s}^{-1}$  westerly jet at 200 mb at the center of the domain, decreasing to zero at the north and south boundaries with a  $\sin e^2$  profile. In the vertical, the  $u$  component of the wind decreases (linearly in  $z$ ) to zero at the surface. The jet, which is invariant in the zonal direction, is in geostrophic and thermal wind balance. This implies a strong meridional temperature gradient at all levels with a concentrated baroclinic zone near the center of the grid. The  $v$  component consists of an altitude independent 3000 km sinusoidal perturbation in both  $x$  and  $y$  with a maximum amplitude of  $1 \text{ m s}^{-1}$  at the center of the domain. The wavelength of the perturbation was chosen to be near the wavelength of maximum instability from linear theory (3246.98 km). The vertical temperature profile was chosen so as to yield a value of the stability parameter which enhances the growth rate of a 3000 km baroclinically unstable wave. The temperature and pressure gradients and both velocity components are

zero at the north and south boundaries and all fields are periodic in the east-west direction.

The initialization procedure involves first specifying the jet profile at each level. Then, using the velocity field at the lowest level, a modified form of the balance equation is applied at the surface to obtain surface pressure. Using the surface pressure and wind field, the balance equation is applied at each level to obtain the geopotential field. Finally, an altitude independent, sinusoidal perturbation is added to the geopotential field and the geostrophic perturbation  $v$  component is determined.

As in Eady's (1949) investigation of baroclinic instability, the model equations are formulated on an  $f$ -plane ( $\beta = 0$ ) and the vertical motion on sigma surfaces ( $d\sigma/dt$ ) vanishes at both the upper and lower boundaries. This implies that  $\omega \simeq 0$  at the surface and  $\omega = 0$  at the upper boundary.

## C. BOUNDARY LAYER PARAMETERIZATIONS

### 1. Introduction

The terms in equations (4.1)–(4.6) involving  $F$ ,  $Q$ , and  $Q_m$  represent viscous and diabatic effects of the boundary layer, radiation, and stable and convective precipitation. The purpose of the boundary layer parameterization is to quantify these terms by evaluating the divergence of the turbulent fluxes of heat, moisture, and momentum from the surface. The rate of change of any prognostic variable  $\xi$  due to the boundary layer physics is

$$\frac{\partial \bar{\xi}}{\partial t} = -\frac{\partial \overline{w'\xi'}}{\partial z} \quad (4.8)$$

where  $\overline{(\phi)}$  indicates an ensemble mean and  $\phi'$  denotes a turbulent deviation from the mean. Viewed in this context, the boundary layer parameterizations used in the

present study represent differing levels in the sophistication of the techniques used to evaluate equation (4.8).

## 2. Adiabatic and Nearly Inviscid Case

The adiabatic and nearly inviscid case involves no boundary layer parameterization (it is nearly inviscid in the sense that the fourth-order horizontal diffusion operator in equations (4.1)–(4.4) is included for computational stability; this pseudo-viscous effect is always present). The lower boundary is insulated and free-slip. No exchanges of heat, moisture, or momentum take place at the surface. This case serves as a control experiment for this investigation.

A convective adjustment scheme is used in order to ensure computational stability. It can be shown that the existence of a super adiabatic lapse rate in any column will lead to an exponential growth in the vertical velocity. Convective adjustment, applied at the end of each timestep, removes super adiabatic lapse rates in such a way as to conserve the total potential energy. The problem of changing the temperatures to produce a neutral lapse rate subject to the constraint of total potential energy conservation reduces to a system of linear equations which is solved using a standard matrix inversion technique (Carnahan et al., 1969).

## 3. K-Theory Boundary Layer Parameterization

In the K-theory boundary layer parameterization, the boundary layer is explicitly resolved and the surface fluxes are based on Monin-Obukhov similarity theory. No *a priori* assumption about the flux profile (above the surface layer) is required.

The surface layer similarity approach used to obtain the surface fluxes was developed by Louis (1979). This method uses analytic functions of  $Ri_B$  of the

form

$$F \begin{cases} = \frac{b Ri_B}{1 + c(Ri_B)^{1/2}} & \text{unstable} \\ = (1 + b Ri_B)^{-2} & \text{stable} \end{cases} \quad (4.9)$$

Equation (4.9) was obtained by fitting curves to the exact values computed by iteration. The surface fluxes are given by

$$u_*^2 = a^2 U^2 F(Ri_B) \quad (4.10)$$

$$u_* \theta_* = a / R U \Delta \theta F(Ri_B) \quad (4.11)$$

where

$$a^2 = k^2 (\ln(z/z_0))^{-2}$$

$$c = c^* a^2 b (z/z_0)^{1/2}$$

and  $a$  is analogous to  $C_{DN}$  and  $b, b, c^*$ , and  $R$  are constants.

The surface roughness,  $z_0$ , is determined from Charnock's formula for flow over water:

$$z_0 = c u_*^2 / g \quad (4.12)$$

where  $c = 0.05$ .

K-theory owes its origin to a physical analogy between turbulent diffusion in the boundary layer and molecular diffusion. In both processes, the flux of a quantity  $\xi$  is proportional to the gradient of that quantity; i.e.,

$$\overline{w' \xi'} = K \frac{\partial \xi}{\partial z} \quad (4.13)$$

Where  $K$  is the eddy diffusivity. The basis of the assumption that the turbulent flux is proportional to the gradient lies in the mixing length hypothesis.

In the present study, the form for  $K$  is that proposed by Louis (1979):

$$K = \ell^2 \frac{\Delta V}{\Delta z} F(Ri_B) \quad (4.14)$$

where the mixing length  $\ell$  is given by Blackadar (1962)

$$\ell = \frac{kz}{1 + kz/\lambda} \quad (4.15)$$

and

$$Ri_B = \frac{g \Delta z \Delta \theta}{\theta (\Delta V)^2} \quad (4.16)$$

The function  $F$  in equation (4.14) is the same as in the surface layer (equations (4.10) and (4.11)) except that  $c$  is given by

$$c = c^* l^2 b \left( (z + \Delta z/2)^{1/2} - 1 \right)^{3/2} \left( z^{1/2} \Delta z^{3/2} \right)^{-1}$$

Note that the mixing length  $\ell$  in equation (4.15) is proportional to height near the surface but asymptotically approaches a reference value  $\lambda$  at higher elevations:

$$\ell = \frac{kz}{1 + kz/\lambda} = \frac{\lambda}{\lambda/kz + 1};$$

for  $kz \ll \lambda, \ell \simeq kz$

for  $kz \gg \lambda, \ell \simeq \lambda$

This behavior is consistent with physical reasoning; near the surface, the size of eddies is constrained by proximity to the surface while aloft, the mixing length does not increase without bound with elevation. In Louis (1979),  $\lambda$  was given a constant value of 100 m. Experience with this version of the parameterization, however, has shown that values of  $\lambda = 150$  m for  $K_M$  and  $\lambda = 350$  m for  $K_H$  yield satisfactory model performance for a wide variety of meteorological situations. Use of these values in simulating frontogenesis is not inappropriate.

Having specified the form of  $K$ , equation (4.8) can be solved.

No convective adjustment scheme is necessary since the parameterized turbulent mixing will quickly respond to the presence of super-adiabatic lapse rates and re-distribute heat accordingly.

#### 4. Second-Order Closure Boundary Layer Parameterization

In this version, no *a priori* assumption about the relationship between the fluxes and vertical gradients is required; the variances and covariances of momentum, heat, and moisture are used directly in determining the boundary layer structure and evolution. In order to close the system of equations, expressions must be obtained for the fluxes. These expressions are derived from the turbulent equation of motion and scalar conservation, which, in turn, are derived from the conventional equations by introducing the decomposition

$$\xi = \bar{\xi} + \xi' \quad (4.17)$$

and applying Reynolds averaging. Expressions for the fluxes are then obtained by cross multiplying the turbulence equations by turbulent momentum and scalar property fluctuation. The resulting expressions are

$$\begin{aligned} \frac{\partial \overline{u'_i u'_j}}{\partial t} + \frac{\partial U_k \overline{u'_i u'_j}}{\partial x_k} = & -\overline{u'_j u'_k} \frac{\partial U_i}{\partial x_k} - \overline{u'_i u'_k} \frac{\partial U_j}{\partial x_k} - \frac{\partial \overline{u'_i u'_j u'_k}}{\partial x_k} \\ & - \frac{1}{\rho} \left[ \frac{\partial \overline{p' u'_j}}{\partial x_i} + \frac{\partial \overline{p' u'_i}}{\partial x_j} \right] + \frac{\overline{p'} \partial u'_j}{\rho \partial x_i} \\ & + \frac{\overline{p'} \partial u'_i}{\rho \partial x_j} - \epsilon_{ikl} f_k \overline{u'_j u'_l} - \epsilon_{ikl} f_k \overline{u'_i u'_l} \\ & + \frac{g}{\Theta_v} [\overline{u'_j \theta'_v} \delta_{i3} + \overline{u'_i \theta'_v} \delta_{j3}] + \nu \left[ \frac{\partial^2 \overline{u'_i u'_j}}{\partial x_k \partial x_k} - 2 \frac{\partial \overline{u'_i \partial u'_j}}{\partial x_k \partial x_k} \right] \quad (4.18) \end{aligned}$$

$$\begin{aligned} \frac{\partial \overline{u'_i s'}}{\partial t} + \frac{\partial U_k \overline{u'_i s'}}{\partial x_k} = & -\overline{u'_k s'} \frac{\partial U_i}{\partial x_k} - \overline{u'_i u'_k} \frac{\partial S}{\partial x_k} - \frac{\partial \overline{u'_i u'_k s'}}{\partial x_k} - \frac{1}{\rho} \frac{\partial \overline{p' s'}}{\partial x_i} \\ & + \frac{\overline{p'} \partial s'}{\rho \partial x_i} - \epsilon_{ikl} f_k \overline{s' u'_l} + \frac{\overline{s' \theta'_v}}{\Theta_v} \delta_{i3} g \\ & + \frac{\partial}{\partial x_k} \left[ \nu s' \frac{\partial u'_i}{\partial x_k} + \gamma_s u'_i \frac{\partial s'}{\partial x_k} \right] - (\nu + \gamma_s) \frac{\partial s'}{\partial x_k} \frac{\partial u'_i}{\partial x_k} \quad (4.19) \end{aligned}$$

The difficulty with this approach is that we have now obtained expressions for the second-order fluxes  $\overline{u'_i u'_j}$  and  $\overline{u'_i s'}$  in terms of the higher order moments  $\overline{u'_i u'_j u'_k}$ . Were

we to continue in this vein to derive expressions for third-order terms, the resulting expressions would contain fourth-order terms. This is the fundamental nature of the turbulence closure problem. Once the turbulent field is decomposed into a mean and a perturbation (using equation (4.17)), the full details concerning the flow's instantaneous behavior can only be reconstructed with knowledge of all ensemble-average statistics of all turbulent moments (Burk, 1978). In second-order closure, we retain only the first two turbulent moments and parameterize the third-order moments in terms of the second-order moments, thus obtaining closure. This is in contrast to K-theory in which the second-order fluxes are parameterized in terms of the mean quantities (K-theory is sometimes referred to as "first-order closure").

The second-order closure boundary layer parameterization utilizes a vertically nested grid structure in which the physics (turbulent diffusion, radiation, and moist thermodynamics) computations are performed on a high vertical resolution grid nested within the regional model grid. The dynamics (horizontal and vertical advection and coriolis and pressure gradient) computations are performed on the low vertical resolution regional model grid. In the present study, the vertical nesting is not used. While the code used to perform the interpolations from the fine grid to the regional model grid is active, there exists a one-to-one correspondence between the fine grid and the regional model grid. This simplification has been introduced in order to facilitate comparison with the K-theory simulation.

The surface layer similarity approach used to obtain the surface fluxes was developed by Liu et al. (1979). This approach implicitly incorporates an interfacial sublayer or inner surface layer in which molecular diffusion is important. It addresses certain fundamental differences between the way in which scalar quantities (e.g., heat and water vapor) and momentum are transported in this inner surface layer. The bulk transfer coefficients for scalar quantities are vastly different from

those for momentum. This difference is, in part, due to different roughness lengths computed for momentum ( $z_0$ ) and for heat and water vapor ( $z_T, z_Q$ ).

The differences between the transport of momentum and that of heat and water vapor are primarily due to the action of pressure forces (normal stresses) on the roughness elements which transport momentum. Thus, momentum is transported in the inner surface layer by both molecular diffusion and pressure forces while heat and water vapor are transported only by molecular diffusion. This results in a decrease in the bulk transfer coefficients for heat and water vapor with increasing wind speed above a threshold value. The transfer coefficient for momentum increases monotonically with increasing wind speed. These differences in the transfer coefficients are due to differences in the roughness lengths, which are obtained by matching profiles in the outer surface layer (where molecular diffusion is not important) to those from the inner surface layer.

The profiles for the outer surface layer are given by

$$\frac{(T - T_s)}{T_s} = \frac{\ln(z/z_T) - \psi_T}{\alpha_H k} \quad (4.20)$$

$$\frac{(Q - Q_s)}{Q_s} = \frac{\ln(z/z_Q) - \psi_Q}{\alpha_E k} \quad (4.21)$$

$$\frac{(U - U_s)}{U_s} = \frac{\ln(z/z_0) - \psi_U}{k} \quad (4.22)$$

where  $\alpha_H = K_H/K_M$  and  $\alpha_E = K_E/K_M$  at neutral stability ( $K_H$ ,  $K_M$ , and  $K_E$  are the turbulent diffusivities for heat, momentum, and moisture, respectively). Matching these expressions with corresponding expressions for the inner surface layer yields expressions for the surface roughness:

$$z_T = \nu a_1 R_r^{b_1} / u_* \quad (4.23)$$

$$z_q = \nu a_2 R_r^{b_2} / u_* \quad (4.24)$$



$$\begin{aligned}
z_0 &= G_1 \nu / u_* & \xi u_* / \nu &\leq r_1 \\
z_0 &= f(\xi u_* / \nu) & r_1 &\leq \xi u_* / \nu \leq r_2 \\
z_0 &= G_2 \xi & r_2 &\leq \xi u_* / \nu
\end{aligned} \tag{4.25}$$

where  $a_1, a_2, b_1, b_2, G_1, G_2$  are constants,  $\nu$  is the kinematic viscosity,  $\xi$  is the diameter of roughness elements, and  $R_r$  is the roughness Reynolds number ( $R_r = z_0 u_* / \nu$ ).

Mellor and Yamada (1974) devised a hierarchy of second-order closure modeling techniques based on the degree of turbulent anisotropy admitted by the equations used. In this work, which represented a landmark in second-order closure theory, four levels were discussed, ranging from level one in which all quantities are treated diagnostically (completely algebraic) to level four in which all quantities are expressed prognostically (completely differential). Subsequently, Mellor and Yamada (1982) identified the "level 2.5" model in which only the mean quantities and the turbulent kinetic energy are treated prognostically. In terms of this turbulence closure hierarchy, we have used both level 2.5 and level 3 closures in the vertically nested model. At level 3, we solve the following prognostic equations for turbulent kinetic energy, temperature variance, moisture variance, and temperature-moisture covariance:

$$\begin{aligned}
\frac{\partial e^2}{\partial t} &= \frac{\partial}{\partial z} \left( Le \frac{\partial e^2}{\partial z} \right) - 2\overline{u'w'} \frac{\partial U}{\partial z} - 2\overline{v'w'} \frac{\partial V}{\partial z} \\
&\quad + 2\beta g \overline{w'\theta'_v} - 2e^3 / \Lambda_1
\end{aligned} \tag{4.26}$$

$$\frac{\partial \overline{\theta'^2}}{\partial t} = \frac{\partial}{\partial z} \left( Le \frac{\partial \overline{\theta'^2}}{\partial z} \right) - 2\overline{w'\theta'_t} \frac{\partial \Theta_t}{\partial z} - 2e\overline{q'w'^2} / \Lambda_2 \tag{4.27}$$

$$\frac{\partial \overline{q'^2}}{\partial t} = \frac{\partial}{\partial z} \left( Le \frac{\partial \overline{q'^2}}{\partial z} \right) - 2\overline{w'q'_w} \frac{\partial Q_w}{\partial z} - 2e\overline{q'w'^2} / \Lambda_2 \tag{4.28}$$

$$\frac{\partial \overline{\theta'_t q'_w}}{\partial t} = \frac{\partial}{\partial z} \left( Le \frac{\partial \overline{\theta'_t q'_w}}{\partial z} \right) - \overline{w'\theta'_t} \frac{\partial Q_w}{\partial z} - \overline{w'q'_w} \frac{\partial \Theta_t}{\partial z} - 2e\overline{\theta'_t q'_w} \tag{4.29}$$

(application of the boundary layer approximation shows horizontal derivatives to be negligible in comparison to vertical derivatives). In equations (4.26)–(4.29),  $e^2/2$  is the turbulent kinetic energy,  $\theta_l$  is the liquid water potential temperature ( $\theta_l = \theta - \theta L/TC_p q_l$ ), and  $q_w$  is the total water substance specific humidity. At level 2.5, equations (4.27)–(4.29) are replaced with diagnostic expressions:

$$\overline{\theta_l'^2} = \Lambda_2 \frac{K_h}{e} \frac{\partial \theta_l}{\partial z} \frac{\partial \theta_l}{\partial z} \quad (4.30)$$

$$\overline{q_w'^2} = \Lambda_2 \frac{K_h}{e} \frac{\partial q_w}{\partial z} \frac{\partial q_w}{\partial z} \quad (4.31)$$

$$\overline{\theta_l' q_w'} = \Lambda_2 \frac{K_h}{e} \frac{\partial \theta_l}{\partial z} \frac{\partial q_w}{\partial z} \quad (4.32)$$

The covariances which must be evaluated to solve equations (4.26)–(4.29) are  $\overline{u'w'}$ ,  $\overline{v'w'}$ ,  $\overline{w'\theta_v'}$ ,  $\overline{w'\theta_l'}$ , and  $\overline{w'q_w'}$ . In equations (4.26)–(4.32),  $L$ ,  $\Lambda_1$ , and  $\Lambda_2$  are scaling factors proportional to a master length scale  $\ell$ . We use the closure constants from Mellor and Yamada (1982):

$$L = 0.2\ell; \quad \Lambda_1 = 16.6\ell; \quad \Lambda_2 = 10.1\ell$$

Yamada and Mellor (1975) show that the equations for the momentum and heat fluxes may be written in the form

$$-\overline{u'w'} = K_m \frac{\partial U}{\partial z} \quad (4.33)$$

$$-\overline{v'w'} = K_m \frac{\partial V}{\partial z} \quad (4.34)$$

$$-\overline{w'\theta_v'} = K_h \frac{\partial \theta_v}{\partial z} - \Gamma \overline{\theta_v'^2} \quad (4.35)$$

where

$$\Gamma = \frac{3A_2 \ell e \beta g}{e^2 + 12A_1 A_2 \ell^2 \beta g \frac{\partial \theta_v}{\partial z}} \quad (4.36)$$

Here,  $\beta$  is the coefficient of thermal expansion ( $= 1/\theta$ ), while  $A_1 = 0.92$  and  $A_2 = 0.74$  are closure constants from Mellor and Yamada (1982). The eddy coefficients

$K_m$  and  $K_A$  are given in Yamada and Mellor (1975) as algebraic functions involving both predicted mean and turbulence variables.

An equation for the total moisture flux may be written as

$$-\overline{w'q'_w} = K_w \frac{\partial Q_w}{\partial z} - \Gamma_w \overline{\theta'_v q'_w} \quad (4.37)$$

where

$$K_w = \frac{3A_2 \ell}{e} \overline{w'^2} \quad (4.38)$$

and

$$\Gamma_w = \frac{3a_2 \ell \beta g}{e} \quad (4.39)$$

The vertical velocity variance in equation (4.38) can be evaluated as

$$\overline{w'^2} = e^3/3 - \frac{2A_1 \ell}{e} K_m \left[ \left( \frac{\partial U}{\partial z} \right)^2 + \left( \frac{\partial V}{\partial z} \right)^2 \right] + \frac{4\beta g A_1 \ell}{e} \overline{w' \theta'_v} \quad (4.40)$$

The remaining unknown quantity in equations (4.26)–(4.29) is  $\overline{w' \theta'_v}$ .

Yamada and Mellor (1979) show that

$$\overline{w' \theta'_v} = \beta_T \overline{w' \theta'_l} + \beta_l \overline{w' q'_l} + \beta_w \overline{w' q'_w} \quad (4.41)$$

where

$$\begin{aligned} \beta_T &= 1 + .609q_w - 1.609q_l \\ \beta_l &= (1 + .609q_w - 3.22q_l) \frac{\theta L}{TC_p} - .609q_l \\ \beta_w &= .609(\theta_l + \frac{\theta L}{TC_p} q_l) \end{aligned} \quad (4.42)$$

Equation (4.41) can be re-arranged to obtain an equation for  $\overline{w' \theta'_l}$ . However, new unknowns have been introduced in equations (4.37) ( $\overline{\theta'_v q'_w}$ ) and (4.41) ( $\overline{w' q'_l}$ ). Yamada and Mellor (1975) give the following expression for  $\overline{w' q'_l}$ :

$$\overline{w' q'_l} = R' (a \overline{w' q'_w} - b \overline{w' \theta'_l}) \quad (4.43)$$

where

$$a = \left[ 1 + \frac{L}{C_p} \frac{\partial Q_{sl}}{\partial T} \right]^{-1} \quad (4.44)$$

$$b = a(T/\theta) \partial Q_{sl} / \partial T \quad (4.45)$$

and  $Q_{sl}$  is the saturation specific humidity at the liquid water temperature  $T_l$ . For now, we regard  $R'$  as known. Substitution of equation (4.37) into equation (4.42) and rearrangement yields

$$\overline{w'\theta'_l} = (\overline{w'\theta'_v} - \beta'_w \overline{w'q'_w}) \beta_T'^{-1} \quad (4.46)$$

where

$$\beta_T' = \beta_T - b\beta_l R'$$

$$\beta_w' = \beta_w + a\beta_l R' \quad (4.47)$$

In order to close equation (4.37), we use equation (45) of Yamada and Mellor (1975):

$$\overline{q'_w \theta'_v} = -\frac{\Lambda_2}{2e} \left[ \beta_T' \left( \frac{\partial Q_w}{\partial z} \overline{w'\theta'_l} + \frac{\partial \theta_l}{\partial z} \overline{w'q'_w} \right) + 2\beta_w' \frac{\partial Q_w}{\partial z} \overline{w'q'_w} \right] \quad (4.48)$$

Equations (4.33), (4.34), (4.35), (4.37), and (4.46) may be regarded as the closure of equations (4.26)–(4.31) in that the five second-order quantities required to close equations (4.26)–(4.31) are expressed by these equations.

The master length scale  $\ell$  appearing in equations (4.27)–(4.29) is of the same form as equation (4.15), however, the asymptotic reference value is not a constant but rather a ratio of first to the zeroth integral moment of the turbulent velocity scale. The vertical integration is terminated at the top of the boundary layer so that isolated turbulent layers aloft cannot lead to unrealistically large values of  $\ell$ . In these layers, a constant value of 50 m is used for the length scale.

Details concerning the vertically nested model can be found elsewhere (Burk and Thompson, 1989; Thompson and Burk, 1991). Here we will only briefly summarize important aspects of the scheme. The computational cycle is initiated by taking a "dynamics time step" ( $\delta t = 120$  s) in which large scale advection, pressure gradient, and Coriolis terms are computed, yielding dynamics tendency terms at each point. These dynamics tendency terms provide synoptic-scale forcing to the prognostic set of equations which embody the parameterized physics. On the first model time-step, the turbulence quantities undergo a "spin-up period" of several iterations during which these quantities are allowed to change while the mean fields and the time integration counter remain fixed. This ensures that the initial turbulence fields will be consistent with the regional model fields.

The predictive equations for the parameterized physics are solved using implicit, tridiagonal finite difference algorithms with upper and lower boundary conditions inserted into the resulting matrices. A form of Gaussian elimination is used to achieve solution.

As with the K-theory parameterization, no convective adjustment scheme is required with the second-order parameterizations.

The three major experiments to be performed (adiabatic and inviscid, K-theory, and second-order closure) along with a variety of sensitivity experiments as discussed in Chapter III, will address the concerns highlighted at the end of Chapter II.

#### **D. EVALUATION OF FRONTOGENETIC FORCING**

The term frontogenesis is defined by Petterssen (1956, p.200) as "...a tendency toward formation of a discontinuity or intensification of an existing zone of transition...". The intensity of frontogenetic forcing can be quantified by deter-

mining the rate at which the gradient of some scalar quantity increases. These considerations lead to the definition of the frontogenetic function, which can be written as

$$F = \frac{d |\nabla_H S|}{dt} \quad (4.49)$$

where  $S$  is some scalar quantity and  $d/dt$  represents a three-dimensional total derivative. Following Bluestein (1986, p.181), the right hand side of (4.49) can be expanded and the resultant terms separated into four groups as follows:

$$\begin{aligned} 1. & \quad \frac{\partial S / \partial x}{|\nabla_H S|} \left[ \frac{\partial}{\partial x} \left( \frac{dS}{dt} \right) \right] + \frac{\partial S / \partial y}{|\nabla_H S|} \left[ \frac{\partial}{\partial y} \left( \frac{dS}{dt} \right) \right] \\ 2. & \quad - \frac{\partial S / \partial x}{|\nabla_H S|} \left( \frac{\partial u}{\partial x} \frac{\partial S}{\partial x} \right) - \frac{\partial S / \partial y}{|\nabla_H S|} \left( \frac{\partial v}{\partial y} \frac{\partial S}{\partial y} \right) \\ 3. & \quad - \frac{\partial S / \partial y}{|\nabla_H S|} \left( \frac{\partial u}{\partial y} \frac{\partial S}{\partial x} \right) - \frac{\partial S / \partial x}{|\nabla_H S|} \left( \frac{\partial v}{\partial x} \frac{\partial S}{\partial y} \right) \\ 4. & \quad - \frac{\partial S / \partial x}{|\nabla_H S|} \left( \frac{\partial w}{\partial x} \frac{\partial S}{\partial z} \right) - \frac{\partial S / \partial y}{|\nabla_H S|} \left( \frac{\partial w}{\partial y} \frac{\partial S}{\partial z} \right) \end{aligned} \quad (4.50)$$

[Note that Bluestein obtains additional terms in his equation (9.11) because he uses the three-dimensional operator,  $\nabla S$ , rather than  $\nabla_H S$ .] The first group above consists of gradients of the substantial derivatives of  $S$  (for the case of  $S$  = potential temperature, the first group can be identified with gradients of diabatic terms). The second group comprises the stretching deformation. The third group consists of the shearing deformation terms. The stretching deformation term quantifies the effect of flow normal to the isentropes in concentrating or reducing the temperature gradient while the shearing deformation term quantifies the effect of a horizontal gradient in flow parallel to the isentropes. The fourth group is referred to as the "tilting term". This term quantifies the effect of a gradient in vertical motion tilting the isentropes into a vertical plane. Bluestein presents further discussion and graphical depictions of the physical interpretation of these terms.

## V. RESULTS

### A. ADIABATIC AND NEARLY INVISCID AT HIGH VERTICAL RESOLUTION

#### 1. Development

In this simulation, which serves as a control for simulations discussed below, the parameterizations for the diabatic and turbulent processes are inactive. As noted in Chapter IV above, this simulation is nearly inviscid in the sense that horizontal diffusion, which constitutes a pseudo-viscous effect, is always present.

The initial conditions for this case include a linear (in  $z$ ) increase in the  $u$  component of the wind from zero near the surface to  $40 \text{ m s}^{-1}$  at 200 mb  $u$  decreases above 200 mb. The  $v$  component consists of a sinusoidal perturbation with a wavelength of 3000 km and an amplitude of  $1 \text{ m s}^{-1}$ . The geopotential field is in geostrophic balance with the wind field (both  $u$  and  $v$ ) and the temperature field is in thermal wind balance with the  $u$  wind field. Temperature decreases with elevation at a rate of  $8 \text{ C/km}$ . The sea surface temperature, which is held fixed in these simulations, is initially set equal to the temperature at the lowest model level. Figure 5.1 shows the sea surface temperature field. With the exception of  $v$  and the geopotential, all fields are constrained to be invariant in the zonal direction initially. Figures 5.2a and b show meridional cross sections of the initial potential temperature and  $u$  component, respectively (the distribution of grid points in the vertical can also be seen).

Given such a baroclinically unstable initial state, rapid cyclogenesis may be anticipated. Figure 5.3 shows a time series of the minimum surface pressure for the present case (AI), the K-theory boundary layer (KTH) discussed in Section

5.2 below, and the second-order closure simulation (2OC) described in Section 5.3 below. Note the rapid deepening beginning near 72 hours. By 120 h, the surface pressure has fallen to 965 mb.

Figure 5.4 shows the surface pressure and near surface potential temperature at 72 h. Although the surface pressure has fallen only to 996 mb at this time, the temperature wave is well developed with a strong warm front and a weak, diffuse cold front. The thermal situation depicted in Fig. 5.4 is consistent with the traditional conceptual model of midlatitude cyclogenesis. Indeed, Fig. 5.4 bears a striking resemblance to a schematic presented by Holton (1979; Fig. 9.9, pg. 238). Figures 5.5a and b show the relative vorticity and divergence at approximately 850 mb, respectively, while Fig. 5.5c shows the vertical motion field at the same level.

Adiabatic and inviscid simulations were performed by Polovarapu and Peltier (1990) using a nonhydrostatic primitive equation model with periodic east-west boundaries and a grid structure very similar to the present one. Figure 5.5a resembles Fig. 13b and Fig. 5.5c closely resembles Fig. 14b of Polovarapu and Peltier, although Fig. 5.5 is for 72 h at 850 mb while Figs. 13b and 14b are for 120 h at an elevation of 1 km. The relative vorticity shown in Fig. 5.5a is large ( $2.1 \times 10^{-4} \text{ s}^{-1}$ ) within the warm frontal zone with a "tail" extending along the cold front. The strong warm front with large relative vorticity in the early stages of frontogenesis is consistent with the results of Levy (1989). The warm front lies within an zone of strong convergence and ascending motion ( $-7.8 \mu \text{ b s}^{-1}$ ) which extends towards the SW in the area ahead of the cold front. The region occupied by the cold air behind the front is characterized by weak divergence and descent.

Shown in Fig. 5.6 is the near-surface potential temperature at hour 84. Substantial frontogenesis has occurred along both of the fronts and the low has deepened to 986 mb. Although the strong convergence is confined to the northern



flank of the low, the vorticity maximum extends to the southwest along the cold front.

Figure 5.7 shows the near surface potential temperature for hour 96. The minimum pressure is 976 mb. There is a well defined cold front and an associated frontal trough. The cold front is now stronger than the warm front, although both fronts have experienced strong frontogenesis during the preceding 24 hours. The maximum in cyclonic relative vorticity has more than doubled during this period (not shown). Although the maximum is confined to the north, there is also strong relative vorticity within the cold frontal zone. An occlusion is forming near the center of the low and the warm air has "wrapped around" the low creating a distinctive pattern in the isentropes within the central portion of the low. This pattern bears a resemblance to the "bent back" warm front discussed by Shapiro and Keyser (1990). A discussion on this topic appears in the Appendix.

At hour 108, the warm front attains its maximum strength and the occlusion occupies a smaller portion of the domain than it does at hour 120. Figure 5.8 shows the near surface potential temperature. The minimum pressure at this time is 968 mb and the cold frontal trough is well-defined. Both of the fronts are quite strong ( $9\text{ C (100 km)}^{-1}$  for the cold front and  $5\text{ C (100 km)}^{-1}$  for the warm front).

Figure 5.9 shows the 850 mb relative vorticity field. Large values ( $3.6 \times 10^{-4}\text{ s}^{-1}$ ) of cyclonic vorticity are confined to the immediate vicinity of the low. The 850 mb divergence field shows strong convergence ( $-0.45 \times 10^{-4}\text{ s}^{-1}$ ) along the cold front. The warm front lies in a region of weak convergence. The vertical motion field shows similarity to the divergence field with ascending motion all along the cold front and with the maximum values ( $\sim 1\text{--}2\text{ cm s}^{-1}$ ) to the north. There is

weak descending motion in the cold air behind the front leading to thermally direct circulation about the cold front.

Shown in Fig. 5.10 are the surface pressure and near surface potential temperature at 120 h. By this time, an intense cyclone has developed with maximum near surface wind speeds of nearly  $60 \text{ m s}^{-1}$ . The distinctive pattern in the near surface isentropes is more pronounced as well. Strong warm and cold fronts and a well-developed occlusion are also present. Figure 5.10b is similar to Fig. 5.10c of Polovarapu and Peltier (1990) for hour 144 of their *f*-plane/westerly jet experiment.

## 2. Frontal Structure and Circulation

A cross section of potential temperature at hour 72 is shown in Fig. 5.11. The cross section extends from the surface to 505 mb in the plane shown in Fig. 5.4b. Note the relatively strong baroclinic zone at low levels in the center of the plane and the strongly stable surface layer to the north. The temperature of the surface in this region is on the order of 5 degrees warmer than the air (see Fig. 5.1), thus, the surface layer is strongly unstable. The surface layer becomes progressively less stable to the south, becoming neutral over the lowest  $\sim 30$  mb near the southern end of the cross section. The front-normal wind component (not shown) exhibits strong convergence near the front; it does not, however, change sign in the frontal zone. There is weak vertical motion near the front with ascent in the warm sector and descent in the cold air behind the front.

Shown in Fig. 5.12 is the potential temperature cross section for hour 84. The baroclinic zone is now much stronger and extends through a greater depth (note the region from  $\sim 950$  mb to 800 mb in Figs. 5.11 and 5.12). There is strong convergence in the front-normal component (not shown). Note that convergence not only strengthens the frontal temperature gradient directly but also increases cyclonic relative vorticity due to vortex stretching. The cyclonic circulation im-

plied by increasing cyclonic vorticity acting on the along-front temperature gradient constitutes a frontogenetic influence for cold fronts (Gidel, 1978). Thus, increased convergence has both a direct and an indirect frontogenetic effect. The vertical circulation is slightly stronger as compared to that at hour 72.

The potential temperature field at hour 96 is shown in Fig. 5.13 (the plane of the cross section is indicated in Fig. 5.7). The front, which is on the western boundary of the domain, has strengthened considerably. One interesting feature of the field is the relatively strong low level inversion in the warm sector. Given the warm advection which has occurred in this region, high stability is not surprising. Nor is it surprising that the isentropes are flat as the potential temperature is horizontally uniform. The surprising aspect is the strength of the inversion at low levels. This thermal structure is the result of the combined effects of horizontal and vertical advection (this area is dominated by weak ascent after hour 72). Warm air advection results in a stable stratification. Away from the surface, vertical advection in the warm air results in a neutral lapse of potential temperature. As vertical motion decreases toward the surface, however, the positive vertical gradient in potential temperature remains unaltered.

There is substantial convergence near the leading edge of the front at this time. A large maximum in vorticity ( $2f$ ) coincides with the leading edge of the front but is confined to a shallow layer.

A potential temperature cross section across the cold front at 108 hours is shown in Fig. 5.14 (the plane of the cross section is indicated in Fig. 5.8). Note the intense cross-front gradient both at the surface and above. Figures 5.15a and b show the components of the wind along the front and normal to it, respectively. The front normal wind changes sign at the front, indicating that air parcels approach the front from both the cold air and the warm sector. A cross section of divergence

is shown in Fig. 5.16. Note that the region of convergence extends upwards along the front. Given this divergence field, weak vertical motion would be expected (Fig. 5.17). Note the ascent ( $\sim 2 \text{ cm s}^{-1}$ ) confined to a narrow updraft immediately ahead of the front. The descending branch of the vertical circulation is somewhat more diffuse with large values some distance behind the front.

The along-front component is strongest at the surface behind the front and very weak above 800 mb. This component exhibits strong cyclonic shear in the frontal zone. The relative vorticity is quite strong (nearly  $3f \text{ s}^{-1}$ ) at the surface near the leading edge of the front (Fig. 5.18).

### 3. Frontal Development

In order to clarify the discussion of frontogenetical forcing, we will first examine the situation at 72 h when the interpretation of the pattern is straight forward (refer to Section 4.4 for a discussion of the frontogenetic forcing). Figure 5.19a shows the total adiabatic frontogenetical forcing at hour 72. Near the warm front, there are two regions of strong frontogenesis separated by strong frontolysis. There is also frontolysis south of the warm front. The dipole in forcing with frontolysis to the north and frontogenesis to the south is primarily due to the tilting term (Fig. 5.19b). Naturally, the tilting term is significant only where there is ascending motion. Strong frontogenesis to the east is due to the combined action of the stretching and shearing deformation (Figs. 5.19c and d). The region of strong frontolysis in the total is smaller than the corresponding area in the tilting term due to frontogenesis in the stretching and shearing deformation. Weak frontogenesis along the cold front is due to stretching deformation in the southern portion and shearing deformation in the northern portion. In that portion of the front where stretching deformation is frontogenetic, the wind, which is not far from normal to the isentropes, is decreasing rapidly downstream. In that portion of the front where shearing deformation is fron-

togenetic, the wind turns cyclonically in the downstream direction (NW becomes W becomes S).

The total frontogenetic forcing for hour 84 (not shown) is strongly frontogenetic along the warm front with very small positive values along the cold front. At hour 96, the distribution of the forcing changes dramatically and is strongly frontogenetic along the cold front and frontolytic at the warm front. Here again, the frontogenesis is due to stretching along the southern portion of the front and shearing along the northern portion. Shearing deformation is responsible for the bulk of the frontolysis along the warm front. At hour 108, there is weak frontogenesis along the cold front with weak frontolysis along the warm front (Fig. 5.20). The tilting term is now predominantly frontolytic. While the stretching deformation is strongly frontogenetic along the southern portion of the cold front strong frontogenesis in the shearing deformation is confined to the northern portion of the front where the cyclonic vorticity is largest. There is significant cancellation between the stretching and shearing deformation along both the warm and cold fronts.

A cross section of the total adiabatic frontogenetic forcing for hour 108 (Fig. 5.21a) shows that there is strong frontogenesis both within and ahead of the frontal zone due primarily to stretching deformation (Fig. 5.21b). The frontogenesis is, in fact, exactly twice as large as at hour 96. The magnitude of the stretching deformation is actually larger than the total due to frontolysis in the tilting term superimposed on the frontal zone. The distribution of the shearing deformation is quite similar to the stretching deformation but it is substantially smaller in this plane.

#### 4. Summary

The results presented in this section demonstrate that, in the absence of boundary layer physical processes, a growing baroclinic wave will generate very

strong warm and cold fronts near the surface. The numerical results are summarized in Table 5.1. Note that values calculated for a strong cold front over the NE Pacific Ocean observed on 16 November 1980 as documented by Fleagle et al. (1988) are included in the last row for comparison. The relative vorticity and convergence within the frontal zone are large, as is the horizontal potential temperature gradient across the front. The results are in qualitative agreement with other published studies of adiabatic and inviscid frontogenesis.

These simulations, however, are unrealistic in several ways. For example, the wind speeds near the center of the low at the surface are too large ( $\simeq 60 \text{ m s}^{-1}$ ). The vertical motion and the circulation about the front are extremely weak; the ascent ahead of the front is equivalent to  $1\text{--}2 \text{ cm s}^{-1}$ , nearly an order of magnitude below observed vertical motion in the vicinity of cold fronts. In contrast to previous kinematic studies of frontogenesis, tilting frontogenesis is of little importance in the total frontogenetic forcing.

In the next section, boundary layer processes are included using the K-theory parameterization discussed in Chapter IV above. Addition of surface drag should both reduce the low-level wind speeds and strengthen frictional convergence which will increase upward motion. Turbulent mixing of heat and momentum will also be active. Thus, the results should be more representative of observed fronts.

## **B. K-THEORY BOUNDARY LAYER**

### **1. Development**

In this experiment, the initial conditions are identical to those in the AI case (Section 5.1 above). The K-theory parameterization is activated at hour 72. Thus, the evolution of the baroclinic wave for the first three days is identical to that discussed in the AI case. A time series of surface pressure is shown in Fig. 5.22

for the present case (KTH), the simulation with surface sensible heat flux excluded (NO FLUX) described in Section 5.2.4 below, and for the simulation with neutral eddy coefficients (NO STABILITY) described in Section 5.2.5 below. Note that less deepening occurs after hour 72; the minimum surface pressure decreases 10 mb in the following 48 hours (in the AI case, the pressure decreased by 30 mb over this period). Time series of minimum surface pressure for the present case and the AI case are shown together in Fig. 5.3.

The near-surface potential temperature 12 hours after the K-theory parameterization is activated (84 hours) is shown in Fig. 5.23. The minimum pressure at this time is 990 mb and the cold and warm fronts are relatively weak.

Figure 5.24 shows the near surface potential temperature at hour 96. At this time, there is a well defined frontal trough near the cold front. Both fronts are relatively weak, although the cold front is slightly stronger than the warm front ( $2 \text{ K (100 km)}^{-1}$  for the cold front;  $1.7 \text{ K (100 km)}^{-1}$  for the warm front). The divergence field at 850 mb (not shown) indicates weak convergence along the cold front. Weak divergence dominates the high pressure region. The vertical motion field exhibits a narrow region of weak ascent extending along both fronts with weak descent behind the cold front.

Figure 5.25 shows the near surface potential temperature for hour 108. Under the influence of continuing frontogenesis, the warm and cold fronts have intensified. The frontal trough is also well developed. The 850 mb relative vorticity is cyclonic along both fronts, although it is smaller along the warm front than it is along the cold front (Fig. 5.26).

At hour 120, the minimum central pressure has fallen to 984 mb and the cold front has strengthened considerably (Fig. 5.27). The warm front has

experienced frontolysis. The maximum near surface wind speed is  $23.6 \text{ m s}^{-1}$  (as compared to nearly  $60 \text{ m s}^{-1}$  in the AI case at 120 h).

The baroclinic wave amplitude is smaller in this case and the potential temperature gradients associated with the warm and cold fronts are dramatically different from the AI case. There are several reasons for this. The wind speed is lower due to surface drag. Temperature gradients and, therefore, available potential energy, are reduced due to upward surface heat flux in the cold air. Frontogenesis is reduced since the geostrophic horizontal deformation is weaker. Branscome et al. (1989) investigated the effect of surface heat and momentum fluxes on the nonlinear development of baroclinic waves. They found that nonlinear surface drag was most important in reducing wave amplitude relative to the inviscid case. This resulted from enhanced dissipation. Reduced wind speeds were also responsible for most of the reduction in horizontal heat transport at low levels. An interesting result is that the inclusion of surface heat flux causes the maximum eddy temperature variances to occur at  $\sim 800 \text{ mb}$  rather than at the surface as in the inviscid case. The results of Branscome et al. are consistent with the present study. The wave amplitude is substantially reduced relative to the AI case and, as will be shown below, the maximum frontal gradients are displaced vertically and occur at 700–800 mb. Simulations discussed below in which surface heat and momentum fluxes are removed are also consistent with the results of Branscome et al..

## 2. Frontal Structure and Circulation

A cross section of potential temperature at hour 84 is shown in Fig. 5.28. While there is some evidence of frontal structure in the temperature field, the front at this time is quite weak. Comparison of this figure to the corresponding one for the AI simulation (Fig. 5.12) clearly shows the influence of surface heat flux; the strongly unstable stratification in the cold air in the AI simulation is replaced here



by a  $\sim 150$  mb deep mixed layer. Strong surface fluxes in the unstable air behind the front promote entrainment and deepening of the boundary layer in the present case.

A cross section of potential temperature for hour 96 is shown in Fig.

5.29. By this time, the cross-front temperature gradient is relatively strong and the ageostrophic circulation about the front has become fairly vigorous. The region of positive relative vorticity corresponds closely to the location of the largest horizontal temperature gradient. The relatively low stability in the warm sector is the result of weak ascent in this region beginning between hours 84 and 96. The frontal zone in this case is dramatically different from the AI simulation at this time (Fig. 5.13), although some similarities are apparent in the warm sector. In this case, the front is weak in comparison to the AI case and there is a deep mixed layer in the cold air. Reduction in the potential temperature gradient across the front in the present case is the result of strong upward heat flux in the cold air.

A cross section of potential temperature at hour 108 is shown in Fig.

5.30. Comparison to Fig. 5.29 shows that the front has moved approximately 500 km over the preceding 12 hours. Note the well-mixed layers both ahead of and behind the cold front extending to 800 mb. In the frontal zone, there is a weak inversion extending from 800 mb to 700 mb with a much stronger inversion above. In the cold air behind the front (north of the 295 K isentrope), there is a much more well-defined inversion at 700 mb. In the strong inversion above the frontal zone, the horizontal potential temperature gradient is twice as large as the near-surface gradient. The potential temperature distribution in the AI case shown in Fig. 5.14 is radically different from the present case. The frontal potential temperature gradient is less than half as large as in the AI simulation and the mixed layer is  $\sim 200$  mb deeper. Clearly, the surface fluxes of heat and momentum and turbulent diffusion

have had a large impact on frontal structure and circulation. Figure 5.31 shows cross sections of the along-front and front-normal wind components. Note the low level-jet in the cold air and strong horizontal shear in the along front component and strong convergence in the front-normal component near the front. The region in which convergence is large extends over a layer approximately 150 mb deep. There is very little vertical shear over the lowest 150 mb, indicating that momentum is well mixed in this layer. This is in contrast to the AI case in which the maximum along front wind is at the surface and the front-normal wind exhibits substantial vertical shear at low levels (Figs. 5.15a and b). The convergence (Fig. 5.32) near the front extends through this layer and back along the frontal zone. There is relatively strong divergence above the surface convergence. The strong convergence results in relatively strong upward motion (Fig. 5.33). There is an ascending jet at the leading edge of the front with strong descent at upper levels in the cold air. The strong cyclonic shear in the along-front component associated with the low-level jet in the cold air leads to a maximum in cyclonic relative vorticity in the frontal zone (Fig. 5.34).

An important result is that the convergence is only about half the value in the AI case ( $0.4 \times 10^{-4} \text{ s}^{-1}$  vs.  $0.7 \times 10^{-4} \text{ s}^{-1}$  for the AI case) but that, near the leading edge, the convergence extends through a deep layer. This is evident in comparing Figs. 5.16 and 5.32. This convergence pattern gives rise to an updraft more than twice as strong as in the AI case ( $4.4 \text{ cm sec}^{-1}$  vs.  $2.0 \text{ cm sec}^{-1}$  for the AI case). The ascending jet is also smaller in both its horizontal and vertical extent while the descending branch of the ageostrophic circulation is also more compact. Thus, the turbulent mixing in concert with the surface fluxes organizes the convergence in such a way as to produce a much more compact and vigorous

transverse circulation. This is primarily the result of mixing of momentum. This will be discussed at length in the following chapter.

It is of interest that the frontal zones depicted in the potential temperature fields displayed above in Figs. 5.29 and 5.30 exhibit no tilt in the vertical over the lowest 100–200 mb. This is in contrast to the adiabatic and nearly inviscid simulations and many observational studies (e.g., Sanders, 1955; Ogura and Portis, 1982) in which the frontal zone has a pronounced vertical tilt. The lack of tilt results from the deep well-mixed boundary layers on both sides of the front. This is to be expected in the cold air, however, one might anticipate higher stability in the warm sector. Nevertheless, the simulated frontal structure is consistent with the structure of observed marine cold fronts (Fleagle et al., 1988). This will be discussed in detail below in the following chapter.

### 3. Frontal Development

The total adiabatic frontogenetic forcing at hour 84 at 850 mb shows strong frontogenesis and frontolysis along the northern portion of the warm front. This is primarily due to tilting with large frontogenetic contributions from shearing and stretching deformation. At hour 96, there is strong frontolysis along the cold front and behind the northern portion of the warm front. This is almost entirely due to tilting with stretching and shearing deformation contributing only along the northern portion of the warm front. The total adiabatic frontogenetic forcing at 850 mb at hour 108, shown in Fig. 5.35, is predominantly frontolytic along both the warm and cold fronts. There is weak frontogenesis ahead of both fronts. This is largely due to tilting, although the frontolysis along the cold front is partially canceled by stretching deformation to the south and shearing deformation to the north. Neither of the horizontal deformation terms contributes significantly along the warm front.

Figure 5.36 shows a cross section of the total adiabatic frontogenetic forcing at 84 hours. Note the dipole structure of the forcing in the layer centered at approximately 800 mb. This pattern is due almost entirely to the tilting term (not shown); the shearing and stretching deformation are both an order of magnitude smaller than the tilting term. The distribution of the tilting term is a consequence of the vertical motion field (not shown) which consists of a weak downdraft in the cold air behind the front. The horizontal gradients in vertical motion associated with the downdraft result in frontogenesis well behind the front with weak frontolysis in the frontal zone extending into the warm sector.

The frontogenetic forcing at 96 hours is shown in Fig. 5.37. The frontolysis at the leading edge of the front is due to tilting. At this time, the vertical motion field consists of a relatively strong updraft with a large gradient in vertical motion on the cold side and a broad, diffuse region of upward motion on the warm side. This results in strong frontolysis within the frontal zone and weak frontogenesis in the warm sector. The total frontogenetic forcing shows a dipole with strong frontogenesis on the cold side of the tilting frontolysis. This is due to the shearing deformation, which is strongly frontogenetic both at the surface at the leading edge and above and behind the leading edge.

Figure 5.38a shows a cross section of the total adiabatic frontogenetic forcing at hour 108. Note the dipole structure with strong frontolysis within the frontal zone and strong frontogenesis immediately ahead of the front centered at  $\sim 850$  mb. This is almost entirely due to the tilting term (Fig. 5.38b). It is an order of magnitude larger than the stretching and shearing deformation and an order of magnitude larger than the tilting term in the AI case. Near the surface, where the tilting term is small (it drops to 50% of its maximum value at 950 mb and decreases rapidly toward the surface), the stretching and shearing deformation play a

more important role. Both terms have a maxima near the surface and the shearing deformation extends upward along the frontal surface. The maximum values are near the surface and above the inversion where the horizontal temperature gradient is largest.

At this time, the updraft ahead of the front is much more compact and symmetric than at hour 96 (Fig. 5.33). The dipole structure apparent in both the tilting frontogenesis and the total frontogenesis results from this distribution of vertical motion. The large gradients in vertical motion result in large magnitude in the tilting term. The largest gradient in vertical motion is within the frontal zone where the vertical motion changes sign. The tilting term is strongly frontolytic within the frontal zone. Ahead of the front, on the warm side of the vertical jet, the reversal in direction of the gradient in vertical motion results in a frontogenetic contribution from the tilting term.

At hour 108, the frontal propagation speed is larger than the front-normal wind speed, which decreases to zero in the frontal zone and then changes sign in the warm sector. This indicates that, relative to the front, air parcels in the cold air are moving away from the front while air parcels in the warm sector are moving towards it. Thus, air parcels in the cold air are moving away from the region in which the temperature gradient is large while air parcels in the warm sector move towards it. This is consistent with a dipole in tilting frontogenesis from a Lagrangian point of view.

Figure 5.38c shows the diabatic frontogenetic forcing. It is strongly frontolytic at the leading edge of the frontal zone and frontogenetic at the trailing edge. The magnitude of the frontolysis exceeds the frontogenesis and the region occupied by frontolysis is larger. If the diabatic term were the only term operating, the front would be destroyed.

The diabatic term involves at least two important sources of frontolysis in this case. One is the frontolytic effect of vertical mixing. In the cold air behind the front, there is a deep mixed layer capped by a strong inversion. Entrainment of warm air into the cold mixed layer has the effect of reducing the temperature gradient across the front. Similarly, heat flux divergence associated with upward surface heat flux in this region will reduce the cross-front temperature gradient. The distribution of surface sensible heat flux ( $\text{W m}^{-2}$ ) for hour 108 is shown in Fig. 5.39. Note that there is upward surface heat flux in the cold air behind the cold front. The effects of surface heat flux and entrainment are not independent in a well mixed BL. If the effect of the surface sensible heat flux were removed from the simulation, the frontolytic influences of both surface heat flux and entrainment should be reduced. Due to the highly nonlinear interaction between the surface heat flux and the parameterized turbulent mixing, however, differences between simulations with and without surface heat flux will involve substantial modifications in the turbulence as well.

Turbulent mixing is dependent upon wind shear and static stability as well as surface heat flux. In the next subsection, results from a simulation in which surface heat flux is eliminated are discussed. In Section 5.2.5, the effect of static stability is removed from the eddy coefficients.

#### 4. Insulated Surface Simulation

The near surface potential temperature field at hour 84 of the simulation with the surface heat flux removed is shown in Fig. 5.40. The warm and cold fronts are much stronger in this case. Over the next 12 hours, the minimum pressure falls 4 mb and both fronts experience significant frontogenesis (Fig. 5.41). Frontogenesis continues over the following 12 hours. Figure 5.42 shows the near surface potential temperature for hour 108. While the pressure distribution is nearly the same as in

the full physics simulation, the potential temperature field is quite different. The warm and cold fronts are both much stronger. The warm "tongue" ahead of the cold front is much more pronounced.

The fact that the surface pressure distribution is similar to that for the simulation with heat flux included indicates that surface heat flux has little impact on baroclinic wave growth. This result is consistent with the study of Branscome et al. (1989) discussed above. A time series of minimum surface pressure is shown in Fig. 5.22 with the time series for the full physics simulation for comparison.

Shown in Fig. 5.43 are cross sections of the potential temperature for hours 84, 96, and 108. Note that the front in this case has a very small vertical scale as compared to the full physics simulation. The front perturbs only the lowest 30 mb of the atmosphere. Since the influence of the front extends over such a limited depth, there is very little response to it in terms of vertical motion. The upward motion at hour 108 amounts to only about  $1 \text{ cm s}^{-1}$ . There is frontolysis in the tilting term but it is a result of large horizontal gradients in  $\omega$  which are in turn the result of the rather disorganized structure of the  $\omega$  field; this frontolysis plays no significant role in the frontal kinematics. The horizontal deformation is frontogenetic, but it is confined to a shallow depth. Thus there is no dipole structure in the frontogenetic forcing; this case is, in this respect, similar to the AI case.

The present case is similar to the AI case in several respects, although there is a  $\sim 30$  mb deep mixed layer in the present case which is absent in the AI case. The total change in potential temperature across the front, for example, is nearly the same as in the AI case. The width of the frontal zone, however, is twice as large in the present case. In both cases, the vertical motion is very weak.

The temperature gradient across the front is much larger in this case than in the full physics simulation. The enhanced cross front temperature gradient

reflects the frontolytic effect of surface fluxes in this case, while the shallow mixed layer implies that the entrainment has been reduced by excluding the heat flux. The mixed layer is maintained by vertical wind shear in the front-normal component.

### 5. Neutral Eddy Coefficient Simulation

The form of the eddy coefficients in the model is given by

$$K_{h,m} = L_{h,m}^2 \left| \frac{\partial V}{\partial z} \right| F(Ri) \quad (5.1)$$

where  $L = kz/(1 + kz/\lambda)$  and where  $\lambda = 150$  for  $K_h$  and 350 for  $K_m$  (for definitions and a more complete description, see Section 4.3.3). Dependence on stability can be eliminated by removing  $F(Ri)$ ; the neutral value of the eddy coefficient is thus

$$\kappa_{h,m} = L_{h,m}^2 \left| \frac{\partial V}{\partial z} \right| \quad (5.2)$$

Figures 5.44a and b show the normalized eddy momentum and heat coefficients, respectively, as a function of Richardson Number for a constant wind shear of  $10 \text{ m s}^{-1} \text{ km}^{-1}$ . The line having zero slope is the neutral value. Under stable conditions ( $Ri > 0$ ), the neutral value is, not surprisingly, a considerable overestimate of the eddy coefficient, while, for unstable conditions ( $Ri < 0$ ), the neutral value is a somewhat better estimate of the stability dependent value, particularly for the eddy heat coefficient.

Owing to the stability characteristic of the free atmosphere away from the surface, the formulation (5.1) gives small values for the eddy coefficient above the BL. In a simulation using (5.2), large eddy coefficients at high elevations lead to unphysical results. Therefore, (5.2) was modified to include a parameter dependent on  $\sigma$ :

$$\kappa_{h,m} = \alpha L_{h,m}^2 \left| \frac{\partial V}{\partial z} \right| \quad (5.3)$$



where

$$\alpha = 1 \quad 1 < \sigma \leq 0.85$$

$$\alpha = 0.1 \quad 0 < \sigma < 0.85$$

This formulation, though somewhat arbitrary, gives satisfactory results.

The near surface potential temperature distribution for hour 108 is shown in Fig. 5.45. While the surface pressure distribution is similar to the full physics case (see Fig. 5.22), the potential temperature distribution is quite different (see Fig. 5.25). Ahead of the cold front, the "tongue" of warm air extends much further to the NW. This takes place in a region which is stable (see the surface heat flux distribution in Fig. 5.39 for the full physics simulation) and is the result of enhanced turbulent mixing (recall that the neutral eddy coefficient overestimates the stability dependent eddy coefficient in stable layers). Surface fluxes are still active in this case, cooling the near surface layer. However, increased mixing of warm air toward the surface reduces heat flux divergence. A similar feature appears in Fig. 5.42 for the no heat flux case.

Shown in Fig. 5.46 is the potential temperature cross sections in the vicinity of the cold front at hour 108. The cross sections at hours 84 and 96 (not shown) are similar to those in the full physics simulation at corresponding times. Although the strength of the front at hour 108 is unchanged, the well defined inversion and mixed layer evident in Fig. 5.30 are absent in this simulation. This is to be expected given the reduced eddy coefficients in the unstable region in the vicinity of the front. The extremely unstable lapse near the surface is also a result of reduced mixing. The along-front and front-normal wind components (not shown) exhibit larger vertical shear above the BL and more divergence in the cold air with a slight increase in convergence near the front. Momentum is well mixed only to 850

mb, which is not surprising given the specification of  $\alpha$  in equation (5.3). The slight increase in convergence over a slightly reduced depth results in ascending motion of the same magnitude as in the full physics simulation. The region of descent is somewhat larger due to enhanced divergence in the cold air.

## 6. Summary

Use of the K-theory parameterization resulted in a more realistic frontal structure than in the AI case. The numerical results are summarized in Table 5.1. Note that the values calculated for a strong cold front over the NE Pacific Ocean observed on 16 November 1980 as documented by Fleagle et al. (1988) are included in the last row for comparison. The vertical circulation was much stronger, in spite of the fact that the convergence was not as strong. This was due to the action of parameterized BL processes.

Simulations in which various physical processes were excluded indicated that surface heat flux was most important in developing frontal structure. Although the direct effect of surface heat flux was frontolytic, the indirect effect through modulation of BL structure was critical in producing realistic frontal features. A simulation was performed in which surface drag was removed. Removal of surface drag resulted in stronger cyclonic circulation and higher frontal propagation speed which enhanced convergence and vertical motion ahead of the front. When the effect of static stability was removed from the eddy coefficients, details of BL and frontal structure were lost but the gross features were unchanged.

Both the convergence and vorticity in the frontal zone were smaller than in the AI case. In a simulation in which both surface heat and momentum fluxes were removed, convergence and vorticity were nearly doubled and were then comparable in magnitude to the AI case.

In the next section, boundary layer physical processes are included using the second-order closure turbulence parameterization discussed in Chapter IV above. While the results described in the previous section demonstrated the impact of a variety of boundary layer processes on frontogenesis through comparison to the adiabatic and inviscid case, the more realistic treatment of turbulence afforded by the second-order closure scheme will serve to highlight the specific processes most important in maritime atmospheric frontogenesis.

## C. SECOND-ORDER CLOSURE BOUNDARY LAYER

### 1. Development

In this simulation, the second order closure physics is activated at hour 72. Very little deepening occurs after this time. The minimum pressure at hour 120 is identical to that in the K-theory simulation. Figure 5.47 shows time series of minimum surface pressure for this case (2OC), for a simulation in which the surface heat flux is removed (2OC NO FLUX) described below in Section 5.3.4, and for a simulation in which the surface drag is removed (2OC NO DRAG) described below in Section 5.3.5. Figure 5.3 shows the time series of minimum surface pressure for the present case, the K-theory simulation (KTH), and the AI simulation (AI) together for comparison. Figure 5.48 shows the near surface potential temperature 12 hours after the physical parameterizations are activated. The low has deepened slightly at this time and the center and frontal trough are better defined than in the K-theory simulation. Temperature gradients at both the warm and cold fronts are also larger. By hour 96, the cold frontal trough has become still more pronounced and the minimum pressure is lower (992 mb for the K-theory vs. 988 mb for the second-order closure). The warm and cold front are also stronger (Fig. 5.49). Figure 5.50 shows the near-surface potential temperature at hour 108. Note the strength of the

fronts. The surface pressure frontal trough (not shown) has sharpened considerably during the preceding 12 hours as compared to the K-theory simulation. The 850 mb relative vorticity at hour 108 is shown in Figure 5.51. The strongest cyclonic vorticity is associated with the low. The vorticity along the cold front is larger than in the K-theory simulation. Figure 5.52 shows the surface pressure and near surface potential temperature for hour 120. The low is somewhat deeper at this time. Note the sharp cold frontal trough and well-defined warm frontal trough.

The strength of the warm front and sharpness of the frontal troughs are unique to this simulation. These features are the result of strong convergence at the front.

## 2. Frontal Structure and Circulation

Figure 5.53 shows a cross section of potential temperature at hour 84. There is a well-defined frontal zone at this time which is nearly vertical below 930 mb. Above 900 mb, the frontal slope is not unlike the slope of typical midlatitude cold fronts. The strength of the potential temperature gradient across the front is approximately  $2\text{ C (100 km)}^{-1}$ , or roughly twice as strong as in the K-theory simulation. The boundary layer in the cold air is not as well mixed as in the K-theory simulation.

During the 12 hours from 84 to 96, the front undergoes significant frontogenesis (Fig. 5.54); the cross front potential temperature gradient reaches  $4\text{ C (100 km)}^{-1}$ . Frontogenesis also occurs in vorticity (Fig. 5.55). The frontal zone is now vertical to  $\sim 890\text{ mb}$  and has a larger slope at higher levels as well. The basic structural features of the front are similar to those for the K-theory simulation, although the front is stronger and vertical over a smaller depth. Strong convergence is apparent throughout most of the cross section. The most prominent feature of the vertical motion field, shown in Fig. 5.56, is the ascending jet above the surface

front with a maximum of  $13 \mu b s^{-1}$  ( $\sim 12.5 \text{ cm s}^{-1}$ ). This value is approximately twice as large as values reported by Fleagle et al. (1988) over the NE Pacific ocean and Ogura and Portis (1982) over the south-central U.S., but only half as large as reported by Sanders (1955) over the south-central U.S.. Most importantly, it is also nearly three times as large as in the K-theory simulation.

There are, in fact, three relative maxima in ascending motion in the warm sector shown in Fig. 5.56. It should be noted in passing that the three regions of ascent ahead of the front are somewhat suggestive of frontal rainbands. The broad region of ascent in the warm sector at this time in the K-theory simulation is a poorly resolved depiction of a similar feature. In view of the relatively coarse horizontal resolution used in these simulations and the lack of moist physics, the significance of this result is unclear.

The potential temperature cross section for hour 108 is shown in Fig. 5.57. The frontal structure at this time is very similar to that at 96 hours, although the front has moved toward the south at an average speed of  $12 \text{ m s}^{-1}$  (note that the plane of the cross section is the same as at hour 96). This structure is similar to that observed in the Storm Transfer and Response Experiment (STREX) documented by Fleagle et al. (1988). In particular, the cross section through the strong maritime cold front of 16 November 1980 (page 55, Fig. 4 of Fleagle et al.) shows many of the same features seen in Fig. 5.57 (e.g., the deep mixed layer and the strong horizontal gradient across the front above the boundary layer). The results of the K-theory simulation do not compare as favorably to the STREX results in that the depth of the mixed layer in the second-order closure simulation is closer to the observations. Figure 5.58 shows the along-front and front-normal wind components at hour 108. Strong convergence and cyclonic vorticity are apparent in the wind field. Note the sign reversal in the front-normal wind within the frontal zone and

the strong cyclonic shear in the along-front wind on the cold side of the low-level jet in the cold air. Figure 5.59 shows a cross section of the relative vorticity and Figure 5.60 shows the divergence for this time. The vertical motion field is shown in Fig. 5.61. Note that the maximum ascent is nearly as large as at hour 96 but that the region of significant upward motion is much smaller (compare the 30 mb  $\text{hr}^{-1}$  contour in figures 5.56 and 5.61).

The near-surface winds in this simulation are much stronger than in the K-theory simulation, indicating that the momentum from higher levels in the boundary layer is being mixed to the surface, thereby strengthening the wind speed and thus the horizontal shear, vorticity, convergence, and vertical motion in comparison to that simulation.

In summary, the comparison of the present results to those for the K-theory simulation has shown that, at hour 84 (Figs. 5.28 and 5.53) the mixed layer in the K-theory simulation is much more well defined, although the frontal gradient is weaker than in the second-order closure simulation. The BL in the later simulation is actually slightly stable at this time. In terms of gross structural features, however, the two fronts are similar. Comparison of Figs. 5.29 with 5.54 reveals that, at this time (hour 96), the size of the temperature gradient across the front is the most significant difference between the two simulations. The convergence is stronger in the second-order closure simulation and the upward vertical motion is nearly three times as large. Cross sections of potential temperature from the two simulations at hour 108 are shown in Figs. 5.30 and 5.57. The fronts at this time are radically different. The cross-front temperature gradient is more than twice as large in the second-order closure simulation. The convergence and vertical motion are also stronger in this simulation due to more vigorous mixing of momentum. The cyclonic shear across the front in the along-front wind component is twice as large

in this simulation, giving rise to much larger cyclonic vorticity. The post-frontal mixed layer is 150 mb deep in the present simulation and nearly 300 mb deep in the K-theory simulation.

### 3. Frontal Development

The total adiabatic frontogenetic forcing for hour 108 is primarily frontolytic along the warm front and there is frontogenesis along the cold front with strong frontolysis behind it (Fig. 5.62). The bulk of the frontogenesis is due to tilting and nearly all of the frontolysis results from tilting. The stretching deformation is frontolytic along the warm front and frontogenetic along the cold front. The shearing deformation is 0 along the warm front and frontogenetic along the cold front. The distribution of frontogenetic forcing is not as well organized as in the K-theory simulation (Fig. 5.35).

The frontogenetic forcing at hours 84 and 96 is shown in Figs. 5.63 and 5.64. At these times, there is strong frontogenesis within and behind the frontal zone with weak and disorganized frontolysis ahead of the front. The frontogenetic forcing at hour 108 is shown in Fig. 5.65a. At this time, the vertical motion field shows a compact, well defined vertical circulation with a single ascending jet immediately ahead of the front and descent behind it. The tilting term shows a dipole signature (Fig. 5.65b). The dipole structure is not as apparent in the total frontogenetic forcing because both shearing and stretching deformation cancel the frontolytic effect of the tilting term. A second region of frontogenesis behind the front is due to shearing deformation. The total forcing is frontogenetic although the net effect of tilting is frontolytic. In the K-theory simulation at this time, while the magnitude of the total forcing is much smaller, the dipole signature is evident (Fig. 5.38) since the shearing and stretching deformation are both an order of magnitude less than the tilting term. The greater significance of stretching and

shearing deformation in the present simulation is a reflection of stronger convergence and vorticity.

Viewed in this context, it might be concluded that the overall effect of the vertical circulation is to destroy the front (since the net effect of the tilting term is frontolytic in both the K-theory and second-order closure simulations). While it is true that the vertical circulation acts to restore geostrophic balance, consideration of the effect of the concentrated, strong updraft ahead of the front leads to a different conclusion. The updraft enhances frontogenesis both by the frontogenetic effect of tilting ahead of the front and because strong convergence at the base of the updraft increases the temperature gradient through stretching deformation and concentrates cyclonic vorticity at the front. Vorticity is also generated through convergence and by the tilting effect on vorticity. Since the along-front southerly flow in the warm sector decreases with elevation, horizontal vorticity is generated in the front-normal plane. With the gradient in vertical motion on the warm side of the vertical jet, cyclonic vorticity is tilted into the vertical. With the front-relative front-normal wind directed toward the front, this vorticity will be concentrated at the front. Thus, the strong updraft is associated with frontogenesis both in temperature (through tilting and stretching deformation) and in vorticity.

Given that both the ascending jet and the horizontal gradient in vertical motion are much stronger in this case than in the K-theory simulation, the impacts of the updraft in terms of tilting frontogenesis, stretching deformation, concentration of vorticity, and vorticity generation through tilting are more apparent in this simulation.

The diabatic frontogenetic forcing is strongly frontolytic throughout the period. The maximum frontolysis is always located at the leading edge of the front and occurs at hour 96. Diabatic frontogenesis occurs within the frontal zone near



850 mb at hours 96 and 108. This location is near the top of the mixed layer where entrainment of high potential temperature air leads to warming. It appears that the inversion is stronger behind the front than it is in the warm sector. This distribution of inversion strength indicates that there is greater warming due to entrainment in the warm sector, which constitutes a frontogenetic effect. This effect was not present in the K-theory simulation.

For additional discussion on interpretation of frontogenetic forcing, see the frontal development section for the K-theory simulation above.

#### 4. Insulated Surface Simulation

Shown in Fig. 5.66 is the surface sensible heat flux for hour 108. Comparison of the surface sensible heat flux distributions for the K-theory and second-order closure simulations provides a striking contrast. Examination of the heat flux distribution for the K-theory simulation (Fig. 5.39) shows a very weak horizontal gradient in the vicinity of the front. The heat flux reaches  $100 \text{ W m}^{-2}$  approximately 400 km behind the front in the cold air. In the second order closure simulation, there is an extremely strong gradient across the cold front with a maximum of  $150 \text{ W m}^{-2}$  adjacent to the front on the cold side. The difference across the front is in excess of  $120 \text{ W m}^{-2}$ . There is a secondary maximum of  $180 \text{ W m}^{-2}$  on the southwest flank of the low where the air-sea temperature difference is largest in both simulations. The gradient across the warm front is negligible in the K-theory case and  $80 \text{ W m}^{-2}$  for the present simulation. Given such a large disparity between the two simulations in surface heat flux, it is of interest to compare K-theory and second-order closure simulations with the heat flux removed.

The near surface potential temperature for hour 108 of the insulated surface simulation is shown in Fig. 5.69. Figures 5.67 and 5.68 show the potential temperature fields for hours 84 and 96, respectively. While the surface pressure

distribution is similar to that for the full physics case (see Fig. 5.47), the distribution of the near surface temperature is quite different. The temperature is lower, the warm air has "wrapped around" the low as in the AI case, and the cold front is stronger than in the full physics case. The warm front, however, is not as strong.

Shown in Fig. 5.70a is a cross section of potential temperature at hour 84 in the vicinity of the cold front. The front at this time is weak and the structure is very similar to that for the full physics simulation (Fig. 5.53). The wind and vertical motion distributions are also similar, although the maximum upward motion is displaced upward by  $\sim 70$  mb. At hour 96, the warm sector is much cooler and the mixed layer behind the front is not as deep (Fig. 5.70b). The wind and vertical motion fields are similar to those in the full physics case.

Figure 5.70c shows a cross section of potential temperature at hour 108 of the simulation with surface heat flux excluded. Note that the depth of the mixed layer is much less in this case and that the cold air behind the front is much colder, although the strength of the front is nearly the same as in the previous simulation. There is much more vertical wind shear in the front-normal component above  $\sim 950$  mb in this case. The maximum convergence is displaced vertically to near 850 mb and is to the rear of the surface front. The maximum upward motion, which is centered near 750 mb, is due to this elevated maximum and is thus completely unrelated to the surface convergence. This indicates that frontogenetic forcing associated with tilting will be insignificant at low levels, as in both the K-theory simulation with heat flux removed and the AI simulation.

The intriguing aspect of this case is that, although it is slightly stronger, the front has not been substantially strengthened by the removal of the surface heat flux. Both the cold air behind the front and the warm sector are 2-3 C colder than in the full physics simulation. Thus, the temperature difference between the cold

air and the warm sector is nearly the same. This is also the case for the K-theory simulation with heat flux removed. In that simulation, however, the horizontal extent of the frontal zone decreases substantially, giving rise to a much stronger front (in fact, the strength of the front in the two simulations with heat flux removed is the same). Apparently, removal of surface heat flux allows the cold air to flow unmodified to the rear of the frontal zone, just as in the second-order closure simulation. The primary difference between the two simulations is in the depth of the mixed layer. In the second order closure simulation, the mixed layer is approximately half as deep as in the full physics simulation ( $\sim 80$  mb vs.  $150$  mb). In the K-theory simulation, the mixed layer depth is an order of magnitude less deep ( $\sim 30$  mb vs.  $300$  mb for the full physics case).

In view of the much stronger heat flux in the second-order closure simulation, its removal might be expected to have a larger effect than a removal in the K-theory simulation. Recalling, however, the similarities between the no heat flux K-theory simulation and the AI simulation leads to the observation that removing heat flux from the K-theory simulation is tantamount to removing all boundary layer processes from the K-theory parameterization. This is because surface heat flux is the most important process in deepening of the boundary layer. In the second-order closure simulation, other physical processes play a significant role as well.

In the next subsection, the effect of surface drag is examined.

## 5. Free Slip Surface Simulation

Figure 5.73 shows the near surface potential temperature for hour 108 of the free-slip surface simulation. Figures 5.71 and 5.72 show the potential temperature fields at hours 84 and 96, respectively. The near surface potential temperature is quite similar to the full physics simulation (Fig. 5.50). The low is significantly stronger in this case, as it was in the K-theory simulation with no surface drag. A

time series of minimum surface pressure is shown in Fig. 5.47 (the time series for the insulated surface and full physics simulations are also shown for comparison). The frontal trough is not as well-defined in this case, however.

Examination of cross sections of potential temperature for hours 84, 96, and 108 shows that only at hour 108 are there significant differences between these cross section and those for the full physics case. The potential temperature cross sections for the present case and the full physics case at hour 108 are shown in Figs. 5.74 and 5.57). In this case, the mixed layer depths are slightly lower on both sides of the front. The wind components (not shown) are substantially higher, as might be expected, but the convergence is only slightly stronger (Fig. 5.75). The vertical motion is somewhat smaller at hour 84 but stronger at hour 96 and substantially stronger at hour 108 (Fig. 5.76). The maximum upward motion is at roughly the same level as in the full physics simulation. As in the K-theory simulation with surface stress removed, removal of surface stress strengthens the wind, geostrophic shearing deformation, and vertical motion without significantly effecting the strength of the cross front temperature gradient. This paradox will be addressed at some length below in Chapter VI.

Stronger wind also results in stronger surface fluxes, which are frontolytic.

In terms of both structure and circulation this front is very similar to that in the previous simulation.

## 6. Level 2 Simulation

The level 2 simulation involves replacing prognostic expressions for all of the second-order terms with diagnostic expressions. An expression for turbulent kinetic energy is obtained by setting the LHS to zero and neglecting turbulent diffusion of turbulent kinetic energy (the first term on the RHS of equation (4.26)),

thereby obtaining a balance between production and dissipation. After some rearrangement, the resulting equation has three terms on the RHS; two terms for shear production and one for buoyant production.

The surface pressure and near-surface potential temperature at hours 84, 96, and 108 (not shown) are very similar to those for the full physics simulation. A cross section of potential temperature for hour 108 is shown in Fig. 5.77. Note that the strength of the front and boundary layer structure in the warm sector are nearly identical to the full physics simulation (Fig. 5.57) but that the depth of the mixed layer within the frontal zone and in the cold air is much less than in the full physics case. Cross sections of the front-normal and along-front wind components (not shown) are consistent with this picture; the distributions are quite similar to the full physics results but features near the surface have a smaller vertical scale. The most important difference between these two simulations is in the vertical motion (Fig. 5.78). The largest ascent is less than half of that in the full physics simulation ( $5 \mu \text{ b s}^{-1}$  vs. 11 for the full physics case shown in Fig. 5.61). The vertical motion field is also relatively disorganized in this simulation.

The results of this simulation show that removing turbulent mixing of turbulent kinetic energy results in a much shallower boundary layer and a weak, disorganized vertical motion field. In the full physics (level 3) simulation, turbulent mixing of turbulent kinetic energy resulted in the transport of turbulent kinetic energy into the vicinity of the inversion, thus partially countering buoyant destruction due to stable stratification. This enhanced entrainment and deepening of the boundary layer. In the level 2 simulation, diffusion of turbulent kinetic energy is neglected and the boundary layer is not as deep. This reduces the depth over which turbulent mixing of momentum occurs which, in turn, reduces integrated mass convergence and vertical motion.

A level 2.5 simulation was also performed. This involves replacing prognostic expressions for all of the second-order terms except turbulent kinetic energy with diagnostic expressions. Prognostic expressions for turbulent kinetic energy and the mean quantities are retained. This greatly simplifies the numerical scheme and level 2.5 models have gained considerable popularity. The scheme has, however, been criticized by Helfand and Labraga (1986) in that it may produce unphysical results in situations in which the turbulence level is changing rapidly (for example, frontogenesis) due to neglect of the time tendency in other second-order quantities (variances and covariances). The results of the level 2.5 simulation are nearly identical to those for the full physics run. This indicates that, in the present implementation, the neglect of the time tendency does not seriously compromise the results. Inclusion of moist thermodynamics may alter this conclusion.

## 7. Summary

Use of the second-order closure simulation produced a depiction of frontal features which was much more realistic than the AI case and somewhat more realistic than the K-theory case. The numerical results are summarized in Table 5.1. Note that values calculated for the strong cold front from the STREX field program documented by Fleagle et al. (1988) are included in the last row for comparison. The magnitude of the potential temperature gradient across both the warm and cold fronts was much larger than in the K-theory simulation. The convergence, vorticity, and vertical motion were all much stronger than in either of the other two cases. The results compared favorably with the observations of maritime fronts from the STREX field program.

At hour 108, the convergence and vertical motion are both three times as large as in the K theory simulation. The vorticity is more than four times stronger. The gradient in potential temperature is twice as large. Both convergence and

vorticity are larger than in the AI case (vorticity is more than twice as strong and vertical motion is seven times as large).

The primary difference between the K-theory and second order closure simulations is the depth of the post-frontal mixed layer. The K-theory scheme is much more active in terms of turbulent mixing of heat and entrainment, both of which are frontolytic. This is due to differences in the length scale formulation. Although both schemes use the Blackadar (1962) formulation for the length scale (4.15), the K-theory scheme uses a constant value in the asymptotic limit (350 m for the eddy heat coefficient). The asymptotic limit in the second order closure scheme is the ratio of the first to the zeroth order moments of the profile of the turbulence and is thus dependent on the vertical distribution of turbulence. This results in a much larger mixing length above the inversion in the K theory scheme than in the second-order scheme. The manifestation of this difference in length scales is in the differing responses of the two turbulence parameterizations to the presence of an inversion. Examination of the vertical profiles of the eddy coefficients in the cold air near the front where the eddy coefficients are largest shows a relatively gradual decrease in the magnitude of the eddy coefficients above the inversion in the K-theory parameterization ( $\sim 1$  order of magnitude  $(100 \text{ mb})^{-1}$ ) and a much sharper decrease with elevation in the second-order scheme (four orders of magnitude between the inversion and the grid point above). Previous experience with the two schemes is consistent with this behavior; the second-order closure scheme strengthens the inversion with time during entrainment more enthusiastically and realistically than does the K-theory scheme. Strengthening of the inversion inhibits further mass entrainment and deepening of the boundary layer in the second-order closure scheme.

The physical interpretation of the differences between the second-order closure and K-theory schemes arises from the concept that the length scale is, in

some sense, related to the scale of the parameterized eddies responsible for turbulent mixing. In the second-order closure scheme, the scale of the parameterized eddies depends on the vertical distribution of turbulent kinetic energy in each vertical column, while in the K-theory scheme, the scale of the eddies has a constant value (in regions where the asymptotic limit applies).

Other reasons for differences include different surface layer parameterization and stronger vorticity and convergence. Experiments were performed in order to determine the effect of the surface layer parameterizations on the simulations (the surface layer parameterizations are discussed in Chapter IV). These experiments indicated that the scheme used in the second-order closure simulations (the Liu et al. (1979) scheme) responds rapidly to changes in surface layer stability. Differences in stability over small spatial scales can result in large horizontal gradients in drag coefficients for momentum and heat. The Louis (1979) scheme used in the K-theory simulation does not respond as rapidly. This behavior is clear from the distributions of surface heat flux discussed in Section 4 above and shown in Figs. 5.66 and 5.39. The larger near surface wind speed due to stronger momentum mixing in the second-order closure case is also partially due to use of the Liu et al. scheme. The results of the additional experiments performed indicate, however, that the differences in the surface layer parameterizations have a smaller impact on the simulations than do the differences in the eddy coefficients discussed above. Larger cyclonic vorticity in the second-order closure simulation is a consequence of stronger convergence and, to a lesser extent, vertical motion. Frontogenesis in vorticity forced by vertical motion is discussed in the frontal development section for the full physics second-order closure simulation above. Stronger convergence results from the stronger frontal temperature gradient and upward vertical motion.



## VI. DISCUSSION

### A. INTRODUCTION

The results of the adiabatic and nearly inviscid simulation demonstrate that, in the absence of boundary layer physical processes, a growing baroclinic wave will generate very strong warm and cold fronts near the surface. Relative vorticity and convergence within the frontal zone are large, as is the horizontal potential temperature gradient across the front. These simulations, however, are unrealistic in several ways. For example, vertical motion and the circulation about the front are extremely weak.

Use of the K-theory parameterization resulted in a more realistic frontal structure than in the AI case. The vertical circulation was much stronger, in spite of the fact that convergence was not as strong. This was due to the action of parameterized BL processes.

Simulations in which various physical processes were excluded indicated that surface heat flux was most important in developing the frontal structure. Although the direct effect of surface heat flux was frontolytic, the indirect effect through modulation of BL structure was critical in producing realistic frontal features. Both convergence and vorticity in the frontal zone were smaller than those in the AI case. When surface heat and momentum fluxes were removed from the simulation, convergence and vorticity were nearly doubled and were then comparable in magnitude to the AI case.

Use of the second-order closure parameterization produced a depiction of frontal features which was much more realistic than the AI case and somewhat

more realistic than the K-theory case. The magnitude of the potential temperature gradient across both the warm and cold fronts was much larger than in the K-theory simulation. Convergence, vorticity, and vertical motion were all much stronger than in either of the other two cases. The results compared favorably with observations of maritime fronts from the STREX field program. The results of this simulation compared more favorably with observations than results of the K-theory simulation because of the more realistic treatment of turbulent mixing in the second order scheme due to use of a physically-based length scale formulation.

Given the results of these simulations, several boundary layer processes important in frontogenesis can be identified. The primary physical processes operative in simulations including boundary layer physics are surface fluxes of heat and momentum and turbulent diffusion of heat and momentum. These four processes are manifested in many different ways and each of them gives rise to nonlinearities and feedbacks which hinder gaining a complete understanding of their impacts on frontogenesis. Some of these processes are important in directly strengthening the frontal temperature gradient while others impact frontogenesis through modification of the secondary transverse circulation, which is crucial in both genesis and maintenance of the frontal zone. Some of these processes are, of course, important in both areas.

#### **B. PROCESSES DIRECTLY INFLUENCING FRONTAL GRADIENTS**

Turning first to surface heat flux, it is obvious that the direct, first order effect is on the frontal temperature gradient and is frontolytic: heat flux divergence associated with the upward surface flux in the cold air causes warming, driving the temperature in the cold air toward that of the warm sector. Surface heat flux is partially responsible for weakening the front in simulations with boundary layer parameterizations as compared to the adiabatic and inviscid simulation. In the

simulation using the K-theory parameterization with surface heat flux excluded, the front was much stronger. Diabatic frontolysis in both the K-theory and the second-order closure simulations had a relative maximum at the surface at the leading edge of the front due to surface heat flux (a secondary maximum was located well behind the front in the cold air coincident with the maximum surface heat flux).

In contrast to surface heat flux, the direct, first order effect of surface drag is on the frontal temperature gradient and is frontogenetic: frictionally-induced convergence at the front contracts the near surface temperature gradient. However, convergence not only strengthens the frontal temperature gradient directly but also increases cyclonic relative vorticity due to vortex stretching. The cyclonic circulation implied by increasing cyclonic vorticity acting on the along-front temperature gradient constitutes a frontogenetic (frontolytic) influence for cold (warm) fronts (Gidel, 1978). Thus, increased convergence has both a direct and an indirect frontogenetic effect on cold fronts. In the adiabatic and nearly inviscid simulation, the bulk of the frontolysis along the warm front resulted from this mechanism. Surface drag also has a second-order effect which is frontolytic. As discussed by Branscome et al. (1989), inclusion of surface drag reduces growth in the amplitude of the baroclinic wave. This, in turn, reduces the strength of the geostrophic shearing deformation. The results of the present study are consistent with those of Branscome et al. (1989).

Vertical turbulent mixing of heat has several more subtle effects on frontogenesis. Many of these are related to entrainment.<sup>1</sup> In the case in which the atmosphere

---

<sup>1</sup>A certain amount of caution is necessary in identifying entrainment with turbulent mixing. Although entrainment results from turbulent mixing and generally increases in intensity as the turbulence level increases, the effects of entrainment are not entirely consistent with mixing, which is regarded as a diffusive process. For example, the effect of entrainment is to *increase* the vertical gradient in potential temperature at the top of the BL. However, the net effect of entrainment is to warm and dry the BL by combining air from the BL with warmer, drier air from the free atmosphere.

is stable aloft and at all levels in the warm sector and unstable behind the cold front, the growing BL behind the cold front will entrain warm air while the warm sector will remain quiescent. Thus, vertical mixing will be frontolytic as the cold air will be warmed by entrainment. This effect acts in concert with warming of the cold air by surface fluxes (since the entrainment flux is directly proportional to surface heat flux in a free convective regime). This process can also result in frontogenesis. In the second-order closure simulation, diabatic frontogenesis occurs within the frontal zone near 850 mb at hours 96 and 108. This location is near the top of the mixed layer where entrainment of high potential temperature air leads to warming. The inversion is stronger behind the front than it is in the warm sector. This distribution of inversion strength indicates that there is greater warming due to entrainment in the warm sector, which constitutes a frontogenetic effect.

Another aspect of surface heat flux and turbulent mixing of heat is in controlling the static stability and boundary layer depth. The importance of the control of boundary layer depth will be discussed below.

An intriguing aspect of the frontal potential temperature fields shown in the previous chapter for the K-theory and second-order closure simulations is that the frontal zone exhibits no tilt in the vertical over the lowest 100–200 mb. This is in contrast to the adiabatic and nearly inviscid simulations (and many observational studies) in which the frontal zone has a pronounced vertical tilt. The well-known formula of Margules also mandates that the slope of a front be nonzero. The simulated frontal structure is, however, consistent with the structure of marine cold fronts observed over the NE Pacific ocean during the Storm Transfer and Response Experiment (STREX) (Fleagle et al., 1988). In order for simulated fronts to have a substantial tilt, the BL near the front on the cold side would have to be very shallow. This region, however, is very statically unstable; in both the simulation

and the STREX data, upward surface heat flux behind the front is nearly  $200 \text{ W m}^{-2}$ . Given this strong instability, a deep mixed layer would be expected. Thus, it appears to be unreasonable to expect maritime cold fronts to exhibit the vertical tilt commonly associated with continental cold fronts.

One effect of the the ageostrophic vertical circulation is to cause the front to tilt (Bluestein, 1986). In the following discussion, we will refer to this as the "sloping effect" in order to avoid confusion with the vertical deformation term of the frontogenetical function. In the upper portion of the BL, warm air is advected toward the cold air by the horizontal branch of the circulation while, in the lower BL, cold air is advected toward the warm air, resulting in a tilted front. From the Sawyer-Elliassen equation, we can infer (following Bluestein) that, if inertial stability (absolute vorticity in the term involving the vertical derivative of the ageostrophic momentum) is large compared to static stability (in the term involving the horizontal derivative of the vertical motion), vertical motion dominates and horizontal motion is inhibited; if absolute vorticity is small compared to static stability, horizontal motion dominates and vertical motion is inhibited. In the second-order closure simulations, the static stability is near zero while the relative vorticity is approximately  $0.6 \times 10^{-4} \text{ s}^{-1}$  so that horizontal motion is inhibited and vertical motion dominates. Thus, the sloping effect of the vertical circulation will be reduced. This provides a dynamic mechanism for production of vertical fronts in the presence of strong instability. In a study of a continental cold front with a substantial vertical tilt, Ogura and Portis (1982) found the maximum relative vorticity to be  $1 \times 10^{-4} \text{ s}^{-1}$ . The static stability (the Brunt-Vaisala frequency) in this case can be crudely estimated from a cross section shown in their Fig. 17 as  $\sim 1.5 \times 10^{-3} \text{ s}^{-1}$ . Therefore, in this continental cold front exhibiting substantial vertical tilt, the static stability is large compared

to the relative vorticity and horizontal motion dominates. Thus, the sloping effect of the vertical circulation is enhanced.

It is ironic that the primary criticism of quasi-geostrophic fronts is that they have no tilt in the vertical (Stone, 1966) given the present results and those of recent observational studies showing that maritime fronts apparently are vertical at low levels. There are, however, other characteristics of quasi-geostrophic fronts, which are referred to as "pseudo-fronts" by Williams (1967), not shared by fronts depicted in the current simulations. For example, the vorticity distribution of fronts in the present study is more realistic than is the case with quasi-geostrophic pseudo-fronts which have regions of strong negative relative vorticity adjacent to the front on the cold side. In addition, pseudo-fronts exhibit extremes of static stability with large positive vertical gradients in potential temperature in the cold air and negative gradients in the warm sector. These unrealistic features greatly enhance the frontolytic effect of adiabatic temperature changes due to vertical motion.

### **C. PROCESSES INFLUENCING THE TRANSVERSE VERTICAL CIRCULATION**

The importance of the thermally direct ageostrophic transverse secondary circulation in both frontogenesis and in the maintenance of mature frontal zones cannot be over-emphasized. Convergence at the surface under the rising branch of the circulation acts frontogenetically, and augments the effects of geostrophic deformation while vertical deformation increases the cross-front temperature gradient. Thus, synoptic-scale, geostrophic deformation is regarded as initiating frontogenesis, whereas the completion and maintenance of the front are due to the vertical circulation (Eliassen, 1959).

The secondary ageostrophic circulation is driven by the dynamics of frontogenesis. It acts to restore thermal wind balance by 1) adiabatic temperature changes due

to vertical motion (which reduce the cross-front temperature gradient) (Bluestein, 1986) and 2) increasing the vertical shear much as the secondary vertical circulation associated with a growing baroclinic wave acts to keep vorticity changes geostrophic and temperature changes hydrostatic. The geostrophic vertical shear is enhanced due to the frontal baroclinic zone (thermal wind). Vertical shear in the along-front wind increases towards the geostrophic value by Coriolis turning of the front-normal ageostrophic wind:

$$\frac{dV}{dt} = -f(\mathbf{k} \times \mathbf{V}_a).$$

The ageostrophic wind is a response to the increased slope of pressure surfaces.

Inclusion of BL physics augments the strength of the ageostrophic circulation and thereby contributes to frontogenesis. Surface drag enhances low-level convergence. Convergence acts frontogenetically in that it enhances the strength of the ascending branch of the secondary ageostrophic circulation. Vertical deformation associated with the circulation increases near-surface baroclinicity and vorticity within the frontal zone. Note also that friction opposes its own dissipative effect on vorticity.<sup>2</sup>

In both the K-theory and second-order closure simulations, vertical deformation was the primary source of frontogenesis while, in the adiabatic and nearly inviscid simulation, the contribution from tilting was much smaller. This resulted from small upward motion in the adiabatic and inviscid case. As discussed above in Chapter V, while the pattern of vertical motion was similar in all three of these simulations, the magnitude was much smaller in the adiabatic and inviscid case.

---

<sup>2</sup>Winds are convergent (divergent) in regions of cyclonic (anti-cyclonic) relative vorticity due to surface friction. Convergence enhances relative vorticity. Thus, friction opposes its own dissipative effect on vorticity through the divergence term (Carlson, 1991). This idea was alluded to by KA82 when they stated that "convergence in the frictionally driven PBL [planetary boundary layer] inflow... counteracts the dissipation of vorticity by PBL friction...".

An important result from the K-theory simulation is that, while the convergence is only about half the value in the AI case, the updraft is more than twice as strong. This results from convergence extending through a deep layer. Thus, the turbulent mixing in concert with the surface fluxes organizes convergence in such a way as to produce a much more compact and vigorous vertical circulation. This is largely accomplished by mixing momentum near the surface so that the horizontal shear exists through a relatively deep layer. In the second-order closure simulation, both convergence and vertical motion are stronger than in the K-theory case. When the effect of surface drag is removed, the vertical motion is much stronger. This leads to the paradoxical conclusion that the transverse ageostrophic circulation is stronger in the absence of surface drag. Closer examination of the results, however, indicates that convergence at and near the surface is nearly the same as in the full physics simulation. The effect of removing surface drag is evident in the wind field (particularly in the front-normal component). The wind is stronger but the strong wind extends almost to the surface. Thus, although the wind is much stronger, the convergence is not. This is an encouraging result in that it verifies the importance of surface drag in enhancing low level convergence. The explanation for enhanced vertical motion lies in mixing of momentum in this case also. Strong convergence extends all the way to the surface as well as existing through a relatively deep layer, giving rise to a large value of integrated mass convergence. In the full physics simulation, wind speed and convergence decrease towards the surface due to surface drag. These results are summarized in Table 6.1.

The results of the level 2 simulation are consistent with the argument that turbulent mixing of momentum is critical in strengthening the transverse ageostrophic circulation as well. When turbulent mixing of turbulent kinetic energy is removed, the vertical motion is less than half as strong as in the full physics simulation.



In summary, there were indications as to the importance of turbulent mixing of momentum in the K-theory simulation. The more realistic treatment of turbulence in the second order closure simulation clarified this issue. The results are consistent with the idea that frictional depletion of momentum at the surface combined with turbulent mixing will cause a momentum deficit throughout the BL. This in itself creates ageostrophic flow since the Coriolis force ( $fv$ ) will be too small relative to  $(1/\rho)\partial p/\partial x$  (see Keyser and Anthes, 1982). The important point is that this ageostrophic flow will be directed towards the front, enhancing convergence over a deep layer. The integrated mass convergence then results in strong upward motion. This also shows that, while the direct effect of surface heat flux and turbulent mixing of heat is frontolytic, the role that heating plays in modulating boundary layer depth is important in frontogenesis.

These results are, to a certain extent, anticipated by the work of Nuss (1989). In simulations of explosive marine cyclogenesis, he found that the prefrontal updraft was driven by frictionally induced boundary layer convergence and the distribution and intensity of this convergence were influenced by stability. Furthermore, the surface wind stress, which is a measure of the downward momentum fluxes in the BL, is also influenced by boundary layer stratification changes. The surface wind stress was found to be largest in unstable regions. Thus, we may conclude based on the results of Nuss that the prefrontal updraft will be enhanced in unstable regions due to increased downward momentum fluxes — a conclusion consistent with that of the present study and with the results of both the K-theory and second-order closure simulations.

This discussion has a bearing on the arguments presented by Koch (1984), Pinkerton (1978), Dorian et al. (1989), and Reeder (1986). These authors discuss scale contraction and intensification of the vertical circulation in the presence of

horizontally differential heat flux (with the strongest heat flux in the warm sector). Reeder explains this based on higher order terms in the divergence equation leading to enhanced convergence in areas experiencing convergence in an insulated surface simulation. This argument has not gained widespread acceptance. In Reeder's simulation, a cold front moved onshore and encountered a deep mixed layer in the warm sector caused by strong upward heat flux from ground heated by insolation. In other studies, the warm sector was heated by horizontally differential surface heat flux arising from other causes. In the present study, there is also an intensification of the vertical circulation in the presence of surface heat flux. The heat flux, however, is largest in the cold air behind the front and constitutes a frontolytic effect. This argument is supported by comparison of results of the K-theory to the second-order closure simulation. Recall that, in the K-theory simulation, the horizontal gradient in surface heat flux was extremely weak while, in the second order closure simulation, the difference across the front was in excess of  $120 \text{ W m}^{-2}$ . The upward vertical motion in the second-order closure simulation was three times as large as in the K-theory simulation. A common theme between the present results and published work is the relatively deep mixed layer in the warm sector. Thus, in all of these cases, vertical turbulent mixing of momentum was taking place in and ahead of the frontal zone. In light of the present results, it is likely that mixing of momentum in the deep mixed layer in and ahead of the frontal zone may explain intensification of the vertical transverse circulation in the presence of horizontally differential surface heat flux.

The adiabatic and inviscid, K-theory, and second-order closure parameterizations comprise a hierarchy in levels of sophistication in treatment of vertical turbulent mixing. The strength of the vertical circulation increases with increasing sophistication. In the adiabatic and inviscid simulation, there is small vertical mo-

tion while, in the second-order closure simulation, the ascent exceeds that in some published observational studies.

Keyser and Anthes (1982) state that "...increasing the vertical resolution in the PBL results in improved vertical structure of the... $\omega$  jet...". Clearly, increasing the vertical resolution is not adequate. The adiabatic and inviscid, K-theory, and second-order closure simulations were all run with the same vertical resolution but only in the second-order closure case is there strong vertical motion resulting from more realistic treatment of turbulent mixing.

**[THIS PAGE INTENTIONALLY LEFT BLANK]**

## VII. CONCLUSIONS

The primary conclusions of the present study are as follows:

1. A hydrostatic primitive equation three-dimensional model simulated the growth of a baroclinic wave from a small amplitude perturbation on a baroclinically unstable flow to a deep low with strong circulation and warm and cold fronts. Lower boundary conditions were specified in a manner consistent with oceanic cyclogenesis/frontogenesis. Analyses of the structure and dynamics of the growing baroclinic wave at 72 h showed its behavior to be consistent with observations and traditional conceptual models. It may thus be concluded that the approach used in this investigation (the use of a numerical model to simulate the growth of a baroclinic wave and development of the associated warm and cold fronts) is sound.
2. The adiabatic and nearly inviscid simulation produced intense fronts with strong convergence and vorticity but with an unrealistically weak vertical transverse circulation. The primary process leading to frontogenesis in this case was geostrophic shearing deformation.
3. The K-theory simulation produced a somewhat more realistic depiction of frontal structure, although the vorticity and convergence were weaker than in the adiabatic and inviscid case. Several boundary layer physical processes played a role in producing more realistic results. Specifically, surface heat and momentum fluxes combined with turbulent mixing of heat promoted the development of a deep, well-mixed boundary layer. Surface drag also reduced

near-surface wind speed and produced frictional convergence. Turbulent mixing of momentum combined with frictional convergence lead to the development of a stronger transverse secondary circulation than in the AI case. The strength of the front was greatly reduced by surface heat flux.

4. Several numerical experiments were performed in which various physical processes were excluded from the K-theory simulation. The results suggested that surface heat flux was the most significant process in producing the results of the full physics simulation.
5. The second-order closure simulation produced stronger vorticity, convergence, and vertical motion than either the K-theory or the adiabatic and inviscid simulation. The front was twice as strong as in the K-theory case but not nearly as strong as in the adiabatic and inviscid case. Results of this simulation compared favorably with observations of maritime fronts from the Storm Transfer and Response Experiment (STREX).
6. Results of numerical experiments in which various physical processes were excluded indicated that both surface heat and momentum fluxes were required to reproduce the results of the full physics simulation.
7. Examination of the results indicated that the use of a length scale based on the vertical distribution of turbulent kinetic energy in the second-order closure scheme resulted in a more realistic parameterization of turbulence than the K-theory scheme, in which the asymptotic limit of the length scale is a constant. This length scale prescription resulted in a sharp decrease in eddy coefficients with elevation above the inversion in the second order closure case and more gradual decrease in the K-theory case. This K-theory formulation resulted

in enhanced entrainment and a mixed layer which was too deep and a front which was too weak as compared to observations from STREX.

8. In both the K-theory and second order closure simulations, the fronts did not tilt in the vertical over the lowest 100–200 mb. This structure is broadly consistent with observations of fronts over the NE Pacific ocean and apparently results from strong upward surface heat flux in the cold air behind the front. Dynamical arguments involving the transverse vertical circulation suggest that vertical fronts may be expected in regions of neutral static stability.

9. Analyses of frontogenetic forcing show that vertical deformation was most important in both the K-theory and second-order closure simulations. Stretching and shearing deformation played small but significant roles in both simulations. In the adiabatic and inviscid simulation, stretching and shearing deformation were important along different portions of the front. Vertical deformation was very small in the vicinity of the fronts.

In the K-theory and second-order closure simulations, frontolysis along both the warm and cold fronts was due to diabatic frontogenesis, which had a relative maximum at the surface at the leading edge of the front. In all three simulations, frontolysis along the warm front was due to shearing deformation, which quantifies the impact of cyclonic circulations on the along-front temperature gradient.

10. In both the K-theory and second-order closure simulations, vertical turbulent mixing of momentum enhanced vertical motion and, therefore, frontogenesis. In the K-theory simulation, upward motion ahead of the front in the warm sector was stronger than in the adiabatic and inviscid case in spite of the fact that the convergence was not as large. In the second-order closure simulation,

convergence and vertical motion were both stronger than in the K-theory simulation. In the second-order closure simulation with surface drag removed, the convergence near the surface was only slightly stronger than in the full physics simulation but the vertical motion was much stronger due to vertical turbulent mixing of momentum.

11. The results suggest the following scenario for midlatitude maritime frontogenesis:

- (a) Geostrophic shearing deformation associated with a growing baroclinic wave begins to develop a strong baroclinic zone on the northeast side of the low with a weaker zone extending south and west at 72 h. At this time, there is large upward motion due to strong convergence in the vicinity of the strong baroclinic zone with little descent and no significant vertical motion associated with the weaker zone. Boundary layer physical processes do not play an important role at this time.
- (b) Twelve hours later, the northern baroclinic zone, now recognizable as a warm front, extends over the low from west to east and southeast in advance of the low. The second baroclinic zone, now recognizable as a cold front, extends southwestward from the south side of the low. The two fronts do not intersect at the low but are separated at the frontal fracture. The thermal gradients across both zones are nearly the same as at 72 h. The upward motion in the vicinity of the warm front is also the same as at 72 h. There is weak upward motion and no descent associated with the southern branch of the warm front. There is now a strong, thermally direct circulation about the cold front and tilting frontogenesis begins to accelerate contraction of the thermal gradient at this location.



Weak tilting frontogenesis along the warm front is canceled by shearing deformation.

- (c) At 96 h, the cold front has strengthened dramatically while the northern and southern portions of the warm front have weakened slightly. The direct circulation about the cold front is now stronger than at any other time. The boundary layer in this region is approximately 150 mb deep and vigorous mixing of momentum is occurring along with frictional convergence, augmenting the strength of the updraft ahead of the front. Strong upward surface heat flux and entrainment are occurring. Both of these processes are frontolytic. Although it has weakened over the last 12 hours, there is still significant upward motion associated with the northern branch of the warm front and little vertical motion along the southern branch. Tilting frontogenesis is still quite strong along the cold front and small along the southern portion of the warm front. The contribution due to tilting along the warm front is canceled by frontolysis in both shearing and stretching deformation.

The warm and cold fronts now intersect and an occlusion is developing to the north of this intersection.

- (d) At 108 h, the strength of the cold front is unchanged. Tilting frontogenesis, which is still strong, is balanced by diabatic frontolysis with a small contribution from the shearing deformation. Boundary layer depth is unchanged. The northern and southern portions of the warm front are again slightly weaker than at 96 h. Frontolysis in the shearing deformation now dominates the total adiabatic frontogenesis along the southern portion of the warm front.

The occlusion is now a prominent feature of the simulation. Horizontal cross sections spanning the domain at different latitudes clearly show warm air being forced aloft at higher latitudes.

- (e) At 120 h, all of the fronts are weaker than at 108 h. The occlusion is now the most prominent feature.

In the near future, this work should be extended in simulations using higher horizontal resolution. This should be possible with currently available computers.<sup>1</sup> Some work in this direction has been performed using nested grids (Gall et al., 1987). In time, it may be possible to understand more fully the specific roles fulfilled by turbulent mixing in frontogenesis through the use of large eddy simulation (LES) of fronts and baroclinic waves. However, this work must await the development of more powerful computers; current LES implementations require hundreds of hours of cpu time for domains on the order of 10's of km-simulation of fronts and baroclinic waves requires domain sizes two orders of magnitude larger.

Another area in which further work is required is in documenting the characteristics of the westward extension of the warm front (WEWF) in the Shapiro and Keyser (1990) conceptual model. Some effort in this direction was made in the present study (see Appendix). The results, although incomplete, are encouraging but not entirely consistent with that model. For example, Shapiro and Keyser do not include an occlusion in their conceptual model. This was not the case in either the adiabatic and inviscid simulation or the second-order closure simulation. Many of the results concerning the occlusion and the WEWF are consistent with more recent publications by Shapiro and his co-workers (e.g., Neiman and Shapiro, 1993; Neiman et al., 1993; Kuo et al., 1992). Further study is also required on the impact

---

<sup>1</sup>The present study was performed on a CY205 computer; large amounts of computer time and the entire central memory were required for the second-order closure simulations.

of differing sea surface temperature distributions on the WEOF and occlusion and interaction of the WEOF with the occlusion.

In the present study, two different surface layer parameterization schemes were used. The more sophisticated scheme used in the second-order closure simulations produced larger horizontal and vertical gradients in fluxes of heat and momentum. In the future, additional surface layer elements should be investigated. In particular, the effects of wave age and sea spray should be included. In the vicinity of a maritime front, unsteadiness in the wind field due to changes in fetch and wind speed and direction could significantly impact the evolution of roughness elements. In addition, sea spray could have a large effect on the drag coefficient for heat and moisture.

**[THIS PAGE INTENTIONALLY LEFT BLANK]**

**Table 4.1: MODEL CHARACTERISTICS**

	Value
Domain Size ( $x$ )	2960 km
Domain Size ( $y$ )	4000 km
$\Delta x$	40 km
$\Delta y$	40 km
$\Delta z$	$\delta$
$\Delta t$	120 seconds
$f$	$1.031 \times 10^{-4}$
Jet Max	40 m/s at 200 mb
Meridional Jet Profile	$\sin^2$
Perturbation Amplitude	1 m/s
No. of Gravity Modes	1 m/s
Horiz. Diffusion Coeff.	$-10^5$

**Table 4.2: VERTICAL STRUCTURE**

	$\delta$	Approximate Geometric Altitude
1	0.0100	29469.
2	0.0350	21450.
3	0.0675	17412.
4	0.1050	14809.
5	0.1500	12758.
6	0.2000	11105.
7	0.2500	9799.
8	0.3000	8694.
9	0.3500	7722.
10	0.4125	6643.
11	0.5000	5322.
12	0.6000	4011.
13	0.7000	2855.
14	0.7875	1941.
15	0.8500	1334.
16	0.8900	961.
17	0.9200	691.
18	0.9500	426.
19	0.9750	211.
20	0.9900	84.
21	0.9970	21.

**Table 5.1: SUMMARY**

	<b>Max <math>\nabla\theta</math> (K/(100 km))</b>	<b>Time of Max <math>\nabla\theta</math> (h)</b>	<b>Max Vorticity (<math>10^{-4}</math>/s)</b>	<b>Max Divergence (<math>10^{-4}</math>/s)</b>	<b>Max <math>\omega</math> (<math>\mu</math> b/s)</b>
AI	10.00	120	3.90	-0.60	-1.67
Kth	1.66	108	1.20	-0.40	-4.44
No Flux	3.75	108	0.80	-0.24	-1.39
No Stab	1.66	108		-0.50	-4.44
2OC	4.00	108	5.60	-1.10	-11.11
No Flux	4.20	96		-1.20	-11.67
No Drag	3.75	108		-1.20	-13.89
Lev12	4.00	96	1.80	-0.48	-5.00
Fleagle et al. (1988)	0.60	—	3.00	-0.55	-7.90

**Table 6.1: FULL PHYSICS VS. NO DRAG**

	<b>Full Physics</b>	<b>No Drag</b>	<b>Percentage Change</b>
$\omega$ ( $\mu$ b/s)	11.11	13.89	20%
Normal Component (m/s)	9.00	14.00	55%
Divergence ( $10^{-4}$ /s)	1.10	1.20	9%



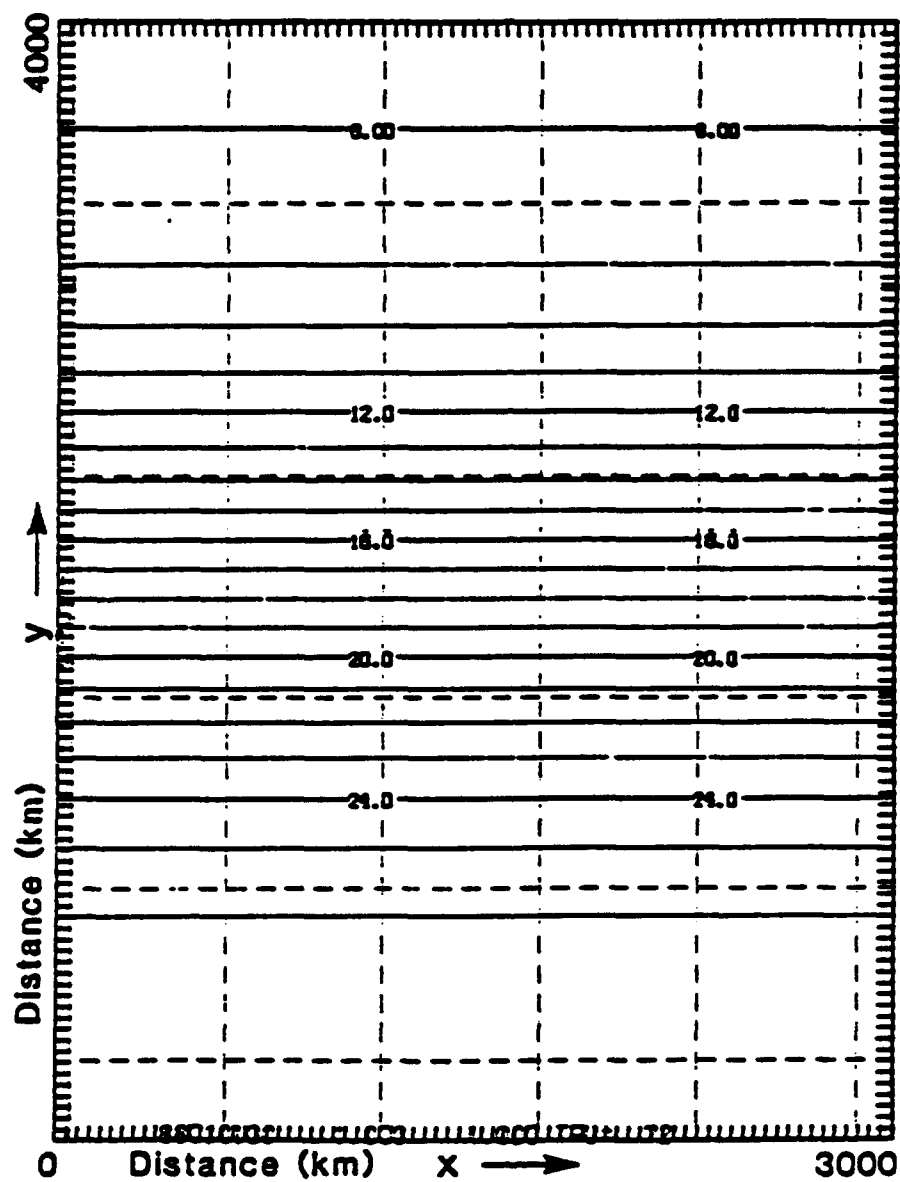
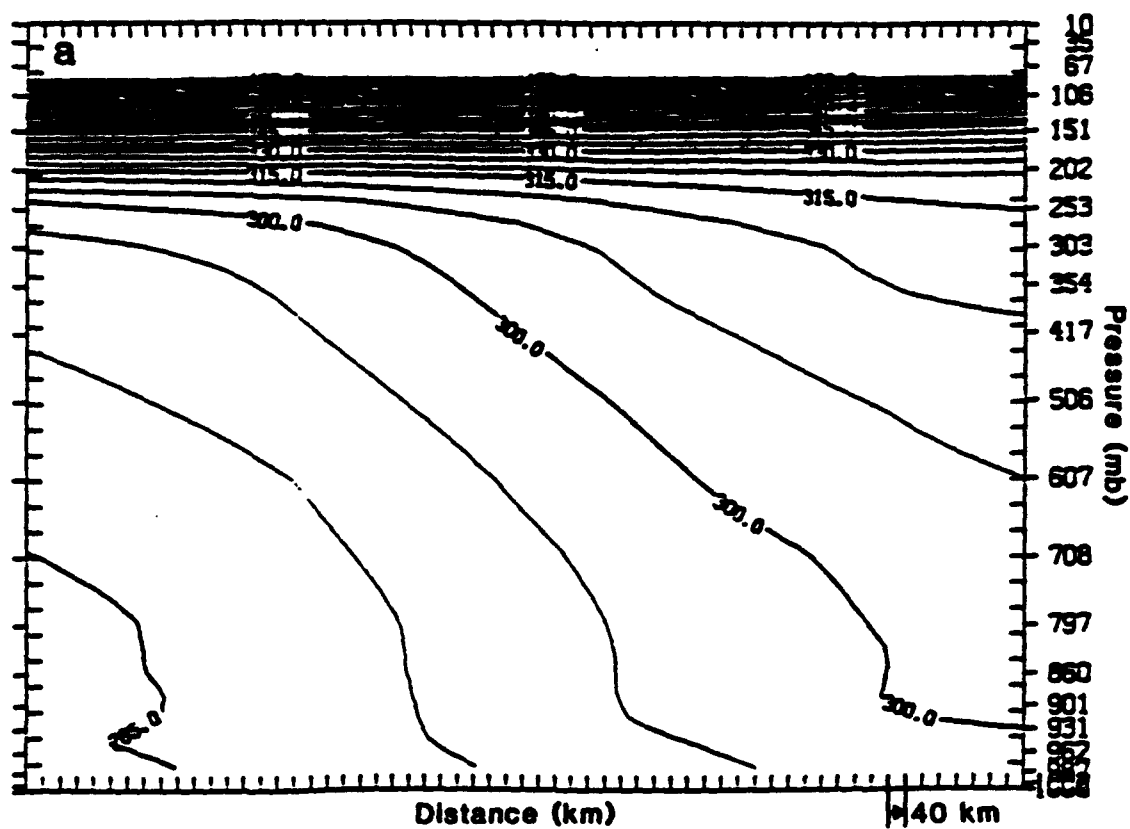


Figure 5.1: Initial sea surface temperature field (C) over the entire model domain.



**Figure 5.2:** Meridional cross sections of the initial a) potential temperature (K) and b) zonal wind component ( $\text{m s}^{-1}$ ) from the surface to 10 mb and from the northern boundary to the southern boundary.

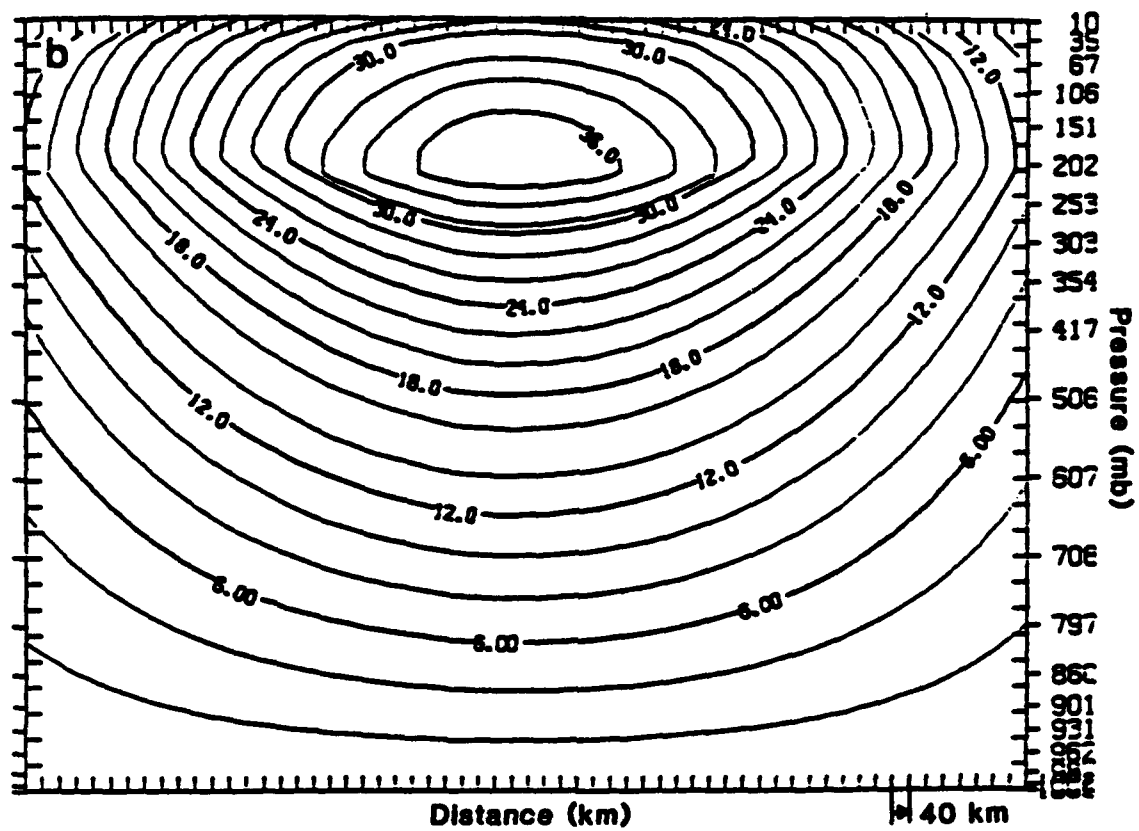
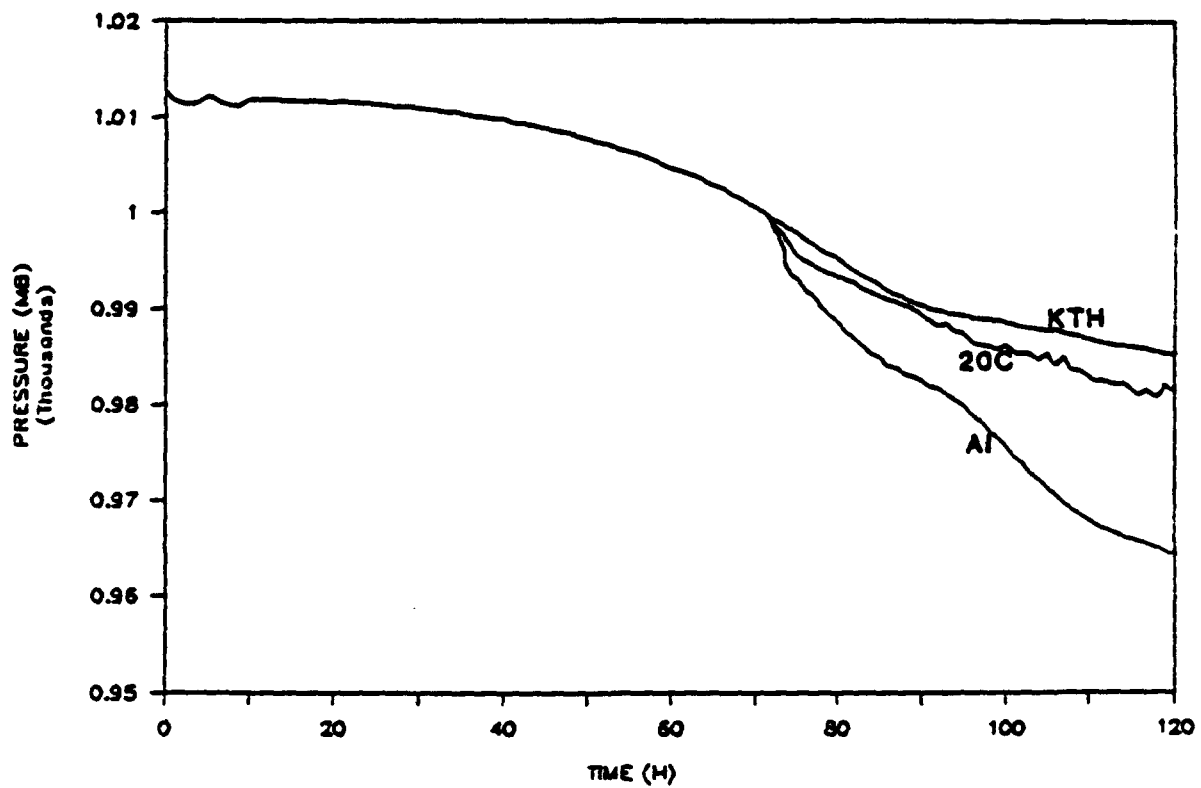


Figure 5.2: Continued.



**Figure 5.3:** Time series of minimum surface pressure (mb) for adiabatic and inviscid simulation (AI), K-theory simulation (KTH), and second-order closure simulation (20C).

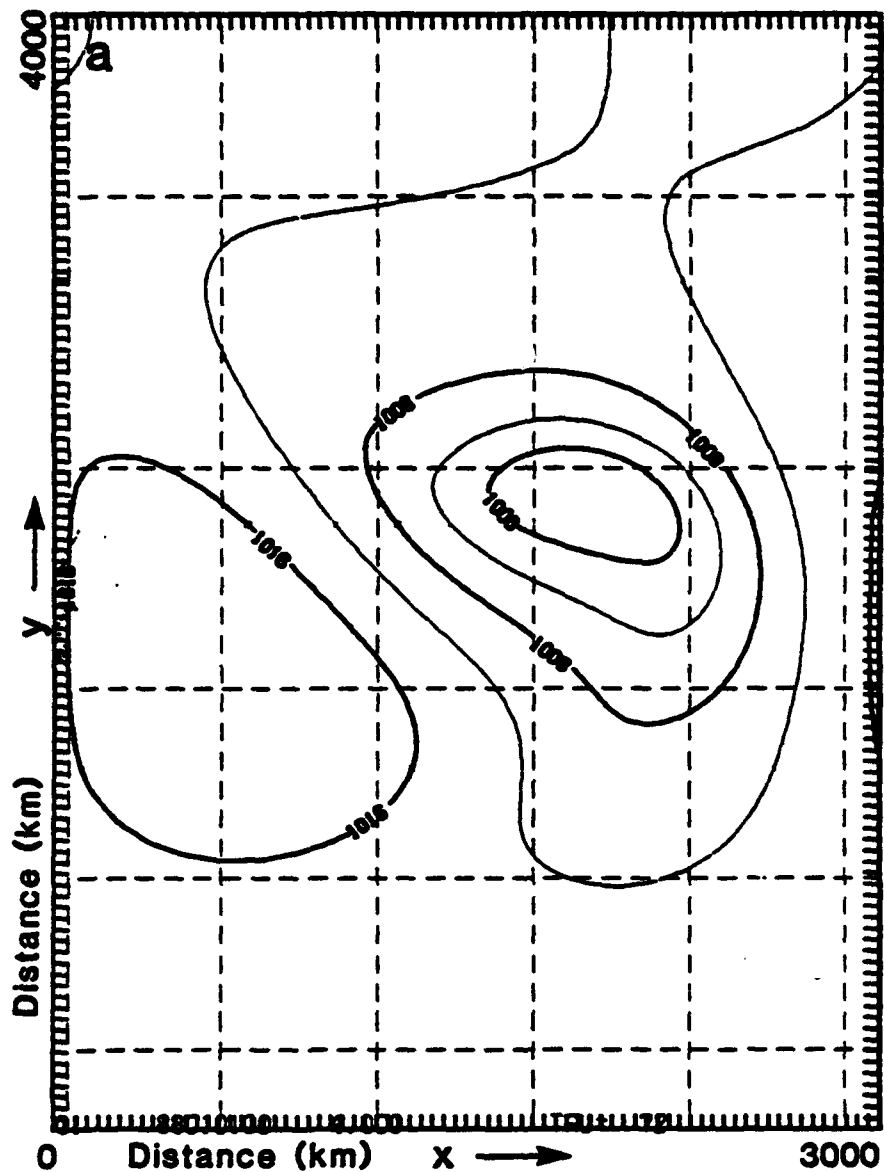


Figure 5.4: a) surface pressure (mb) and b) near-surface potential temperature (K) fields at hour 72.

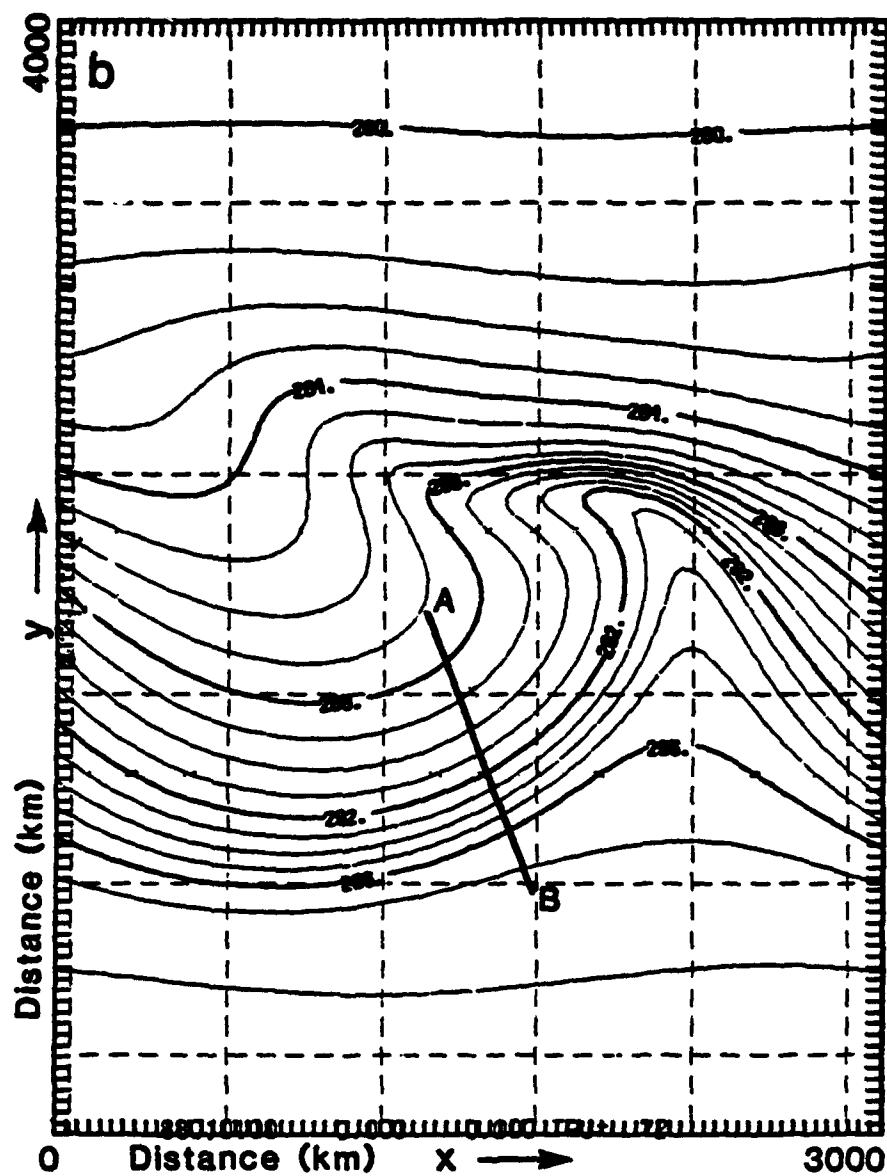


Figure 5.4: Continued.

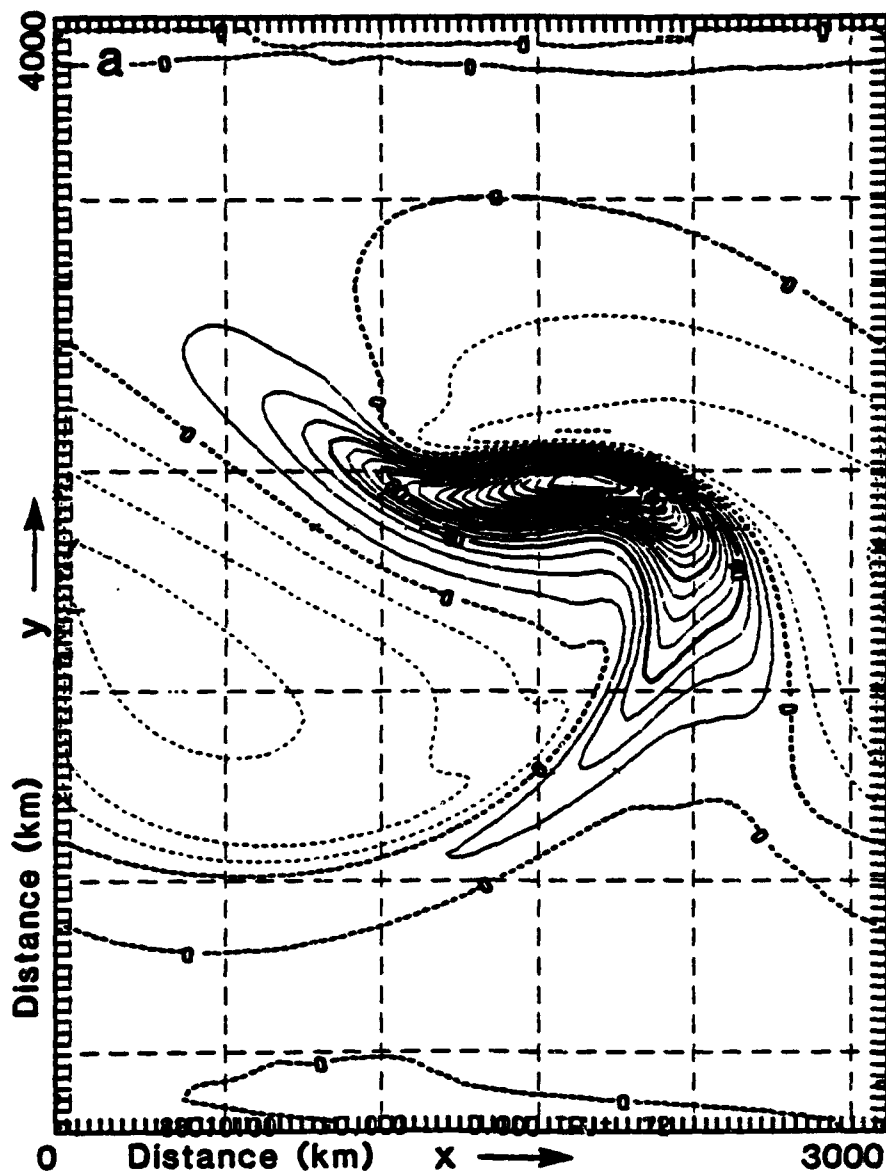


Figure 5.5: a) 850 mb relative vorticity ( $\times 10^{-6} \text{ s}^{-1}$ ), b) divergence ( $\times 10^{-6} \text{ s}^{-1}$ ), and c) vertical motion ( $\times 10^{-5} \text{ mb s}^{-1}$ ) at hour 72.

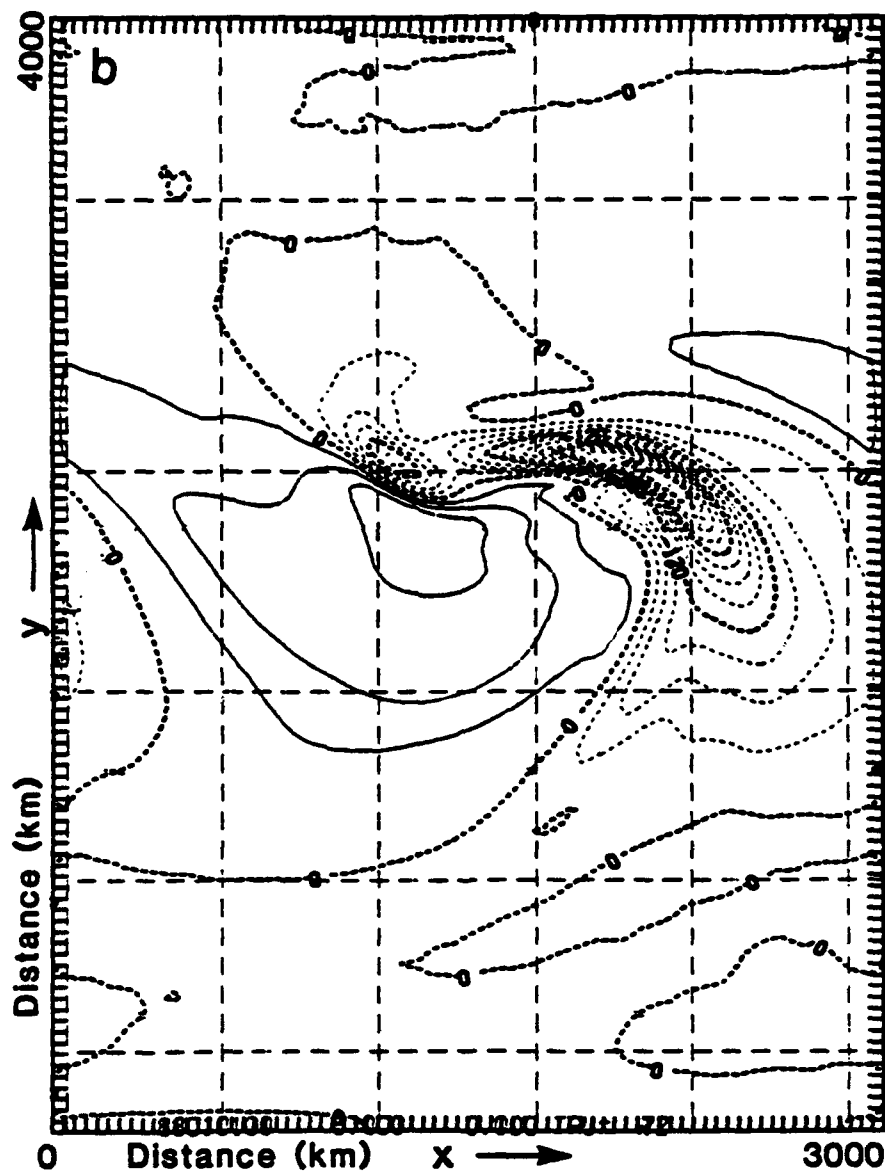


Figure 5.5: Continued.



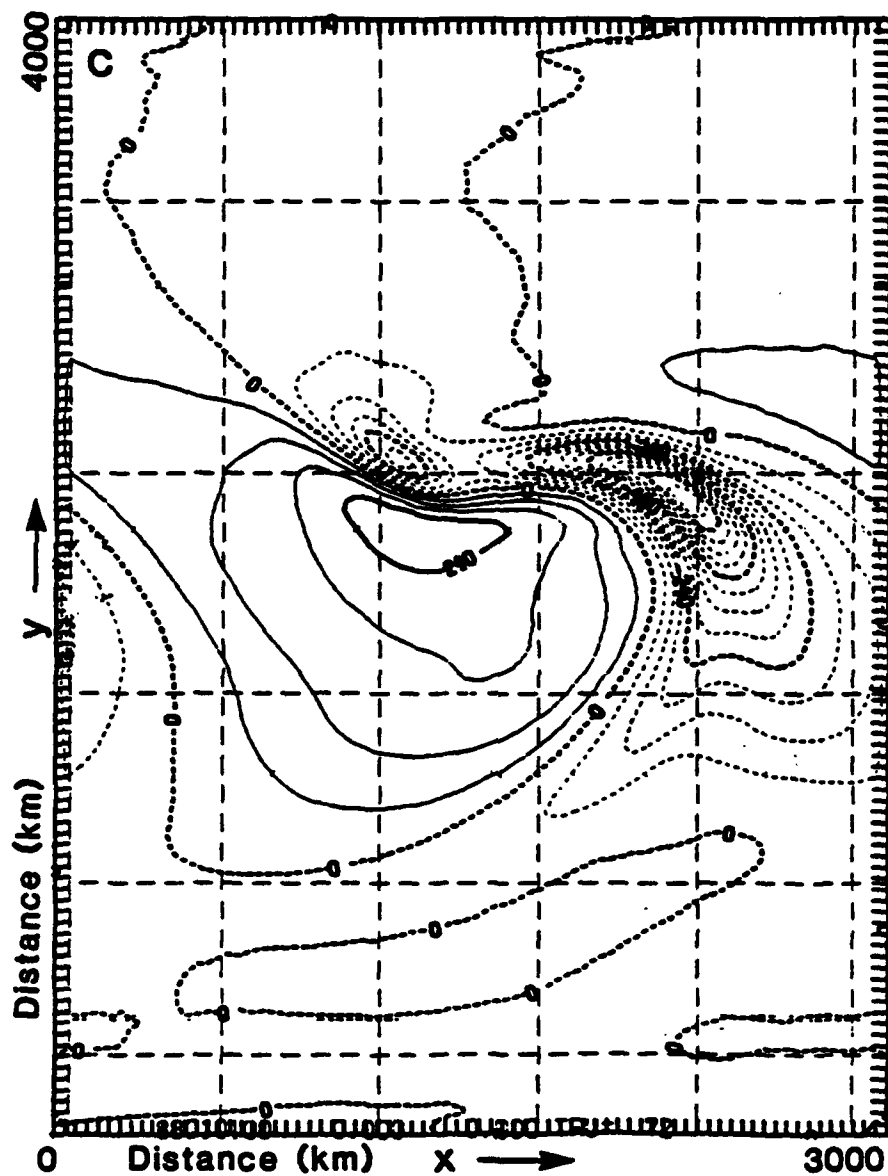


Figure 5.5: Continued.

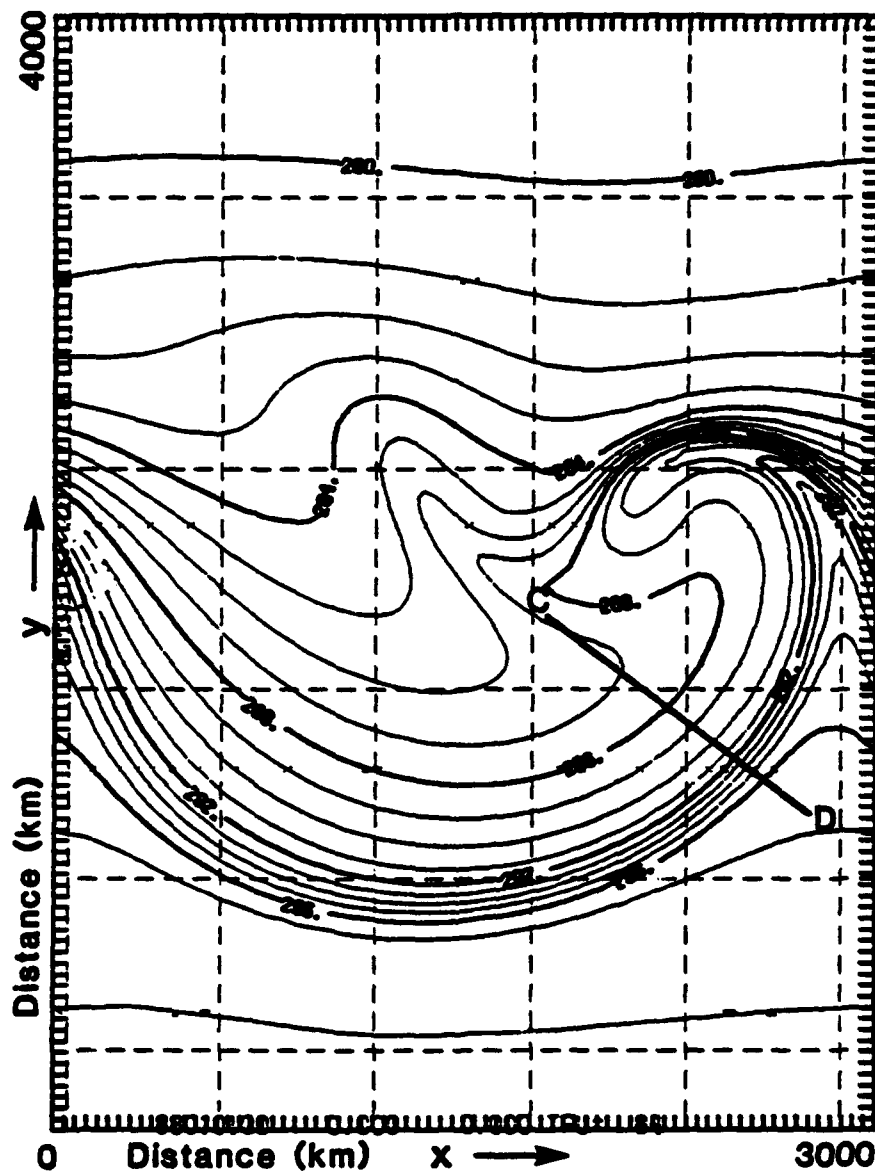


Figure 5.6: Near-surface potential temperature (K) fields at hour 84 (AI).

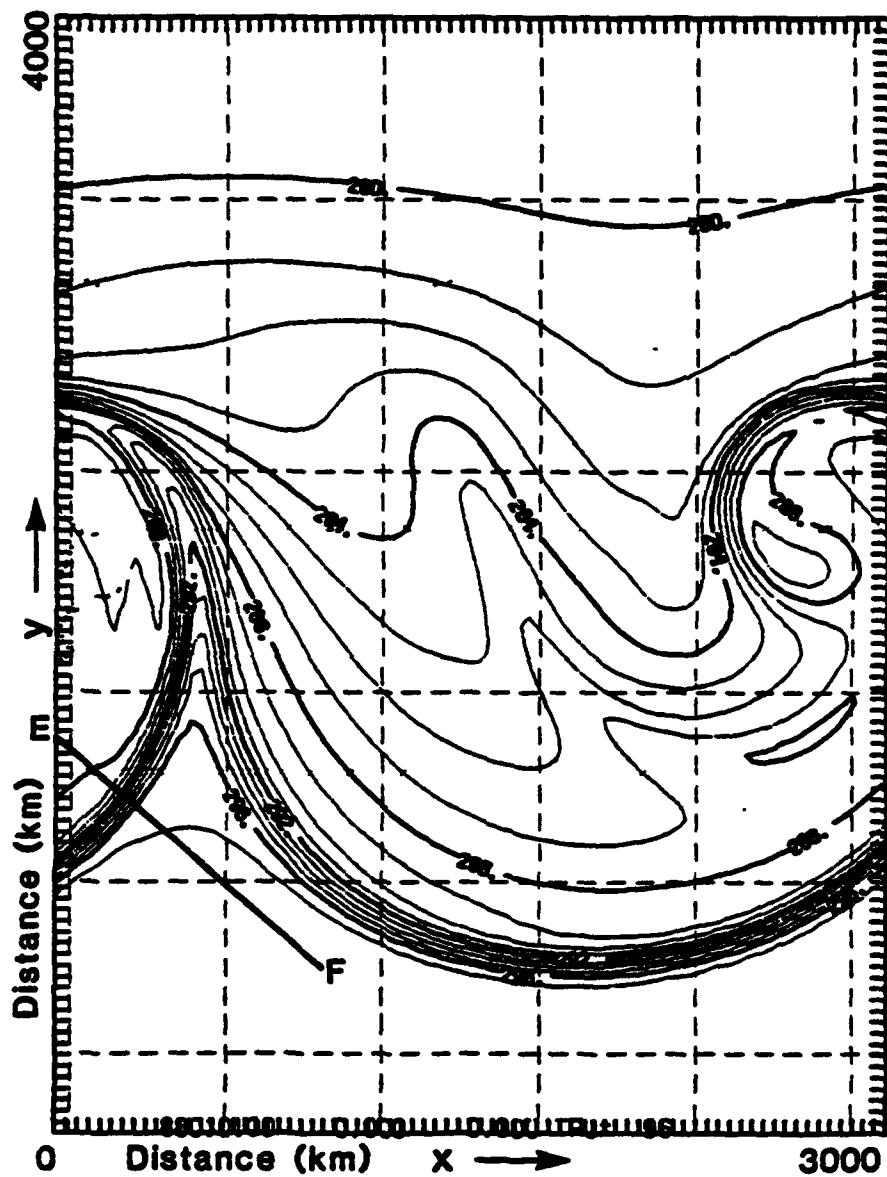


Figure 5.7: Near-surface potential temperature (K) fields at hour 96 (AI).

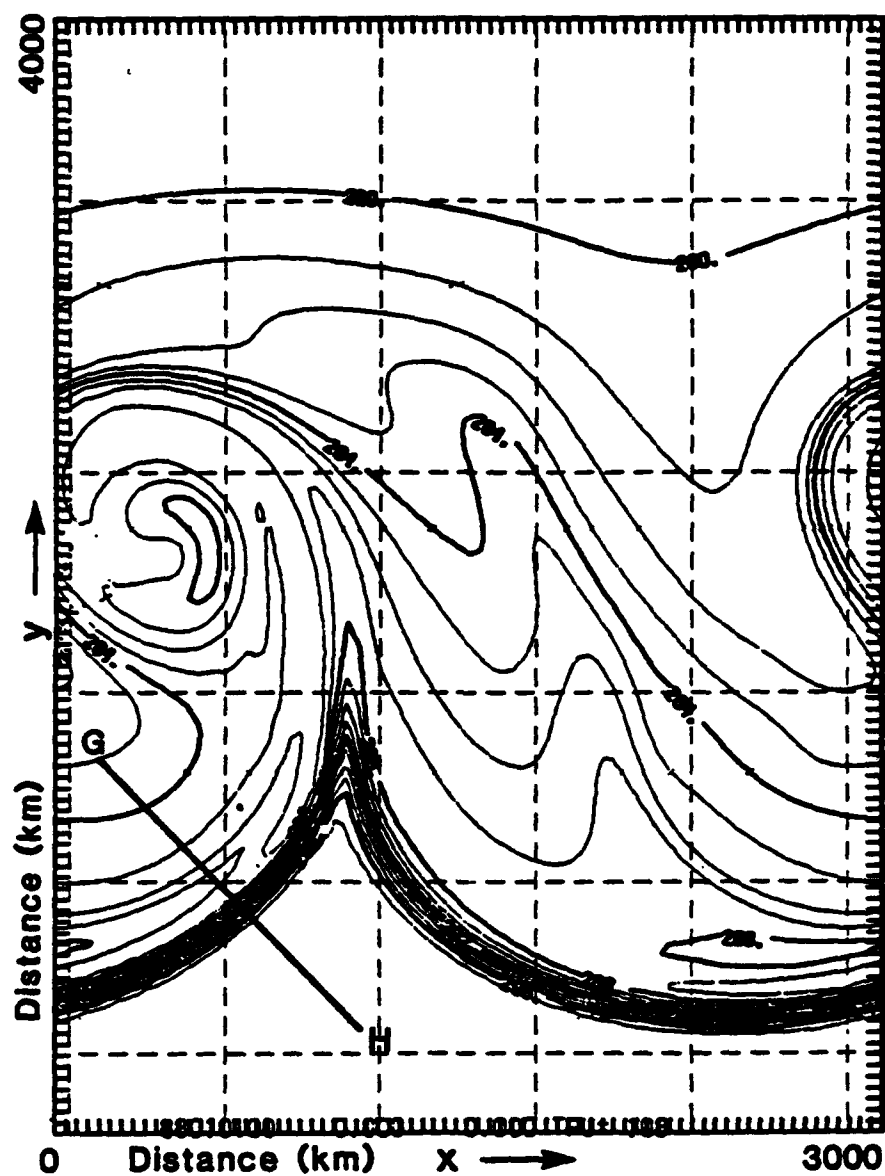


Figure 5.8: Near-surface potential temperature (K) fields at hour 108 (AI).

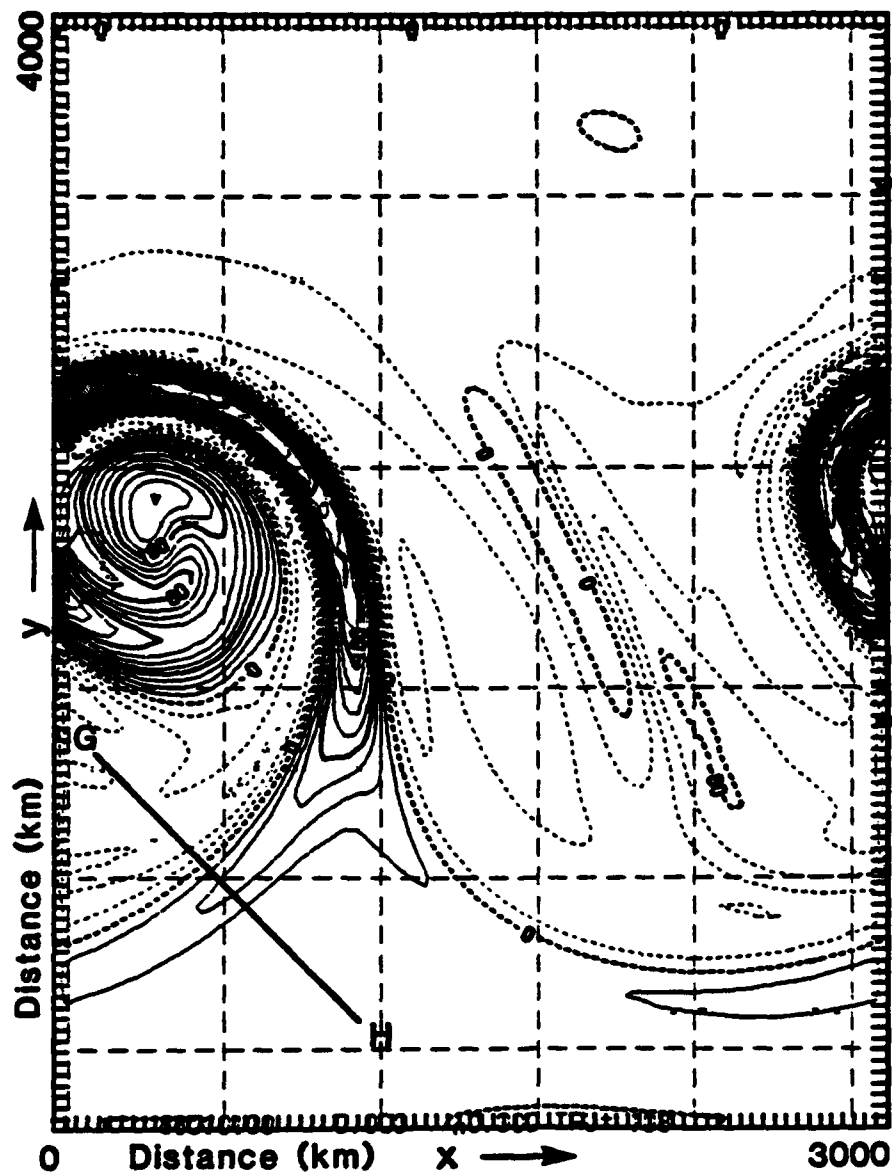


Figure 5.9: 850 mb relative vorticity ( $\times 10^{-6} \text{ s}^{-1}$ ) at hour 108 (AI).

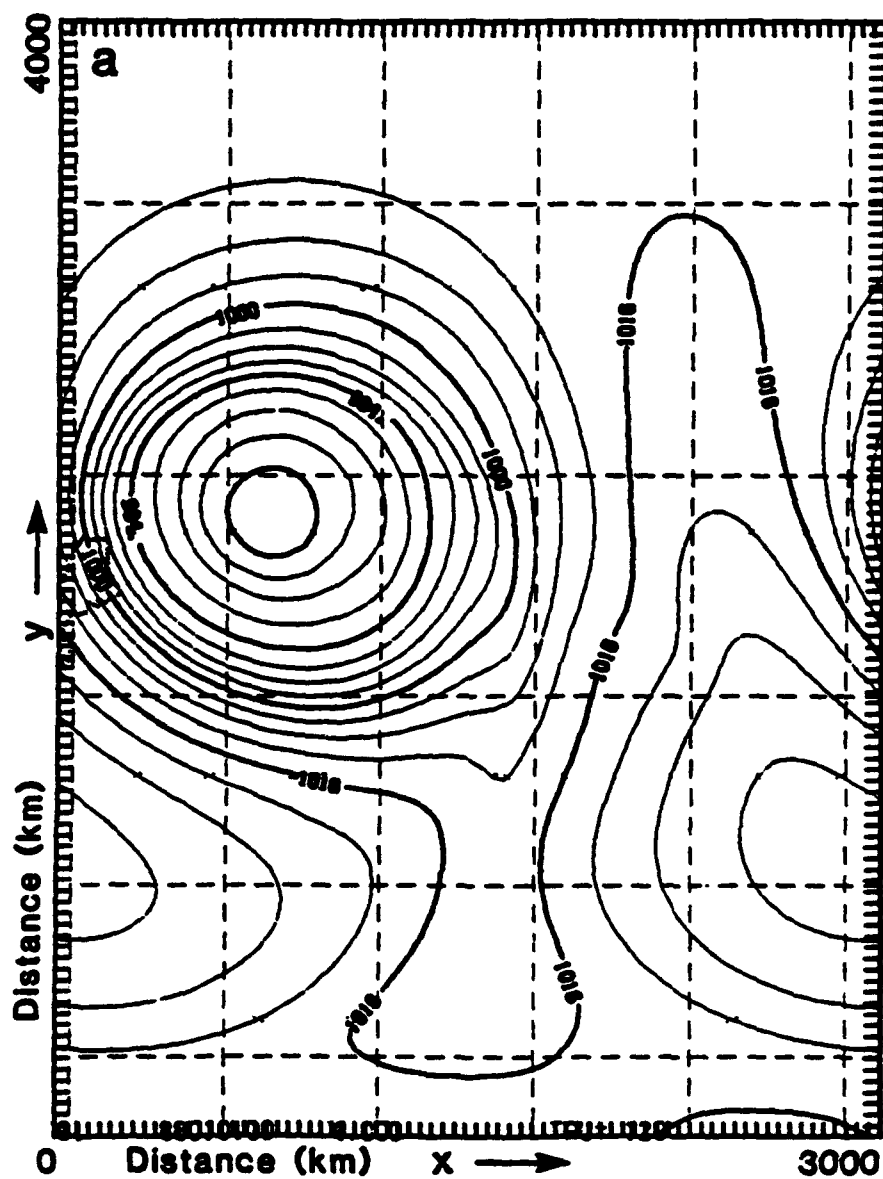


Figure 5.10: a) surface pressure (mb) and b) near-surface potential temperature (K) fields at hour 120 (AI).

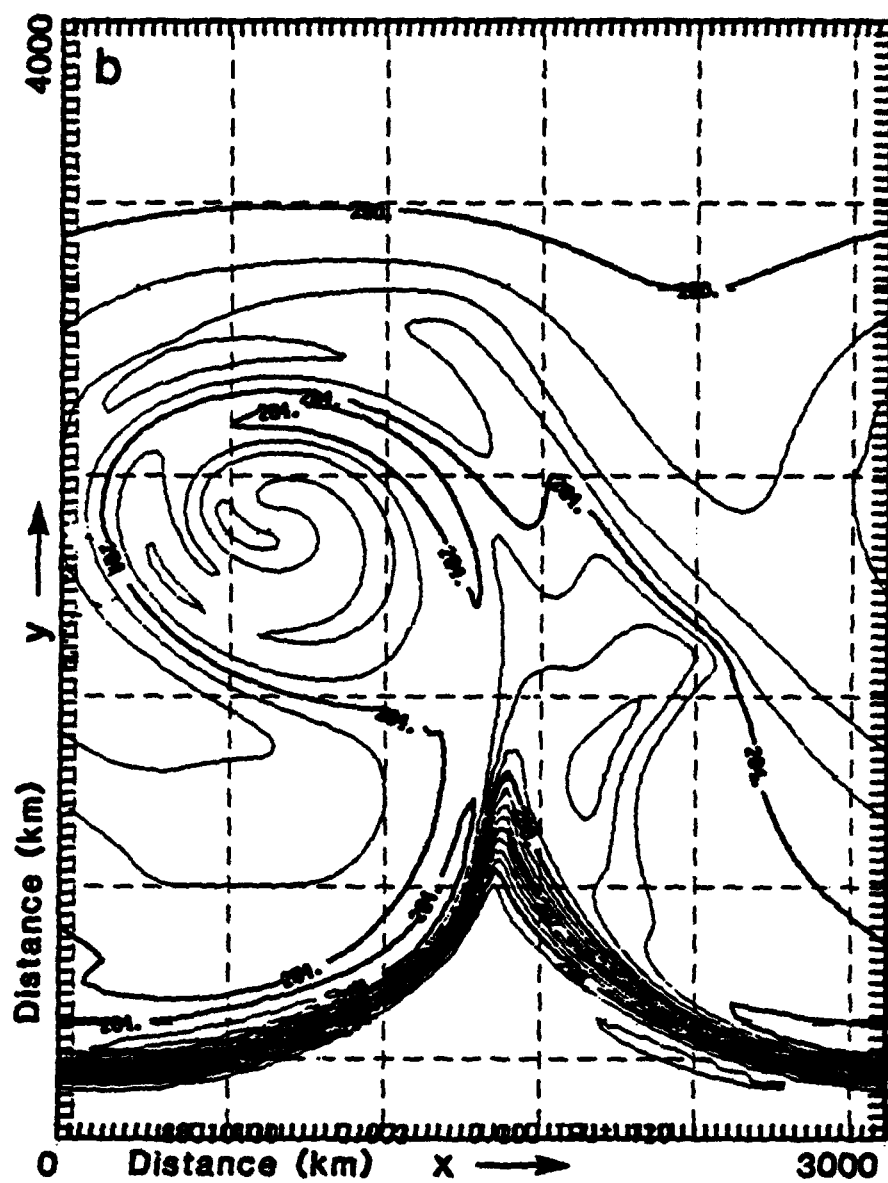
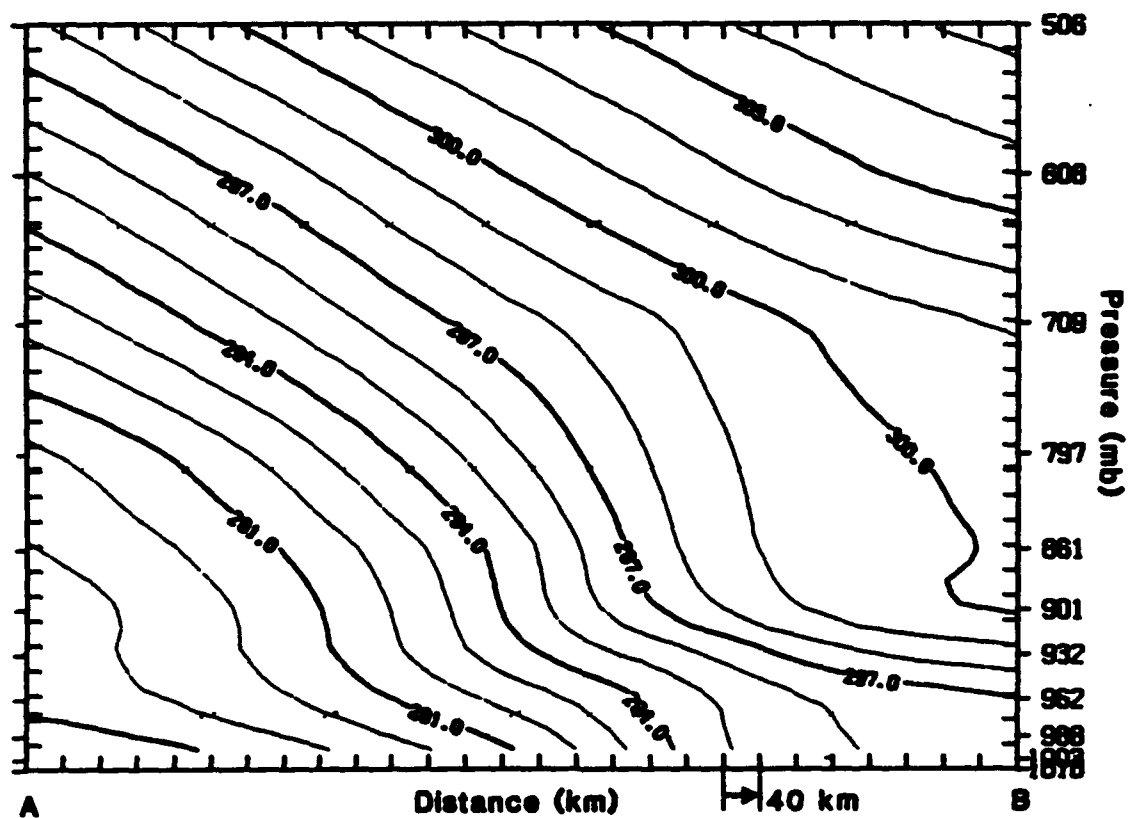


Figure 5.10: Continued.



**Figure 5.11:** Vertical cross section of potential temperature (K) at hour 72 From the surface to ~ 500 mb and from 0 to 1320 km. The plane of the cross section, denoted by AB, is shown in Fig. 4b (AI).



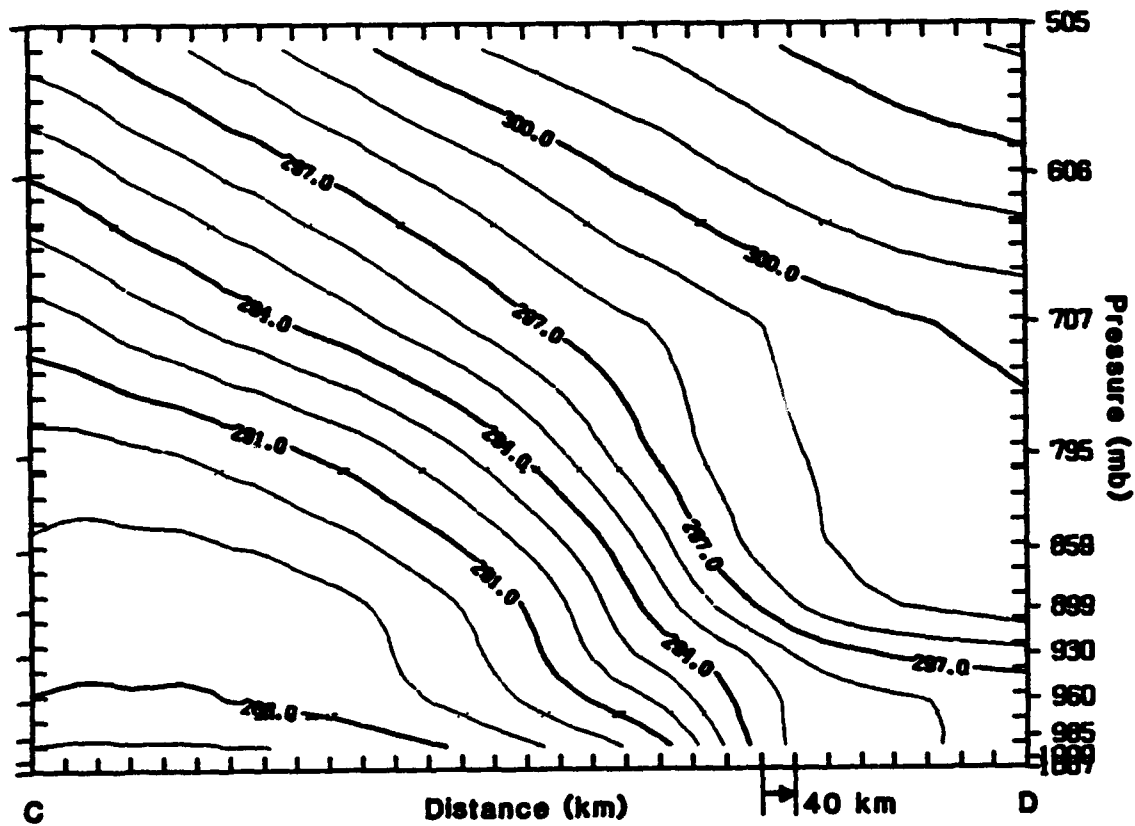
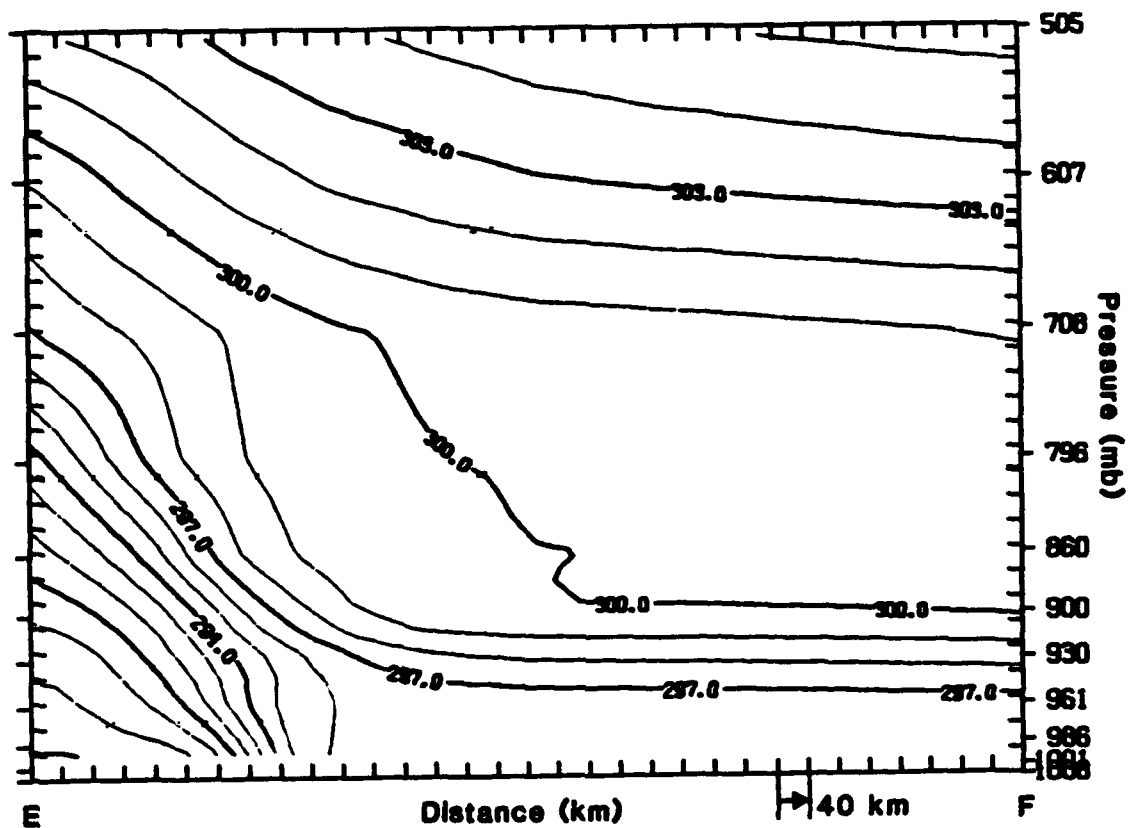


Figure 5.12: Cross section of potential temperature (K) at hour 84. The plane of the cross section, denoted by CD, is shown in Fig. 6 (AI).



**Figure 5.13:** Cross section of potential temperature (K) at hour 96. The plane of the cross section, denoted by EF, is shown in Fig. 7 (AI).

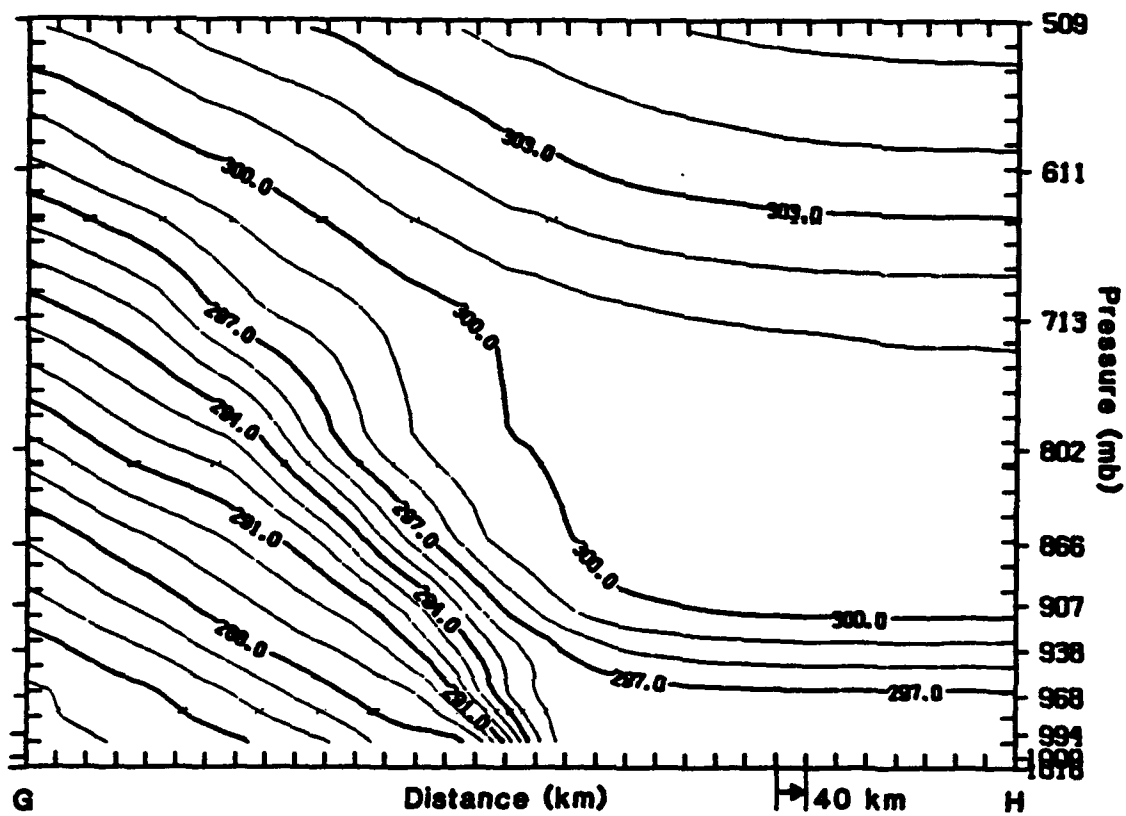
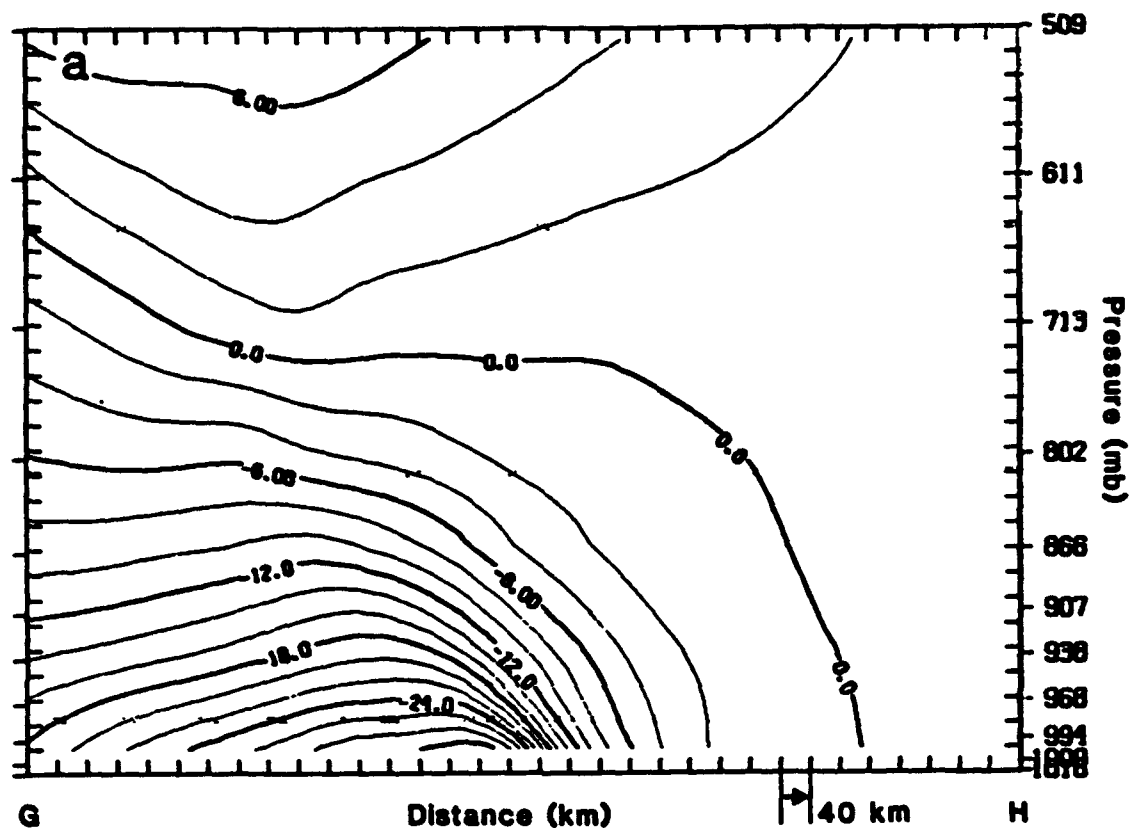


Figure 5.14: Cross section of potential temperature (K) at hour 108. The plane of the cross section, denoted by GH, is shown in Fig. 8 (AI).



**Figure 5.15:** Cross sections of a) along-front wind component and b) front-normal wind component ( $\text{m s}^{-1}$ ) at hour 108 (AI).

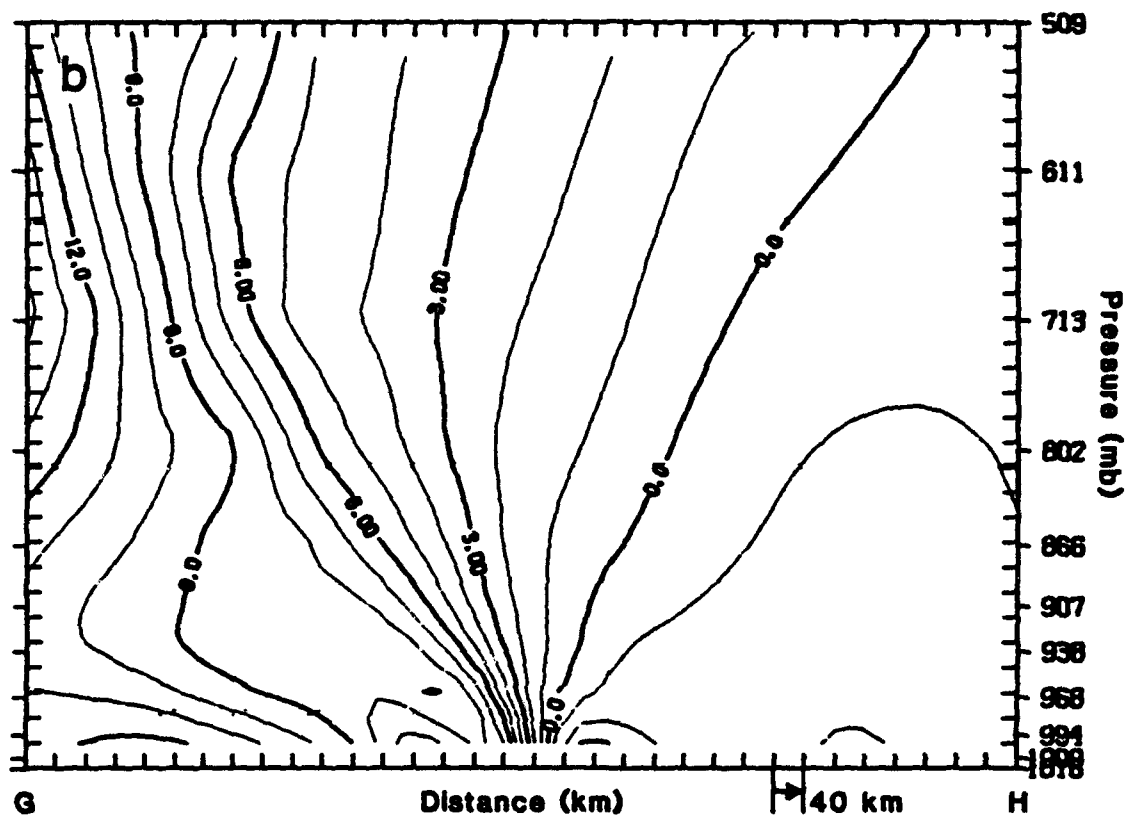


Figure 5.15: Continued.



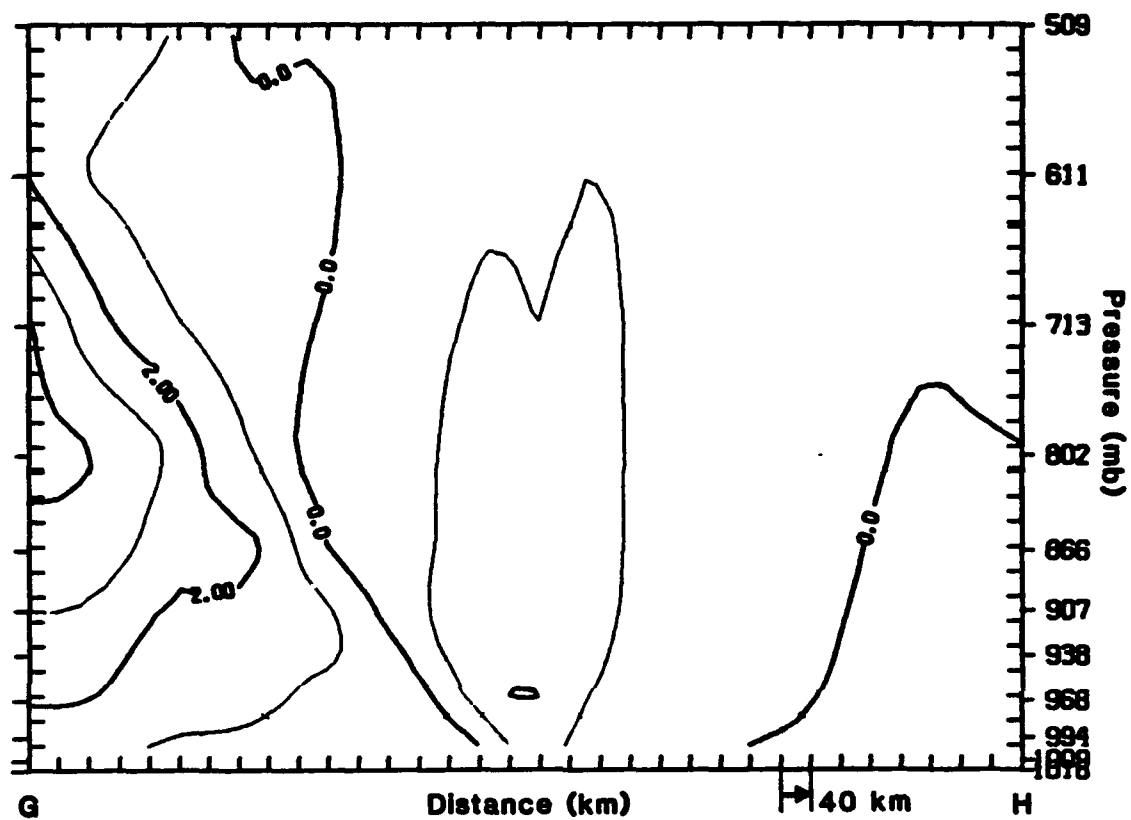
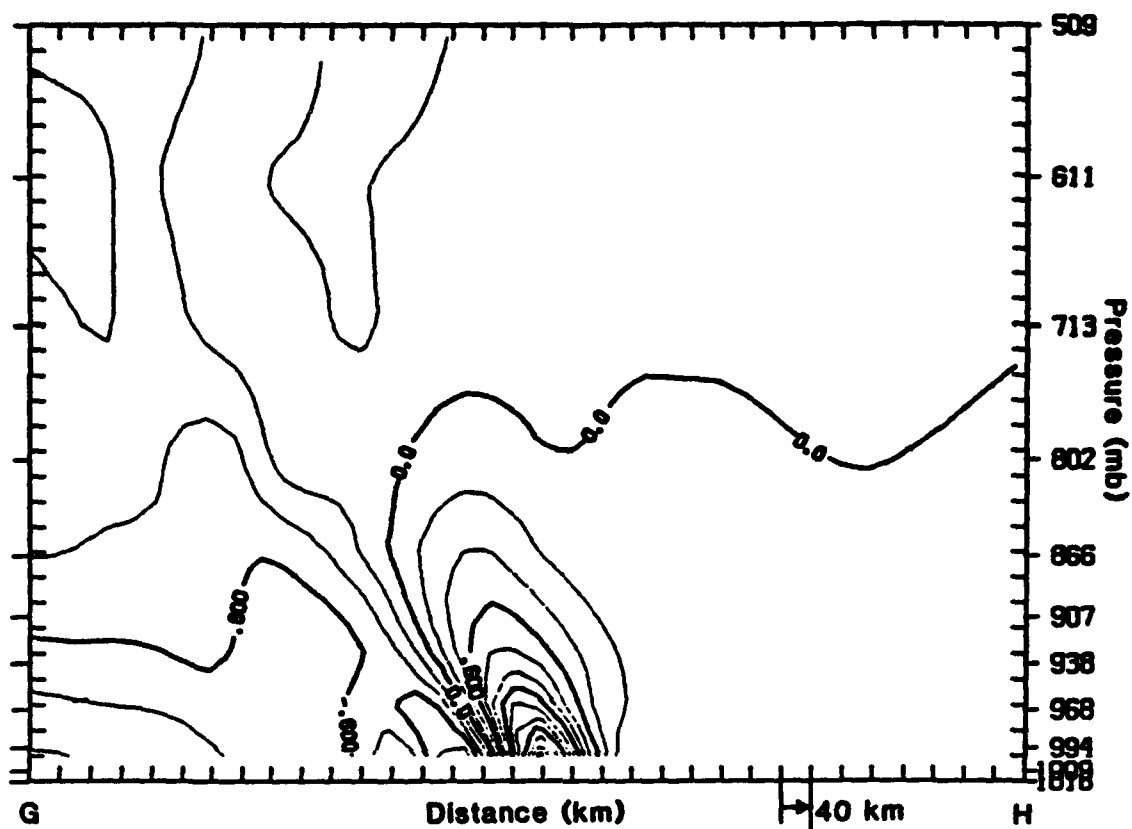


Figure 5.17: Cross section of vertical motion ( $\mu \text{ b s}^{-1}$ ) at hour 108 (AI).



**Figure 5.18:** Cross section of relative vorticity ( $\times 10^{-4} \text{ s}^{-1}$ ) at hour 108. The plane of the cross section, denoted by GH, is shown in Fig. 9 (AI).



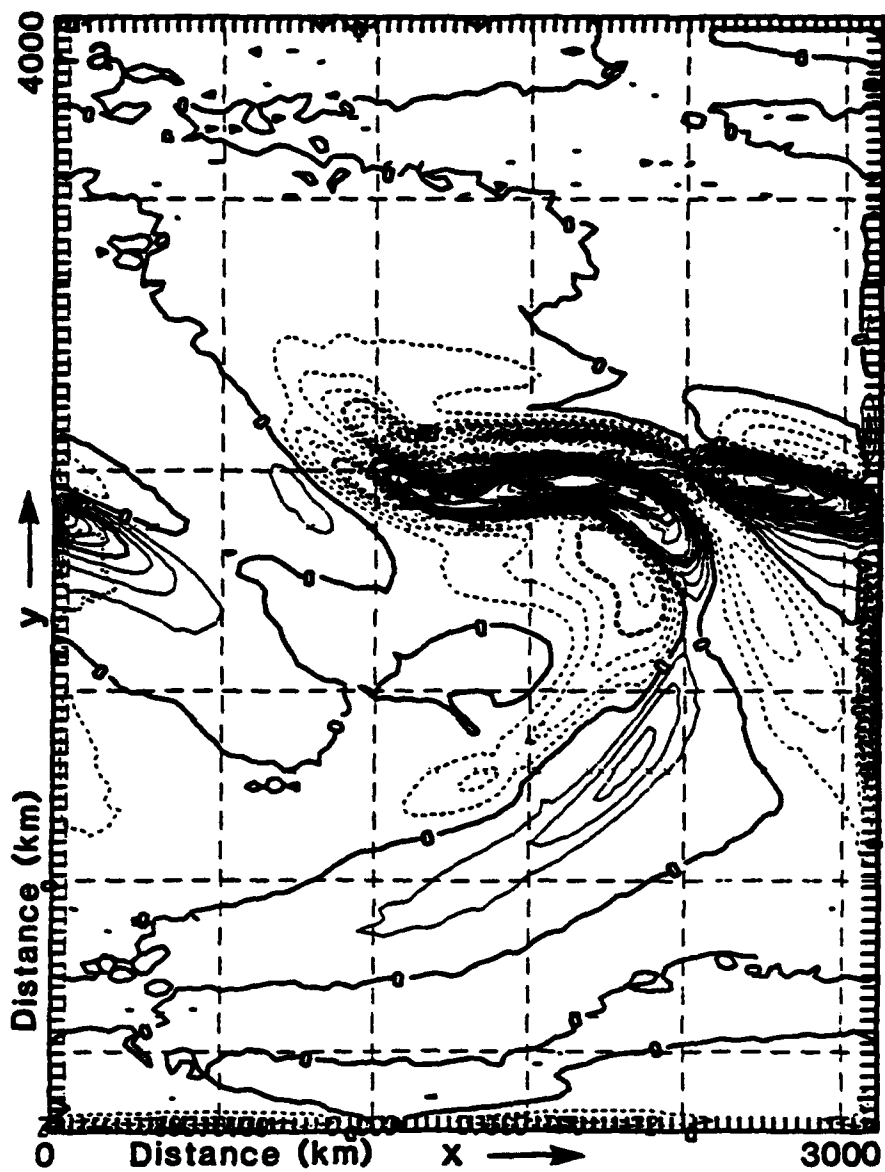


Figure 5.19: a) total adiabatic frontogenetic forcing ( $\times 10^{-11} \text{ K s}^{-1} \text{ m}^{-1}$ ) at hour 72 at 850 mb, b) tilting term, c) stretching deformation, and d) shearing deformation.

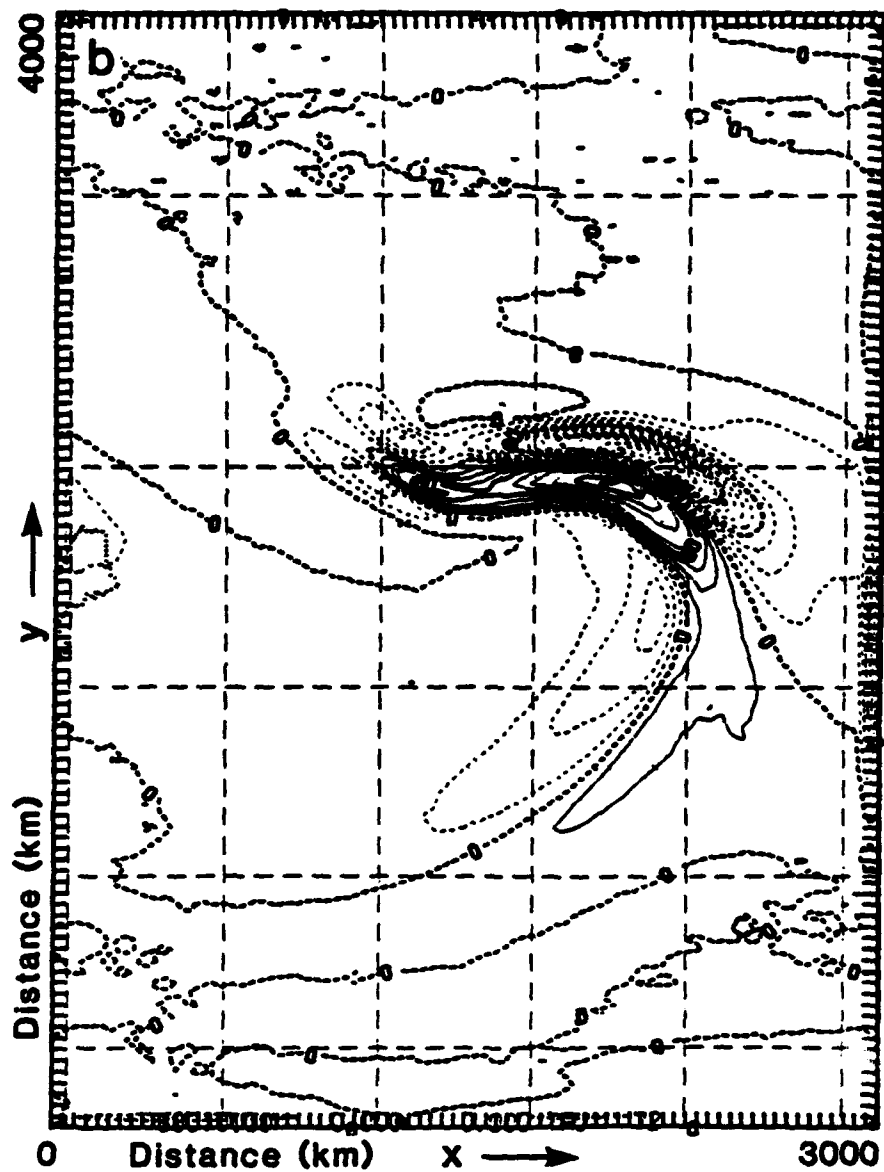


Figure 5.19: Continued.

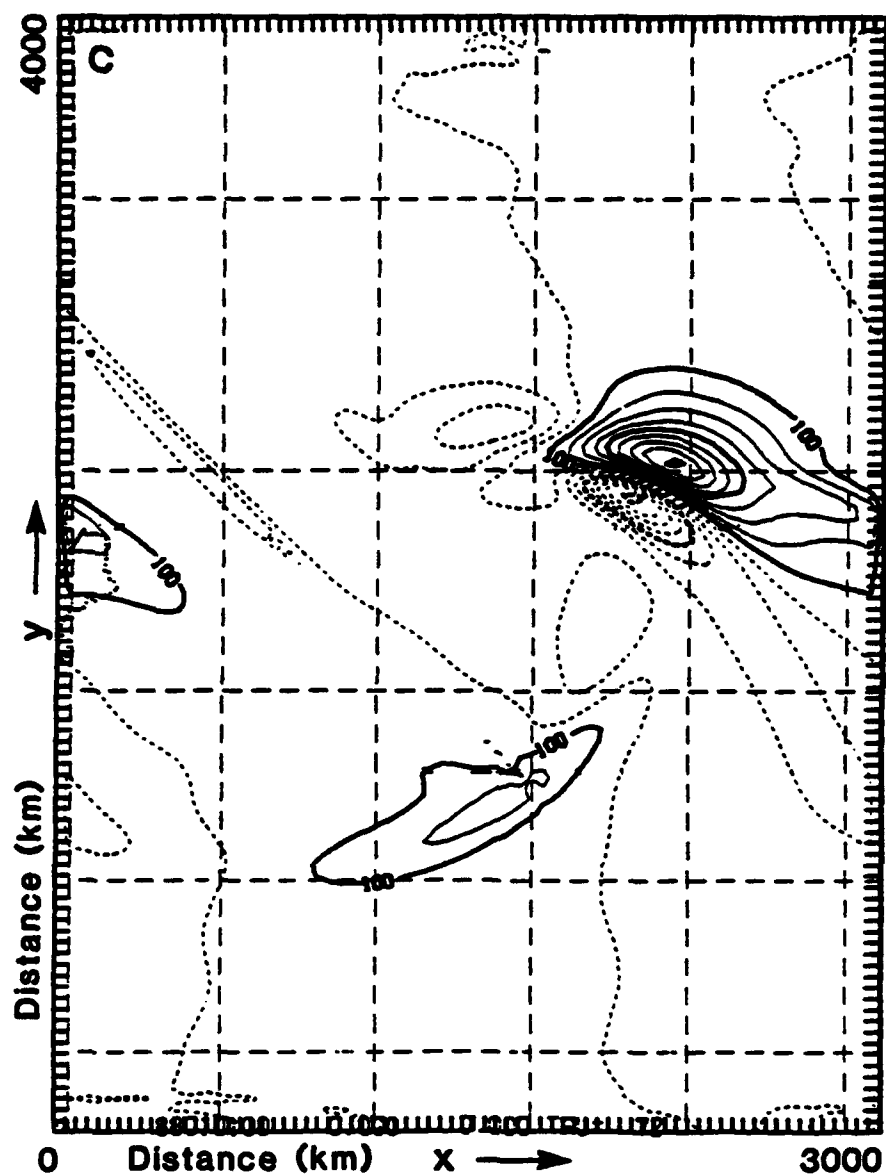


Figure 5.19: Continued.

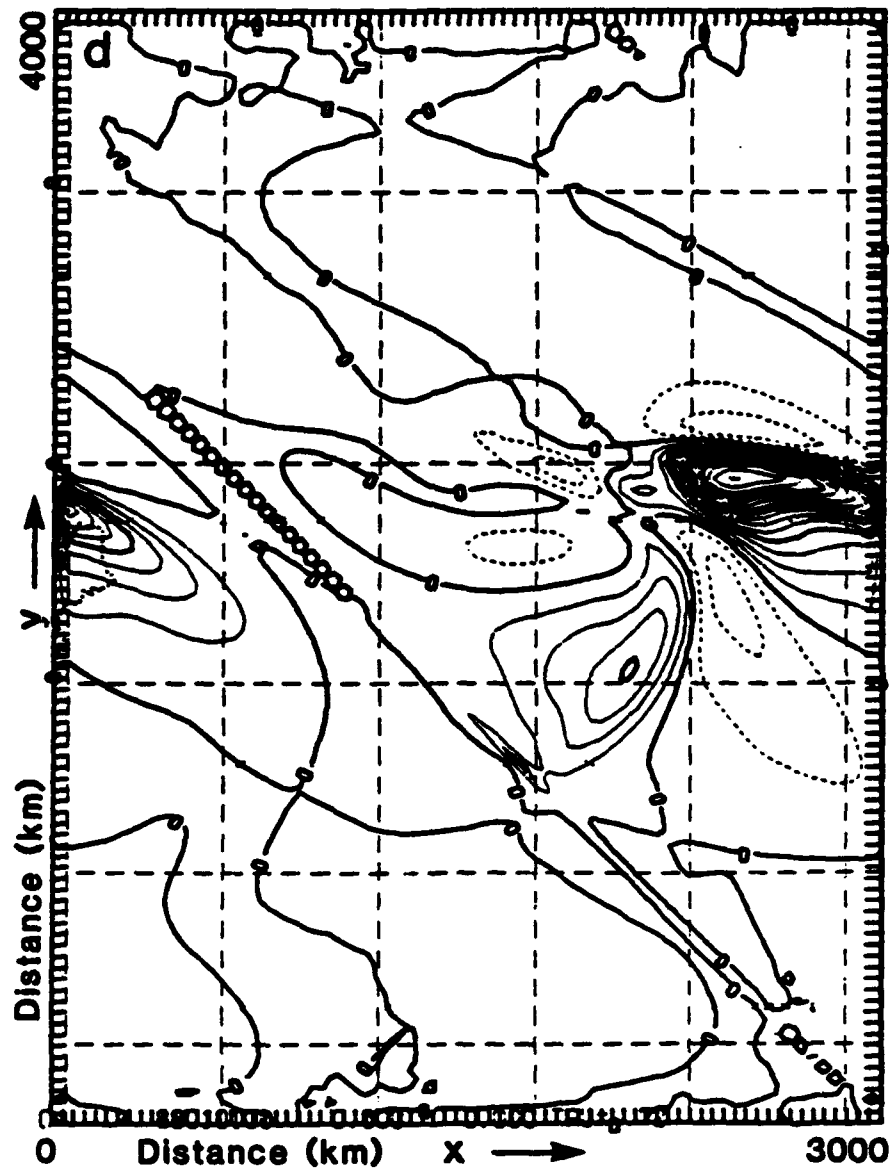


Figure 5.19: Continued.

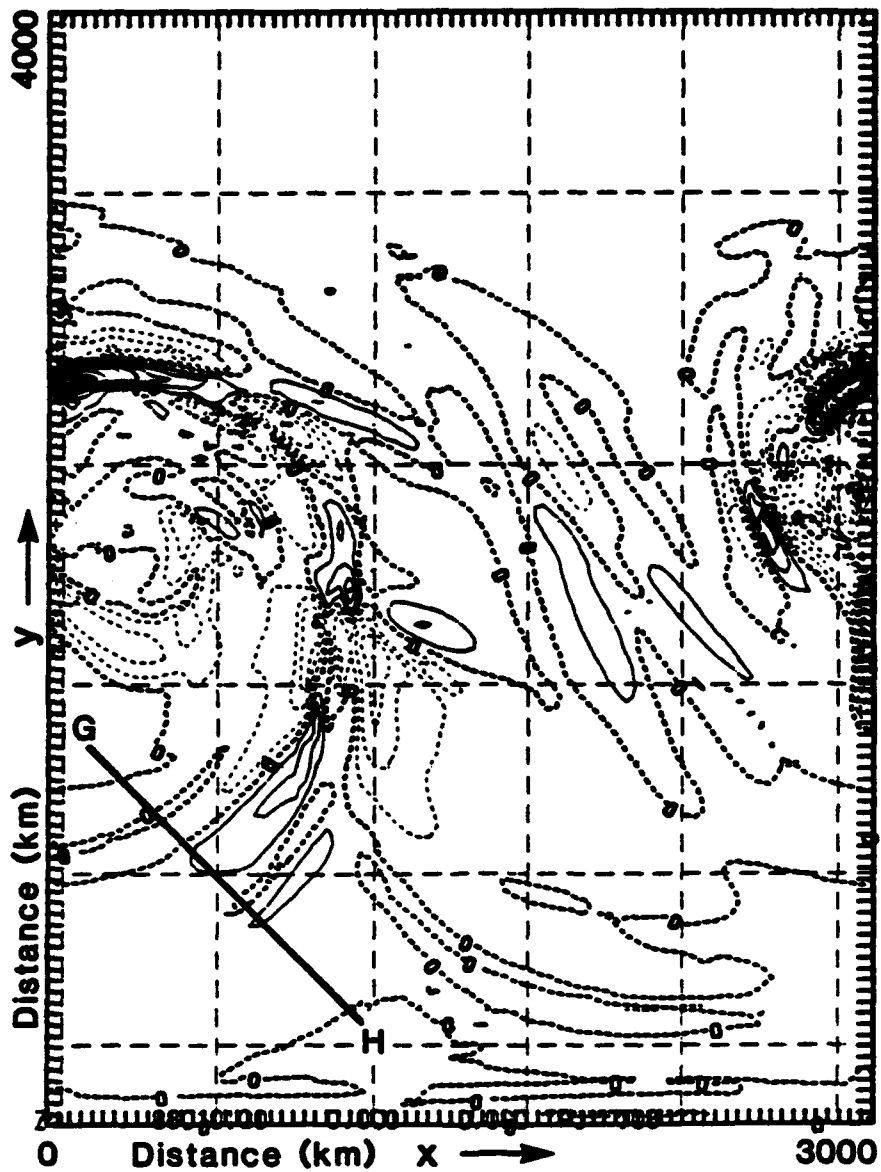


Figure 5.20: Total adiabatic frontogenetic forcing at hour 108 at 850 mb (AI).

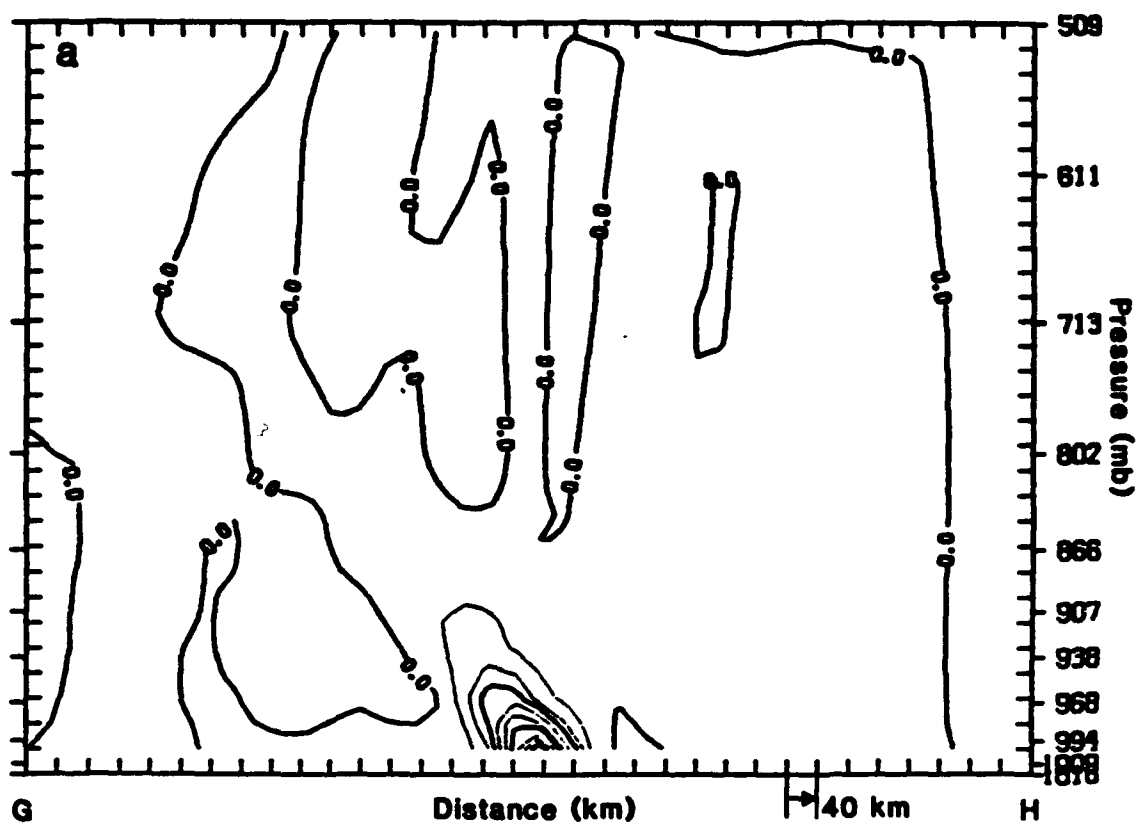


Figure 5.21: a) cross section of total adiabatic frontogenetic forcing ( $\text{K s}^{-1} \text{ m}^{-1}$ ) at hour 108 and b) stretching deformation (AI).

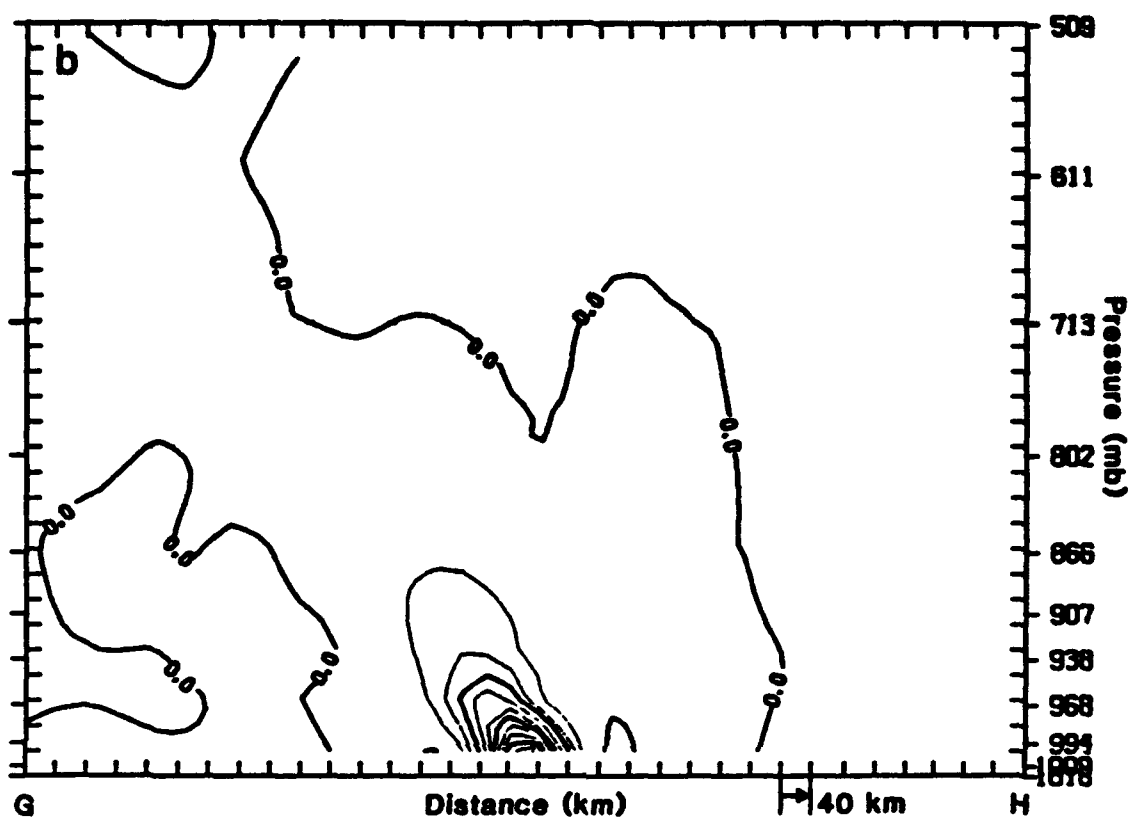
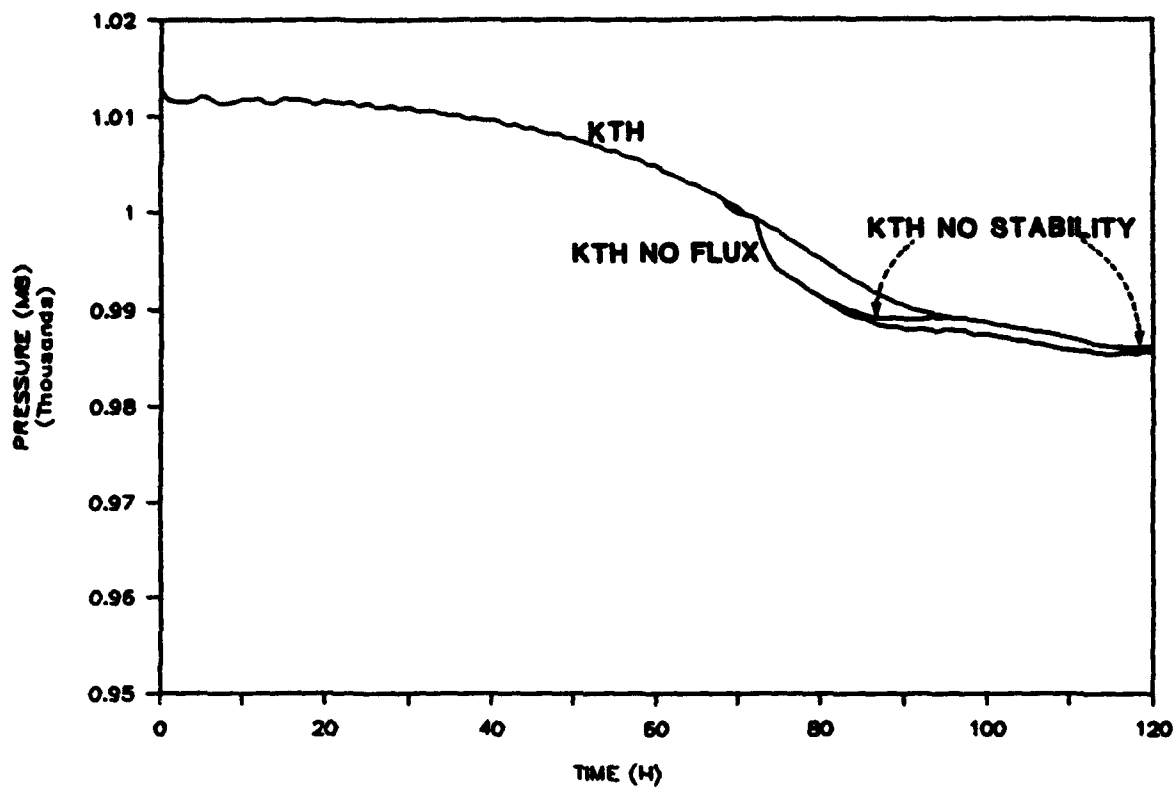


Figure 5.21: Continued.



**Figure 5.22:** Time series of minimum surface pressure (mb) (KTH).



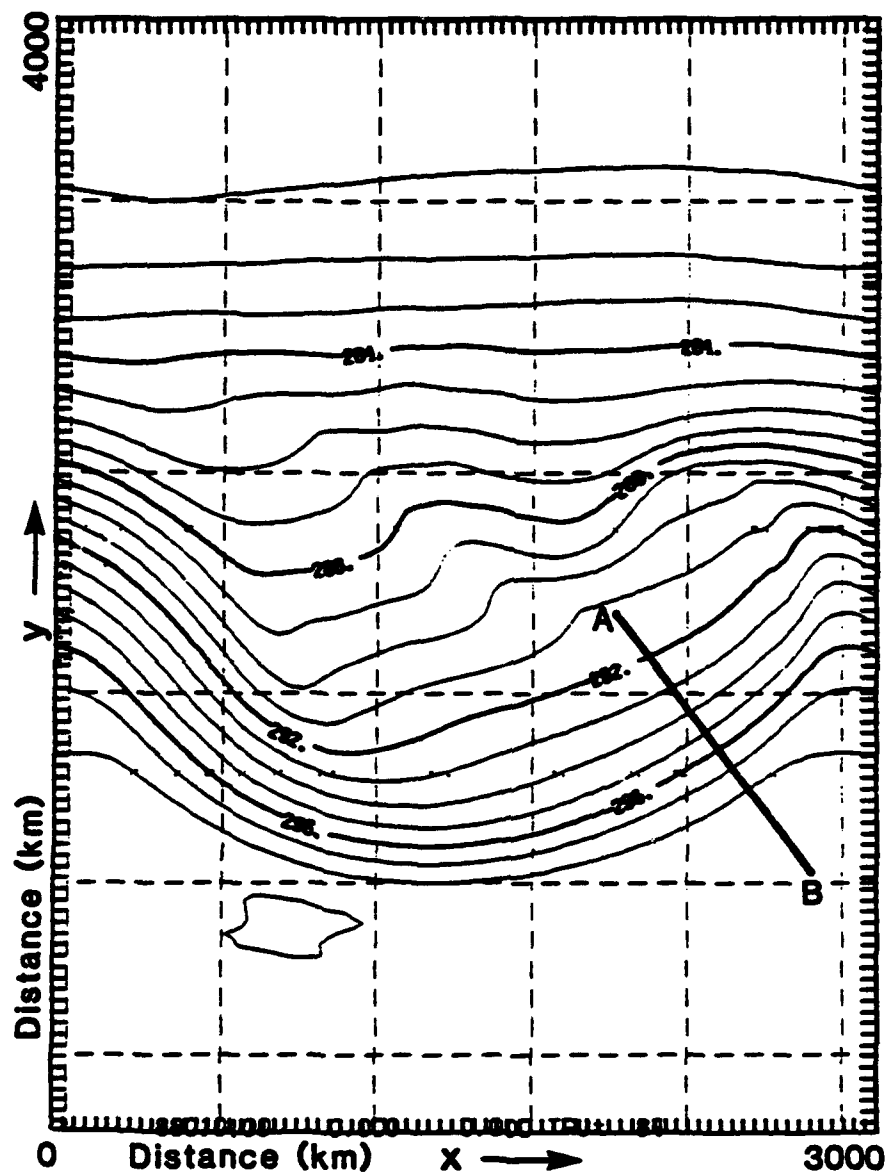


Figure 5.23: Near-surface potential temperature (K) fields at hour 84 (KTH).

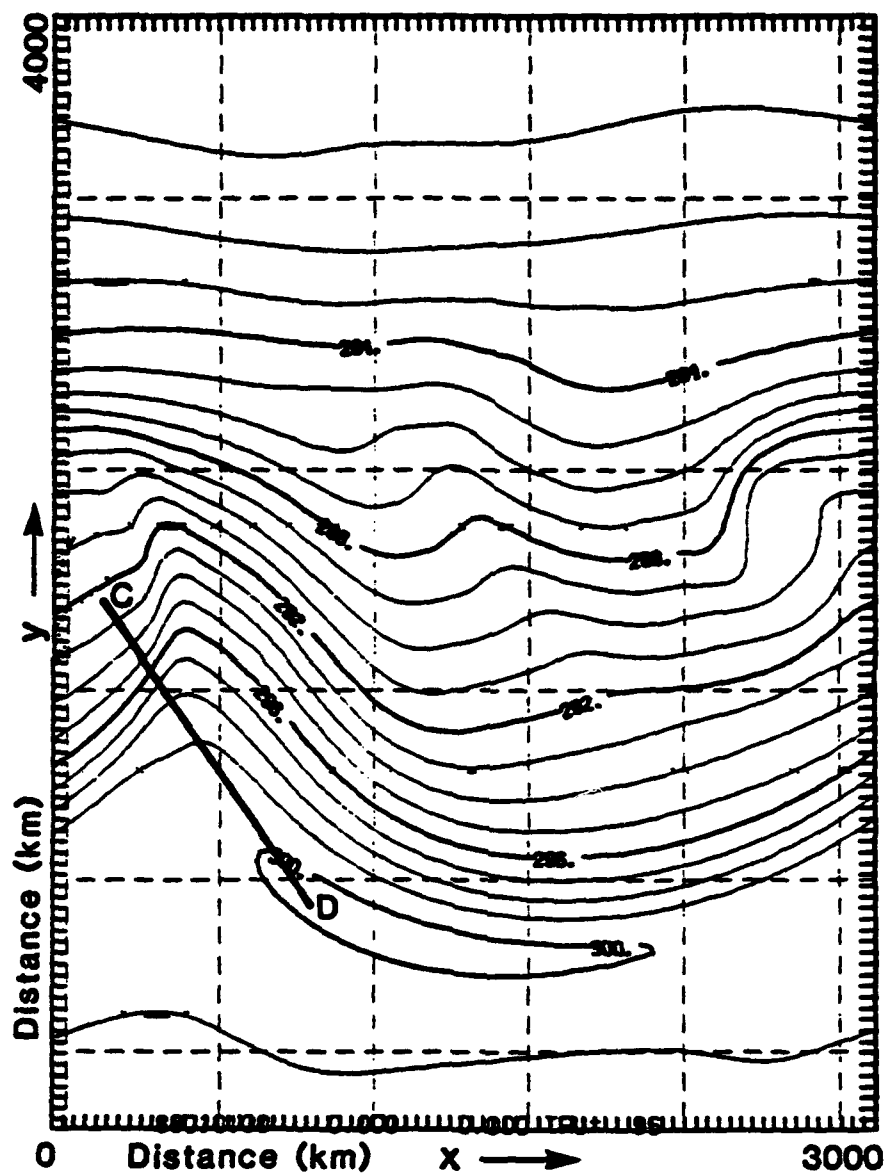


Figure 5.24: Near-surface potential temperature (K) fields at hour 96 (KTH).

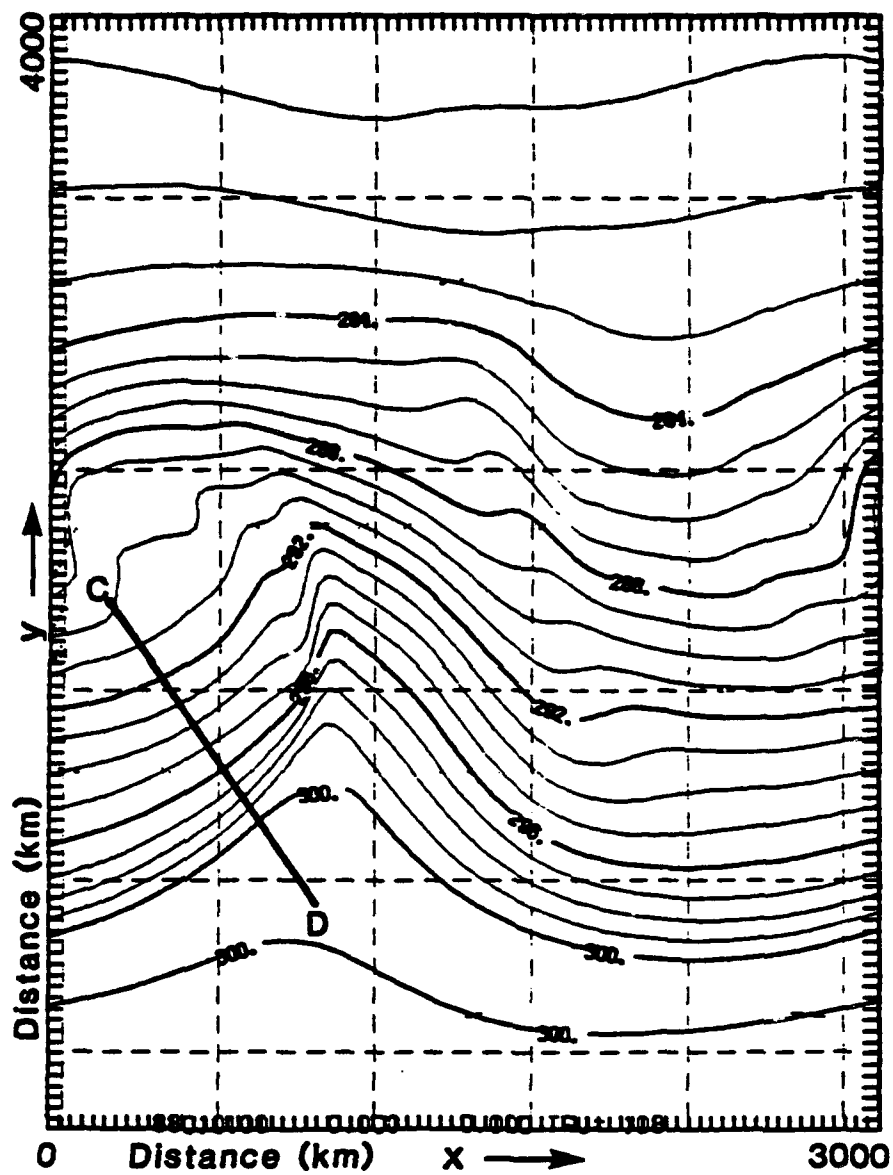


Figure 5.25: Near-surface potential temperature (K) fields at hour 108 (KTH).

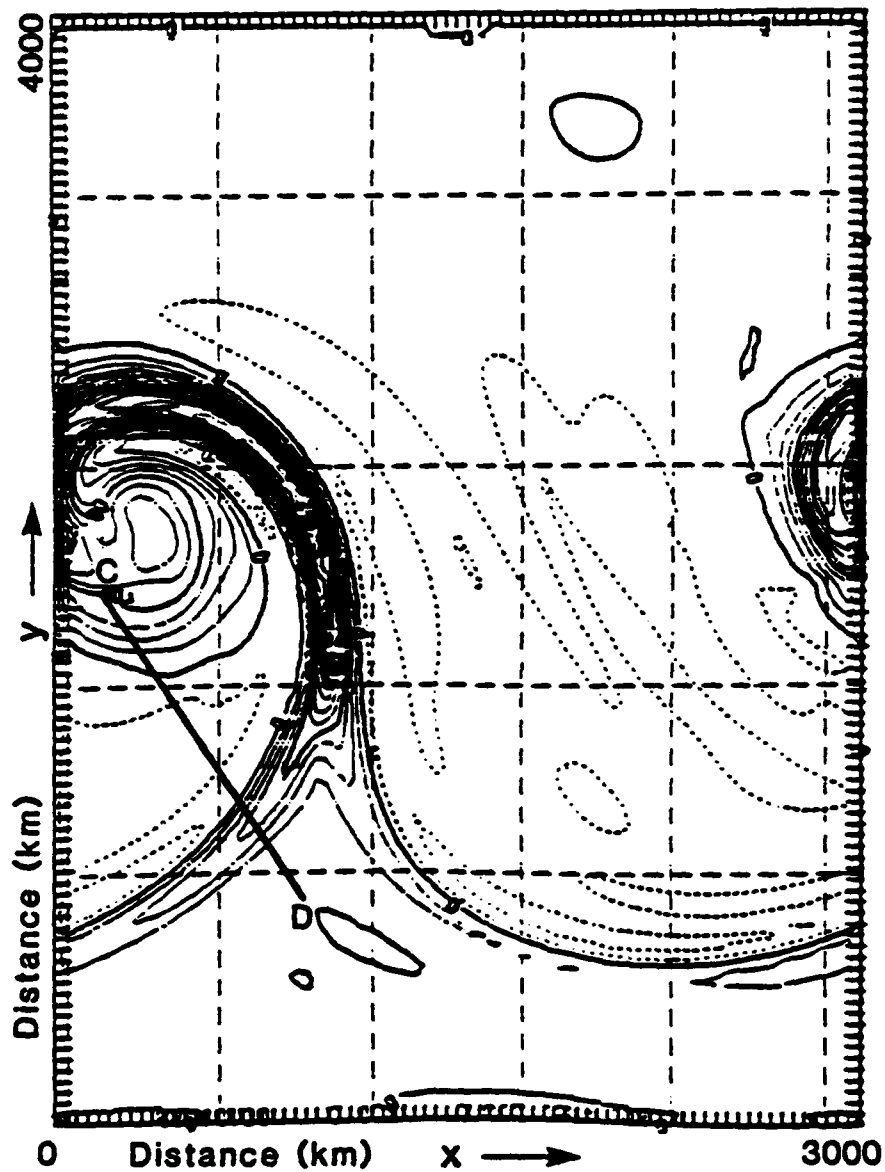
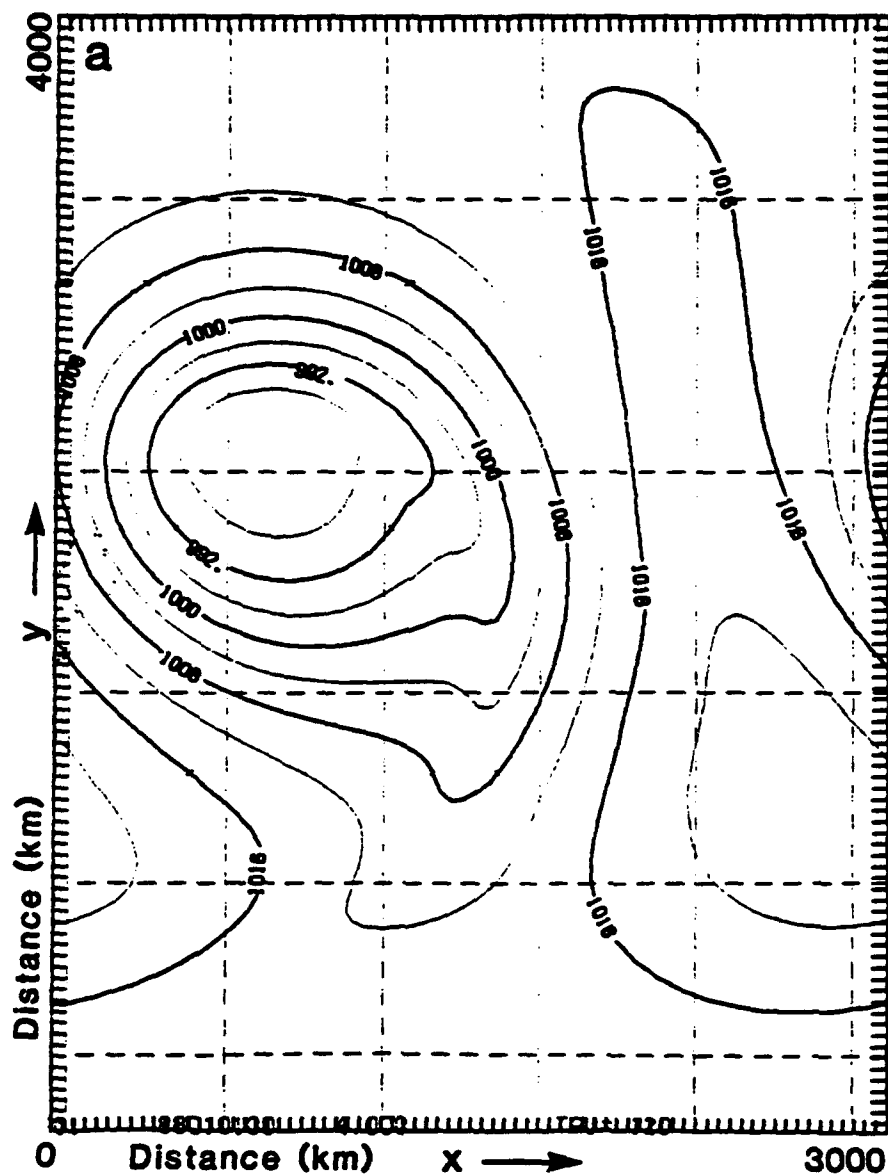


Figure 5.26: 850 mb relative vorticity ( $\times 10^{-6} \text{ s}^{-1}$ ) at hour 108 (KTH).



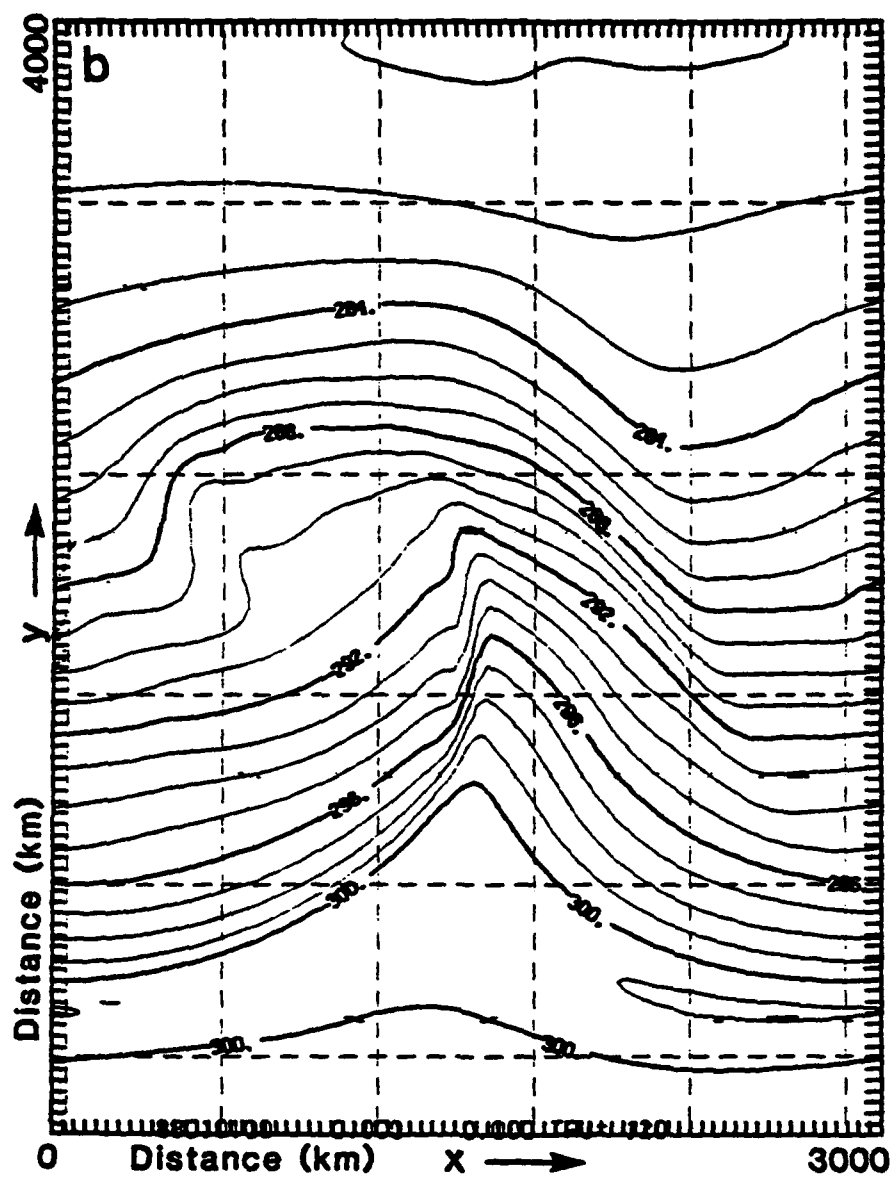
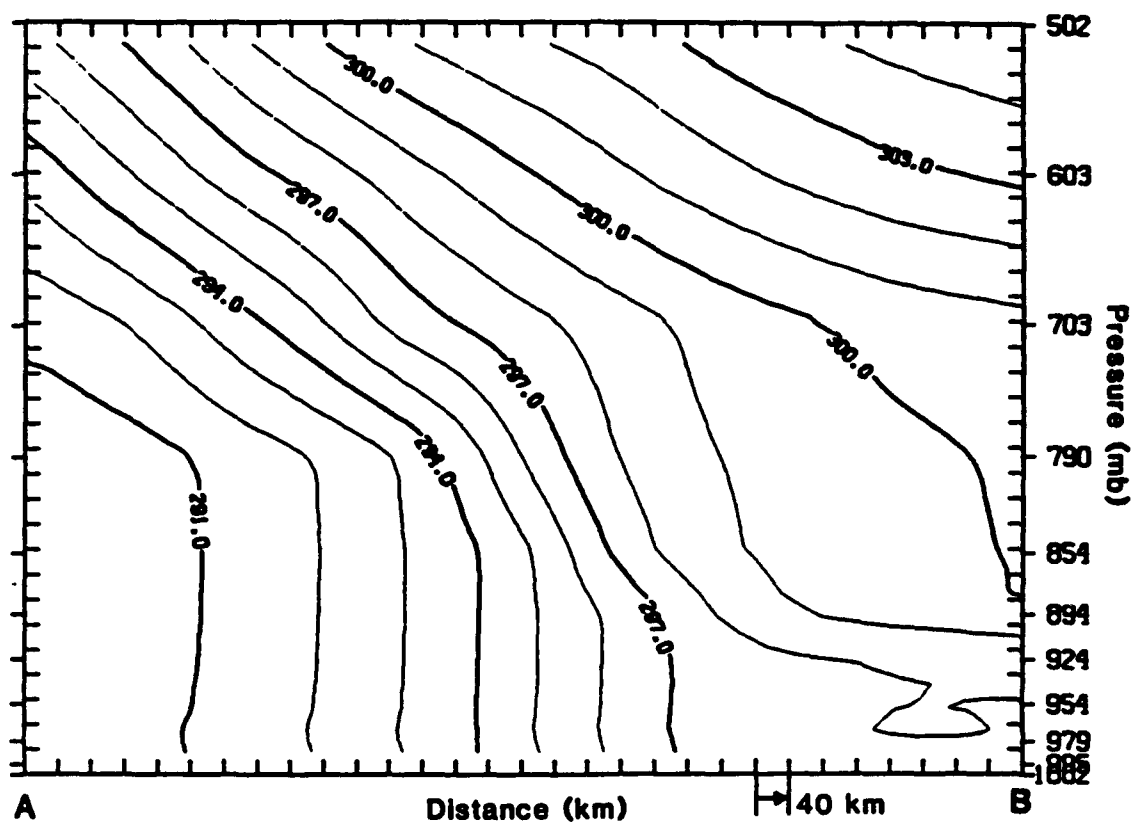
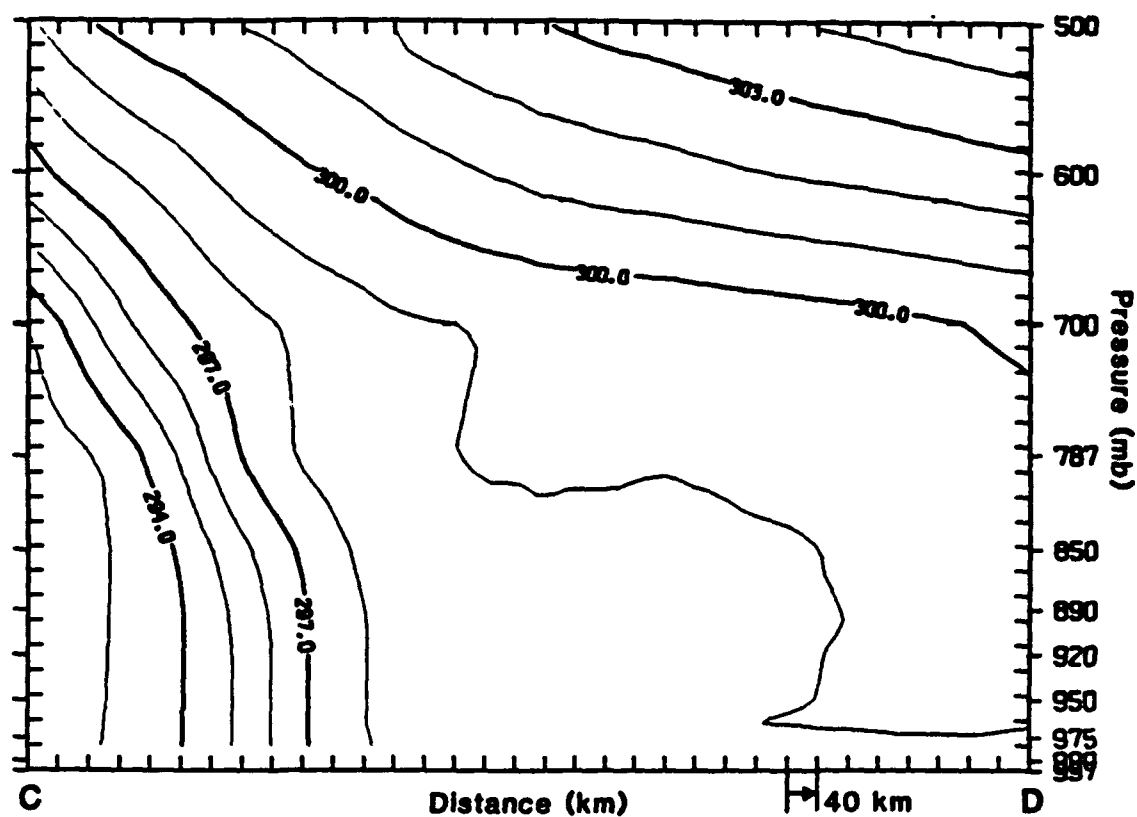


Figure 5.27: Continued.



**Figure 5.28:** Cross section of potential temperature (K) at hour 84. The plane of the cross section is shown in Fig. 23 (KTH).



**Figure 5.29:** Cross section of potential temperature (K) at hour 96. The plane of the cross section is shown in Fig. 24 (KTH).



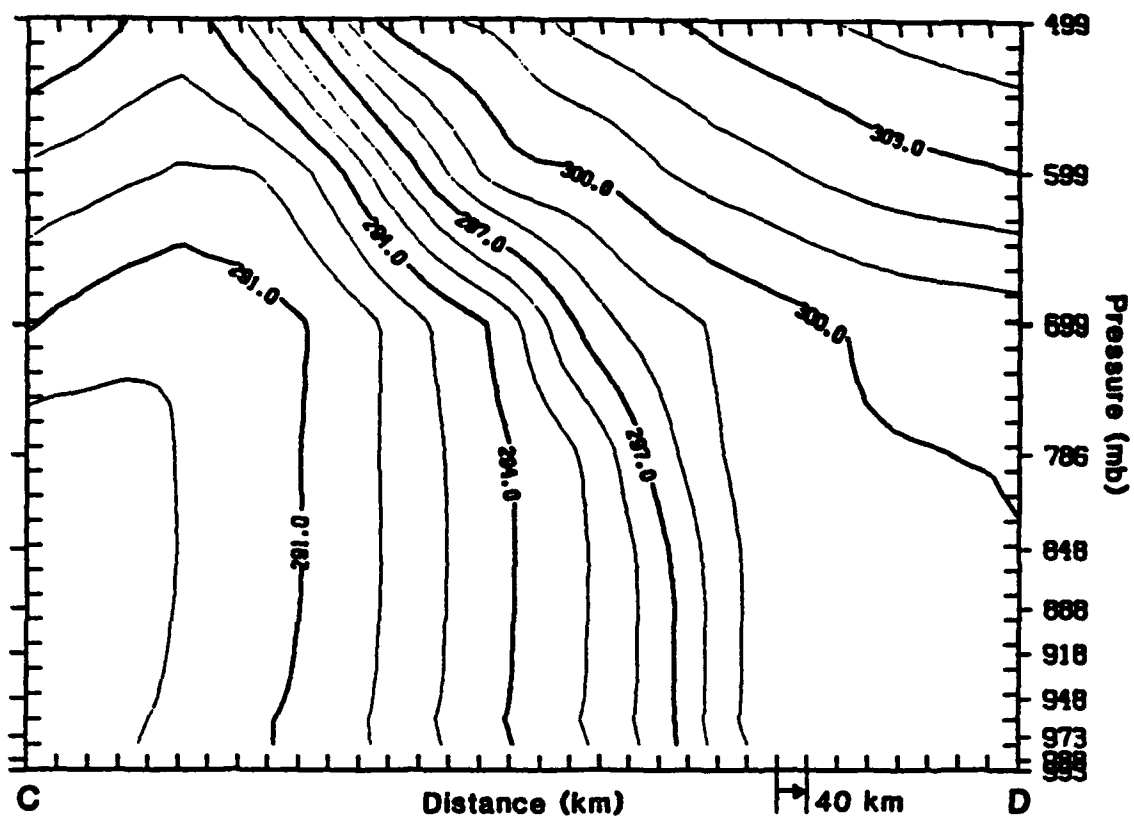


**Figure 5.30:** Cross section of potential temperature (K) at hour 108. The plane of the cross section is shown in Fig. 25 (KTH).

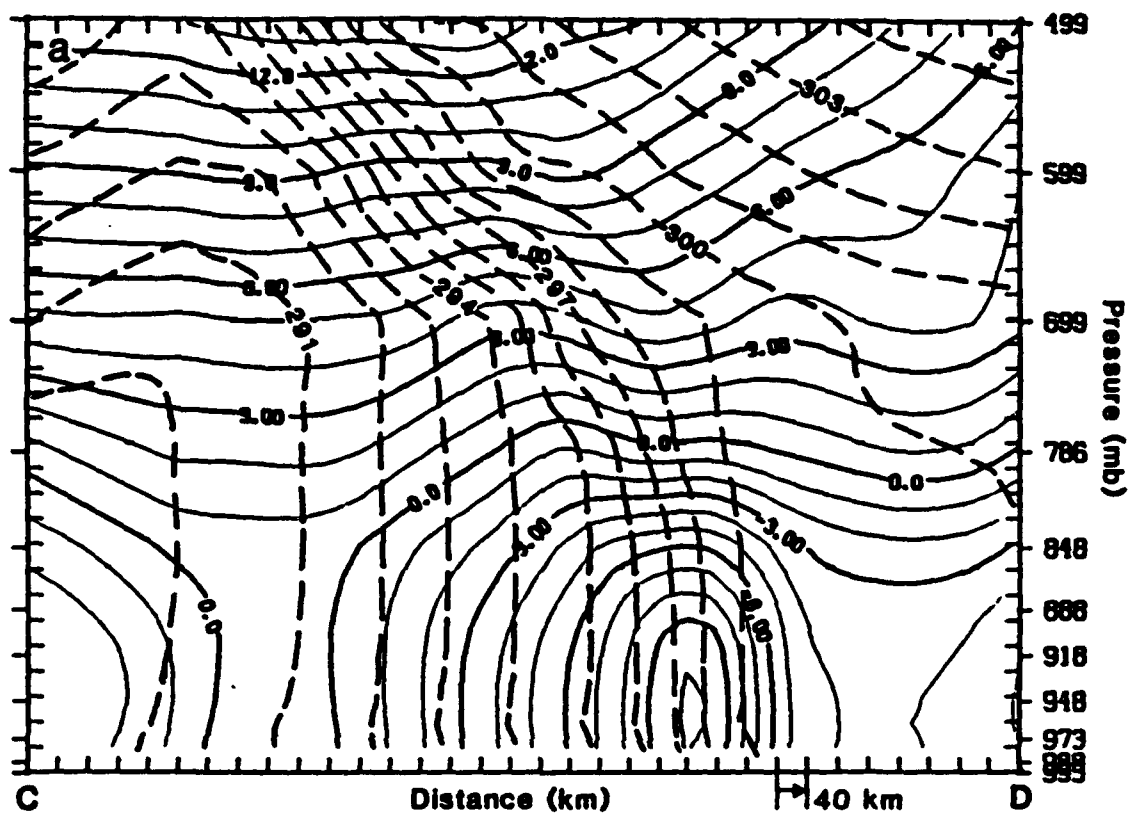


**Figure 5.31:** a) cross section of along-front wind component and b) front-normal wind component ( $\text{m s}^{-1}$ ) at hour 108 (KTH).

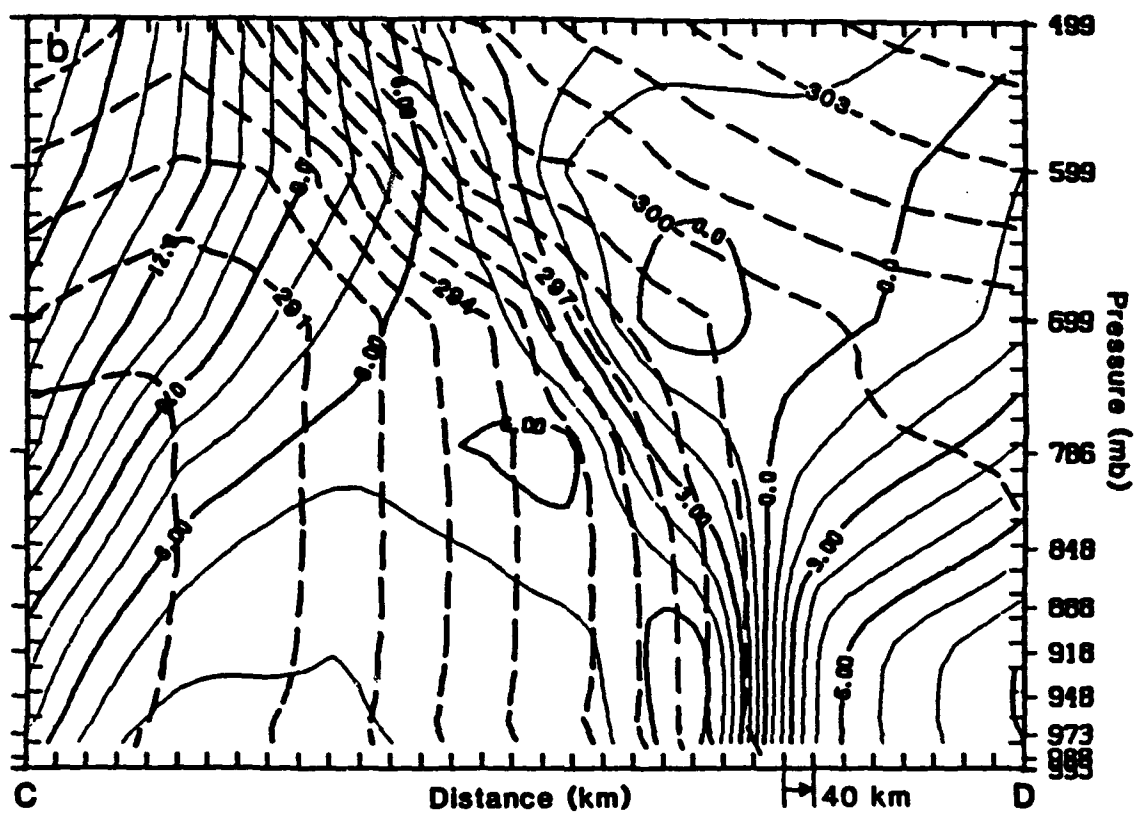
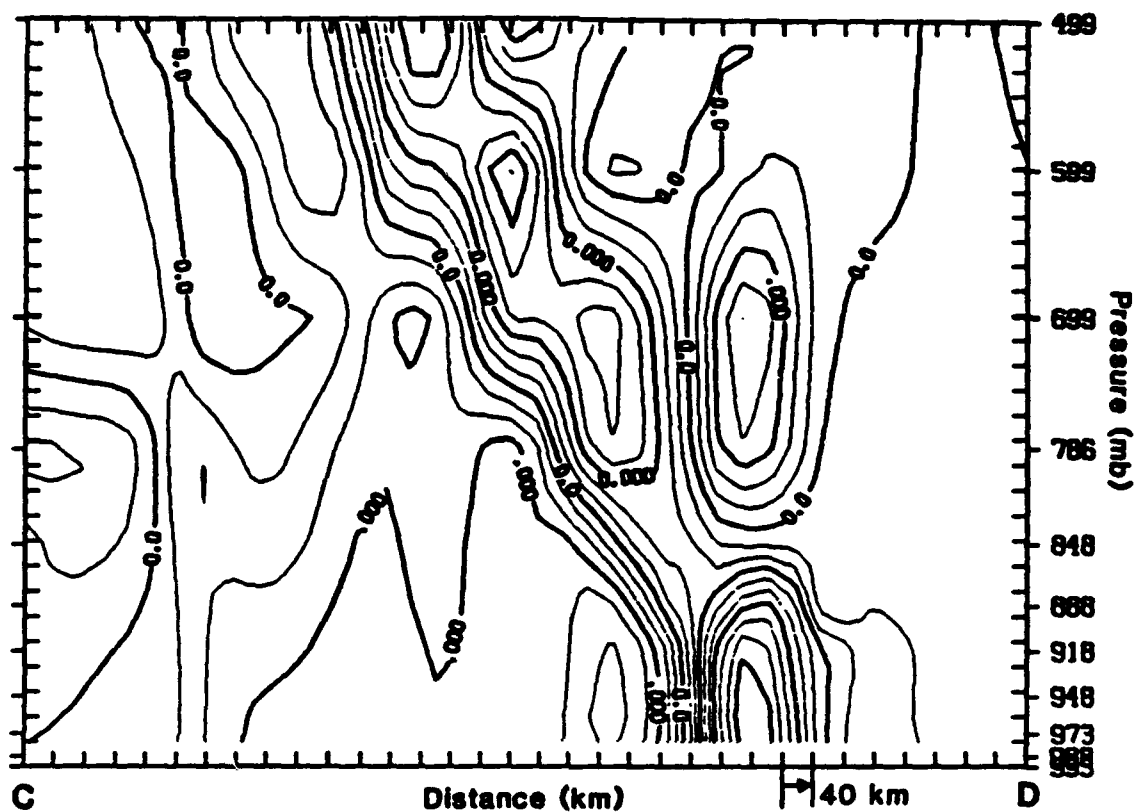


Figure 5.31: Continued.



**Figure 5.32:** Cross section of divergence ( $s^{-1}$ ) at hour 108 (KTH).

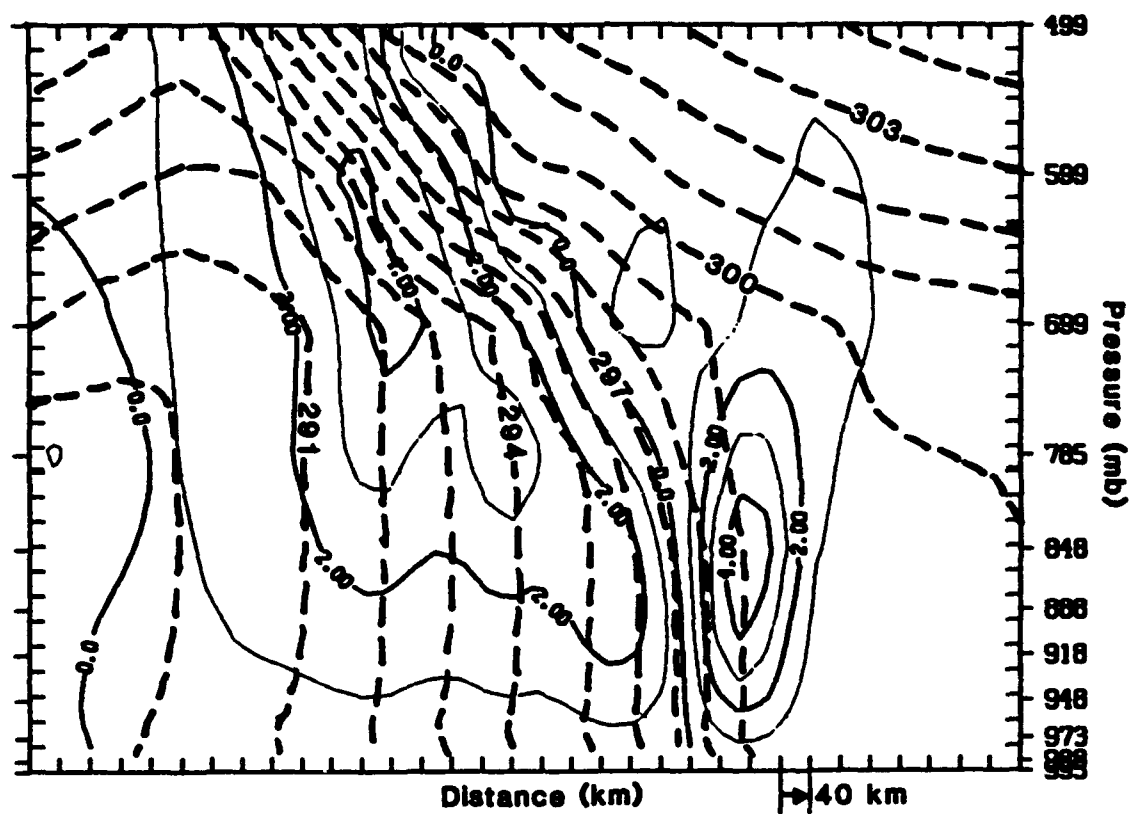
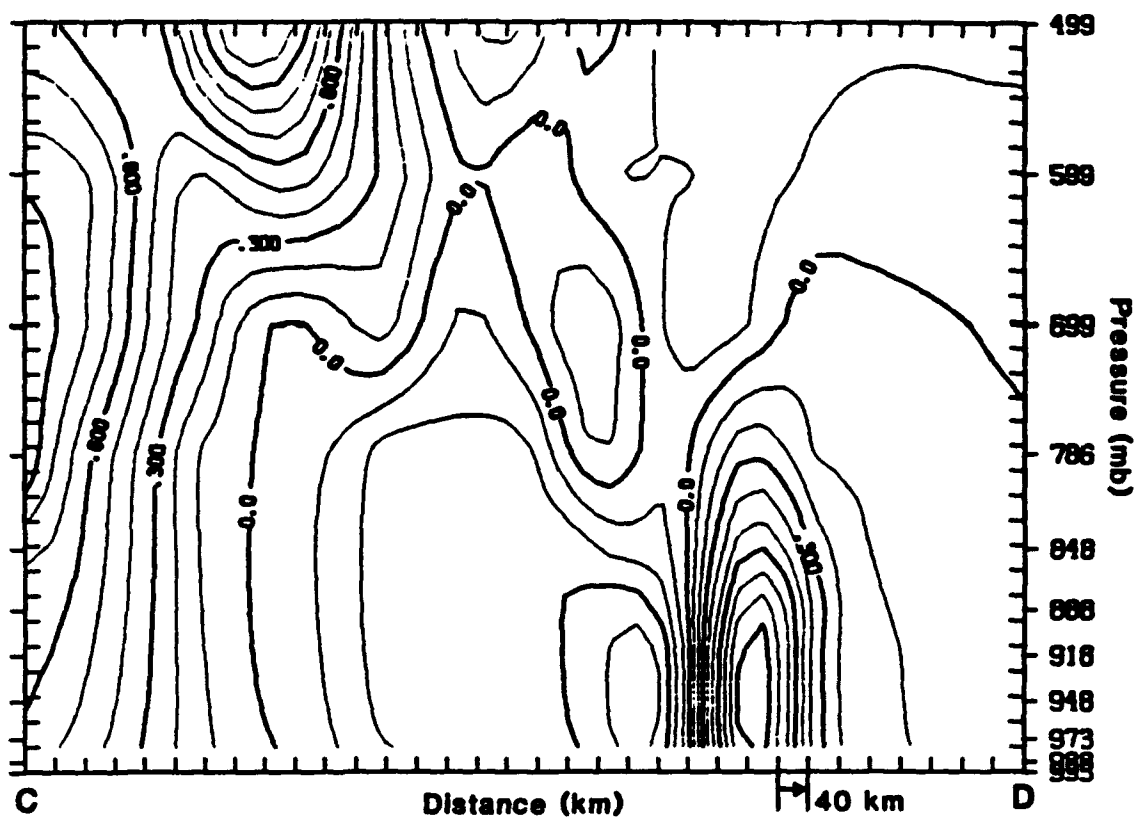


Figure 5.33: Cross section of vertical motion ( $\mu \text{ b s}^{-1}$ ) at hour 108 (KTH).



**Figure 5.34:** Cross section of vorticity at ( $\times 10^{-4} \text{ s}^{-1}$ ) hour 108. The plane of the cross section is shown in Fig. 26 (KTH).

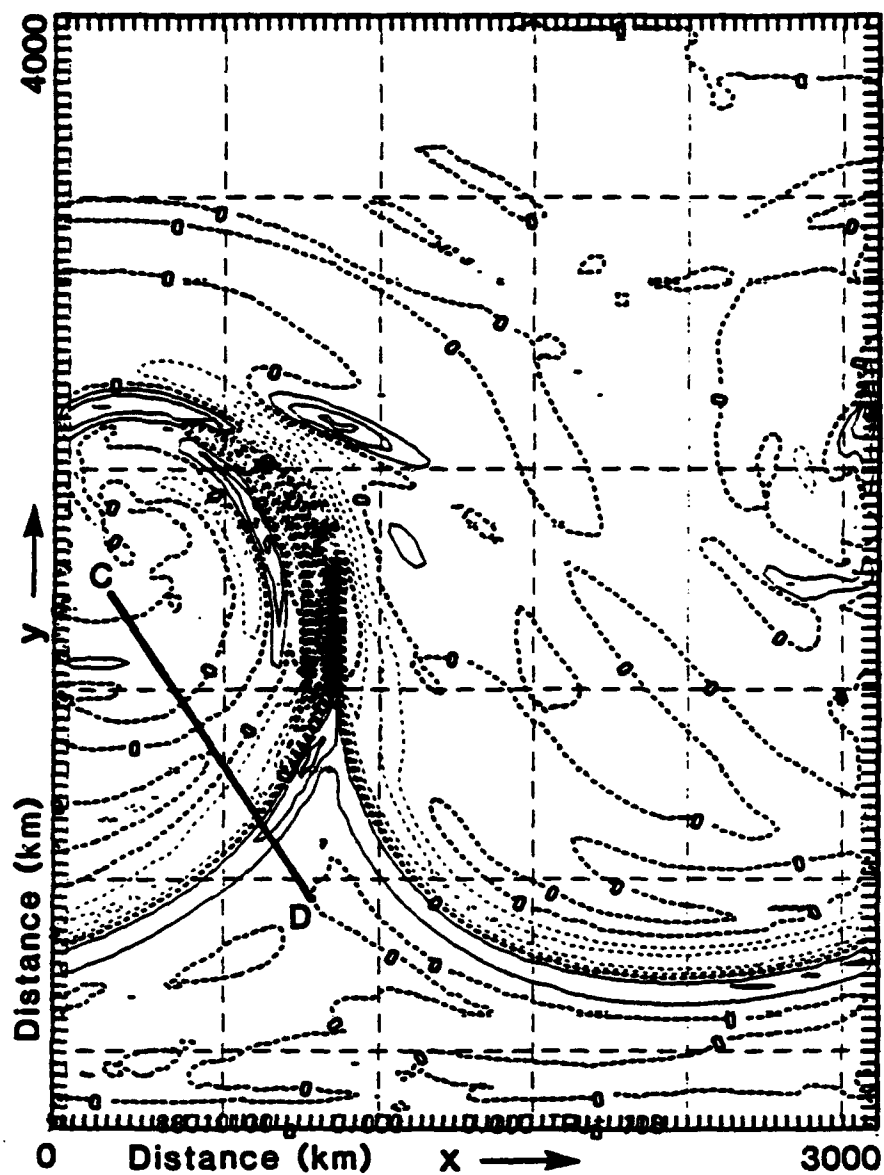
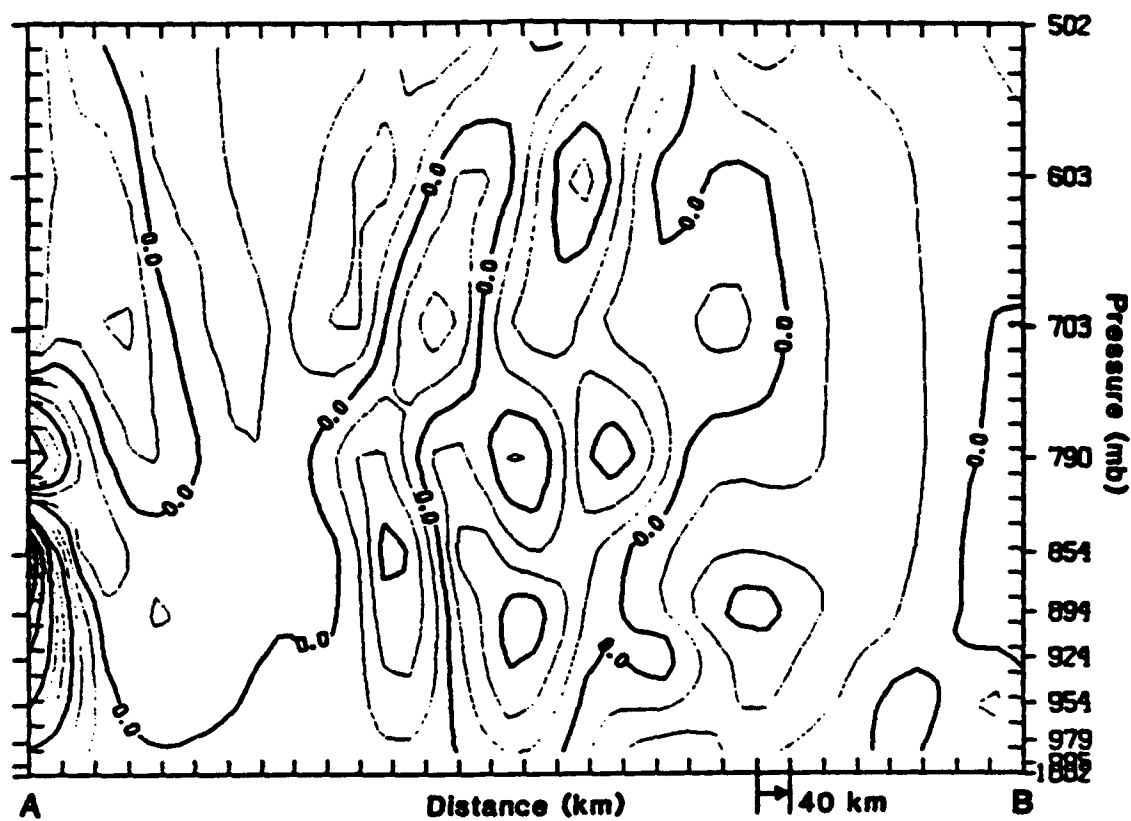
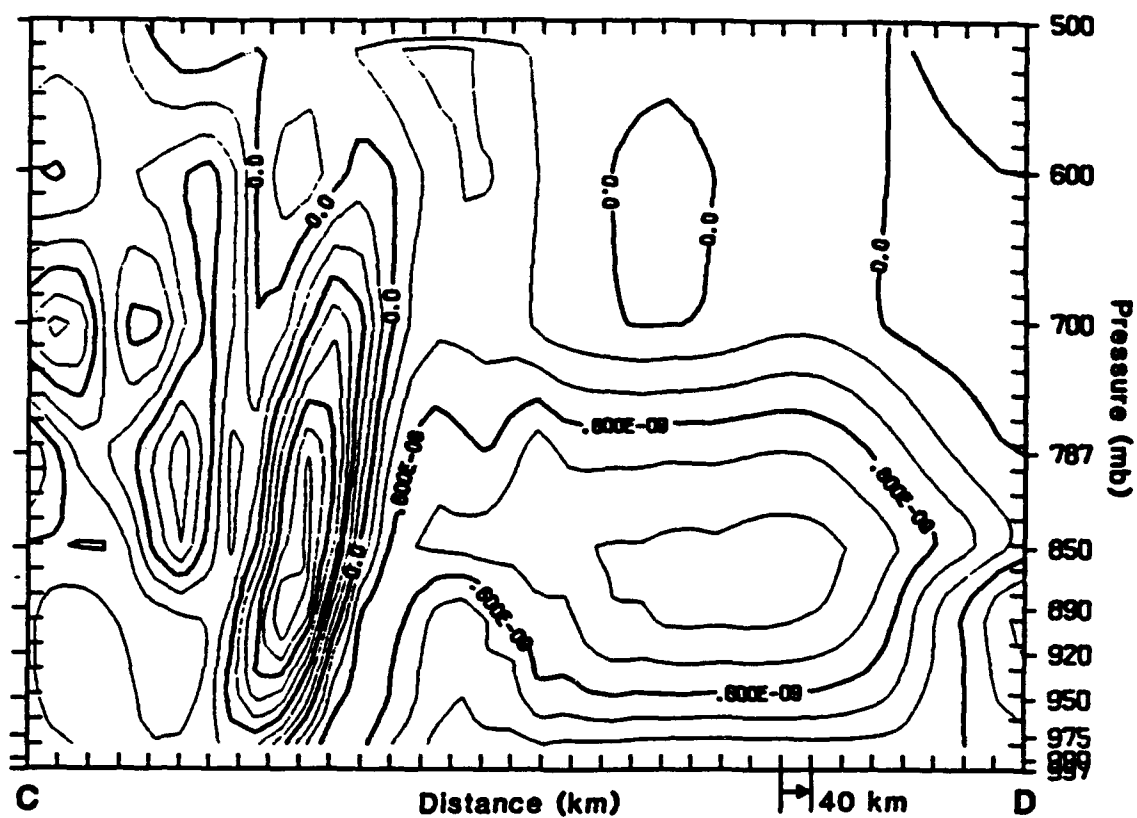


Figure 5.35: Total adiabatic frontogenetic forcing at hour 108 ( $\times 10^{-10} \text{ K s}^{-1} \text{ m}^{-1}$ ) at 850 mb (KTH).



**Figure 5.36:** Cross section of total adiabatic frontogenetic forcing ( $\text{K s}^{-1} \text{ m}^{-1}$ ) at hour 84 (KTH).





**Figure 5.37:** Cross section of total adiabatic frontogenetic forcing at hour 96 (KTH).

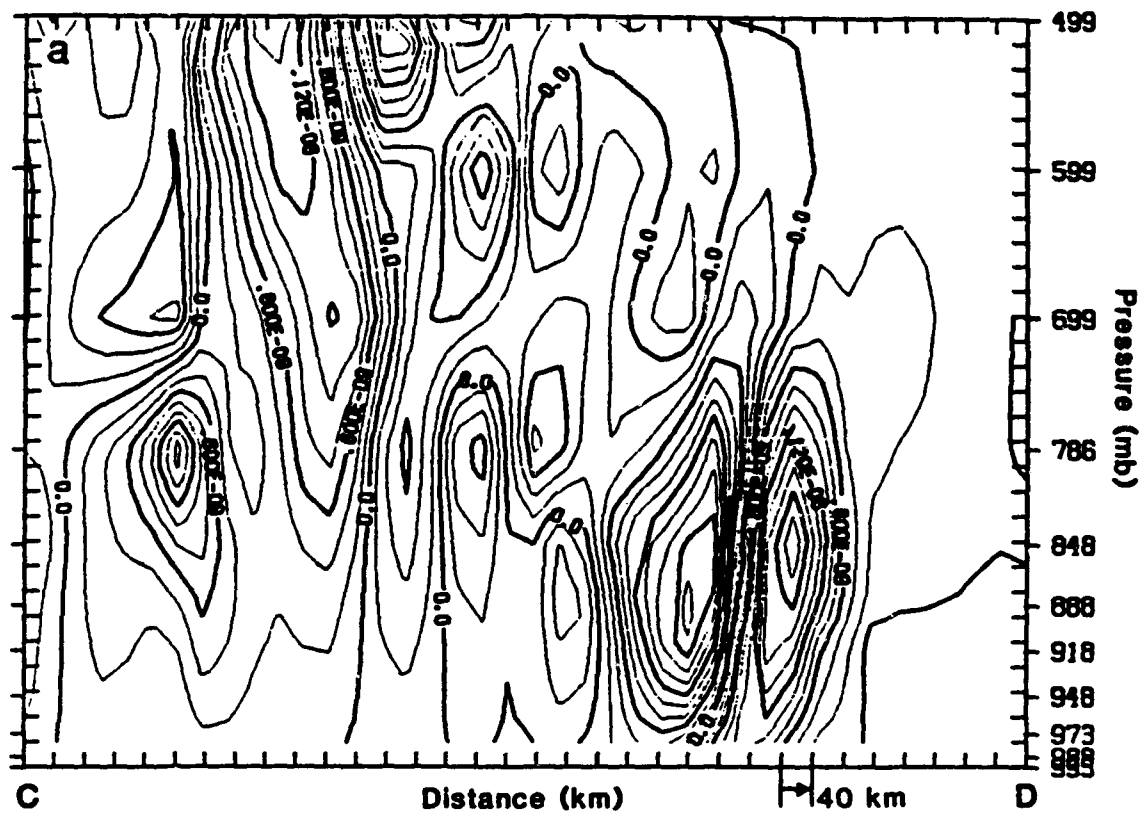


**Figure 5.38:** a) cross section of total adiabatic frontogenetic forcing at hour 108, b) tilting term, and c) diabatic term (KTH).





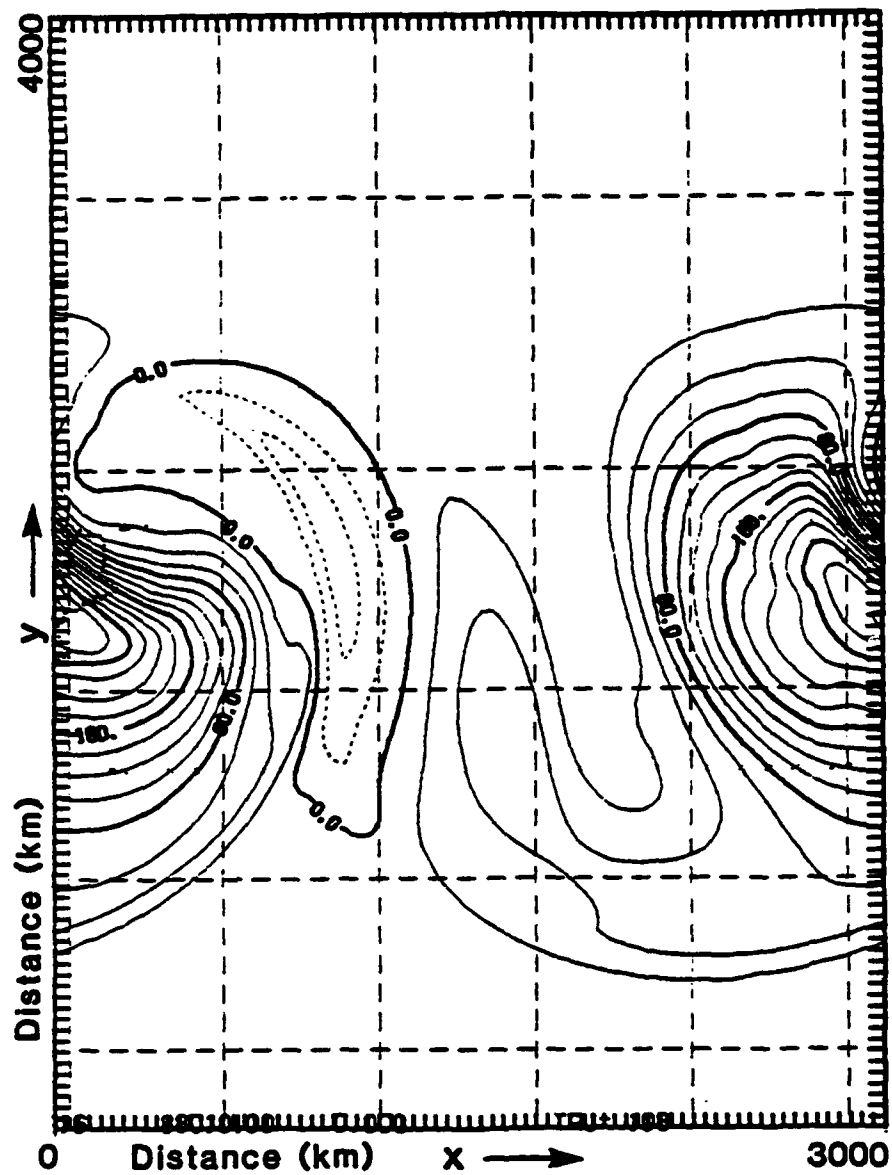


**Figure 5.39:** Surface sensible heat flux ( $\text{W m}^{-2}$ ) at hour 108 (KTH).

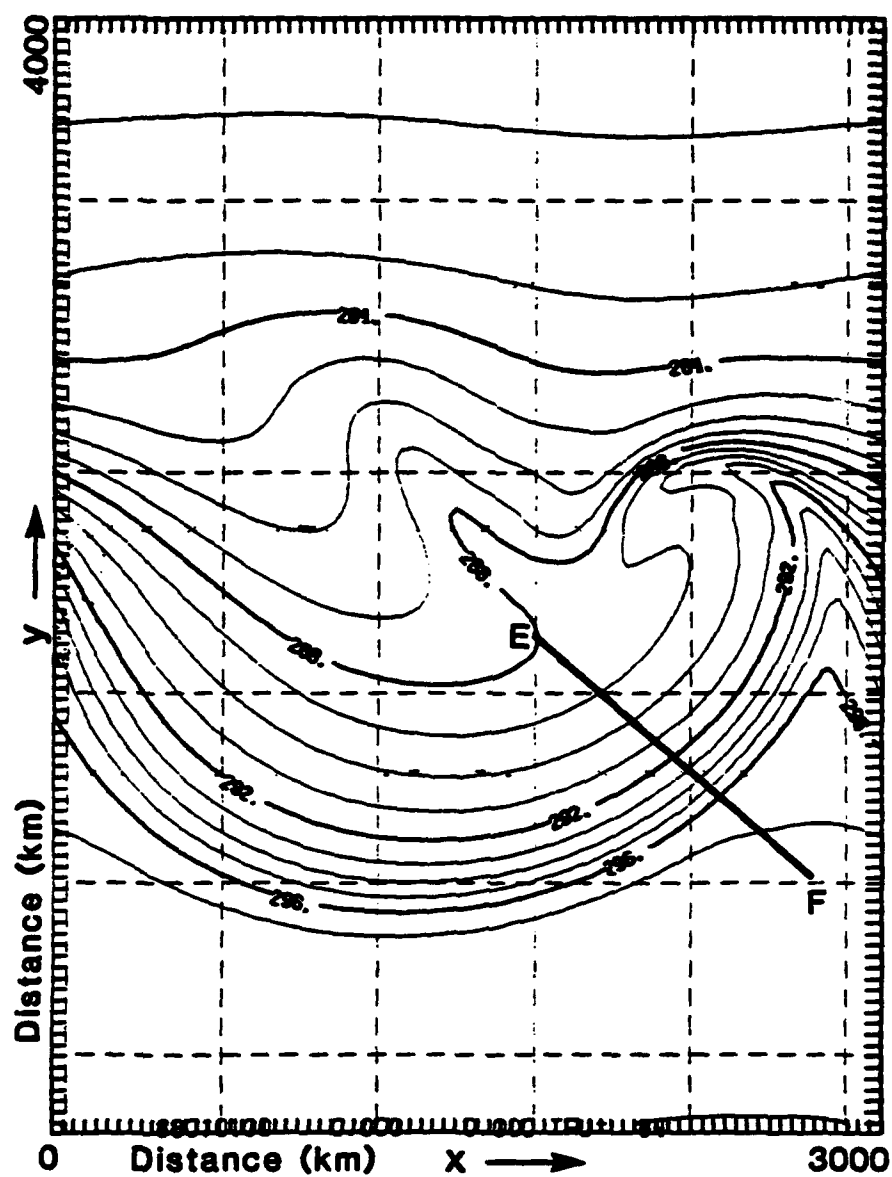
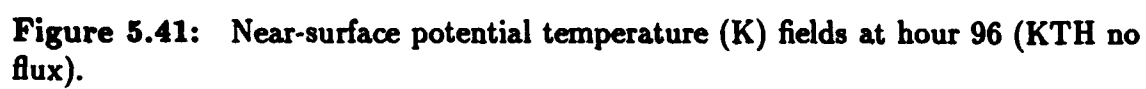


Figure 5.40: Near-surface potential temperature (K) fields at hour 84 (KTH no flux).



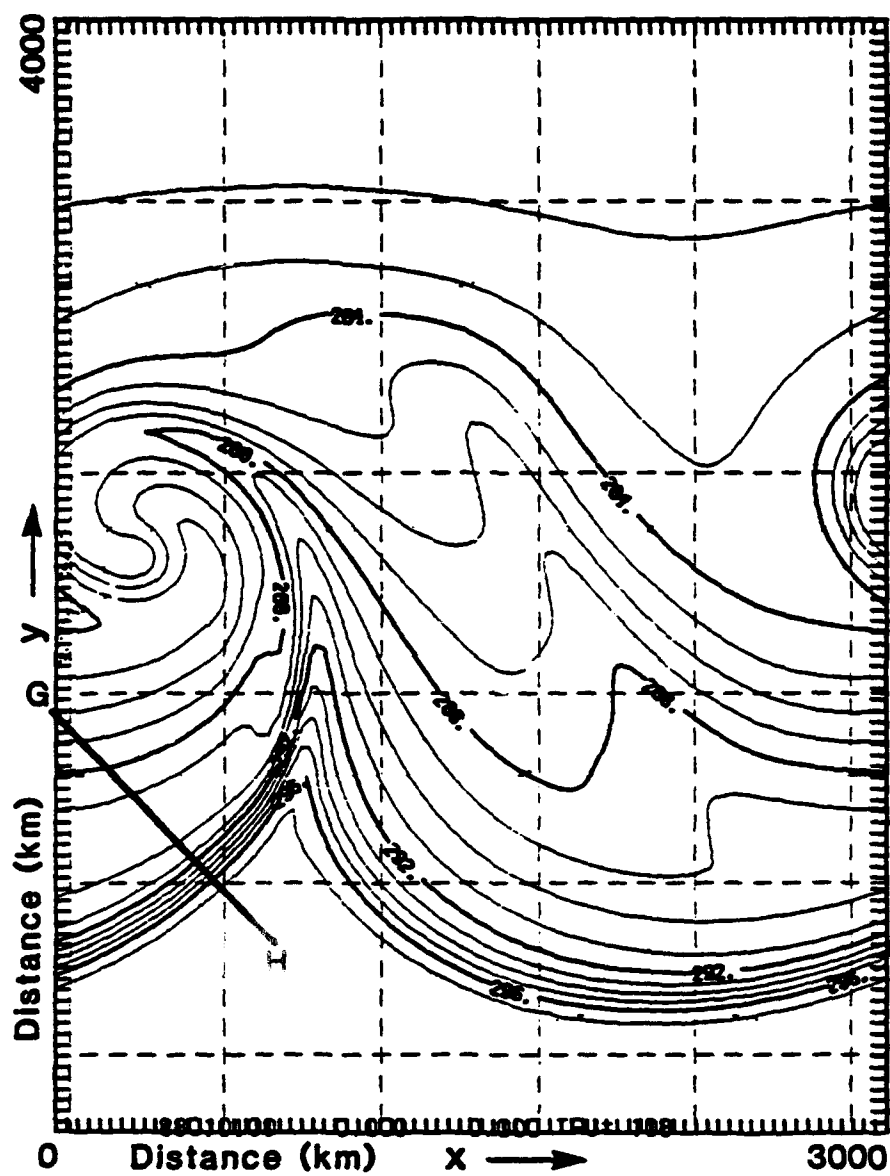
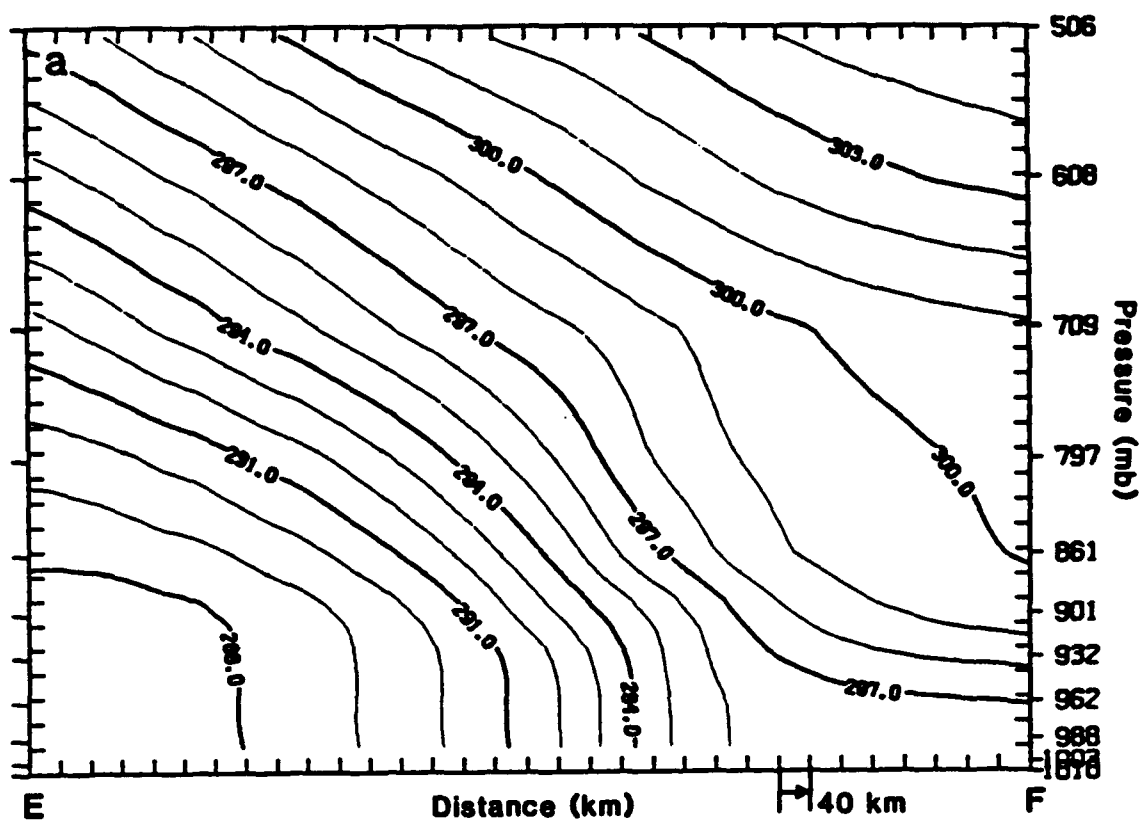


Figure 5.42: Near-surface potential temperature (K) fields at hour 108 (KTH no flux).





**Figure 5.43:** a) cross section of potential temperature (K) at hour 84, b) at hour 96, and c) at hour 108. The planes of the cross sections are shown in Figs. 40, 41, and 42 (KTH no flux).

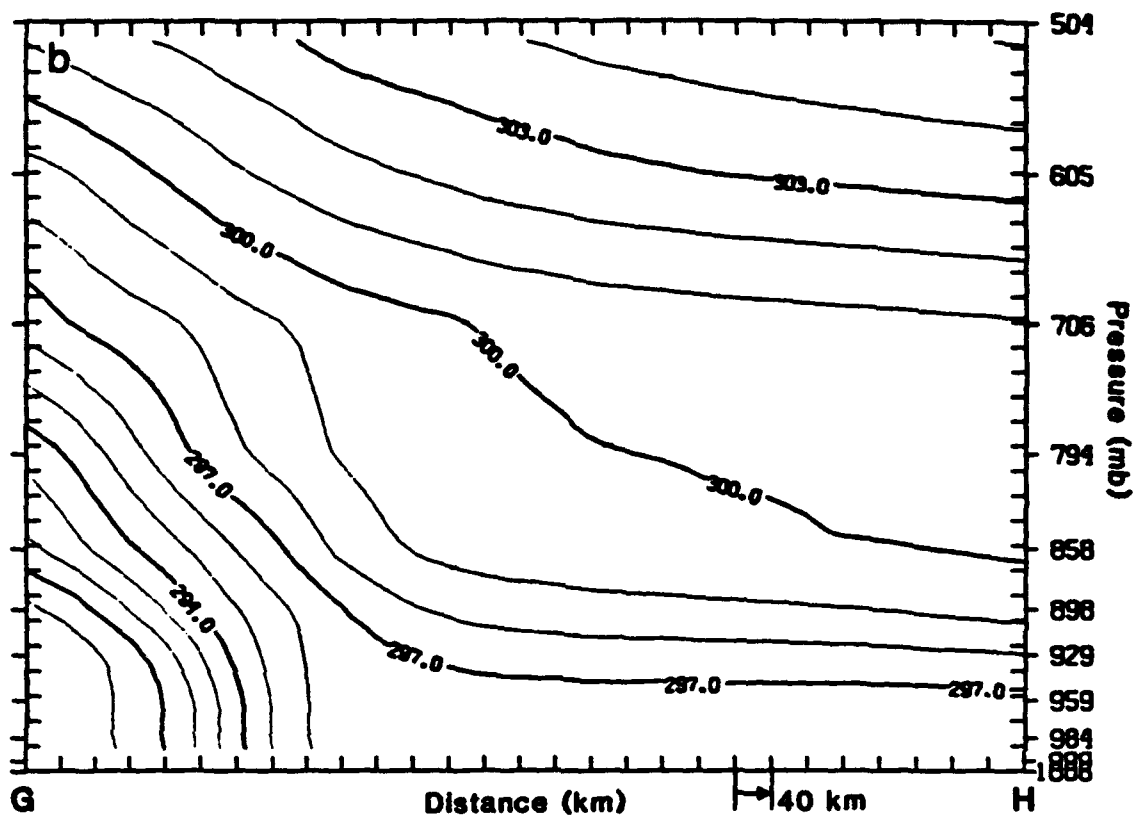


Figure 5.43: Continued.

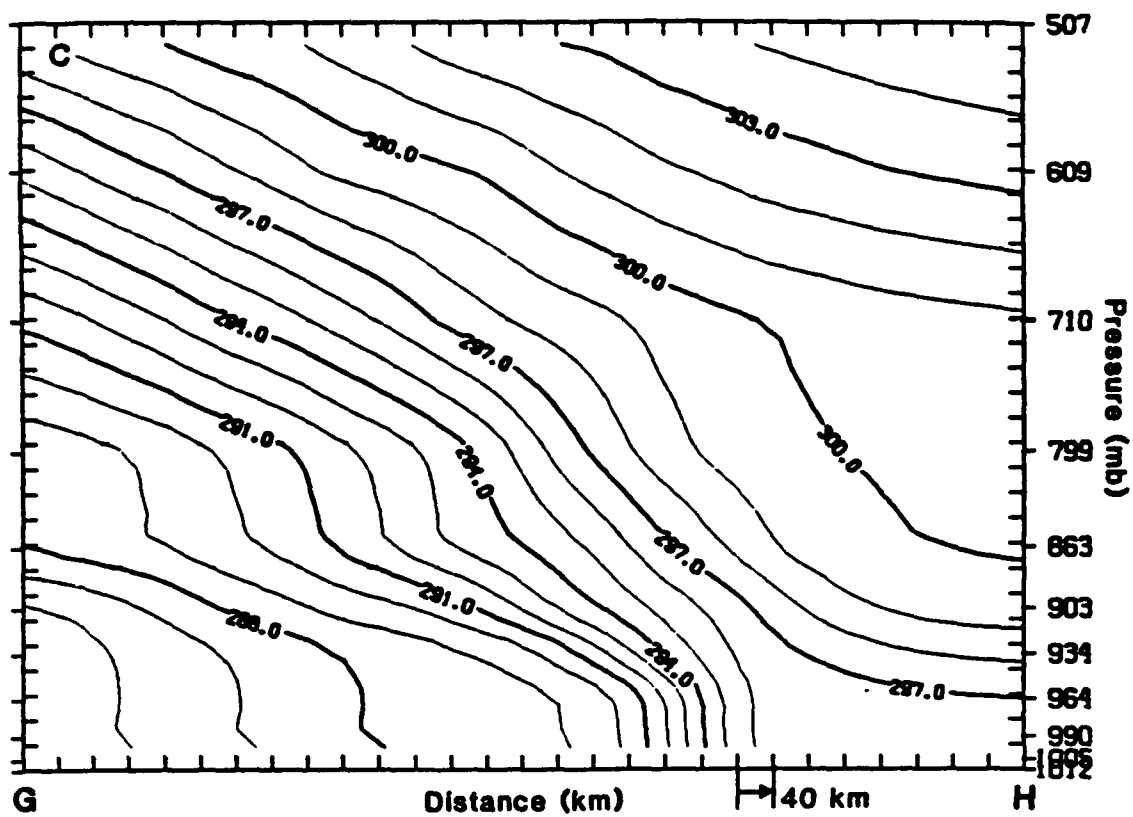
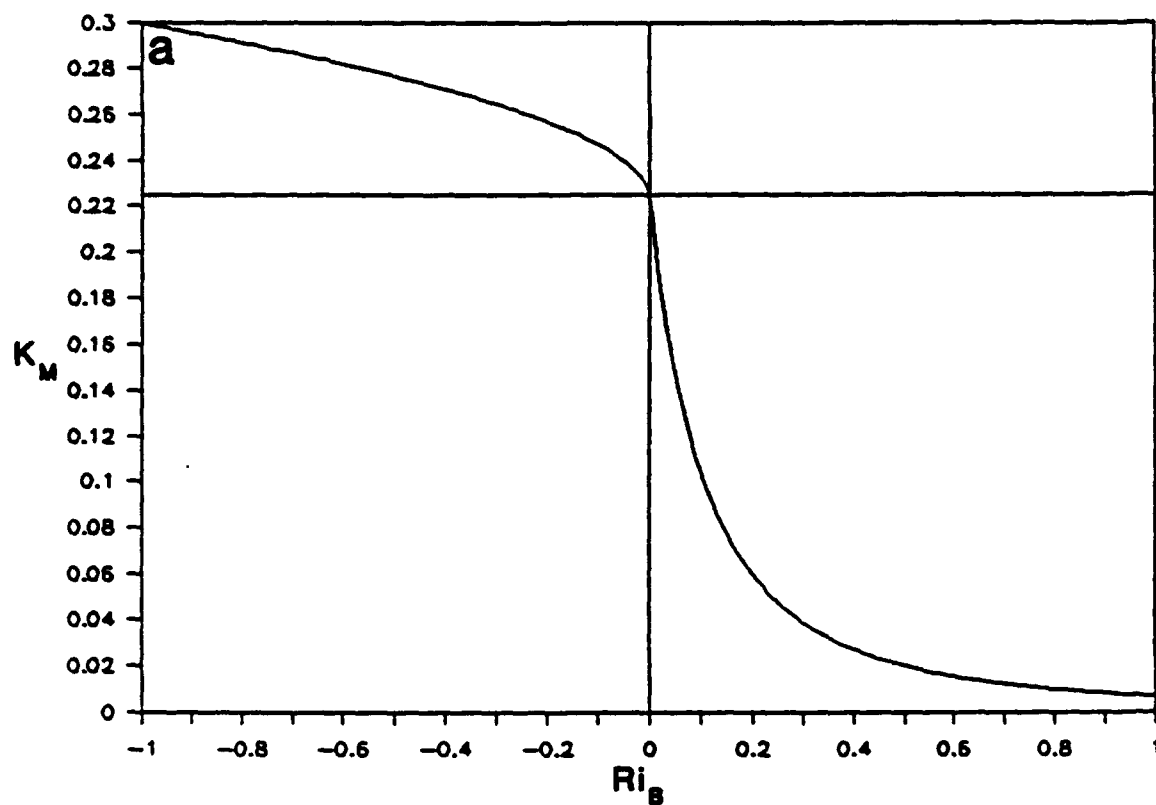
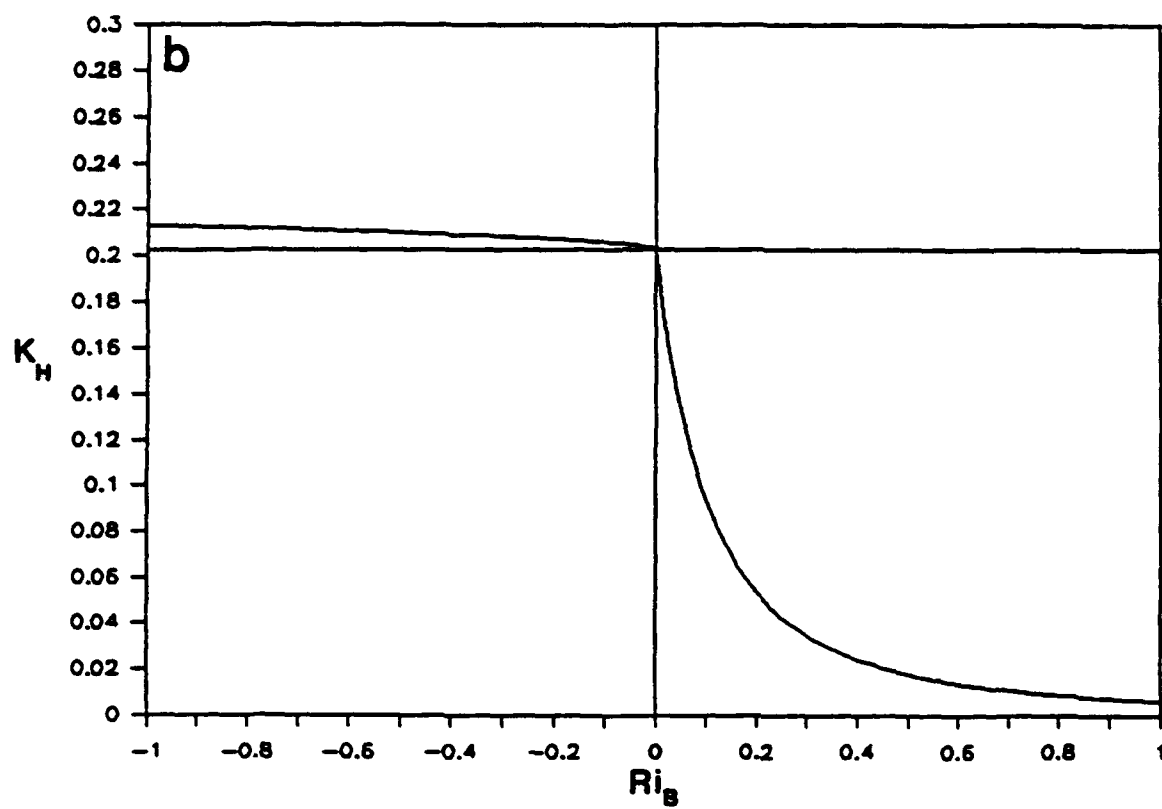


Figure 5.43: Continued.



**Figure 5.44:** a) normalized eddy coefficient for momentum ( $K_m$ ) and b) normalized eddy coefficient for heat ( $K_h$ ) (KTH).



**Figure 5.44: Continued.**

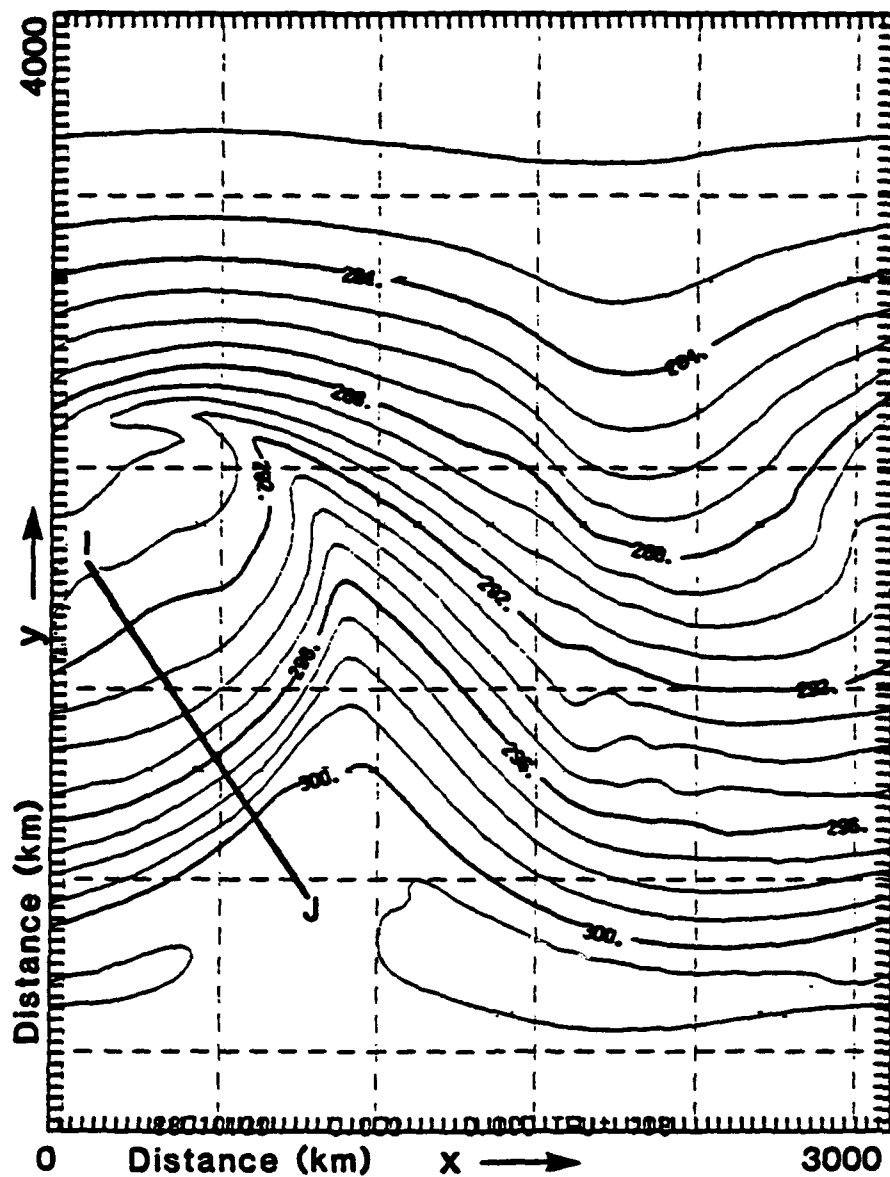


**Figure 5.45:** Near-surface potential temperature (K) fields at hour 108 (KTH no stab).

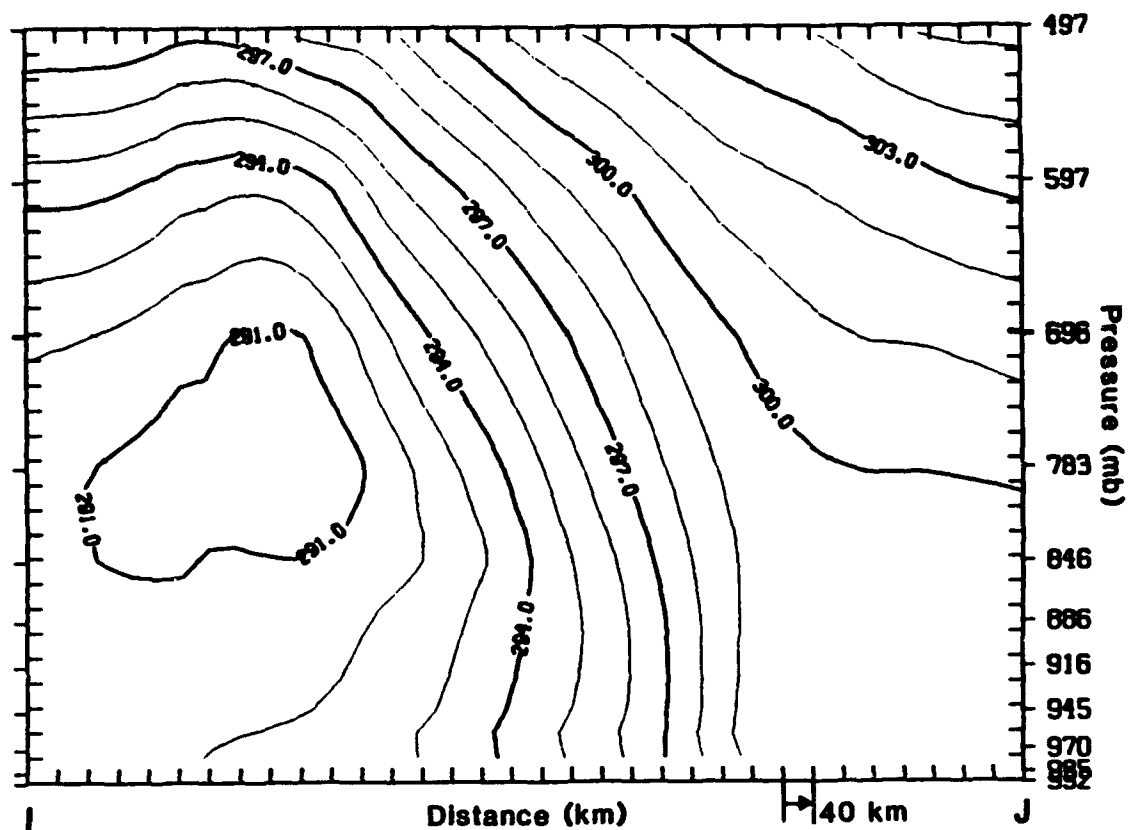


**Figure 5.46:** Cross section of potential temperature (K) at hour at hour 108. The plane of the cross section is shown in Fig. 45 (KTH no stab).

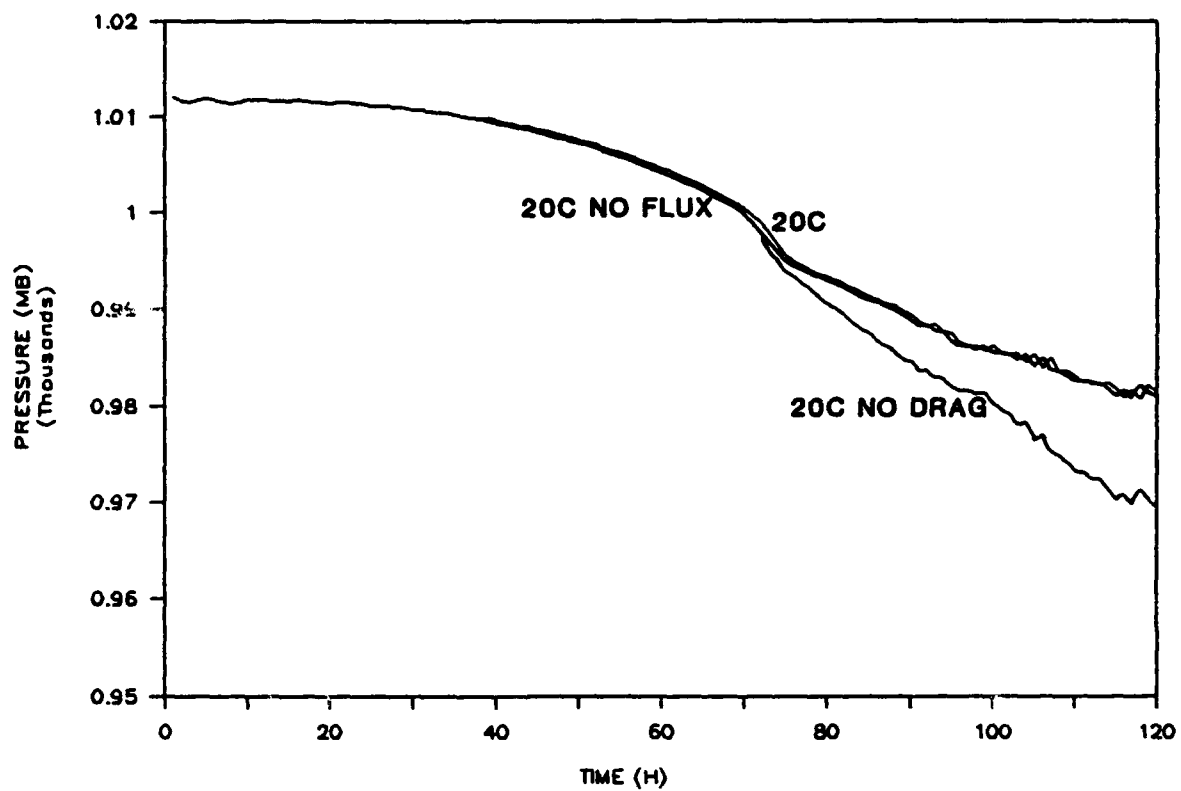


**Figure 5.47:** Time series of minimum surface pressure (mb) (20C).



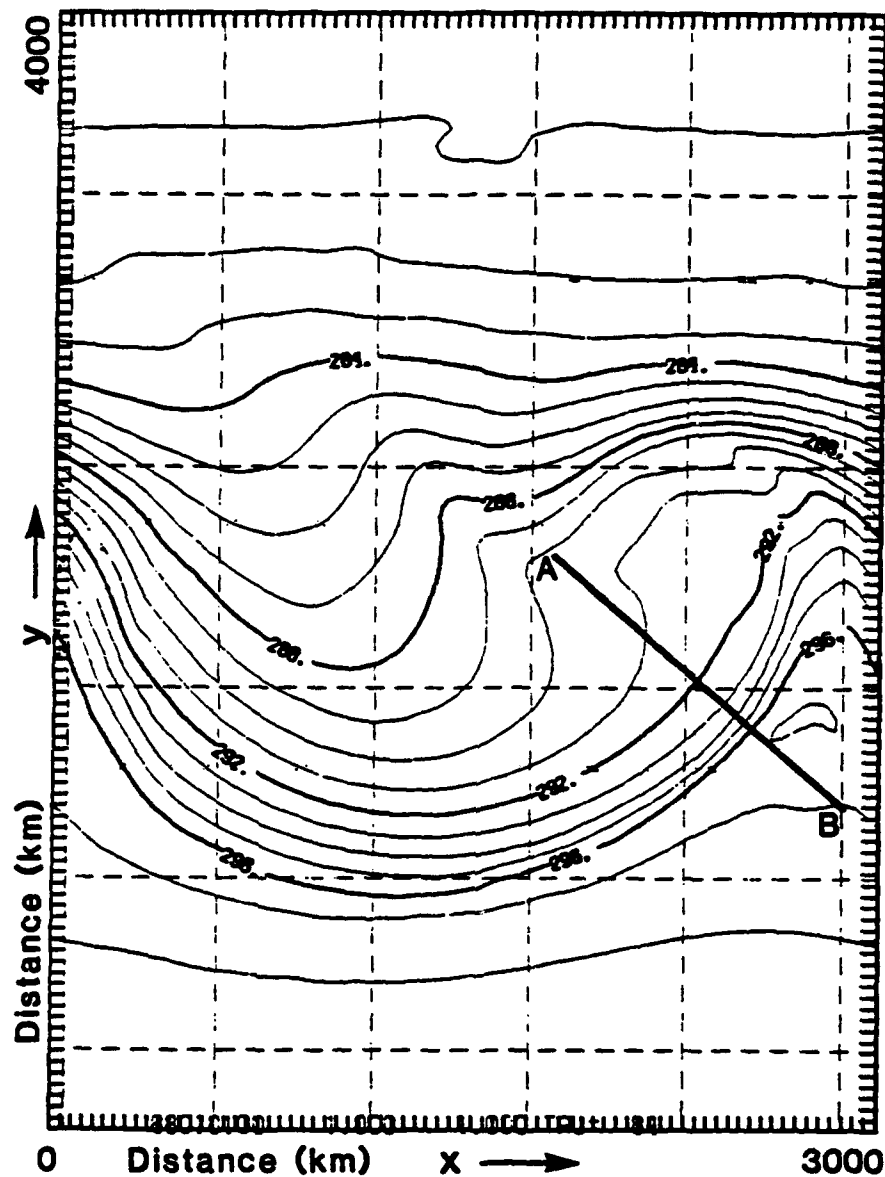


Figure 5.48: Near-surface potential temperature (K) fields at hour 84 (20C).

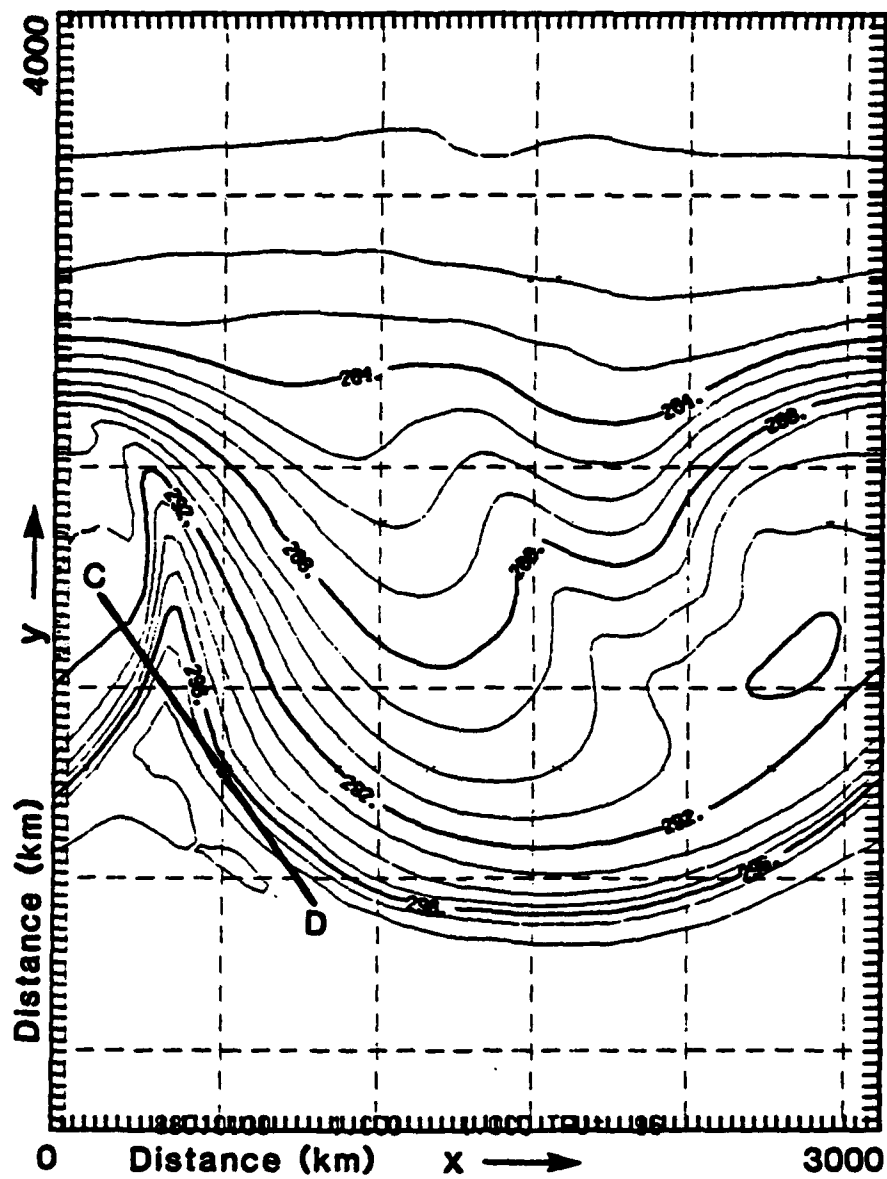


Figure 5.49: Near-surface potential temperature (K) fields at hour 96 (20C).

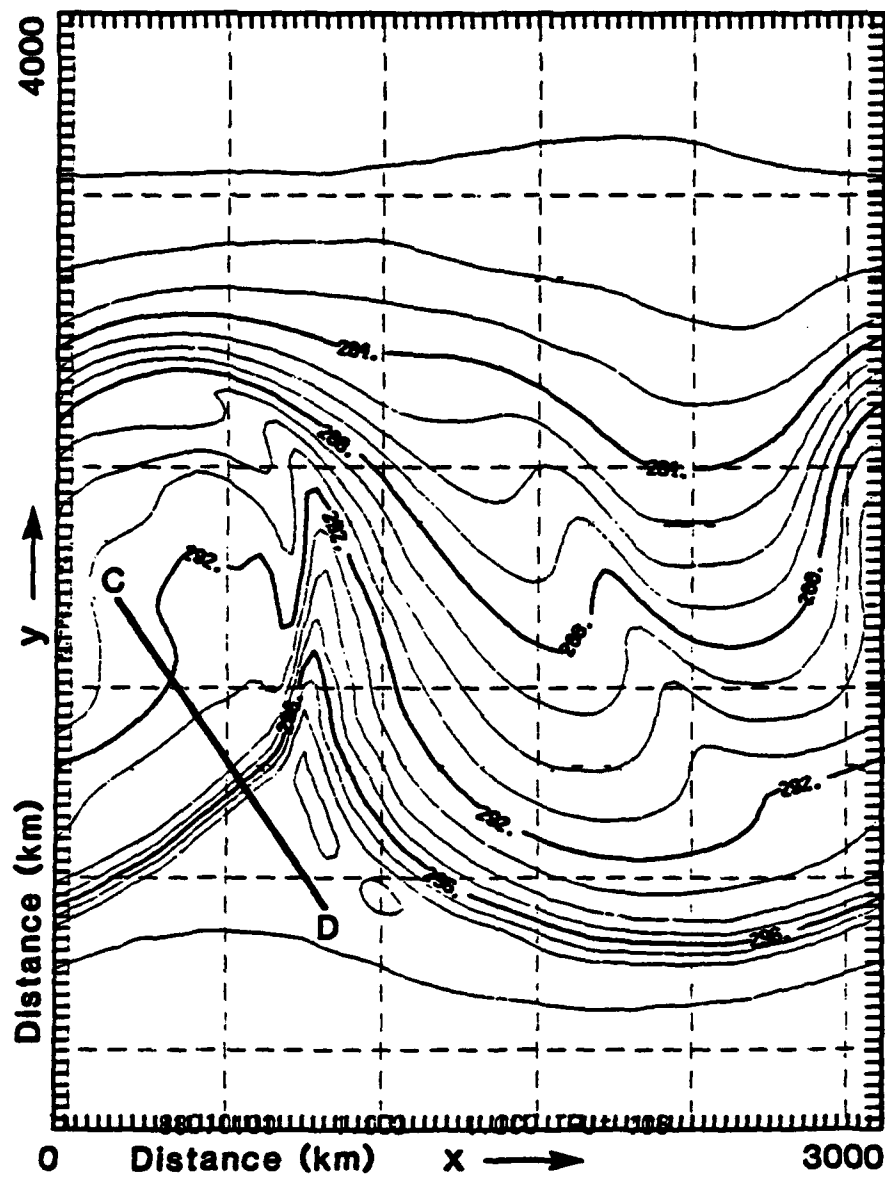


Figure 5.50: Near-surface potential temperature (K) fields at hour 108 (20C).

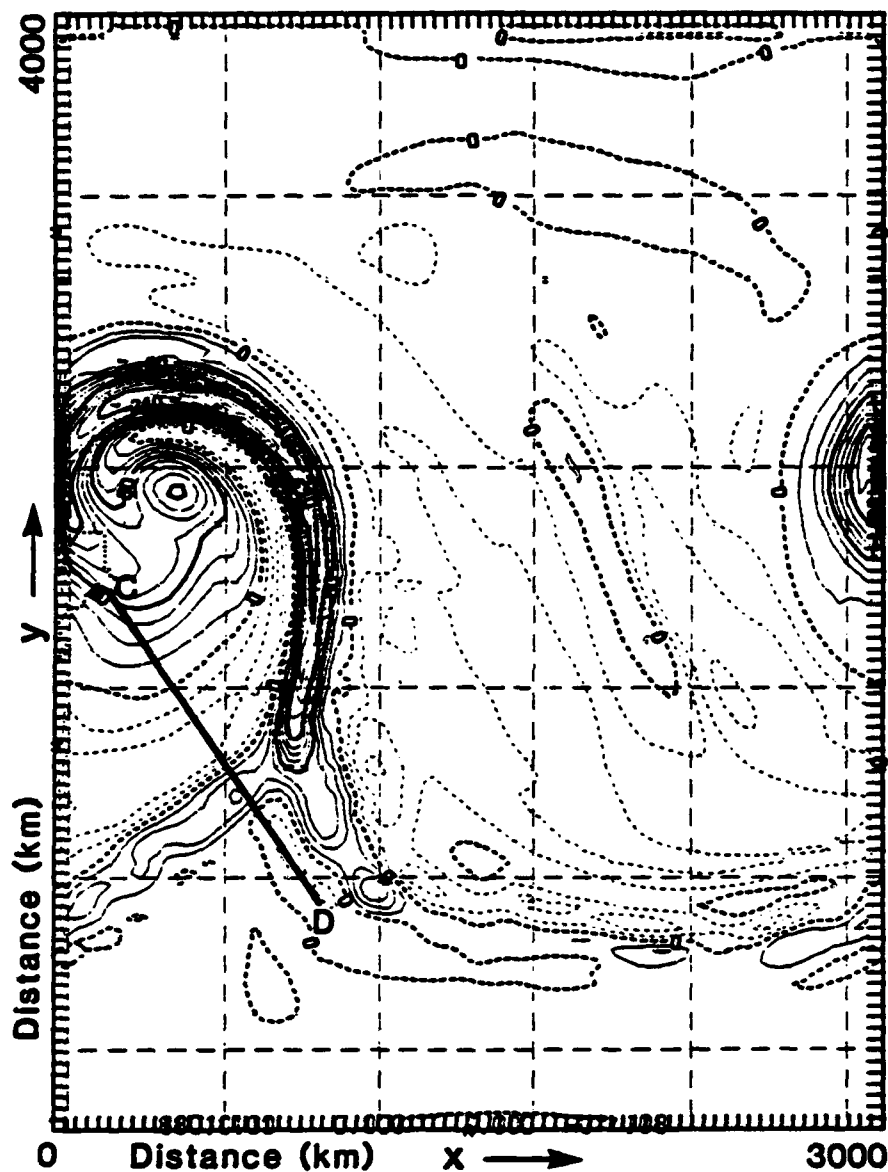


Figure 5.51: 850 mb relative vorticity ( $\times 10^{-6} \text{ s}^{-1}$ ) at hour 108 (20C).

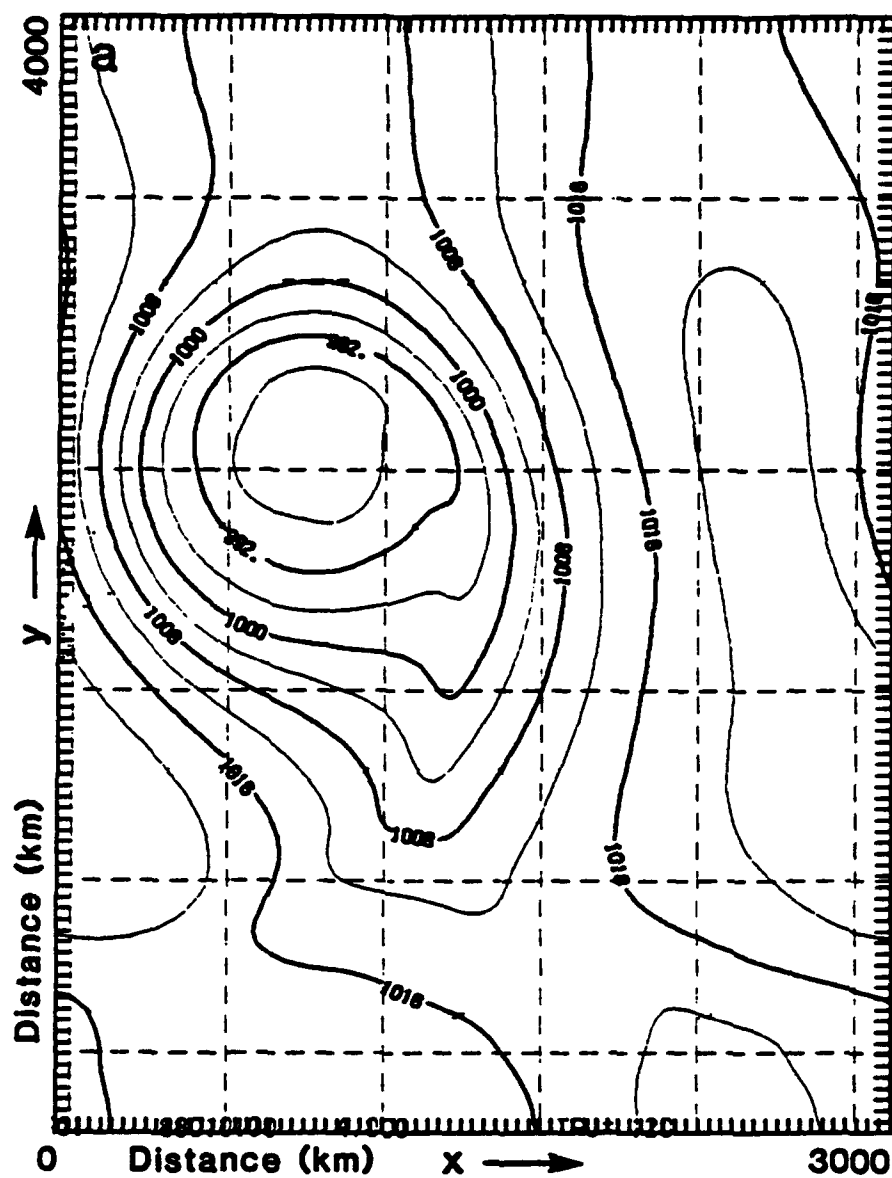


Figure 5.52: a) surface pressure (mb) and b) near-surface potential temperature (K) fields at 120 hour (20C).

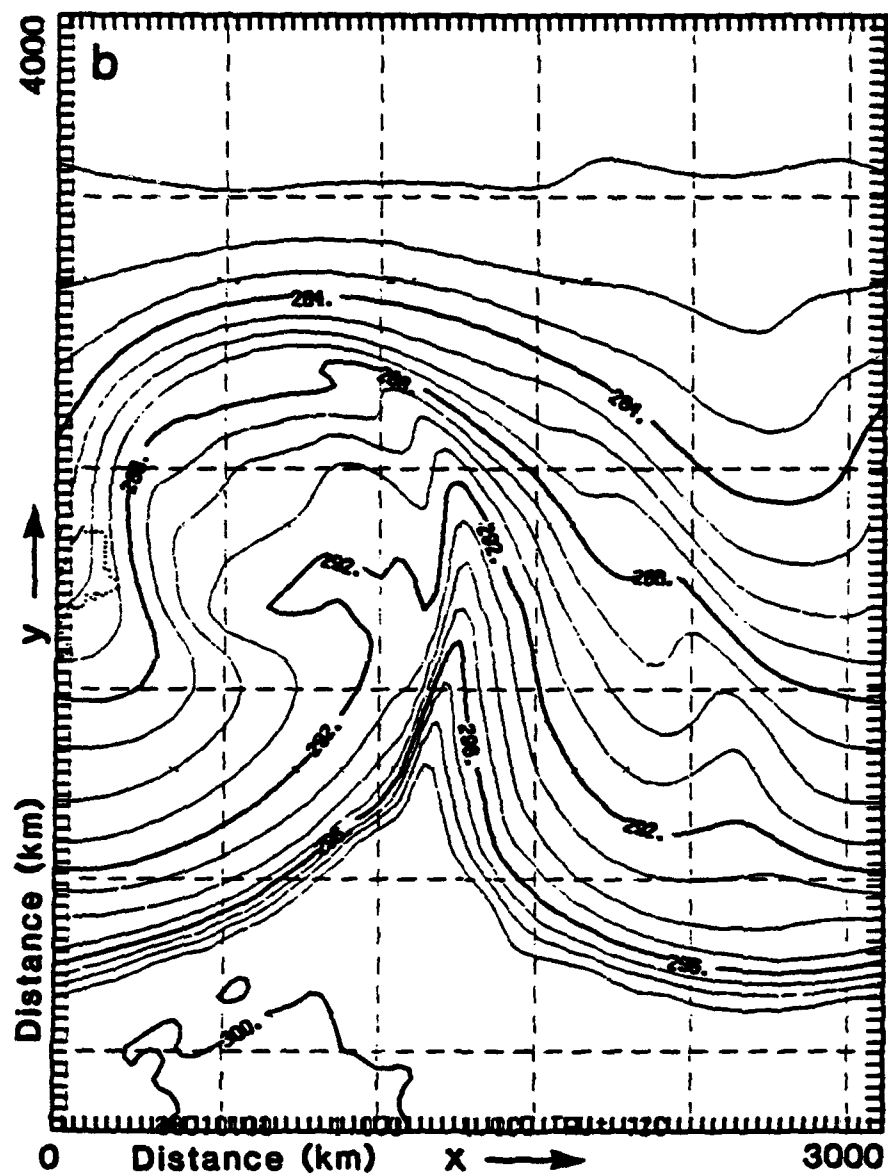
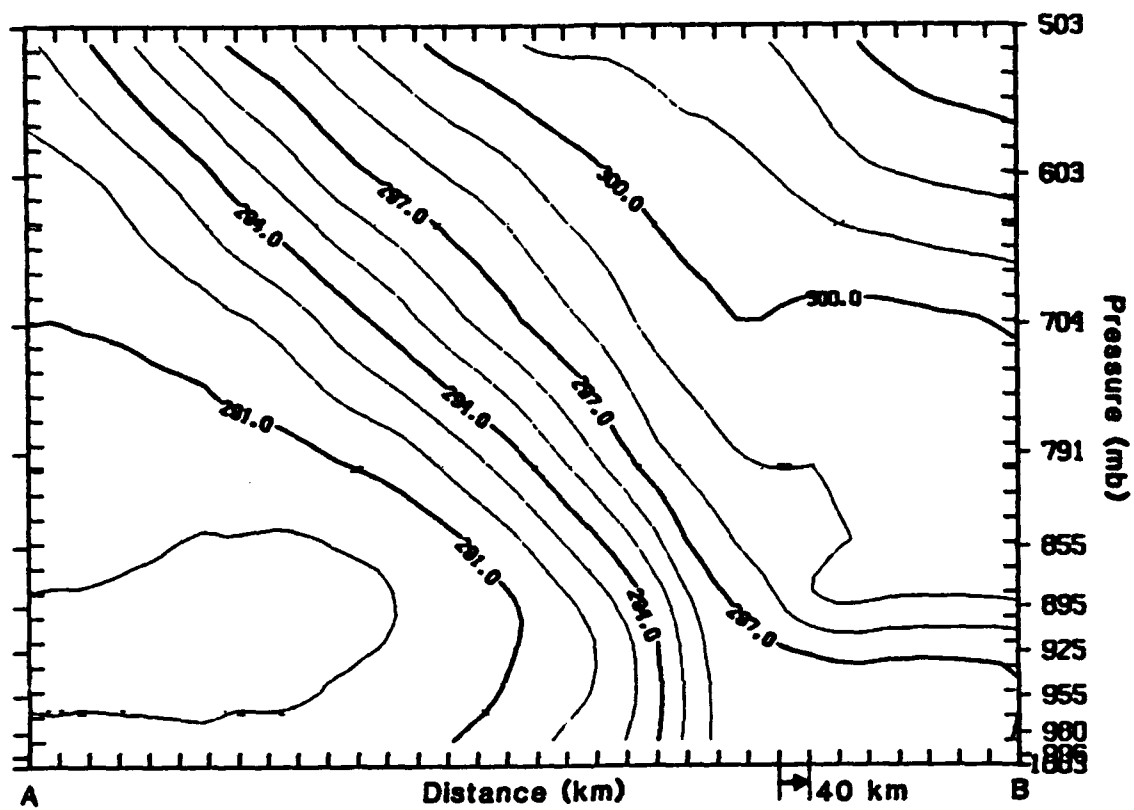
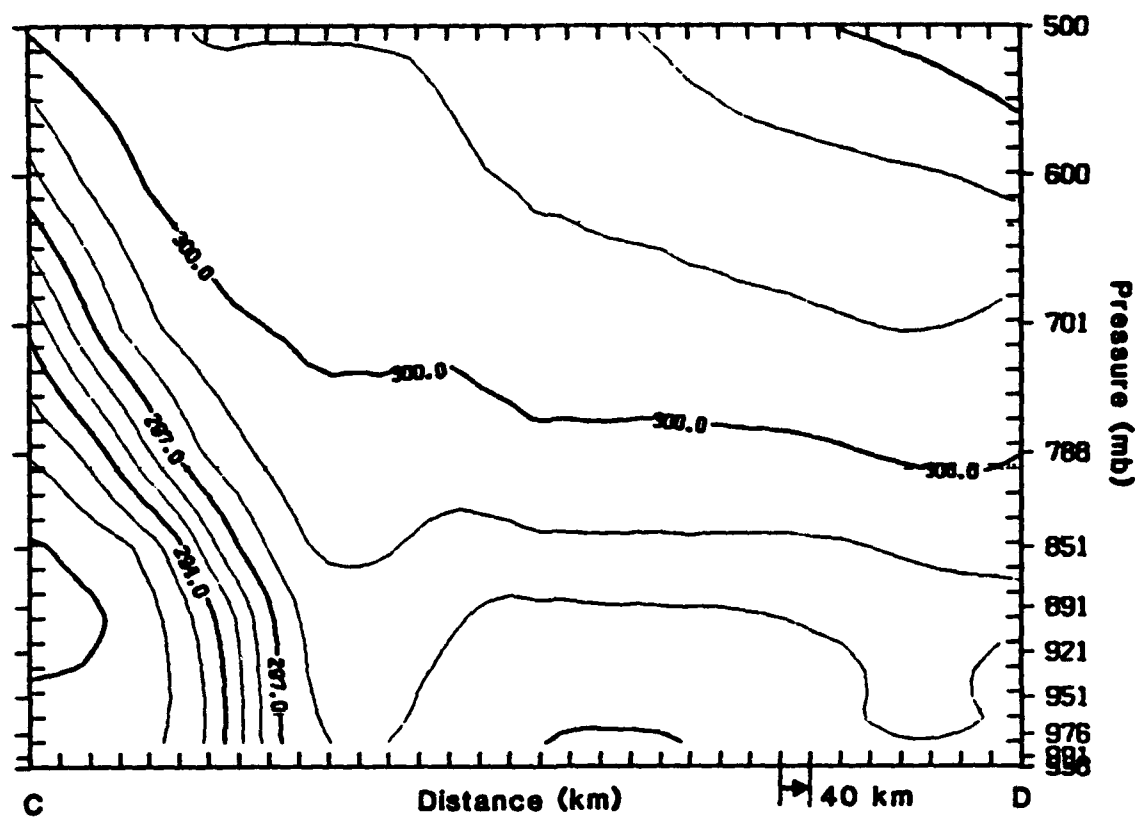


Figure 5.52: Continued.



**Figure 5.53:** Cross section of potential temperature (K) at hour 84. The plane of the cross section is shown in Fig. 48 (20C).



**Figure 5.54:** Cross section of potential temperature (K) at hour 96. The plane of the cross section is shown in Fig. 49 (20C).



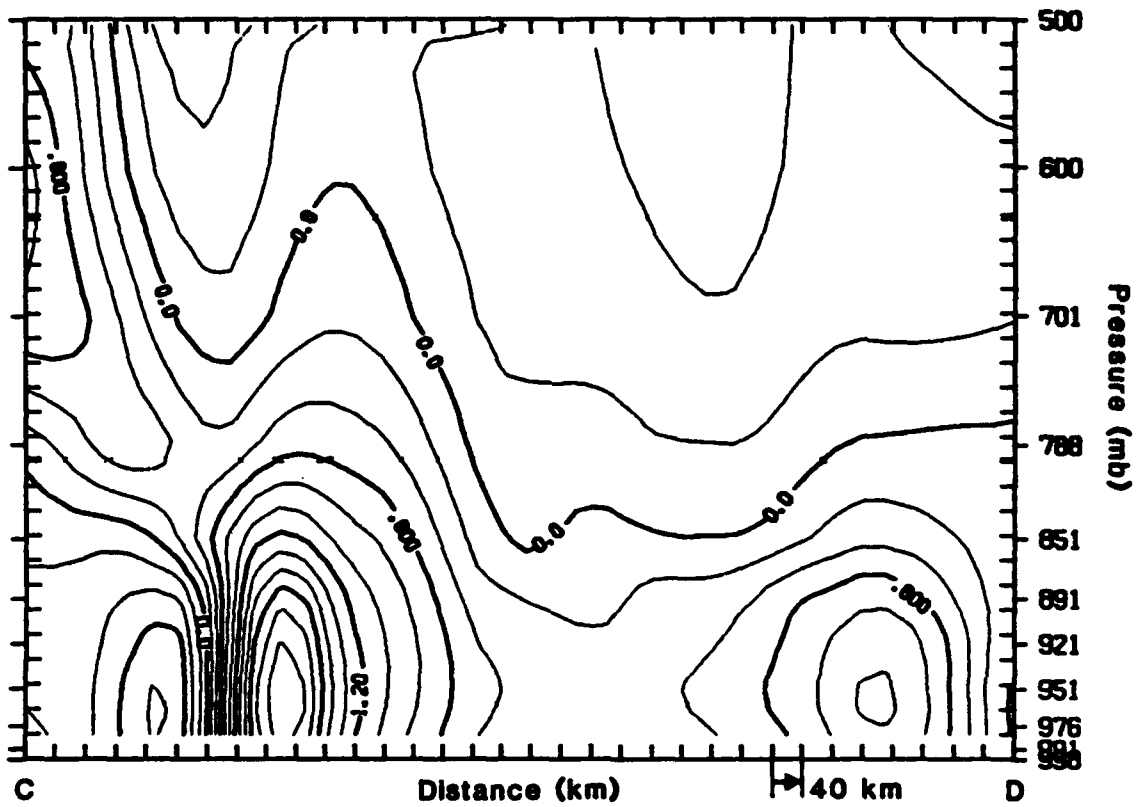


Figure 5.55: Cross section of vorticity ( $\times 10^{-4} \text{ s}^{-1}$ ) at hour 96 (20C).

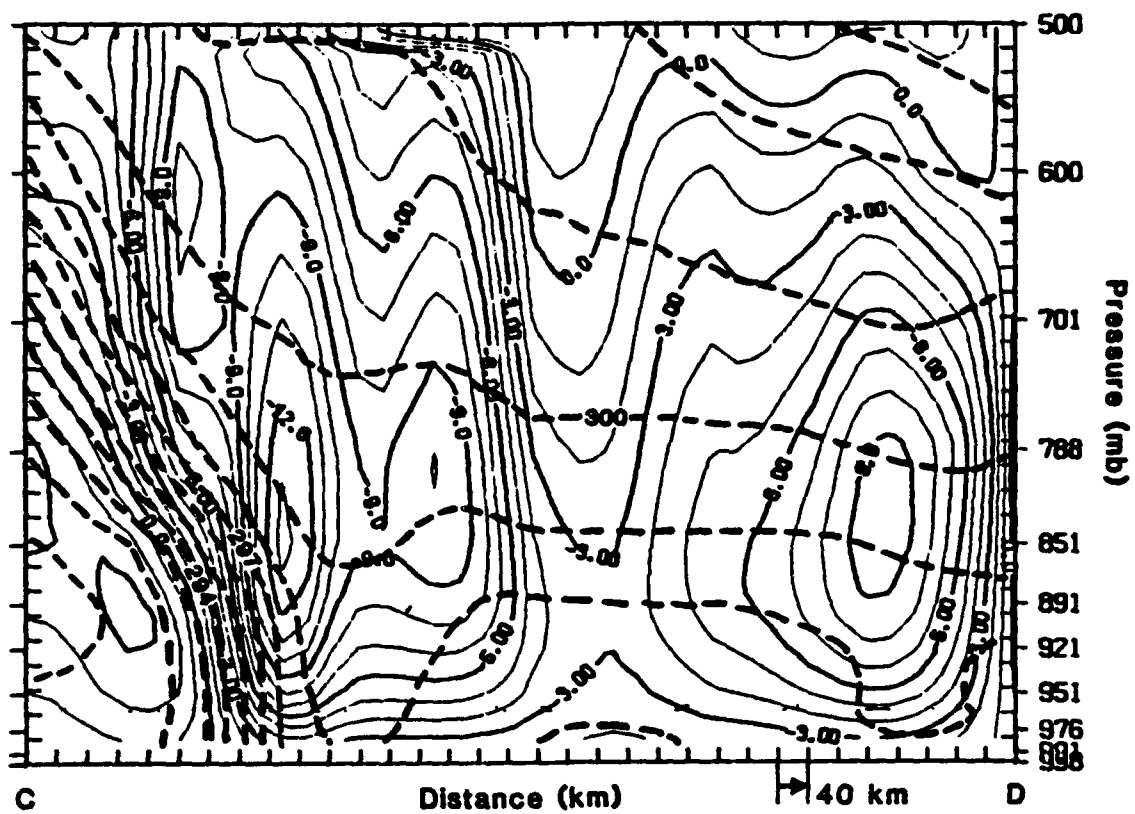
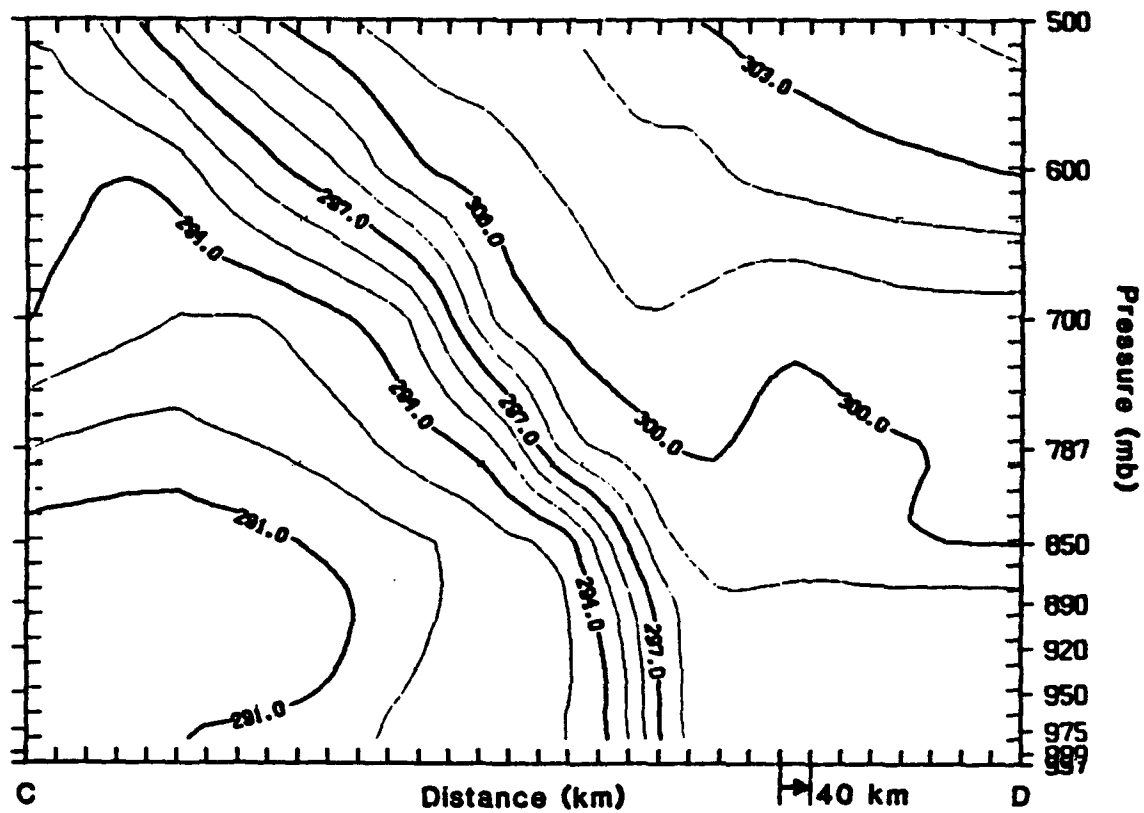
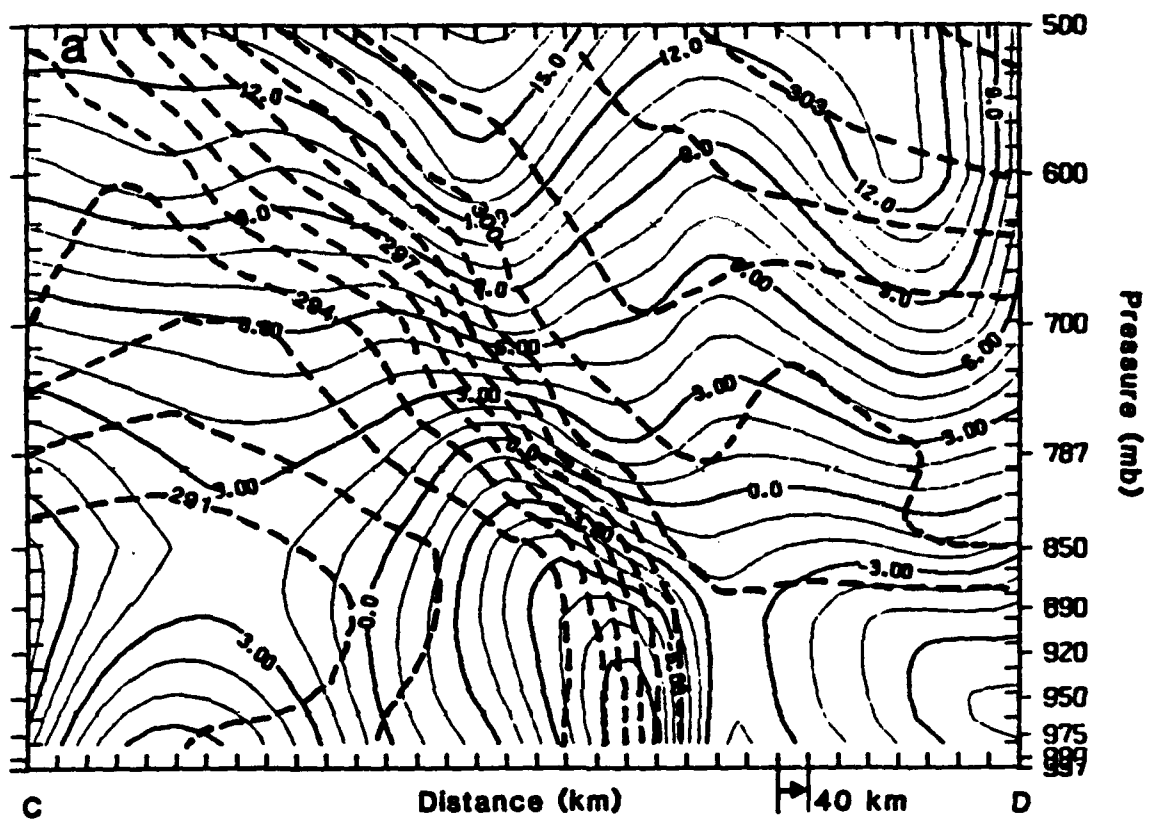


Figure 5.56: Cross section of vertical motion ( $\mu \text{ b s}^{-1}$ ) at hour 96 (20C).



**Figure 5.57:** Cross section of potential temperature (K) at hour 108. The plane of the cross section is shown in Fig. 50 (20C).



**Figure 5.58:** a) cross section of along-front wind component and b) front-normal wind component ( $\text{m s}^{-1}$ ) at hour 108.

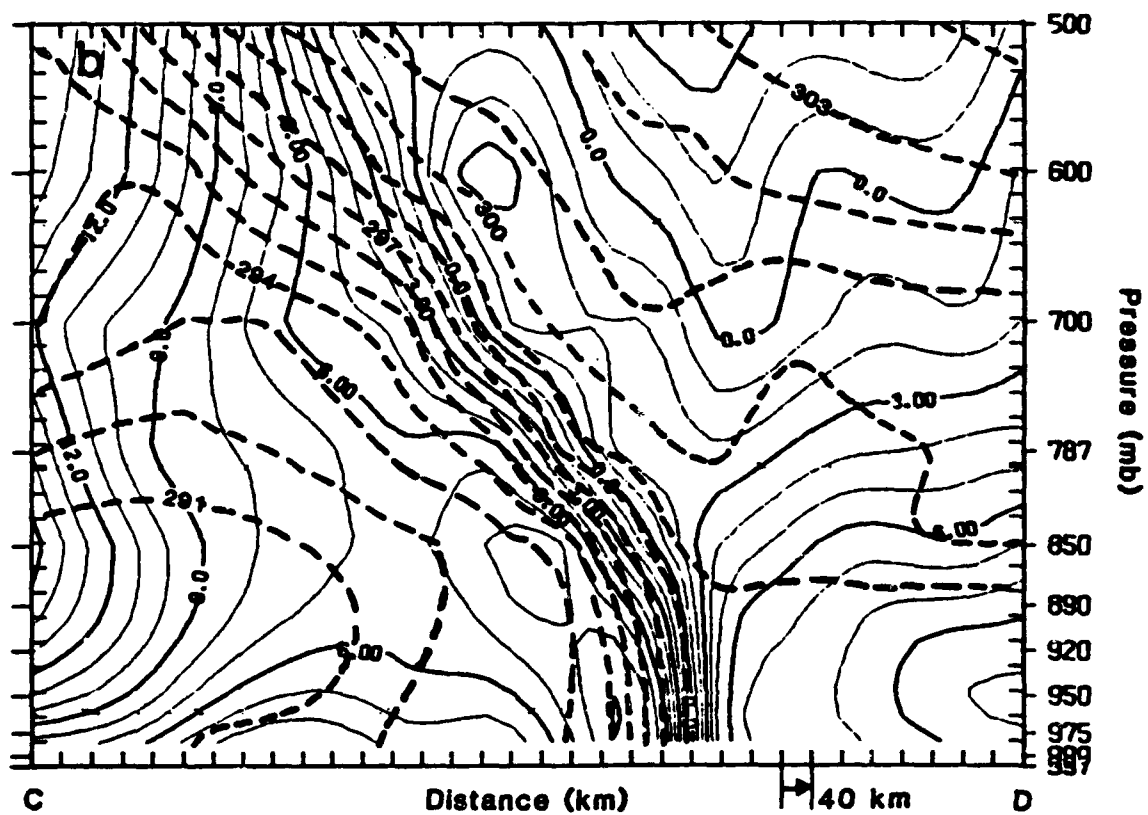
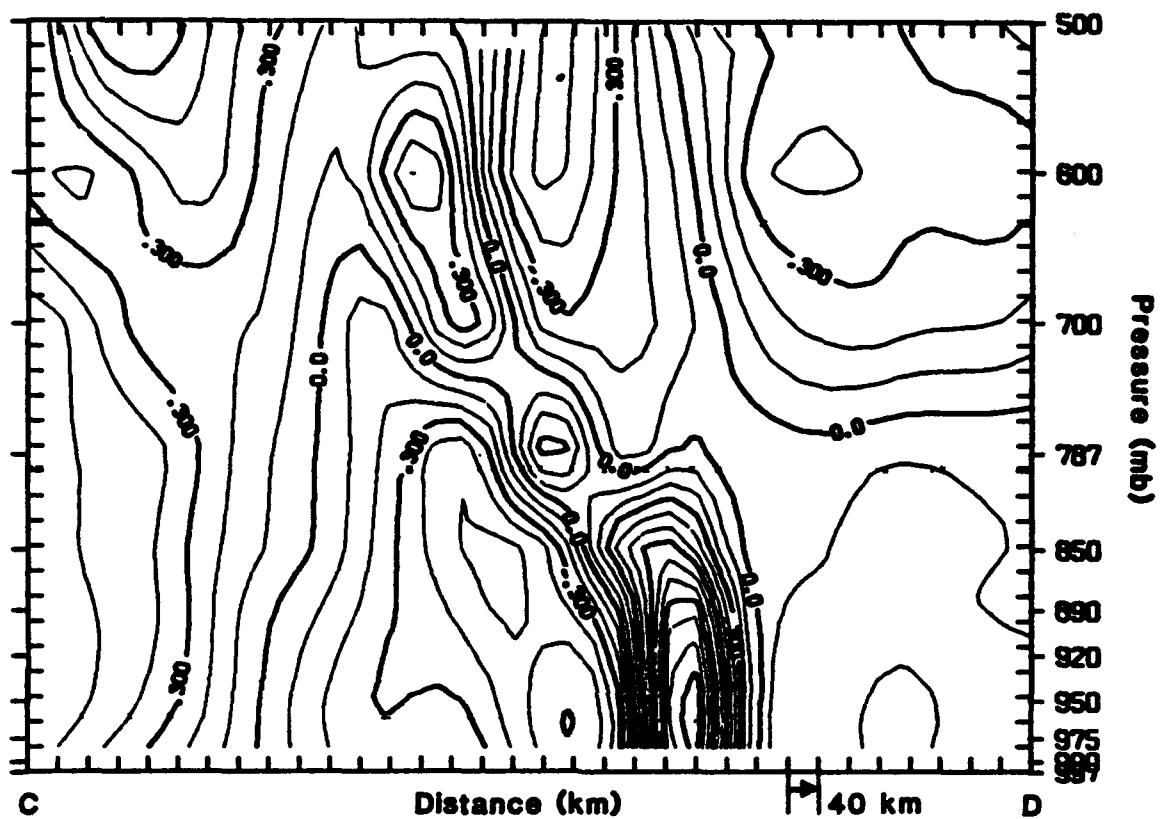
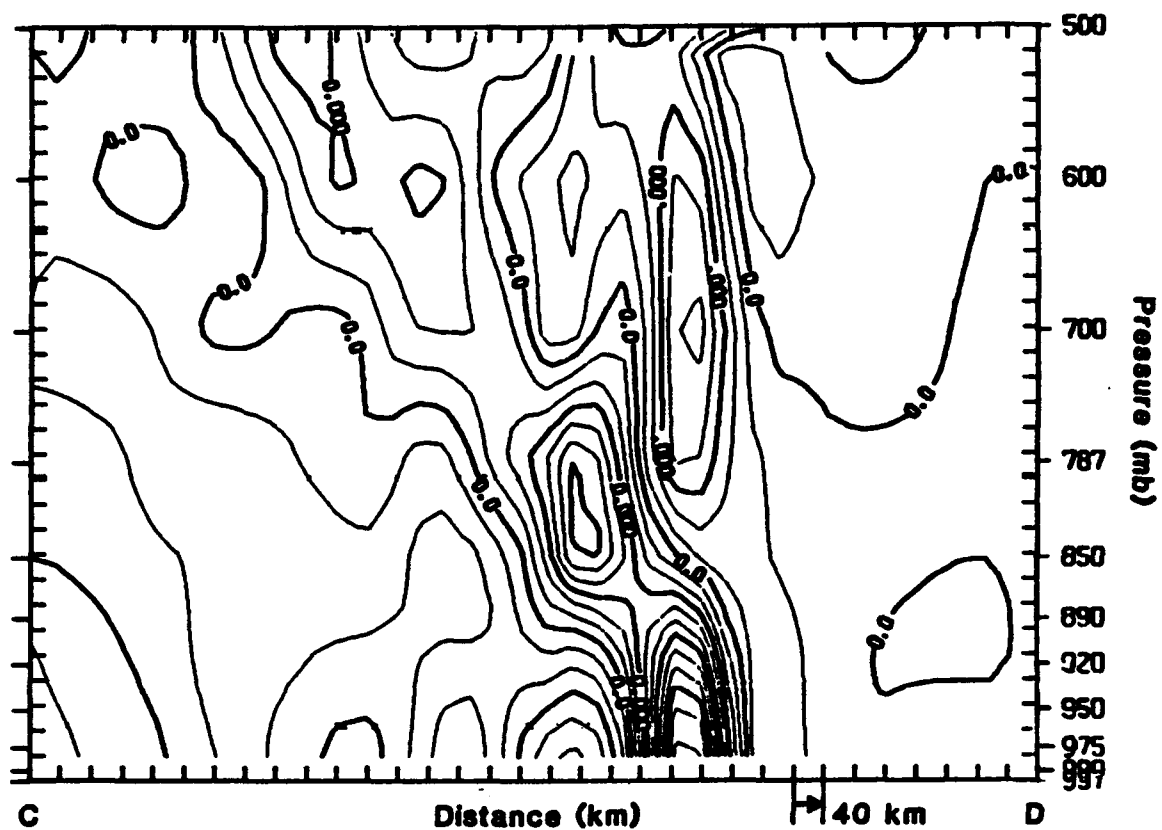


Figure 5.58: Continued.



**Figure 5.59:** Cross section of vorticity ( $\times 10^{-4} \text{ s}^{-1}$ ) at hour 108. The plane of the cross section is shown in Fig. 51 (20C).



**Figure 5.60:** Cross section of divergence ( $\times 10^{-4} \text{ s}^{-1}$ ) at hour 108 (20C).

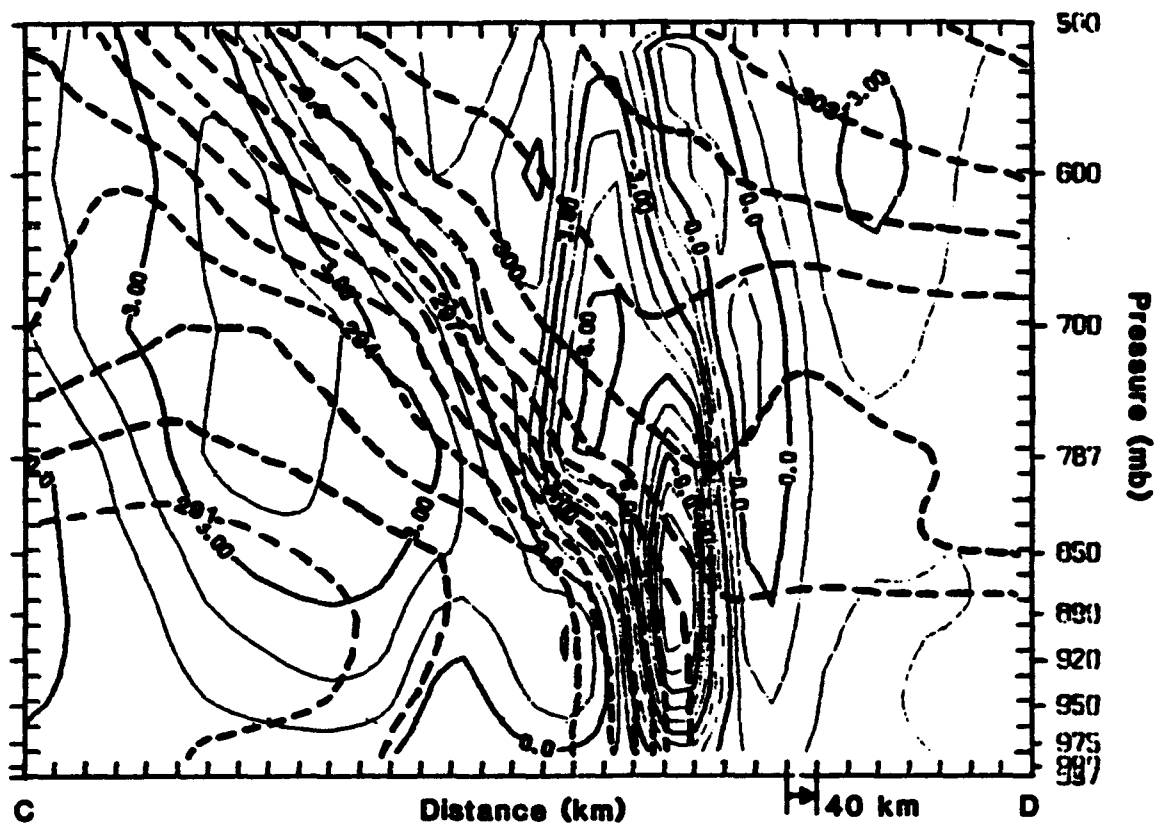


Figure 5.61: Cross section of vertical motion ( $\mu \text{ b s}^{-1}$ ) at hour 108 (20C).



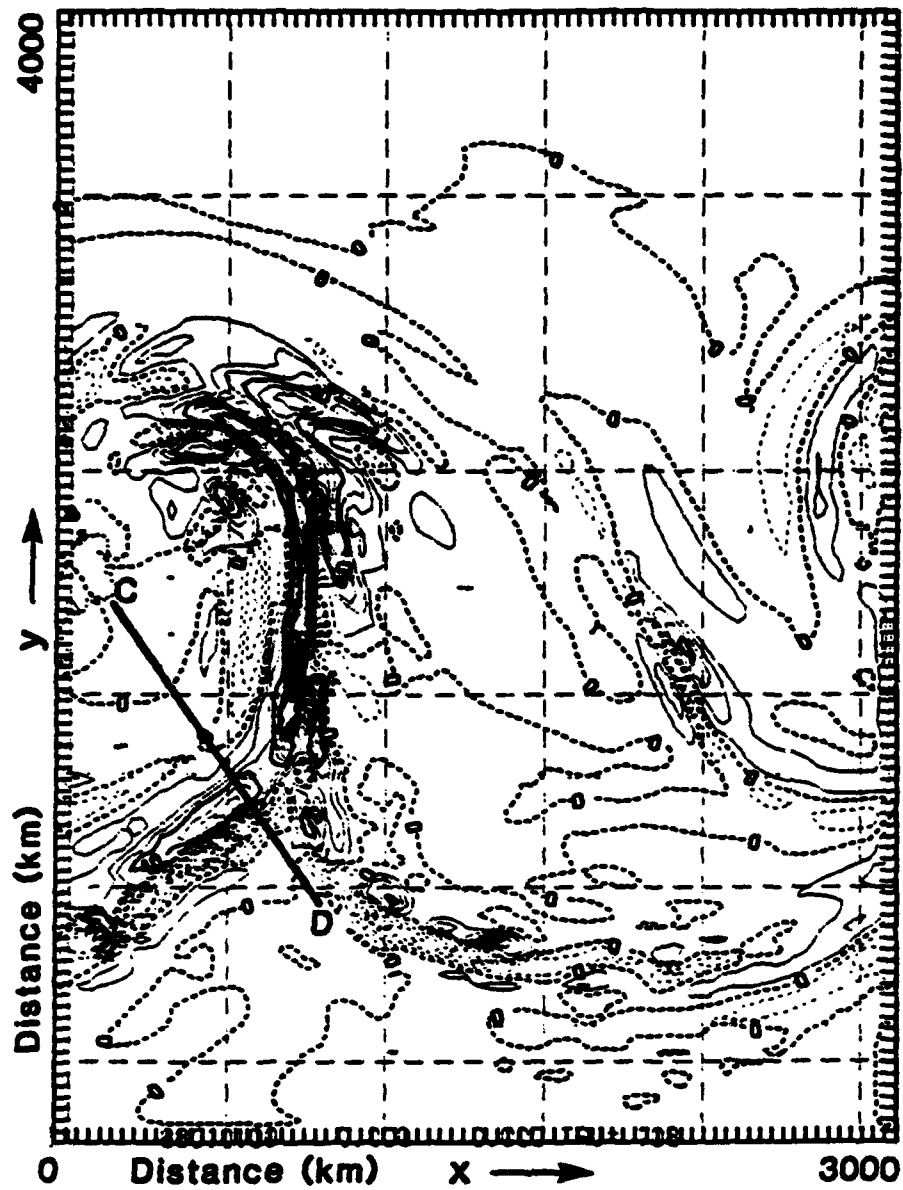
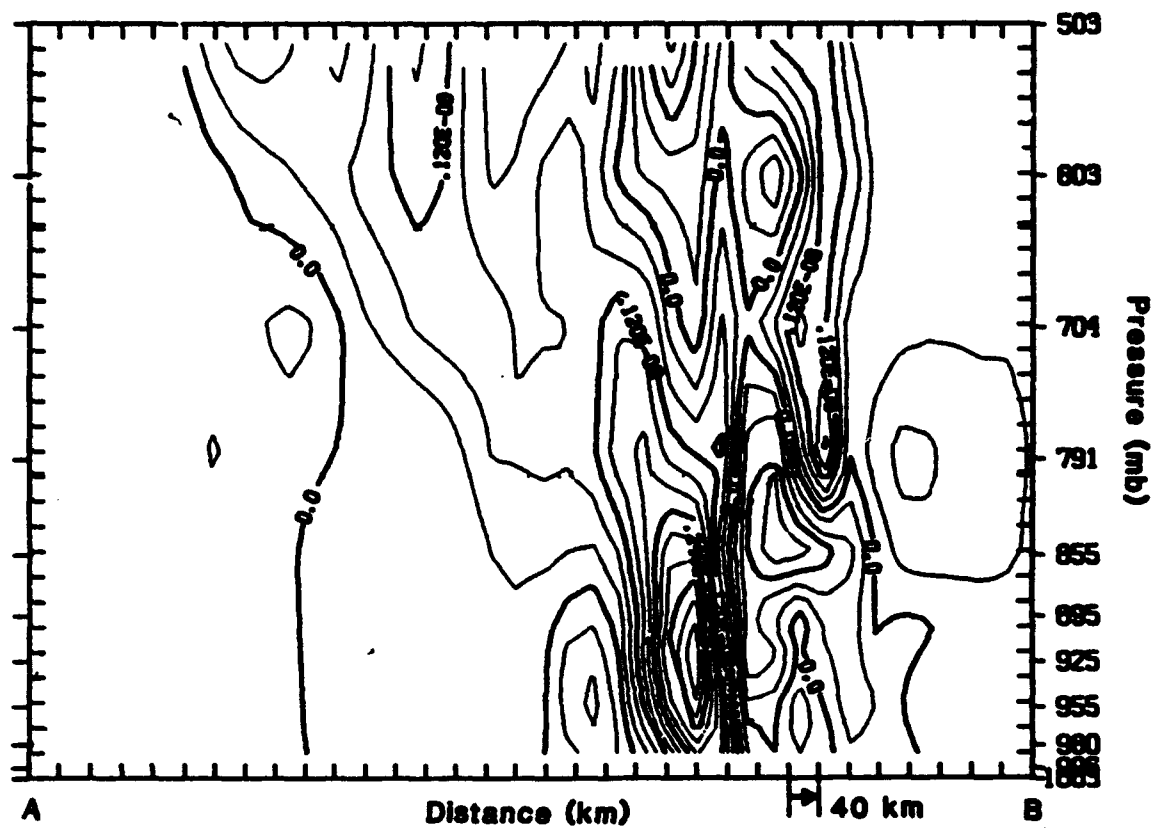


Figure 5.62: Total adiabatic frontogenetic forcing ( $\times 10^{-10} \text{ K m}^{-1} \text{ s}^{-1}$ ) at hour 108 at 850 mb (20C).



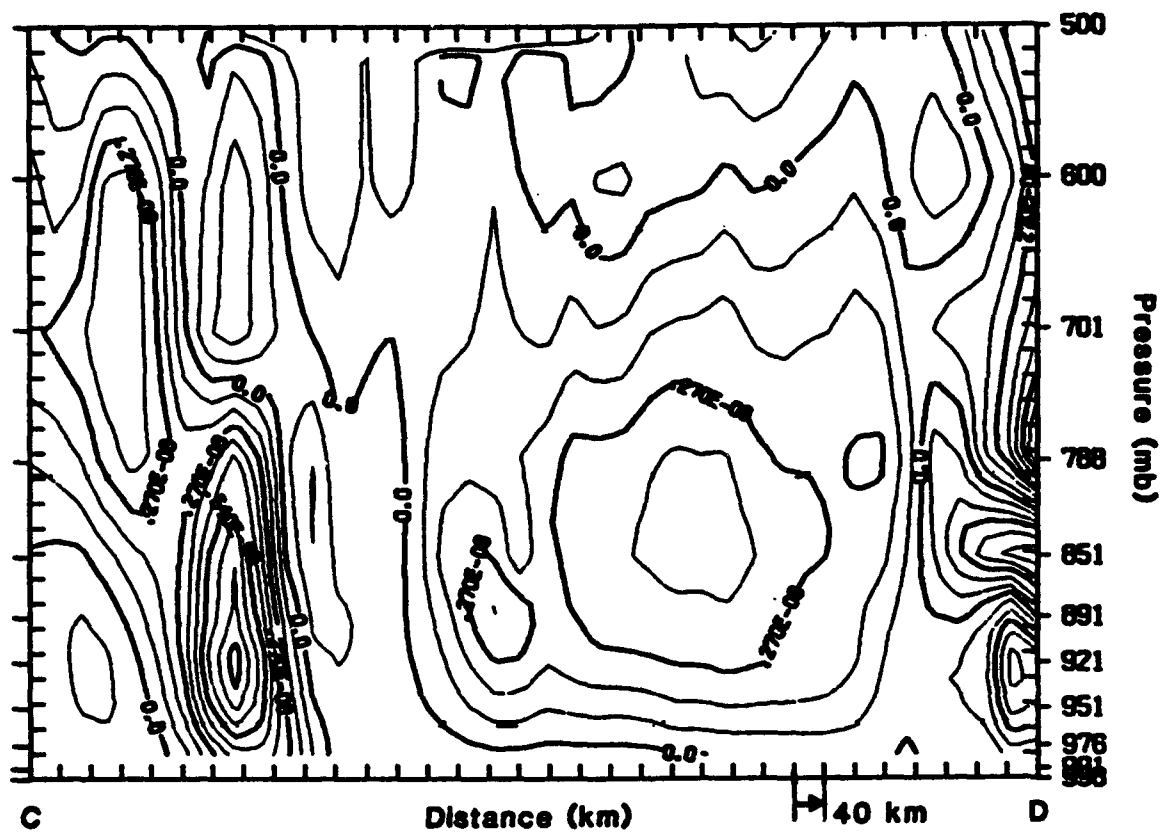
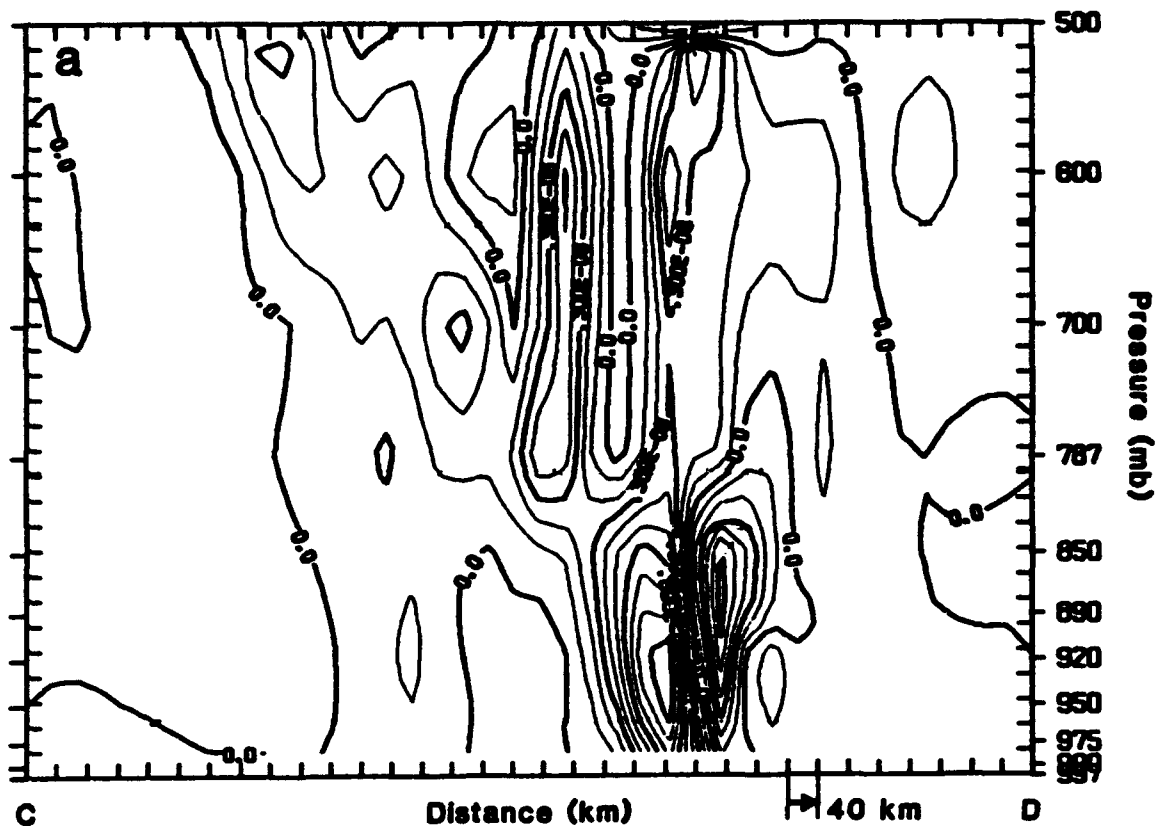


Figure 5.64: Cross section of total adiabatic frontogenetic forcing at hour 96 ( $\times 10^{-10} \text{ K m}^{-1} \text{ s}^{-1}$ ) (20C).



**Figure 5.65:** a) cross section of total adiabatic frontogenetic forcing ( $\times 10^{-10} \text{ K m}^{-1} \text{ s}^{-1}$ ) and b) tilting frontogenesis at hour 108. The plane of the cross section is shown in Fig. 62 (20C).



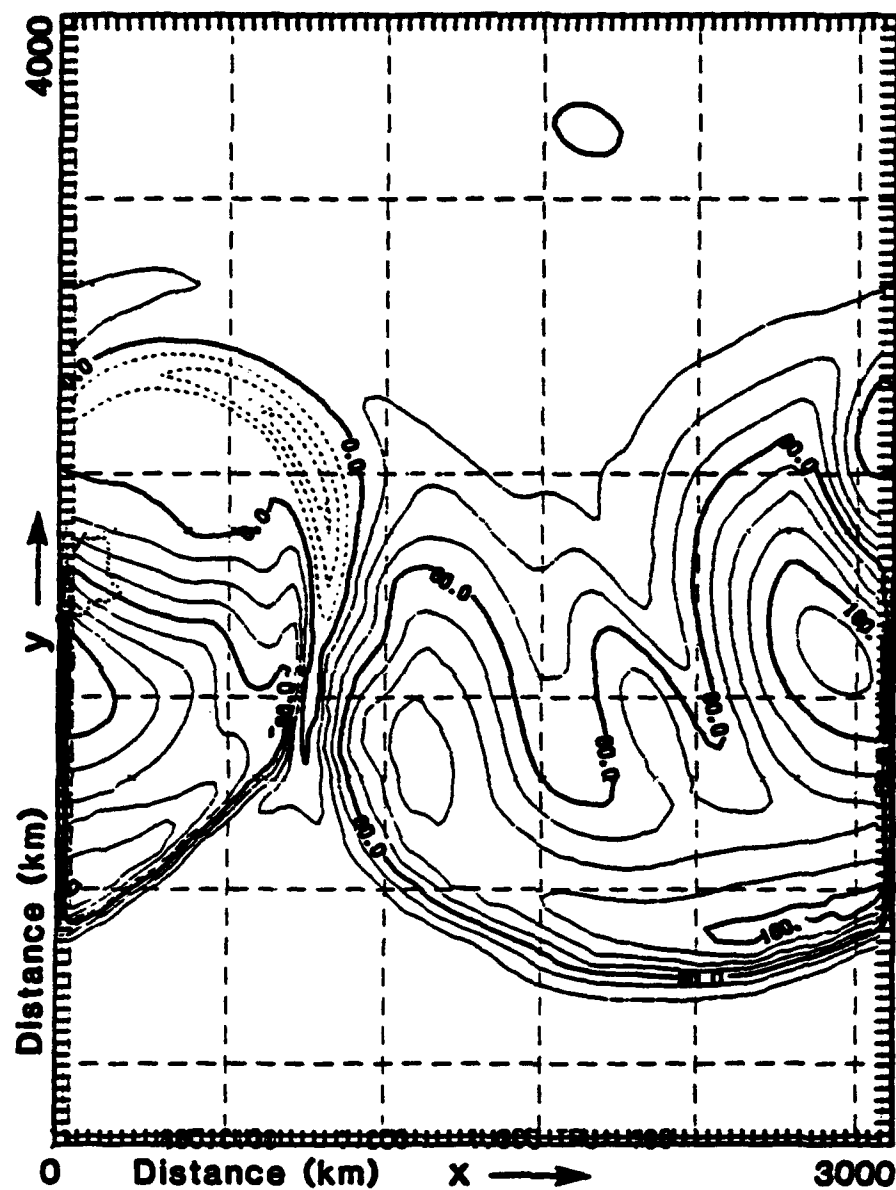


Figure 5.66: Surface sensible heat flux ( $\text{W m}^{-2}$ ) at hour 108 (20C).

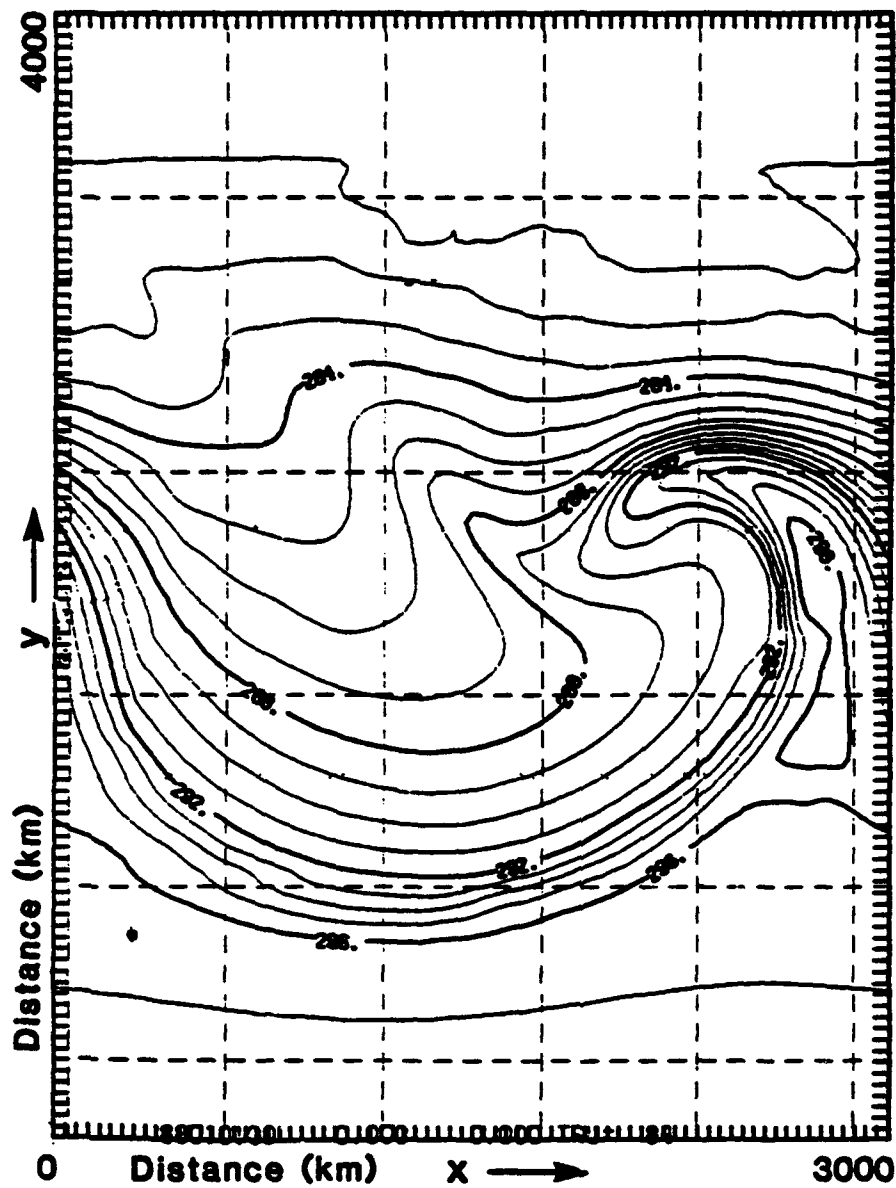


Figure 5.67: Near-surface potential temperature (K) field at hour 84 (20C no flux).

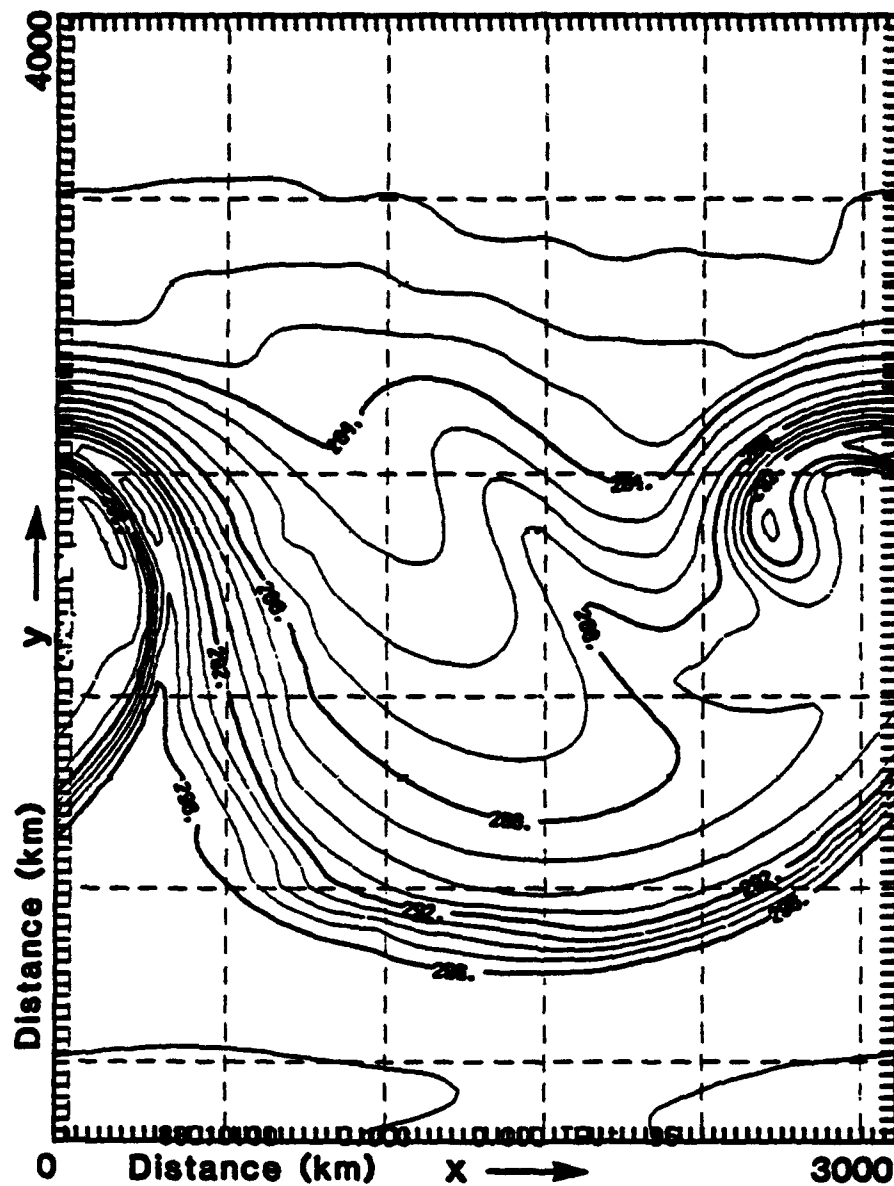
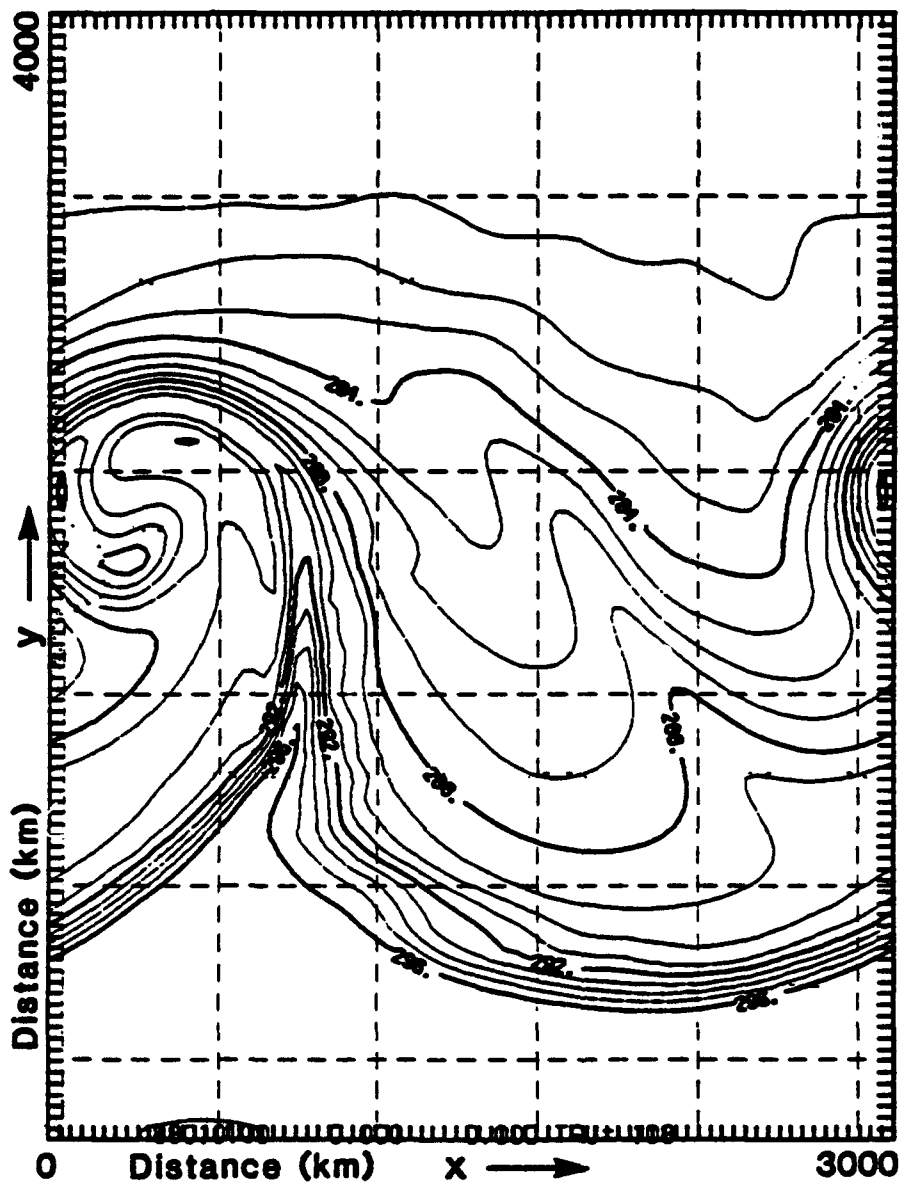


Figure 5.68: Near-surface potential temperature (K) field at hour 96 (20C no flux).





**Figure 5.69:** Near-surface potential temperature (K) field at hour 108 (20C no flux).

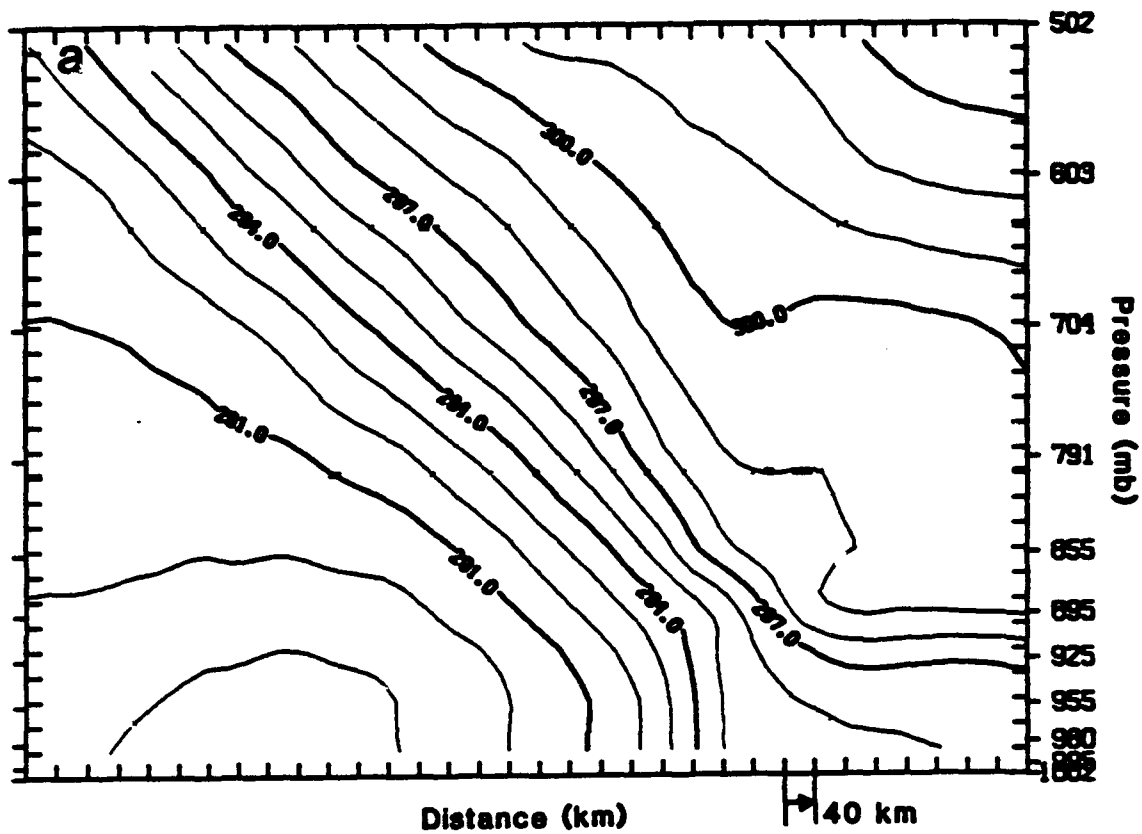


Figure 5.70: a) cross section of potential temperature (K) at hour 84 (the plane of the cross section is shown in Fig. 5.48), b) at hour 96 (see Fig. 5.49), and c) at hour 108 (see Fig. 5.50) (2OC no flux).

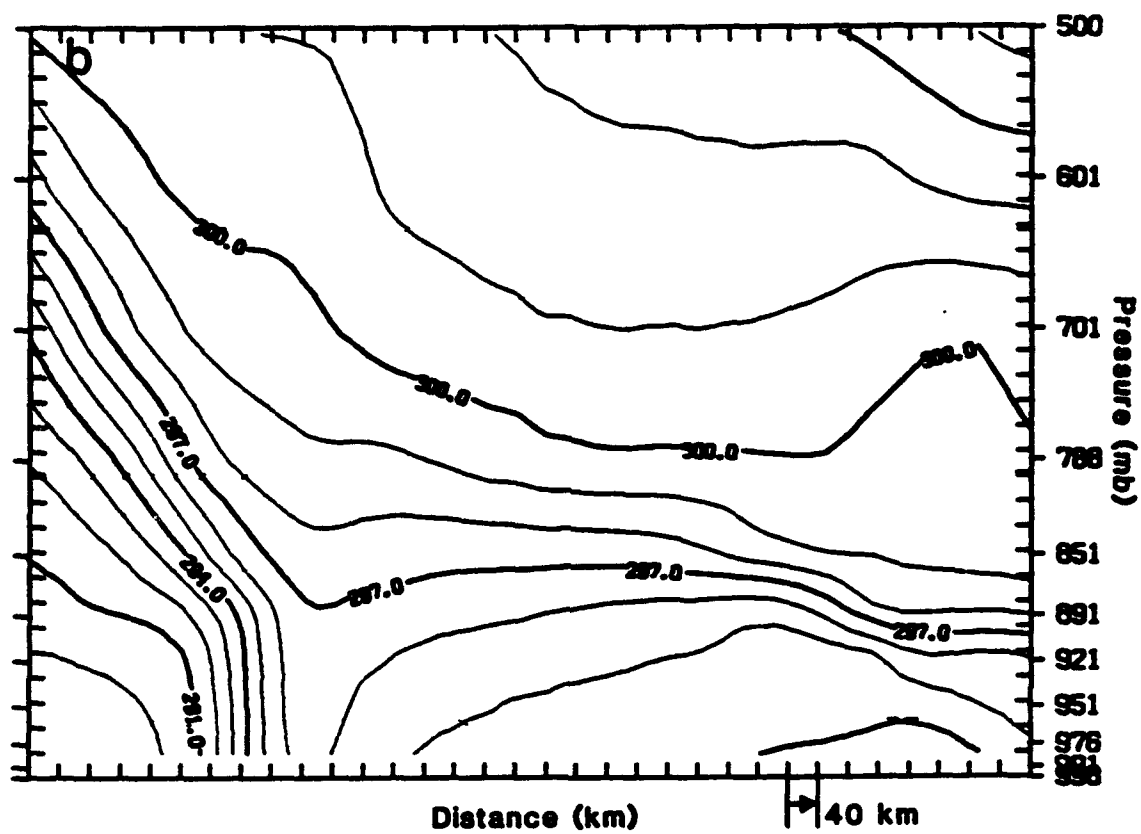


Figure 5.70: Continued.

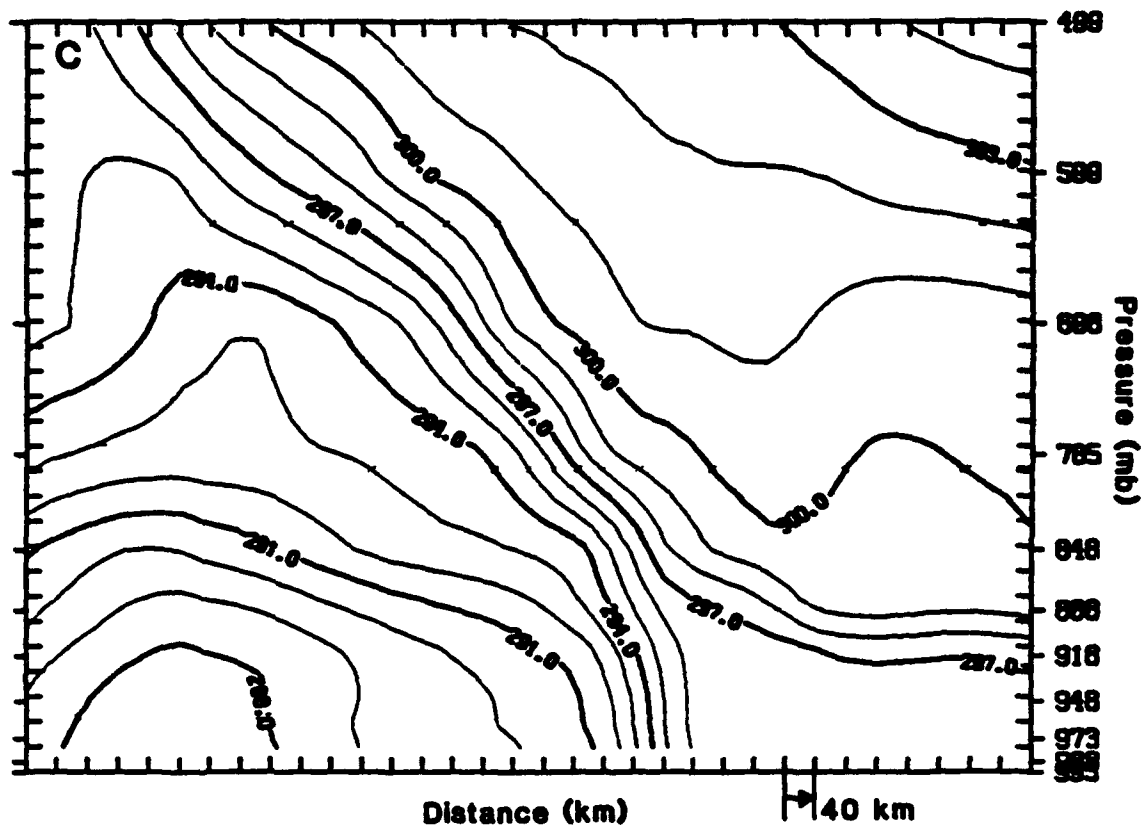
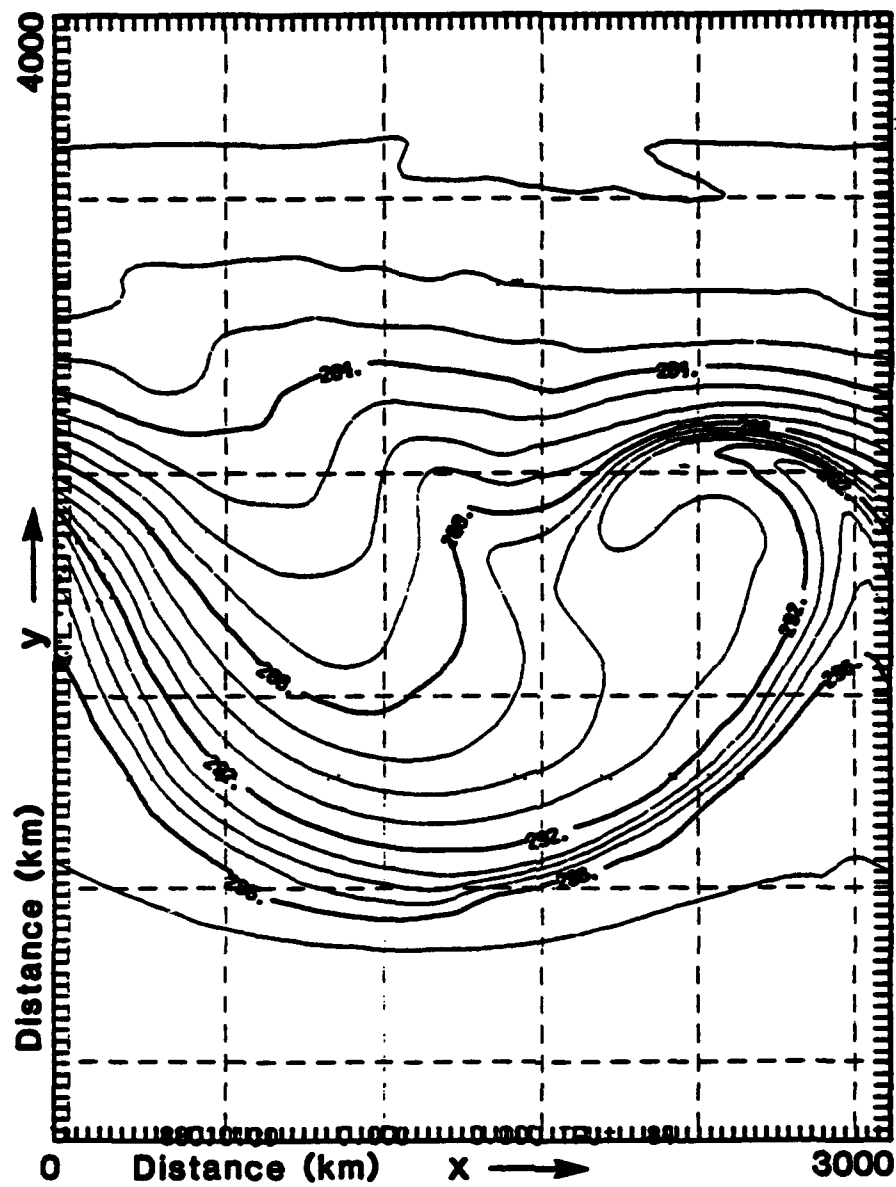


Figure 5.70: Continued.



**Figure 5.71:** Near-surface potential temperature (K) field at hour 84 (20C no drag).

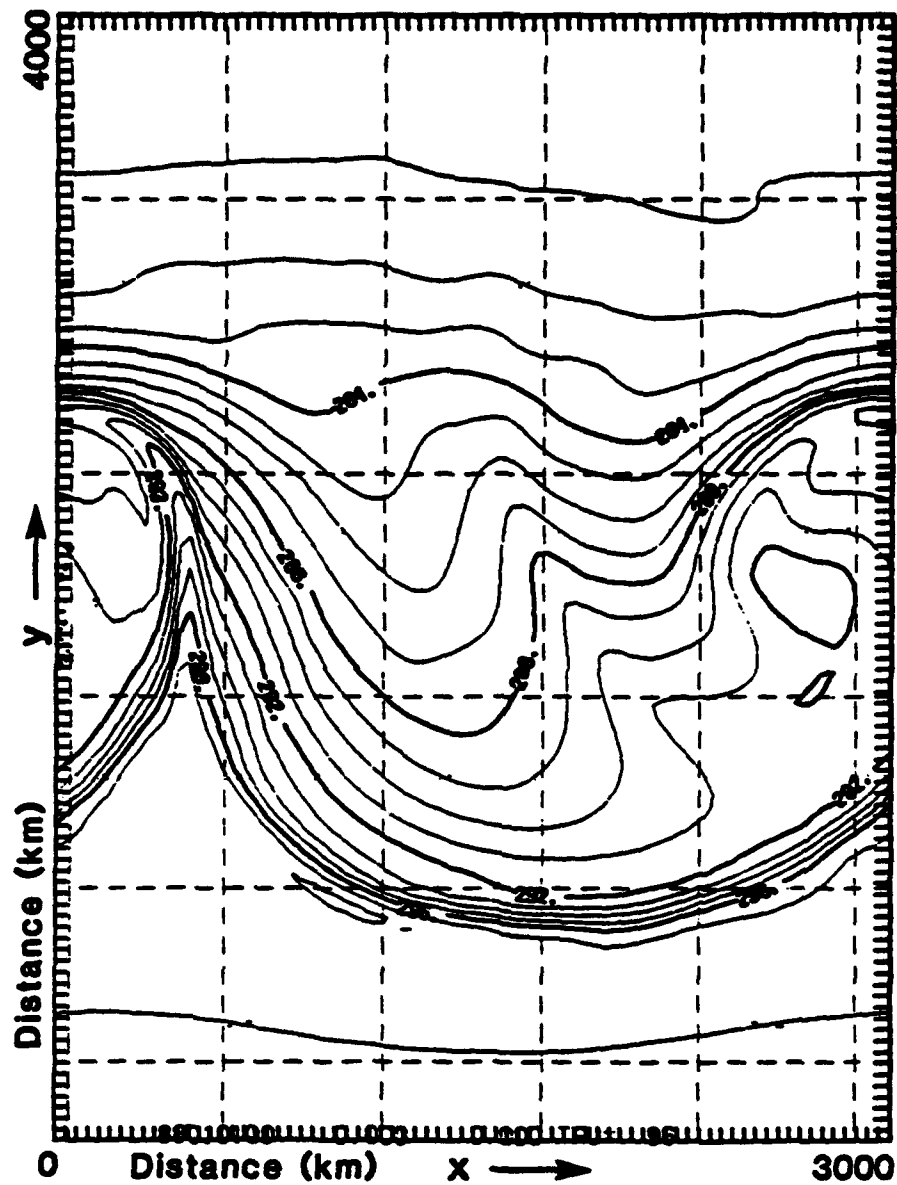
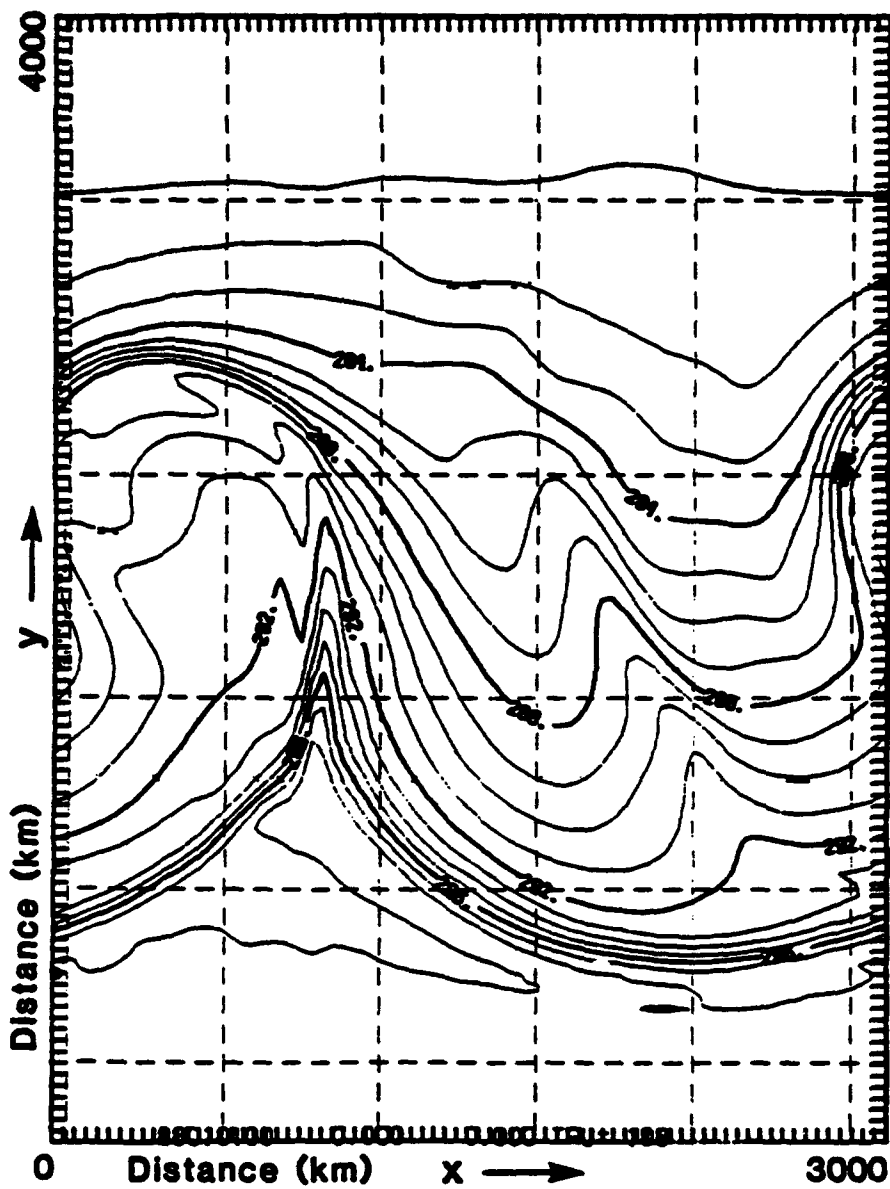


Figure 5.72: Near-surface potential temperature (K) field at hour 96 (20C no drag).



**Figure 5.73:** Near-surface potential temperature (K) field at hour 108 (20C no drag).







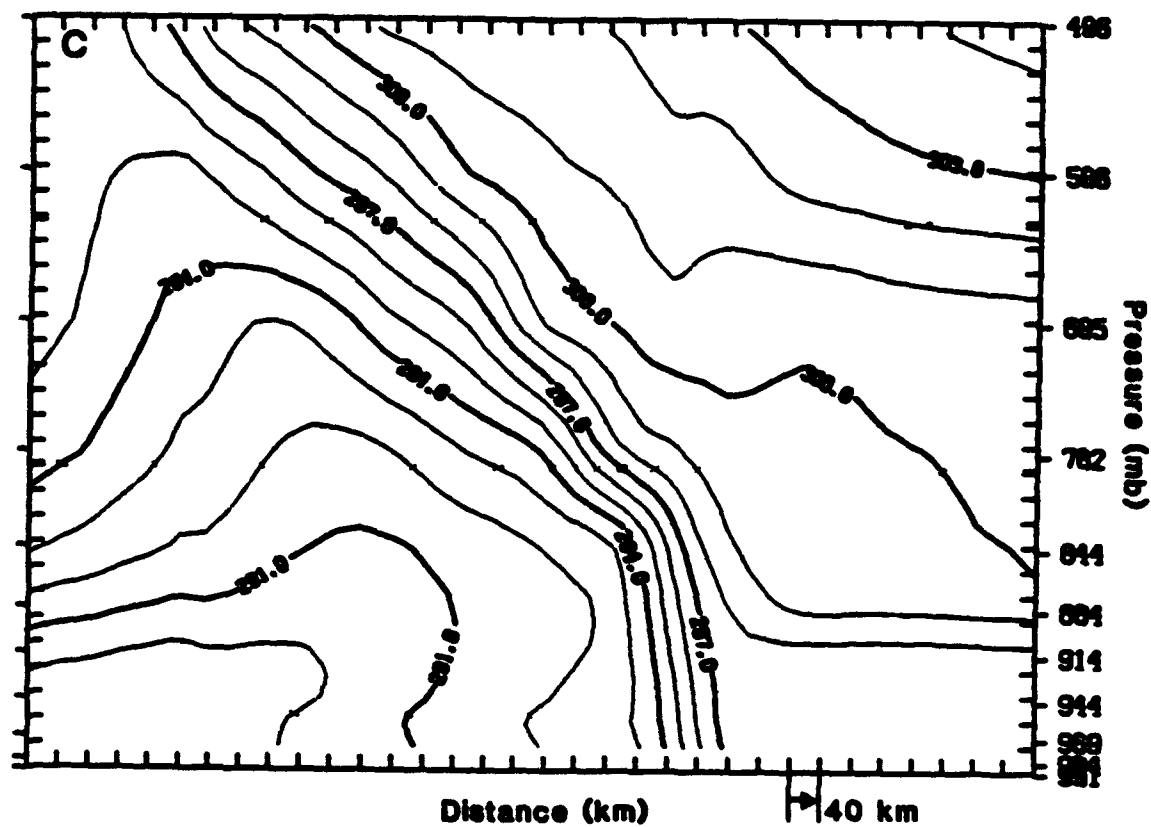
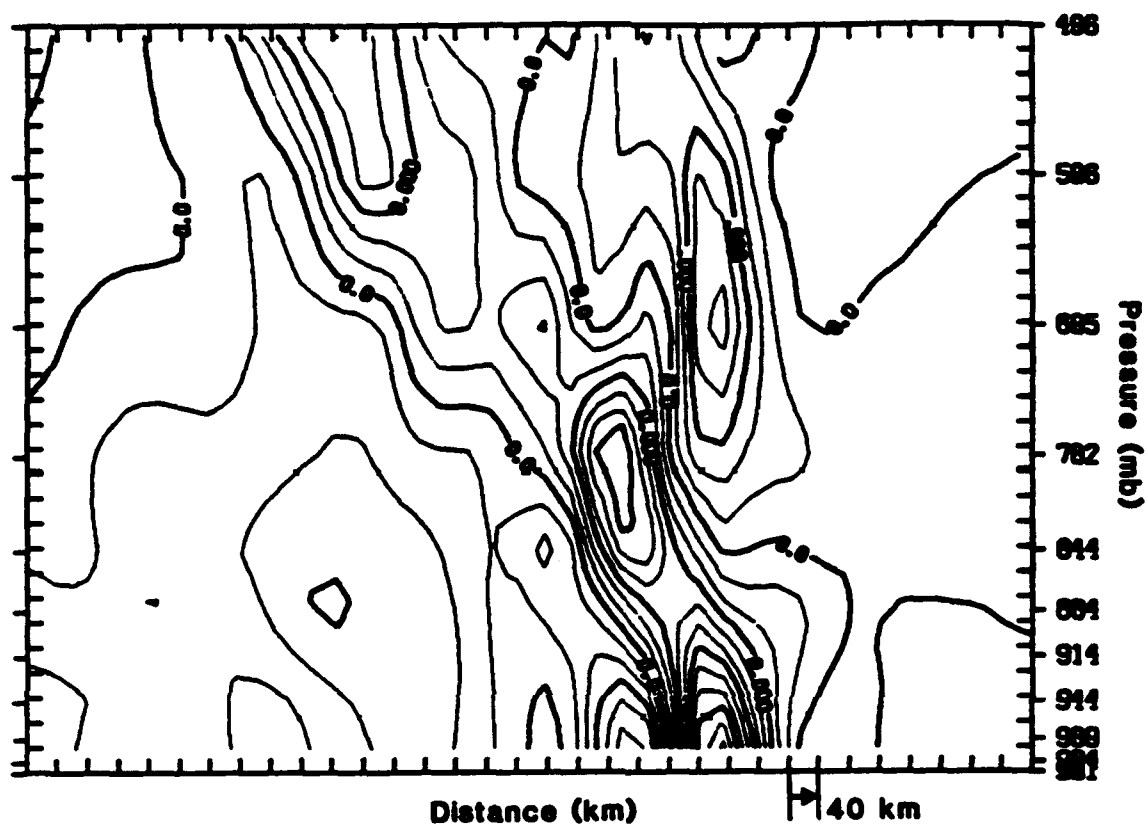


Figure 5.74: Continued.



**Figure 5.75:** Cross section of divergence ( $\times 10^{-4} \text{ s}^{-1}$ ) at hour 108 (2OC no drag).

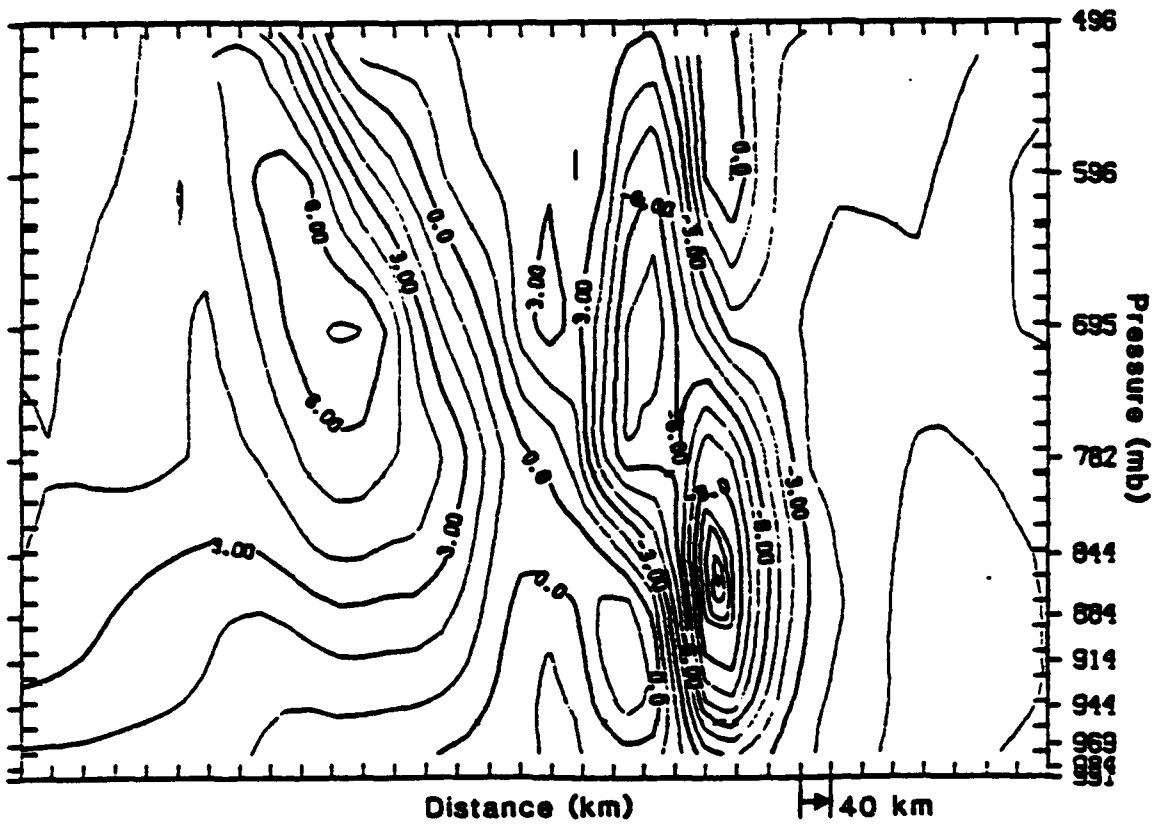
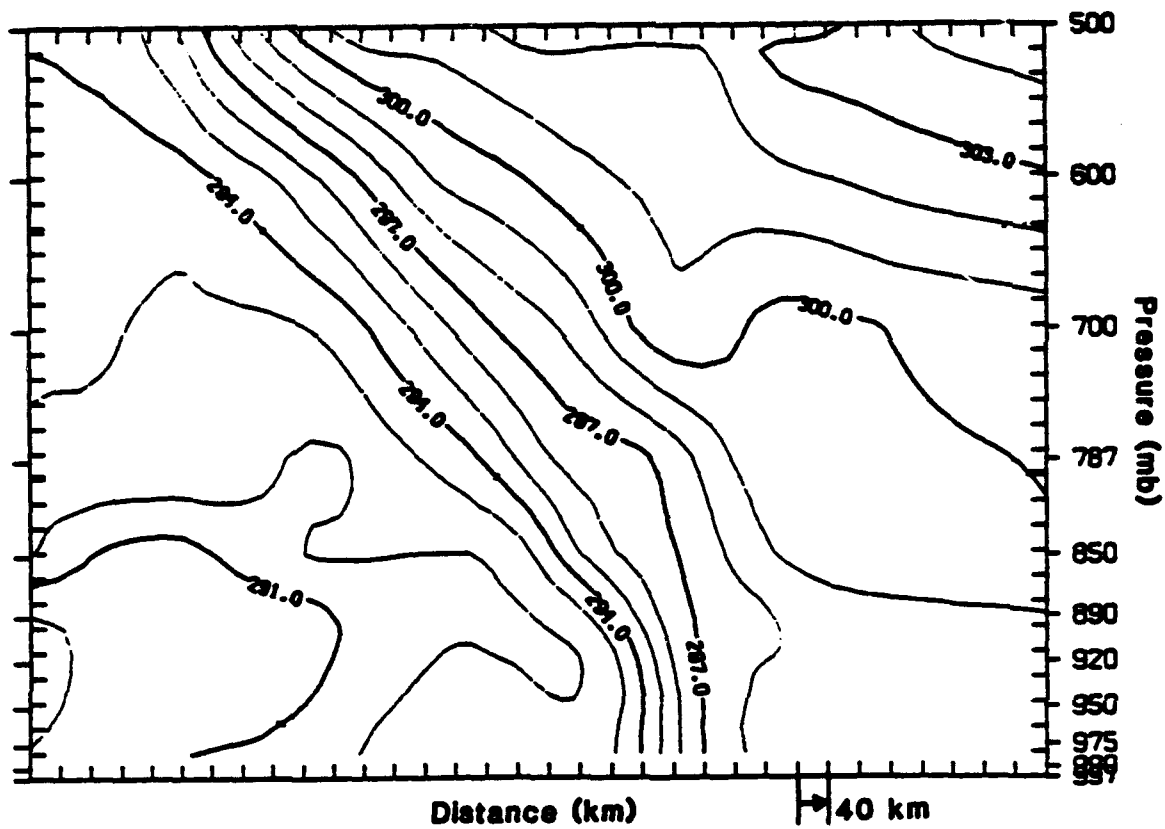
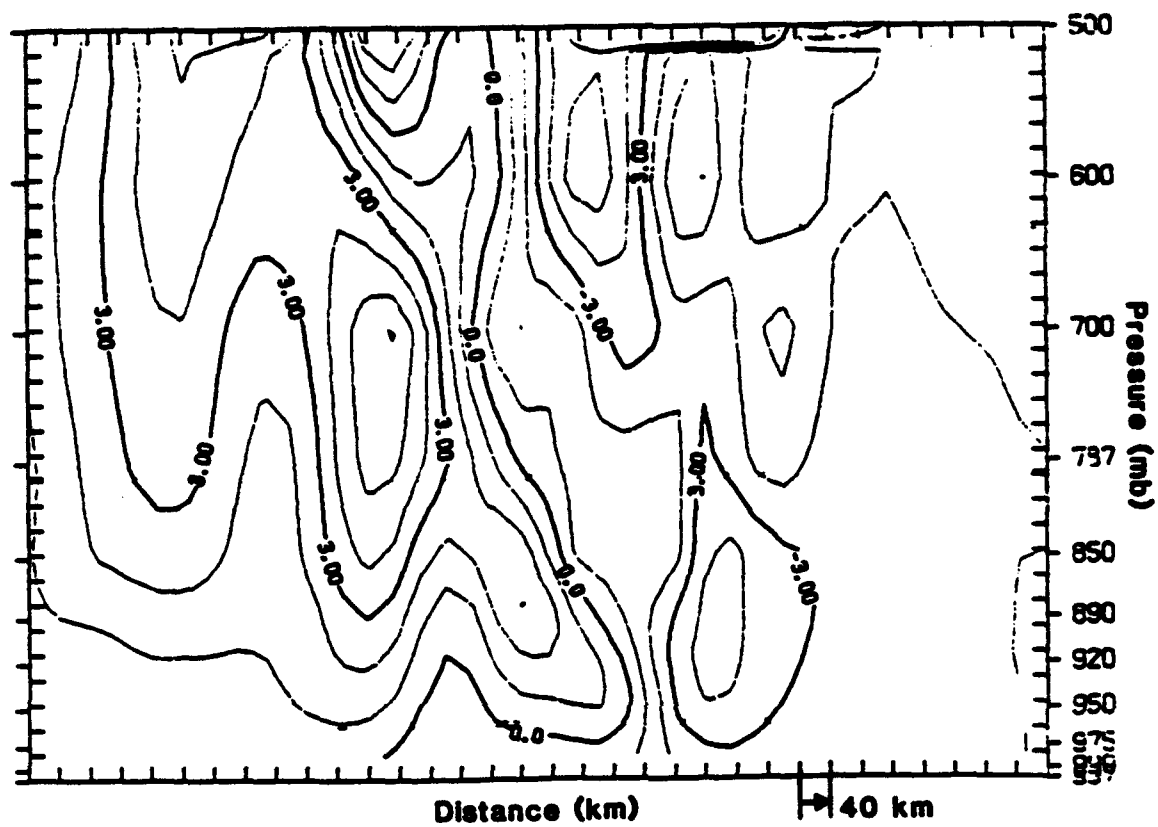


Figure 5.76: Cross section of vertical motion ( $\mu \text{ b s}^{-1}$ ) at hour 108 (2OC no drag).



**Figure 5.77:** Cross section of potential temperature at hour 108 (2OCL2).



**Figure 5.78:** Cross section of vertical motion ( $\mu \text{ b s}^{-1}$ ) at hour 108 (2OCL2).

## APPENDIX

### T-BONE STRUCTURE

In a recent paper, Shapiro and Keyser (1990) (hereinafter SK) present a "conceptual visualization of cyclone-frontal evolution" which is remarkable in that it represents one of the few substantive alteration of the Norwegian frontal cyclone model in 70 years. This model was originally presented by Bjerknes (1919) and Bjerknes and Solberg (1921 1922). The model, which enjoyed initial wide acceptance, was further supported by observational studies (Bjerknes and Palmen, 1937; Sanders, 1955). In the mid 1960's, the first weather satellites presented eloquent testimony to the veracity of the Norwegian model. According to Reed (1990), numerous examples can be found (in early satellite imagery) in which the cloud patterns conform at each stage to the classical (Norwegian) scheme. Nevertheless, as Shapiro and Keyser note, recent observational and numerical studies of cyclogenesis and frontogenesis display certain features not accounted for in this model.

The fundamental departure from the Norwegian model occurs in the second stage of frontal evolution. In stage 2 of the Norwegian model, the temperature wave has attained sufficient amplitude that the warm and cold fronts are discernible and the cloud shield begins to develop (Fig. A.1). In stage 2 of the SK model, as the temperature wave attains similar amplitude, "frontal fracture" occurs in which the warm and cold fronts separate and the warm front extends to the west into the northerly flow west of the cyclone center (Fig. A.2). In subsequent stages in the Norwegian model, the fronts remain connected and an occlusion forms in the final stage. In the SK model, the warm front continues to wrap around the cyclone and a warm seclusion forms in the final stage. The absence of the occluded stage in the

SK model is a major departure from the Norwegian model. Of equal importance, however, is the presence of the westward extension of the warm front (WEWF), which is not a feature of the Norwegian model at all. In many cases, the baroclinic zone associated with the WEWF is even stronger than that associated with the cold front. Both the absence of the occlusion and the presence of the WEWF are directly attributable to the frontal fracture occurring in stage 2. The authors emphasize that *the essence of the frontal evolution in their model was realistically simulated using adiabatic numerical models*. While boundary layer processes modify the time scales and intensity of baroclinic waves, the basic structural evolution is driven by the adiabatic components.

The authors offer no explanation for the strength of the WEWF or for the frontal fracture, which is manifested as a loss of baroclinicity in the cold front near the cyclone center. The strength of the WEWF may be due to the shearing deformation; while cyclonic shear is frontolytic for warm fronts, it is frontogenetic for cold fronts and for the WEWF due to the sense of the along front temperature gradient. The loss in baroclinicity near the cyclone center can be explained using the results of Keyser et al. (1988). In this analytical study, an E-W band of isentropes is superimposed on an axisymmetric vortex. As this pattern evolves, strong frontogenesis occurs in the NE and SW quadrants, however, while the isentropes near the center of the vortex undergo rotation, the potential temperature gradient remains unaltered. This can be explained in terms of the angles between the axes of dilatation and the potential temperature gradient. The authors include an analysis of the vector frontogenetic forcing which reveals that the maximum magnitude is in the NE and SW quadrants while the rotational component has a relative maximum near the center of circulation.



The results of the adiabatic and inviscid simulation in the present study are not entirely consistent with the SK model. While the frontal fracture, seclusion, and WEOF are present, there are also strong indications that an occlusion has formed. Frontal fracture occurs at hour 72. The results of the adiabatic and inviscid simulation show that the WEOF weakens from hour 84 (Fig. A.3) to hour 120 (Fig. A.4). The WEOF undergoes strong frontogenesis from hour 72 to hour 84. At this early stage, strong convergence leads to frontogenesis. It is not clear presently why the WEOF weakens after hour 84. Further investigation will be required to clarify this point. The warm frontal seclusion also is displayed in Fig. A.4. This figure is similar to Fig. 10.19 of SK. An alternative depiction of the seclusion and WEOF is given in Fig. A.5, which shows the near-surface potential temperature distribution at 120 h. Note the strength of the northern section of the WEOF, which is comparable to that of the cold front at this time.

Evidence for the existence of an occlusion can be seen in cross sections of potential temperature from three planes at different latitudes for hour 108 (not shown). The warm air is seen to rise to the north from one plane to another. The warm air can be delineated by the location of the 288 K isentrope. In the southernmost cross section, the 288 K isentrope intersects the surface at two locations 400 km apart. In the intermediate cross section 400 km to the north, the intersections are 200 km apart and, in the northernmost cross section 400 km further north, there is only one intersection.

It is curious that the simulation produces both a seclusion and an occlusion. This suggests that the absence of an occlusion in the SK model constitutes a flaw. Close examination of the results suggests that the seclusion forms in the early stages of cyclogenesis between hour 72 and hour 96. During this time, warm air flows northward into the center of the low. The near surface potential temperature is

above 290 K at hour 84 in the center of the low. Near hour 96, the frontal fracture appears to "heal" and the warm and cold fronts re-unite in the southeast quadrant of the low. At this point, the flow of warm air into the center of the low is halted as the warm air begins to move aloft in the manner of the classical occlusion process. The results indicate that the potential temperature in the center of the low never exceeds 290 K and the area enclosed by the 290 K isentrope grows smaller with time as the occlusion grows larger.

It thus appears that the fourth and final stage of the SK model is actually an intermediate stage. The simulation strongly suggests that, in the final stage, the warm and cold fronts re-unite, sealing the seclusion and forming an occlusion.

Published work by Shapiro and his co-workers subsequent to SK (e.g., Neiman and Shapiro, 1992; Keyser, 1993, personal communication) have discussed the presence of occlusions at various stages of cyclogenesis. This suggests that the model as presented by SK has perhaps been amended to some extent to include the possibility of an occlusion in later stages.

The results of the second-order closure simulation are, not surprisingly, quite different from those for the adiabatic and inviscid simulation. The inclusion of boundary layer physics has a profound effect on the simulation. Figure A.6 shows a cross section of potential temperature at hour 84. While the warm front, cold front, and WEOF are clearly present, they are much weaker in the present simulation. There is no indication of a seclusion near the surface. Shown in Fig. A.7 is a north-south cross-section of potential temperature at hour 108, corresponding to Fig. A.4 (although there is a 12 h time difference).

In this case, the seclusion is not as well-defined as in the AI case and does not extend to the surface. The southern side of the outward sloping baroclinic ring is not well-defined at hour 108, although there is a weak baroclinic zone extending

from approximately 850 mb to 600 mb delineated by the 291 and 294 K isentropes. At hour 84, the seclusion is most apparent at 850 mb. From hour 84 to hour 108, the seclusion extends upward and is most well-defined at 700 mb by hour 108 (see Fig. A.8). This is entirely consistent with the results of Neiman and Shapiro (1993). In their investigation of a cyclogenesis event during ERICA, Neiman and Shapiro found the first evidence of a seclusion at 850 mb. The WEOF and seclusion then developed upward, reaching 500 mb after 18-24 h. The relatively small scale of the seclusion is also consistent with Neiman and Shapiro.

Strong evidence for the existence of an occlusion in this case is provided by examination of cross sections at different latitudes (not shown). The warm air can be delineated by the position of the 296 K isentrope. In southernmost cross section, the 296 K isentrope intersects the surface at two locations approximately 280 km apart. At an intermediate location 400 km to the north, the intersections are 50 km apart and, in the northern cross section 400 km further north, the 296 K isentrope is nowhere lower than 750 mb.

SK present a modification to the classical Norwegian polar frontal cyclone which incorporates many of the features depicted in recent observational and numerical investigations of the life cycles of baroclinic waves and fronts. The fundamental differences between the SK model and the Norwegian model are the absence of an occlusion, the presence of a seclusion, and the westward extension of the warm front. Both the absence of an occlusion and the WEOF are attributable to the frontal fracture which occurs in the early phase of the amplification of the temperature wave. The authors claim that adiabatic numerical models capture the essence of frontal evolution in their model.

The results of the adiabatic and inviscid simulation are, to a large extent, consistent with the model proposed by SK. The frontal fracture, WEOF, and seclusion

are all present in the simulation. There is also, however, an occlusion in the results. The seclusion appears to form in the early stages of cyclogenesis, prior to the formation of the occlusion. As the occlusion begins to form, the flow of warm air into the center of the low is halted.

The results of the second-order closure simulation are quite different. The warm and cold fronts and the WEOF are all much weaker in this simulation. There is no indication of a seclusion at the surface. A north-south cross section through the WEOF, however, shows some indication of a weak elevated seclusion. This simulation also produces a well-defined occlusion.

In conclusion, the results suggest that introduction of concepts of the frontal fracture and WEOF in the SK model constitute an important contribution to the understanding of the life cycle of baroclinic waves and fronts. The shortcoming of the model is that it fails to account for the last stage of the life cycle in which the model shows the warm and cold fronts reuniting, sealing the seclusion and leading to the development of an occlusion. The fact that the introduction of the second-order closure boundary layer caused the seclusion to be nearly undetectable while the observations of maritime cold fronts clearly showed the presence of a seclusion suggests that there may be additional physical processes important in forming the seclusion that are not accounted for in the second-order closure simulation.

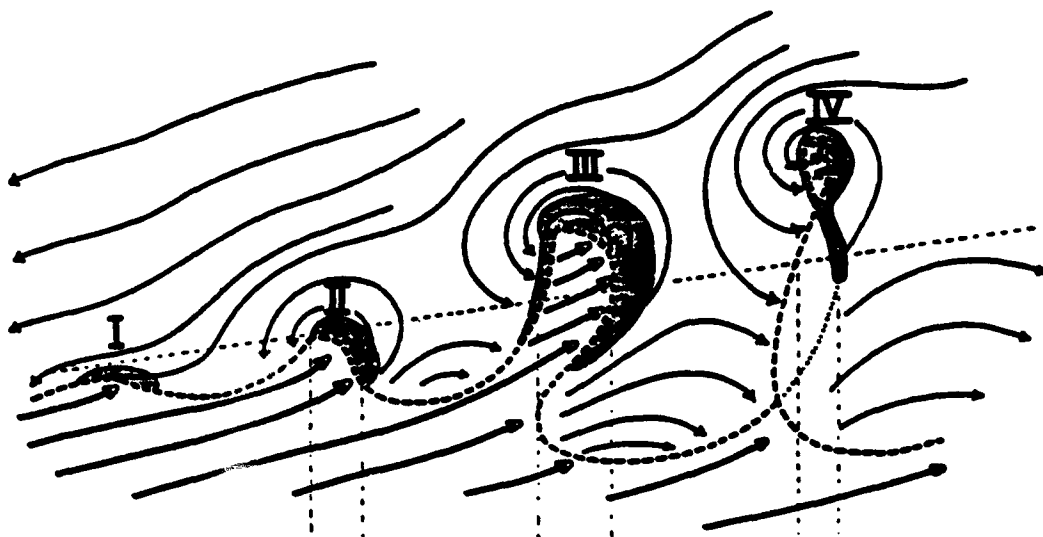


**Figure A.1:** Norwegian model schematic.

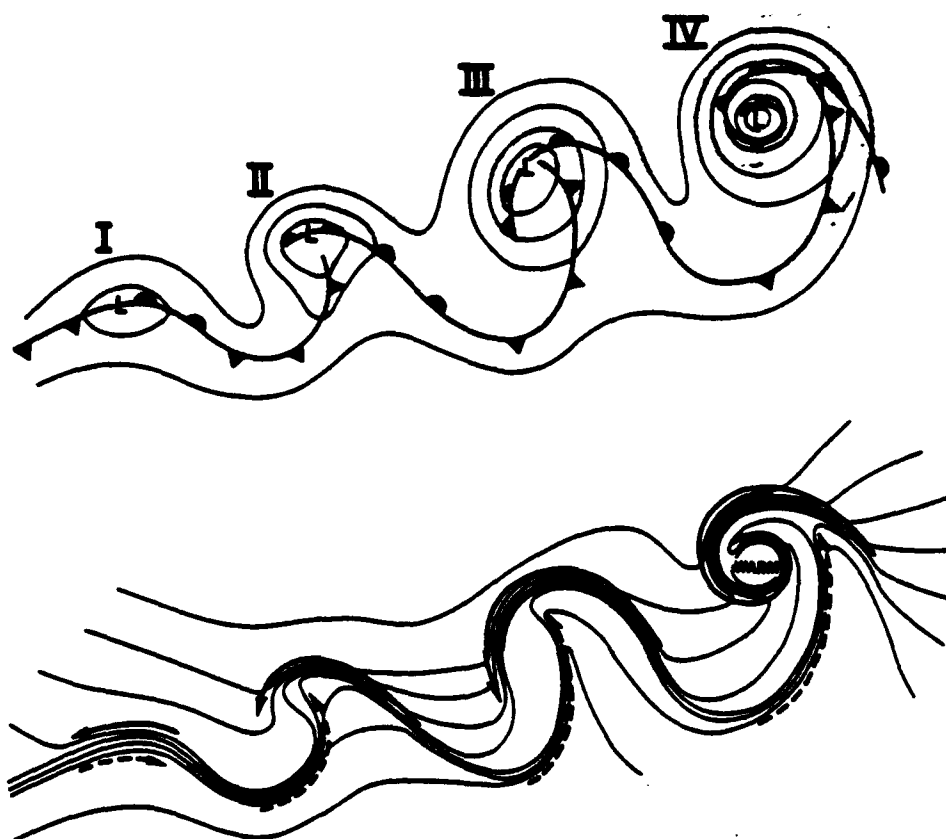


**Figure A.2:** SK model schematic.

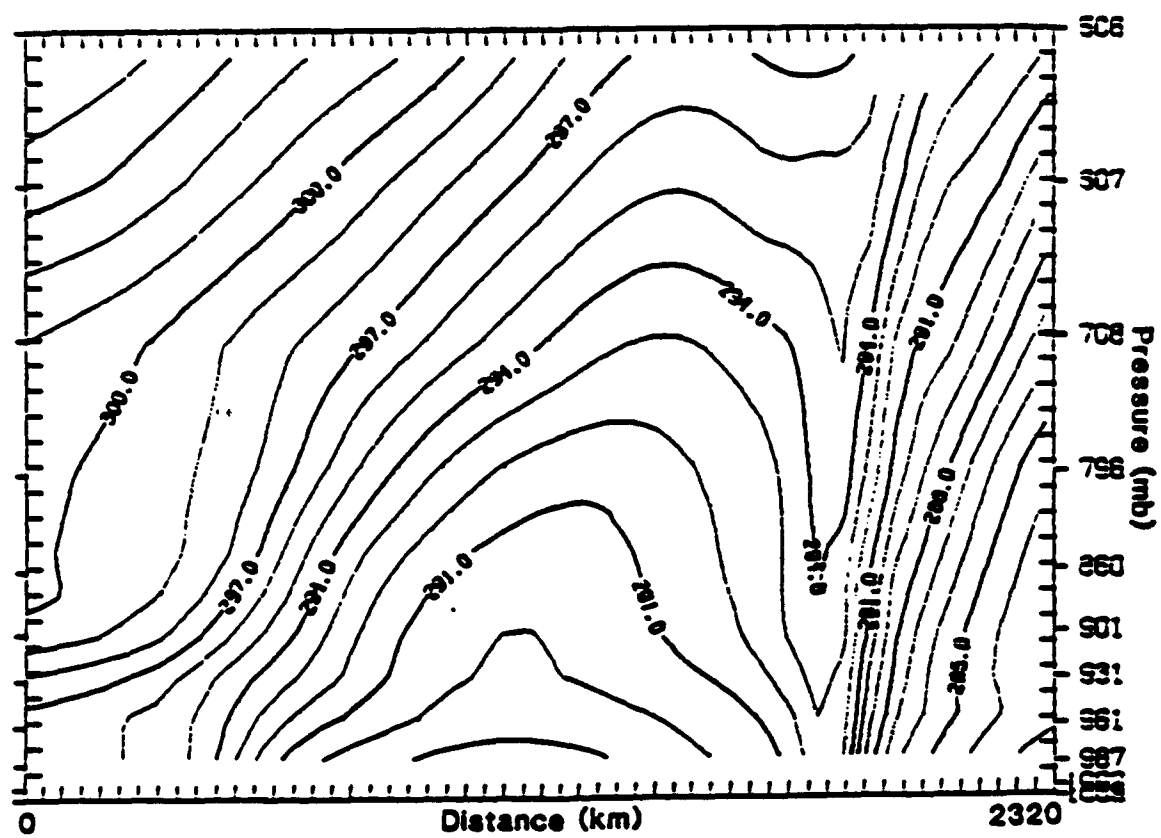
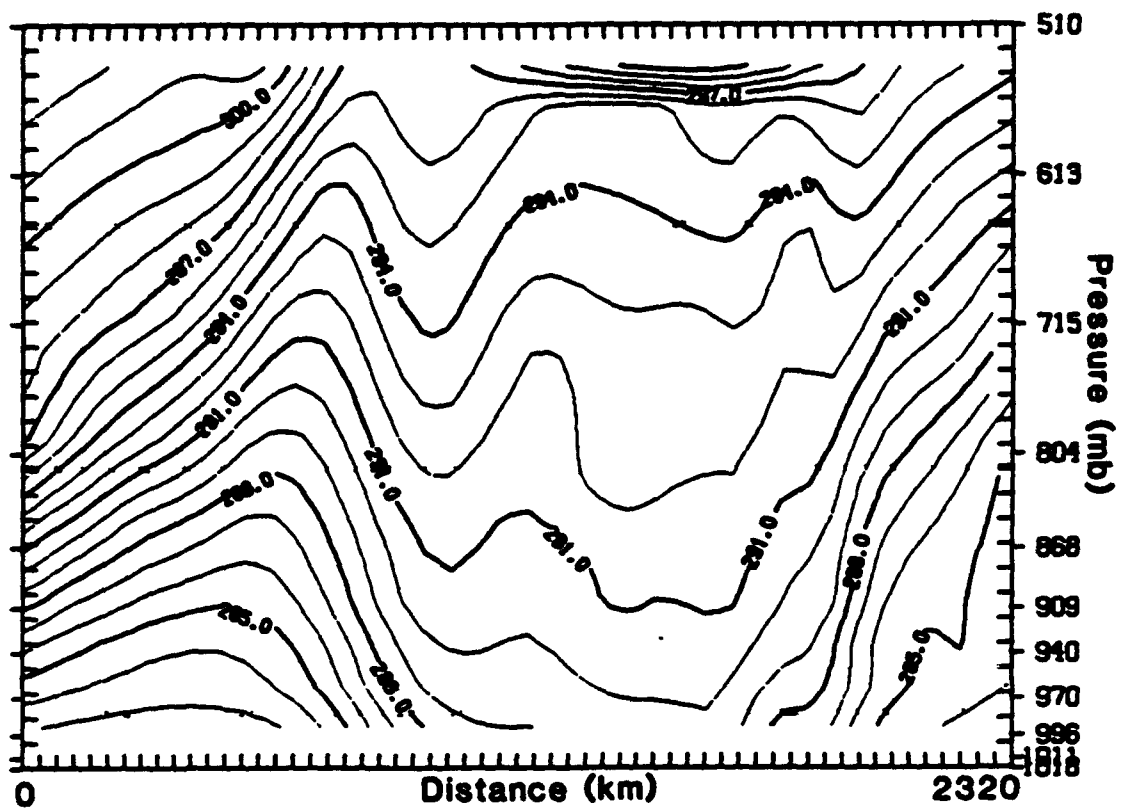


Figure A.3: Cross section of potential temperature at hour 84 (AI).



**Figure A.4:** Cross section of potential temperature at hour 120 (AI).



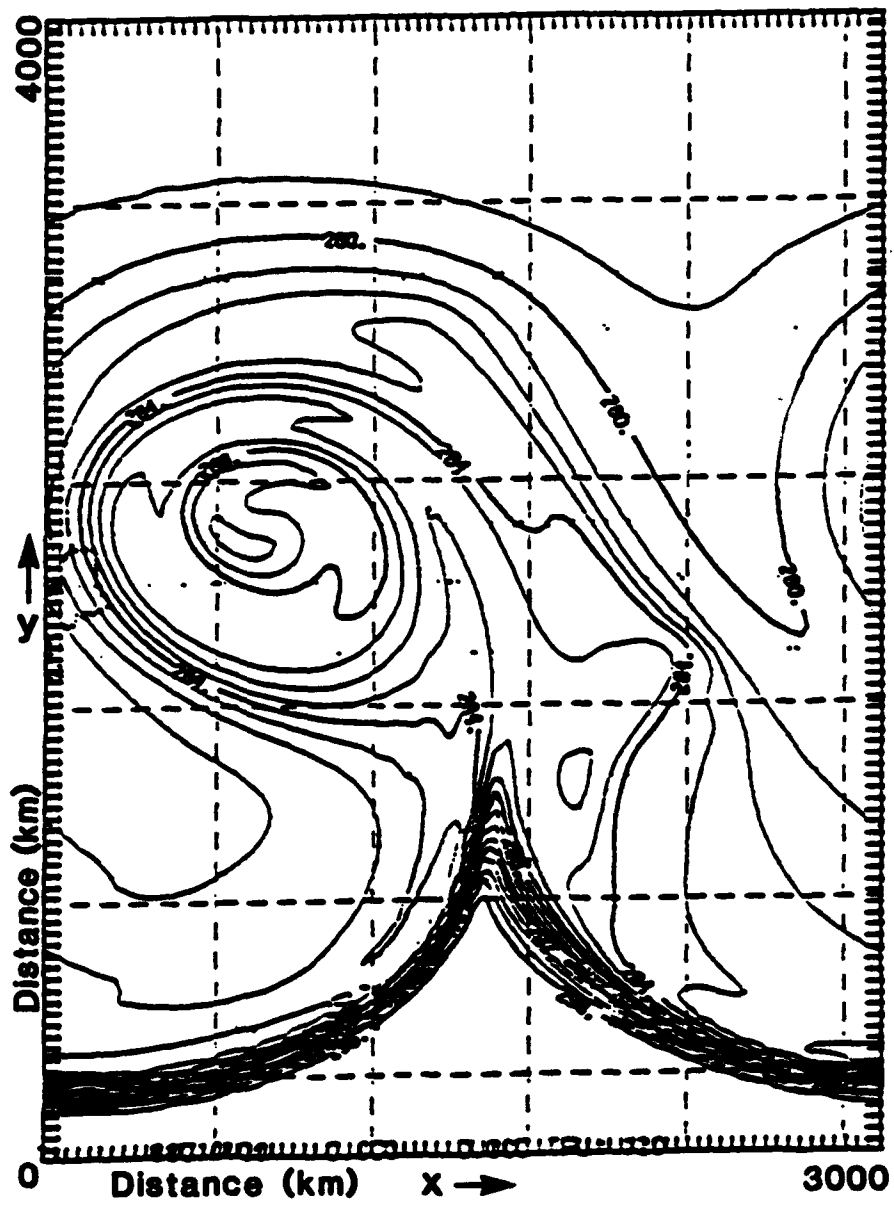


Figure A.5: Near-surface potential temperature distribution at hour 120 (AI).

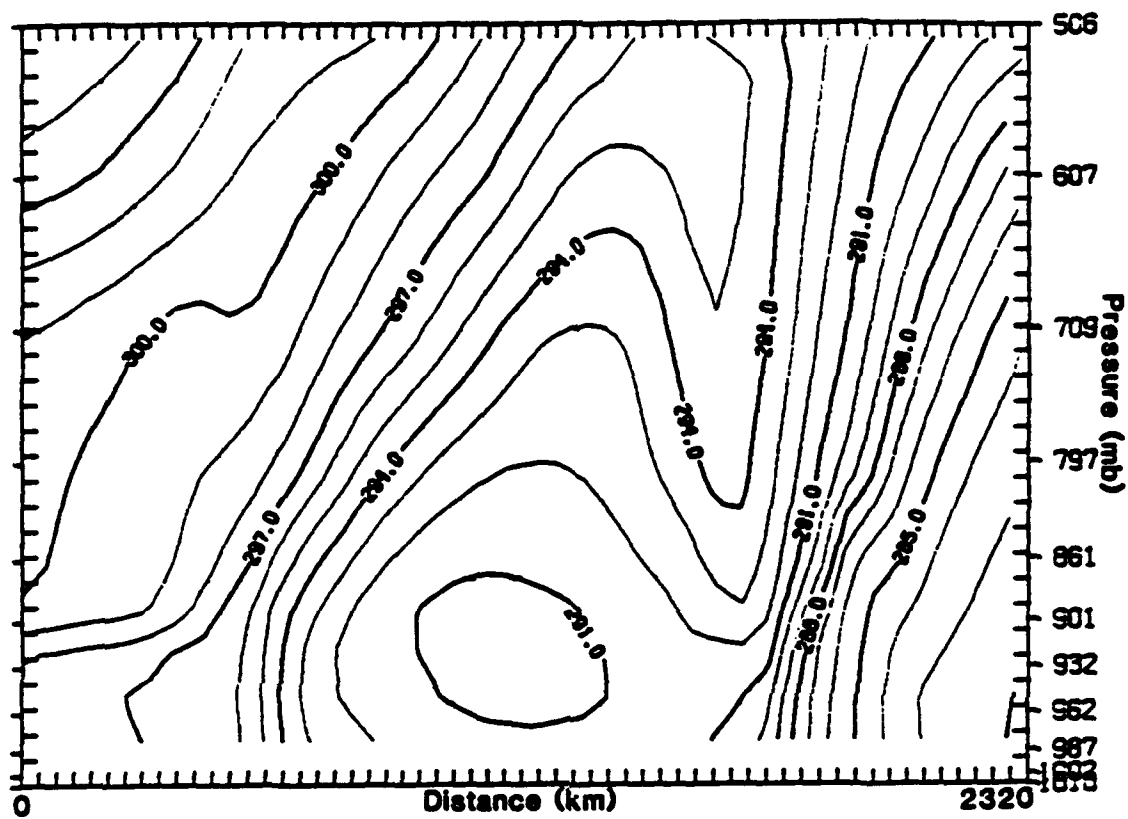
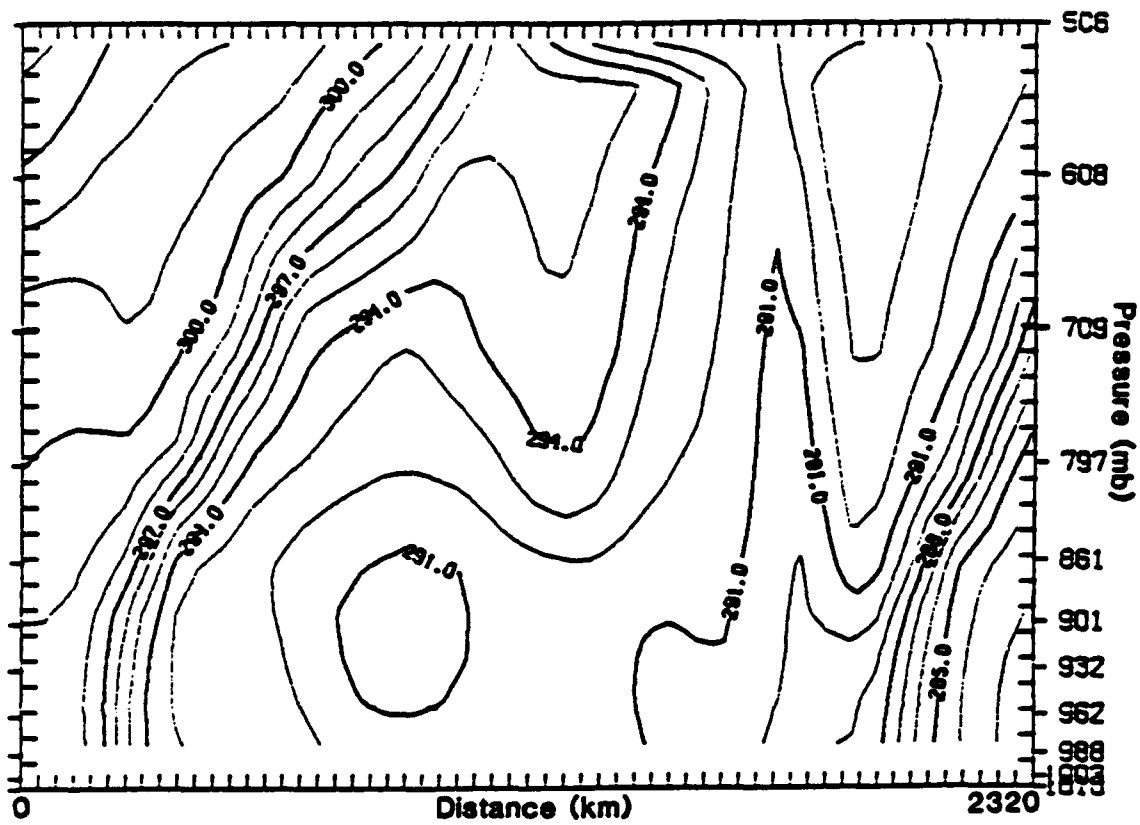


Figure A.6: Cross section of potential temperature (K) at hour 84 (20C).



**Figure A.7:** Cross section of potential temperature (K) at hour 108 (20C).

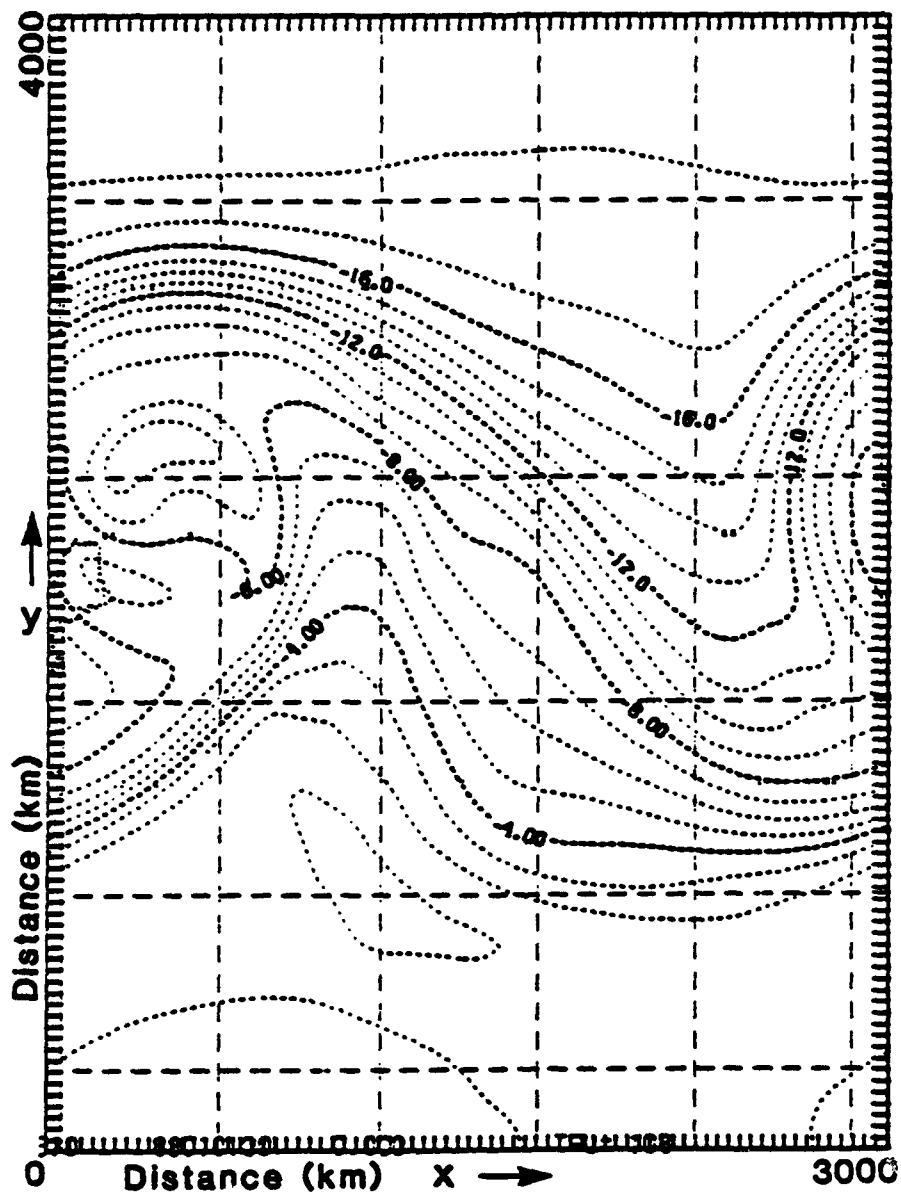


Figure A.8: 700 mb temperature distribution at hour 108 (20C).

## REFERENCES

- Andrews, D. G. and B.J. Hoskins, 1978: Energy spectra predicted by semi-geostrophic theories of frontogenesis, *J. Atmos. Sci.*, **35**, 509-512.
- Anthes, R. A., E.-Y. Hsie, and Y.-H. Kuo, 1986: Description of the Penn State/NCAR mesoscale model version 4 (MM4), NCAR Technical note.
- Arakawa, A. and V. R. Lamb, 1977: Computational design of the UCLA general circulation model, *Methods in Computational Physics*, Vol. 17, Academic Press, New York, 265 pp.
- Bjerknes, J., 1919: On the structure of moving cyclones, *Geofys. Publ.*, **1**, 1-8.
- Bjerknes J. and E. Palmen, 1937: Investigations of selected European cyclones by means of serial ascents, *Geofys. Publ.*, **12**, 1-62.
- Bjerknes, J. and H. Solberg, 1921: Meteorological conditions for the formation of rain, *Geofys. Publ.*, **2**, 1-60.
- Bjerknes, J. and H. Solberg, 1922: Life cycle of cyclones and the polar front theory of atmospheric circulation, *Geofys. Publ.*, **3**, 1-18.
- Blackadar, A. K., 1962: The vertical distribution of wind and turbulent exchange in a neutral atmosphere, *J. Geophys. Res.*, **67**, 3095-3103.
- Bluestein, H. B., 1986: Fronts and jet streaks: A theoretical perspective., *Mesoscale Meteorology and Forecasting*, P. S. Ray, ed., American Meteorological Society, Boston, MA, 793 pp.
- Blumen, W., 1980: A comparison between the Hoskins-Bretherton model of frontogenesis and the analysis of an intense surface frontal zone, *J. Atmos. Sci.*, **37**, 65-77.
- Blumen, W. 1981: The geostrophic coordinate transformation, *J. Atmos. Sci.*, **38**, 1100-1105.
- Blumen, W. and R. Wu, 1983: Baroclinic instability and frontogenesis with Eckman boundary layer dynamics incorporating the geostrophic momentum approximation, *J. Atmos. Sci.*, **40**, 2630-2637.
- Bond, N. A. and R. G. Fleagle, 1985: Structure of a cold front over the ocean, *Quart. J. R. Met. Soc.*, **111**, 739-759.

- Branscome, L. E., W. J. Gutowski, and D. A. Stewart, 1989: Effect of surface fluxes on the nonlinear development of baroclinic waves, *J. Atmos. Sci.*, **46**, 460-470.
- Burk, S. D., 1978: Use of a second-moment turbulence closure model for computation of refractive index structure coefficients, NAVENVPREDRSCHFAC Technical Report TR 78-04, NAVENVPREDRSCHFAC, Monterey, CA, 58 pp.
- Burk, S. D. and W. T. Thompson, 1989: A vertically-nested regional numerical weather prediction model with second-order closure physics, *Mon. Wea. Rev.*, **117**, 2305-2324.
- Businger, J. A., J. C. Wyngaard, Y. Isumi, and E. F. Bradley, 1971: Flux profile relationships in the atmospheric surface layer, *J. Atmos. Sci.*, **27**, 181-189.
- Carbone, R. E., 1982: A severe frontal rainband. Part I: Stormwide hydrodynamic structure, *J. Atmos. Sci.*, **39**, 258-279.
- Carnahan, B., H. A. Luther, and J. O. Wilkes, 1969: *Applied Numerical Methods*, Wiley and Sons, New York, 604 pp.
- Charney, J. G., 1947: The dynamics of long waves in a baroclinic westerly current, *J. Meteorol.*, **4**, 35-162.
- Deardorff, J. W., 1970a: A three-dimensional numerical investigation of the idealized planetary boundary layer, *Geophysical Fluid Dynamics*, **1**, Gordon and Breach Scientific Publishers, London, 410 pp.
- Deardorff, J. W., 1970b: Preliminary results from a numerical integration of the unstable planetary boundary layer, *J. Atmos. Sci.*, **27**, 1209-1211.
- Deardorf, J., 1972: Parameterization of the planetary boundary layer for use in general circulation models, *Mon. Wea. Rev.*, **100**, 93-106.
- Deardorf, J., 1978: Efficient prediction of ground surface temperature and moisture, with inclusion of a layer of vegetation, *J. Geophys. Res.*, **83**, 1889-1903.
- Dorian, P. B., S. E. Koch, and W. C. Skillman, 1988: The relationship between satellite-inferred frontogenesis and squall line formation, *Weather and Forecasting*, **3**, 319-342.
- Dutton, J. A., 1986: *The Ceaseless Wind*, Dover Publications, Inc., New York, 617 pp.
- Dyer, A. J., 1965: The flux gradient relation for turbulent heat transfer in the lower atmosphere, *Q. J. Roy. Met. Soc.*, **91**, 151-157.
- Eady, E., 1949: Long waves and cyclone waves, *Tellus*, **1**, 33-52.

- Eliassen, A., 1948: The quasi-static equations of motion, *Geofys. Publ.*, **17**, 44 pp.
- Eliassen, A., 1990: Transverse circulations in frontal zones, *Extratropical Cyclones: The Erik Palmén Memorial Volume*, C. W. Newton and E. O. Holopainen, eds., American Meteorological Society, Boston, MA.
- Fleagle, R. G., N. A. Bond, and W. A. Nuss: Atmosphere-ocean interaction in mid-latitude storms, *Meteorol. Atmos. Phys.*, **38**, 50-63.
- Gall, G., R. Blaklee, and R. C. J. Someerville, 1979: Baroclinic instability and the selection of the zonal scale of the transient eddies of middle latitudes, *J. Atmos. Sci.*, **36**, 767-784.
- Gall, R. L., R. T. Williams, and T. Clark, 1987: On the minimum scale of fronts, *J. Atmos. Sci.*, **44**, 2562-2574.
- Gall, R. L., R. T. Williams, and T. Clark, 1988: Gravity waves generated during frontogenesis, *J. Atmos. Sci.*, **45**, 2204-2219.
- Garner, S. T., 1989: Comments on "On a theory of the evolution of surface cold fronts," *J. Atmos. Sci.*, **46**, 1872-1873.
- Gidel, L. T., 1978: Simulation of the differences and similarities of warm and cold surface frontogenesis, *J. Geophys. Res.*, **83** (C2), 915-928.
- Gill, A. E., 1982: *Atmosphere-Ocean Dynamics*, Academic Press, Orlando, FL, 662 pp.
- Haltiner, G. J. and R. T. Williams, 1980: *Numerical Prediction and Dynamic Meteorology*, Wiley and Sons, New York, 477 pp.
- Haney, R. L., 1981: Lecture notes on Air-Sea Interaction, Naval Postgraduate School, Monterey, CA.
- Helfand, H. M. and J. C. Labraga, 1988: Design of a nonsingular level 2.5 second-order closure model for the prediction on atmospheric turbulence, *J. Atmos. Sci.*, **45**, 113-132.
- Hines, K. M. and C. R. Mechoso, 1993: Influence of surface drag on the evolution of fronts, *Mon. Wea. Rev.*, **121**, 1152-1175.
- Hodur, R. M., 1987: Evaluation of a regional model with an update cycle, *Mon. Wea. Rev.*, **115**, 2707-2718.
- Holton, J. R., 1979: *An Introduction to Dynamic Meteorology*, 2nd Ed., Academic Press, NY, 391 pp.

- Hoskins, B. J., 1971: Atmospheric frontogenesis models: Some solutions, *Quart. J. R. Met. Soc.*, **97**, 139-153.
- Hoskins, B. J., 1975: The geostrophic momentum approximation and the semi-geostrophic equations, *J. Atmos. Sci.*, **32**, 233-242.
- Hoskins, B. J., 1982: The mathematical theory of fronts, *Ann. Rev. Fluid Mech.*, **14**, 131-151.
- Hoskins, B. J. and F. P. Bretherton, 1972: Atmospheric frontogenesis models: mathematical formulation and solution, *J. Atmos. Sci.*, **29**, 11-37.
- Hoskins, B. J., and N. N. West, 1979: Baroclinic waves and frontogenesis. Part II: Uniform potential vorticity jet flows — cold and warm fronts, *J. Atmos. Sci.*, **36**, 1663-1680.
- Kaplan, M. L., J. W. Zack, V. C. Wong, and J. J. Tuccillo, 1982: Initial results from a mesoscale atmospheric simulation system and comparisons with the AVE-SESAME data set, *Mon. Wea. Rev.*, **110**, 1564-1590.
- Keyser, D., 1981: Frontogenesis in the planetary boundary layer of an amplifying, two-dimensional baroclinic wave, Ph.D. dissertation, Department of Meteorology, The Pennsylvania State University, University Park, PA.
- Keyser, D., 1986: Atmospheric fronts: An observational perspective, *Mesoscale Meteorology and Forecasting*, P. S. Ray, ed., American Meteorological Society, Boston, MA.
- Keyser, D. and R. A. Anthes, 1982: The influence of planetary boundary layer physics on frontal structure in the Hoskins-Bretherton horizontal shear model, *J. Atmos. Sci.*, **39**, 1783-1802.
- Keyser, D. and M. J. Pecnick, 1985: A two-dimensional primitive equation model of frontogenesis forced by confluence and horizontal shear, *J. Atmos. Sci.*, **42**, 1259-1282.
- Keyser, D. and M. J. Pecnick, 1987: The effect of along-front temperature variation in a two-dimensional primitive equation model of surface frontogenesis, *J. Atmos. Sci.*, **44**, 577-604.
- Keyser, D., and M. A. Shapiro, 1986: A review of the structure and dynamics of upper-level frontal zones, *Mon. Wea. Rev.*, **114**, 452-499.
- Keyser, D., M. J. Reeder, and R. J. Reed, 1988: A generalization of Petterssen's frontogenesis function and its relation to forcing of vertical motion, *Mon. Wea. Rev.*, **116**, 762-780.



- Koch, S. E., 1984: The role on an apparent mesoscale frontogenetic circulation in squall line initiation, *Mon. Wea. Rev.*, **112**, 2090-2110.
- Kuo, H. L., 1974: Further studies of the parameterization of the influence of cumulus convection on large scale flow, *J. Atmos. Sci.*, **31**, 1232-1240.
- Kuo, Y.-H., R. J. Reed, and S. Low-Nam, 1991a: Effects of surface energy fluxes during the early development and rapid intensification phases of seven explosive cyclones in the western Atlantic, *Mon. Wea. Rev.*, **119**, 457-476.
- Kuo, Y.-H., M. A. Shapiro, and E. G. Donall, 1991b: The interaction between baroclinic and diabatic processes in a numerical simulation of a rapidly intensifying extratropical marine cyclone, *Mon. Wea. Rev.*, **119**, 368-384.
- Kuo, Y.-H., R. J. Reed, and S. Low-Nam, 1992: Thermal structure and airflow in a model simulation of an occluded marine cyclone, *Mon. Wea. Rev.*, **121**, 2280-2297.
- Levy, G., 1989: Surface dynamics of observed maritime fronts, *J. Atmos. Sci.*, **46**, 1219-1232.
- Levy, G. and C. S. Bretherton, 1987: On a theory of the evolution of surface cold fronts, *J. Atmos. Sci.*, **44**, 3413-3418.
- Levy, G. and C. S. Bretherton, 1989: Reply (to comment by S. T. Garner), *J. Atmos. Sci.*, **46**, 1874-1875.
- Liu, T., K. Katsaros, and J. Businger, 1979: Bulk Parameterization of air-sea exchanges of heat and water vapor including the molecular constraints at the interface, *J. Atmos. Sci.*, **36**, 1722-1735.
- Louis, J.-F., 1979: A parametric model of vertical eddy fluxes in the atmosphere, *Boundary Layer Meteorol.*, **17**, 187-202.
- Madala, R. V., 1982: *Finite Difference Techniques for Vectorized Fluid Dynamics Calculation*, Springer-Verlag, Hamburg, FRG, 276 pp.
- Margules, M., 1906: Über temperaturschichtung in stationär bewegter und ruhender, *luft. Hann-Band. Meteorol. Z.*, 243-254.
- Mellor, G. L. and T. Yamada, 1974: A hierarchy of turbulence closure models for planetary boundary layers, *J. Atmos. Sci.*, **31**, 1791-1806.
- Mellor, G. L. and T. Yamada. 1982: Development of a turbulence closure model for geophysical fluid problems, *Rev. Geophys. Space Phys.*, **20**, 851-875.

- Moore, G. W. K., 1991: Frontogenesis in the presence of surface heating, *J. Atmos. Sci.*, **48**, 63-75.
- Neiman, P. J. and M. A. Shapiro, 1993: The life cycle of an extratropical marine cyclone. Part I: Frontal-cyclone evolution and thermodynamic air-sea interaction, *Mon. Wea. Rev.*, **121**, 2153-2176.
- Neiman, P. J., M. A. Shapiro, and L. S. Fedor, 1993: The life cycle of an extratropical marine cyclone. Part II: Mesoscale structure and diagnostics, *Mon. Wea. Rev.*, **121**, 2177-2199.
- Neiman, P. J., M. A. Shapiro, E. G. Donall, and C. W. Krietzberg, 1990: Diabatic modification of an extra-tropical marine cyclone warm sector by cold underlying water, *Mon. Wea. Rev.*, **118**, 1576-1590.
- Nuss, W. A., 1989: Air-sea interaction influences on the structure and intensification of an idealized marine cyclone, *Mon. Wea. Rev.*, **117**, 351-369.
- Ogura, Y. and D. Portis, 1982: Structure of the cold front observed in SESAME-AVE III and its comparison with the Hoskins-Bretherton frontogenesis model, *J. Atmos. Sci.*, **39**, 2773-2792.
- Orlanski, I. and B. Ross, 1977: The circulation associated with a cold front. Part I. Dry case, *J. Atmos. Sci.*, **34**, 1619-1633.
- Orlanski, I., B. Ross, L. Polinsky, and R. Shaginaw, 1985: Advances in the theory of atmospheric fronts, *Advances in Geophysics*, **28B**, Academic Press, Inc., NY, 252 pp.
- Palmen, E. and C. W. Newton, 1969: *Atmospheric Circulation Systems*, Academic Press, NY, 603 pp.
- Panofsky, H. A., 1963: Determination of stress front wind and temperature measurements, *Q. J. Roy. Met. Soc.*, **89**, 85-94.
- Pedlosky, J., 1979: *Geophysical Fluid Dynamics*, Springer-Verlag, NY, 624 pp.
- Petterssen, S., 1956: *Weather Analysis and Forecasting*, 2nd Ed., Vol. I, McGraw-Hill Book Co., NY, 428 pp.
- Phillips, N. A., 1956: The general circulation of the atmosphere: A numerical experiment, *Q. J. Roy. Meteorol. Soc.*, **82**, 123-164.
- Pinkerton, J. E., 1978: Numerical experiments on boundary layer effects on frontal structure, Ph.D. dissertation, Drexel University, Philadelphia, PA.

- Polavarapu, S. M. and W. R. Peltier, 1990: The structure and nonlinear evolution of synoptic scale cyclones: Life cycle simulations with a cloud-scale model, *J. Atmos. Sci.*, **47**, 2645-2672.
- Reed, R. J., 1990: Advances in knowledge and understanding of extratropical cyclones during the past quarter century: An overview, *Extra-Tropical Cyclones: The Erik Palmen Memorial Volume*, C. W. Newton and E. O. Holopainen, eds., American Meteorological Society, Boston, MA.
- Reeder, M. J., 1986: The interaction of a surface cold front with a prefrontal (sic.) thermodynamically well-mixed boundary layer, *Aust. Met. Mag.*, **34**, 137-148.
- Richtmeyer, R. D. and K. W. Morton, 1967: *Difference Methods for Initial Value Problems*, Wiley, New York.
- Sanders, F., 1955: An investigation of the structure and dynamics of an intense surface frontal zone, *J. Meteorol.*, **12**, 542-552.
- Shapiro, M. A., 1984: Meteorological tower measurements for a surface cold front, *Mon. Wea. Rev.*, **112**, 1634-1639.
- Shapiro, M. A. and D. Keyser, 1990: Fronts, jet streams, and the tropopause, *Extra-Tropical Cyclones: The Erik Palmen Memorial Volume*, C. W. Newton and E. O. Holopainen, eds., American Meteorological Society, Boston, MA.
- Shapiro, M. A., T. Harpel, D. Rotholl, and F. Mosher, 1985: The frontal hydraulic head: A micro-scale (1 km) triggering mechanism for mesoscale weather systems, *Mon. Wea. Rev.*, **111**, 1166-1183.
- Schubert, W. H., 1985: Semigeostrophic theory, *J. Atmos. Sci.*, **42**, 1770-1772.
- Stone, P. H., 1966: Frontogenesis by horizontal wind deformation fields, *J. Atmos. Sci.*, **23**, 455-465.
- Tennekes, H., 1973: A model for the dynamics of the inversion above a convective boundary layer, *J. Atmos. Sci.*, **30**, 558-567.
- Thomspon, W. T. and S. D. Burk, 1991: An investigation of an arctic front with a vertically nested mesoscale model, *Mon. Wea. Rev.*, **119**, 233-261.
- Williams, R. T., 1967: Atmospheric frontogenesis: A numerical experiment, *J. Atmos. Sci.*, **24**, 627-641.
- Williams, R. T., 1968: A note on quasi-geostrophic frontogenesis, *J. Atmos. Sci.*, **25**, 1157-1159.

- Williams, R. T., 1972: Quasi-geostrophic versus nongeostrophic frontogenesis, *J. Atmos. Sci.*, **29**, 3-10.
- Williams, R. T., 1974: Numerical simulation of steady-state fronts, *J. Atmos. Sci.*, **31**, 1286-1296.
- Williams, R. T. and J. Plotkin, 1968: Quasi-geostrophic frontogenesis, *J. Atmos. Sci.*, **25**, 201-206.
- Yamada, T. and G. L. Mellor, 1975: A simulation of the Wangara atmospheric boundary layer data, *J. Atmos. Sci.*, **32**, 2309-2329.

## INITIAL DISTRIBUTION LIST

	No. Copies
1. Defense Information Center Cameron Station Alexandria, VA 22304-6145	2
2. Library, Code 52 Naval Postgraduate School Monterey, CA 93943-5101	2
3. Chairman, Code MR Department of Meteorology Naval Postgraduate School Monterey, CA 93943-5101	1
4. Dr. William T. Thompson Naval Research Laboratory Marine Meteorology Division 7 Grace Hopper Avenue Monterey, CA 93943-5502	6
5. Dr. R. T. Williams, Code MR/Wu Department of Meteorology Naval Postgraduate School Monterey, CA 93943-5101	3
6. Dr. K. L. Davidson, Code MR/Ds Department of Meteorology Naval Postgraduate School Monterey, CA 93943-5101	1
7. Dr. R. H. Franke, Code MA/Fe Chairman, Department of Mathematics Naval Postgraduate School Monterey, CA 93943-5101	1

		No. Copies
8.	Dr. R. W. Garwood, Code OC/Gd Department of Oceanography Naval Postgraduate School Monterey, CA 93943-5101	1
9.	Dr. C. H. Wash, Code MR/Wx Department of Meteorology Naval Postgraduate School Monterey, CA 93943-5101	1
10.	Dr. P. Hirschberg, Code MR/Hs Department of Meteorology Naval Postgraduate School Monterey, Ca 93943-5101	1
11.	Dr. T. Holt, Code MR/Ht Department of Meteorology Naval Postgraduate School Monterey, CA 93943-5101	1
12.	Dr. W. Nuss, Code MR/Nu Department of Meteorology Naval Postgraduate School Monterey, CA 93943-5101	1
13.	Dr. M. Peng, Code MR/Pg Department of Meteorology Naval Postgraduate School Monterey, CA 93943-5101	1
14.	Ms. J. May Library, Code 84 Fleet Numerical Meteorology and Oceanography Center Monterey, CA 93943-5502	1

		No. Copies
15.	Dr. J. Hovermale Superintendent Naval Research Laboratory Marine Meteorology Division 7 Grace Hopper Avenue Monterey, CA 93943-5502	1
16.	Dr. S. D. Burk Naval Research Laboratory Marine Meteorology Division 7 Grace Hopper Avenue Monterey, CA 93943-5502	1
17.	Mr. J. Clark Naval Research Laboratory Marine Meteorology Division 7 Grace Hopper Avenue Monterey, CA 93943-5502	1
18.	Dr. J. Doyle Naval Research Laboratory Marine Meteorology Division 7 Grace Hopper Avenue Monterey, CA 93943-5502	1
19.	Dr. J. Glendening Naval Research Laboratory Marine Meteorology Division 7 Grace Hopper Avenue Monterey, CA 93943-5502	1
20.	Mr. R. Langland Naval Research Laboratory Marine Meteorology Division 7 Grace Hopper Avenue Monterey, CA 93943-5502	1
21.	Professor W. Blumen Campus Box 391 University of Colorado Boulder, CO 80309	1

		No. Copies
22.	Dr. Robert Bornstein Chairman, Department of Meteorology San Jose State University One Washington Square San Jose, CA 95192	1
23.	Dr. P. F. Lester Department of Meteorology San Jose State University One Washington Square San Jose, CA 95192	1
24.	M. R. J. Sznajder Manager, Meteorological Products Kavouras, Inc. 6301 34th Avenue South Minneapolis, MN 55450	1
25.	Dr. Alan Weinstein, Code 322 Director, Ocean and Atmospheric Physics Division Office of Naval Research 800 North Quincy Street Arlington, VA 22217-5660	1